



**Florentina Violeta  
Maxim**

**Estratégias *bottom up* para o controlo morfológico  
das partículas de BaTiO<sub>3</sub>**

**Bottom up strategies for the morphology control of  
BaTiO<sub>3</sub> particulates**



**Florentina Violeta  
Maxim**

**Estratégias *bottom up* para o controlo morfológico  
das partículas de BaTiO<sub>3</sub>**

**Bottom up strategies for the morphology control of  
BaTiO<sub>3</sub> particulates**

Dissertação apresentada à Universidade de Aveiro para cumprimento dos requisitos necessários à obtenção do grau de Doutor em Ciência e Engenharia de Materiais, realizada sob a orientação científica da Professora Doutora Paula Maria Lousada Silveirinha Vilarinho, Professora Associada do Departamento de Engenharia Cerâmica e do Vidro da Universidade de Aveiro, e da Doutora Paula Celeste da Silva Ferreira, Equiparada a Investigadora Auxiliar do Departamento de Engenharia Cerâmica e do Vidro - Centro de Investigação em Materiais Cerâmicos e Compósitos da Universidade de Aveiro.

Dissertation presented to the University of Aveiro to obtain the Doctor degree in Materials Science and Engineering, under the scientific guidance of Dr. Paula Maria Lousada Silveirinha Vilarinho, Associated Professor of the Department of Ceramics and Glass Engineering of the University of Aveiro, and Dr. Paula Celeste da Silva Ferreira, Assistant Researcher of the Department of Ceramics and Glass Engineering - Centre for Research in Ceramics and Composite Materials of the University of Aveiro.

I acknowledge the Portuguese  
Foundation for Science and Technology  
(FCT) for the financial support through  
the PhD grant (SFRH/BD/23375/2005)

*Pentru părinții mei Mihai și Geța  
A mi Tomas*

## **o júri**

presidente

**Prof. Doutor Aníbal Manuel de Oliveira Duarte**  
Professor Catedrático da Universidade de Aveiro

**Prof. Doutora Verónica Cortés de Zea Bermudez**  
Professora Associada com Agregação da Escola de Ciências da Vida e do Ambiente da  
Universidade de Trás-os-Montes e Alto Douro

**Prof. Doutor Tito da Silva Trindade**  
Professor Associado com Agregação da Universidade de Aveiro

**Prof. Doutora Paula Maria Lousada Silveirinha Vilarinho**  
Professora Associada da Universidade de Aveiro. (Orientadora)

**Doutor Vincenzo Buscaglia**  
Investigador Principal do Instituto de Energia e Interfases do Conselho Nacional de Investigação,  
Génova, Itália.

**Doutora Paula Celeste da Silva Ferreira**  
Investigadora Auxiliar do CICECO – Centro de Investigação em Materiais Cerâmicos e Compósitos  
da Universidade de Aveiro. (Co-Orientadora)

## agradecimentos

I could not end this thesis without mentioning all those people who supported and helped me during these unforgettable 4 years of my life. Certainly, there are many to whom I must be grateful, and the doubt that somebody is forgotten in these few words is always present. This is why, in the first place, I want to express my gratitude to all those who surrounded me and in some way contributed to this work.

First of all, I am deeply grateful to my supervisor *Prof. Dr. Paula Vilarinho* for her continuous support and encouragement, for her frequent suggestions and discussions and specially, for her confidence in me to perform this work and to introduce me to many scientific personalities in the field who helped in my scientific development. I am also very grateful to my co-supervisor *Dr. Paula Ferreira* for her scientific support and more importantly for her true friendship and patience through all these years showing me that to live far from home is not impossible.

I would like to express my sincere gratitude to all my colleagues from the Department of Ceramics and Glass Engineering for their valuable help and empathy during all these years, from the administrative and technical staff to all the PhD and Postdoc students from the 3<sup>rd</sup> floor, as well as all the members of the Electroceramics Group, for the excellent atmosphere of work and scientific interchange. Special thanks to *Marta, Augusto, Ana, Conceição, Célia, Rosário, Celeste, Aiyng* and *Igor* for their help in the characterization of my samples.

I express also my gratitude to *Prof. Paul Bowen* and *Dr Anne Aimable* for their scientific and moral support through my Short Term Scientific Mission under the COST 539 action at EPFL Switzerland, to *Dr. Rui Borges* and *Prof. Margarida Godinho* for the MoCVD samples preparation. I want to thank also to *Prof. Ian Reaney* for the inspiring discussions and to *Dr. Marc Willinger* for his help with the TEM.

I want to express all my thanks to the multinational group of friends I gained during this period: the Spanish girls *Merche* (my friend and confidant), *Eva* and *Laura* with their partners *Duncan* (English), *Harvey* (Cuban) and *Pedro* (Portuguese); the Portuguese girls *Xana* and *Susana* with their Cuban halves *Javier* and *Cheo*. And also to the Brazilian girls, *Flavita* and *Bi*, and the Portuguese girl *Aninha* „as minhas meninas da casa de felicidade”. All of them made my stay in Portugal very pleasant and unforgettable.

Special thanks to my dear Cuban friend, *Yoyi* and her husband *Yosvani* for preparing and helping me to find the true love, *Jorge Tomas Camejo* (mi Tomas) who, despite of his age, teach me and show me how simple is to be happy with small stuff. Por esto y por muchas otras cosas que tu sabes, te iubesc mult de tot.

Mii de multumiri *Ginutei* mele care m-a ascultat mereu, mi-a dat cele mai bune sfaturi si niciodata nu m-a lasat la greu aratandu-mi astfel adevaratul inteles al unei prietenii pe viata.

As vrea de asemenea sa multumesc d-nei Tanasescu pentru sprijinul si increderea acordate. Multumesc Corinei care a fost mereu „langa” mine prin intermediul internetului.

Si nu in ultimul rand vreau sa multumesc familiei mele dragi surorii mele *Amalia*, nepoatei *Irina* si cumnatului *Mihai* care mi-au fost mereu alaturi chiar la o distanta fizica de 4000 km. Si in special vreau sa multumesc parintilor mei *Geta* si *Mihai Craiciu* care au crezut, cred si or sa creada mereu in mine sprijinindu-ma mereu oricat de „copil neastamparat” am fost. **Multumesc lui Dumnezeu ca v-a ales pe voi ca sa-mi fiti parinti!**

## palavras-chave

Nanoestruturas, ferroelétricos, perovskites, titanato de bário, nanotubos de titanato de sódio ou de hidrogénio, síntese hidrotermal, síntese com aditivos, síntese em fase vapor, cinética, microscopia de força piezoelétrica.

## resumo

As propriedades funcionais dos materiais ferroelétricos tais como a polarização reversível, piroelectricidade, piezoelectricidade, elevada actividade óptica não linear e comportamento dielétrico não linear são fundamentais para a sua aplicação em sensores, microactuadores, detectores de infravermelhos, filtros de fase de microondas e memórias não-voláteis. Nos últimos anos, motivado pelas necessidades industriais de redução do tamanho dos dispositivos microelectrónicos, aumentando a eficiência volumétrica, tem sido feito um grande esforço ao nível da investigação para desenvolver estruturas ferroelétricas à escala micro- e nano- métrica. É sabido que a redução de tamanho em materiais ferroelétricos afecta significativamente as suas propriedades. Neste sentido e considerando que foi previsto teoricamente por cálculos *ab initio* que estruturas do tipo nanocilindros e nanodiscos apresentariam um novo tipo de ordem ferroelétrica e, na expectativa de alcançar conhecimento para o desenvolvimento de uma nova geração de dispositivos microelectrónicos, existe um grande interesse em desenvolver métodos de fabrico de nanoestruturas ferroelétricas unidimensionais (1D) tais como nanocilindros e nanotubos.

As estratégias de fabrico de nanoestruturas 1D até agora descritas na literatura indicam claramente as dificuldades inerentes à sua preparação. Existem duas grandes vias de síntese destas nanoestruturas: i) o método “top-down” que consiste na redução de tamanho de um dado material até à obtenção duma estrutura 1D; e ii) o método “bottom-up” em que átomos, iões e moléculas são agrupados para formar um material 1D. O método “top down” envolve em geral técnicas de desgaste, como o uso do feixe de electrões, que apesar de permitirem elevada precisão no posicionamento e no controlo do tamanho, falham em termos de resolução, exigem muito tempo e causam facilmente defeitos que deterioram as propriedades físicas destes materiais. Na metodologia “bottom up” a utilização de moléculas ou estruturas “molde” tem sido a mais explorada. As estruturas 1D podem também ser preparadas sem recorrer a “moldes”. Neste caso a agregação orientada é promovida pelo recurso a aditivos que controlam o crescimento dos cristais em direcções preferenciais.

Neste contexto, neste trabalho utilizaram-se duas estratégias “bottom up” de baixo custo para a preparação de nanopartículas de titanato de bário ( $\text{BaTiO}_3$ ) com morfologia controlada:

- 1) síntese química (em solução e em fase vapor) com utilização de nanotubos de titanato (NTs) como “moldes” e precursores de titânio
- 2) síntese química em solução com presença de aditivos.

Os nanotubos de titanato de sódio foram preparados por síntese hidrotermal. Como existiam muitas dúvidas acerca da natureza estrutural e do mecanismo de formação dos NTs, a parte inicial do trabalho foi dedicada à realização de um estudo sistemático dos parâmetros intervenientes na síntese e à caracterização da sua estrutura e microestrutura. Foi demonstrado que os NTs têm a fórmula geral  $\text{A}_2\text{Ti}_2\text{O}_5$  ( $\text{A} = \text{H}^+$  or  $\text{Na}^+$ ), e não  $\text{TiO}_2$  (anátase) com defendido por vários autores na literatura, e podem ser preparados por método hidrotermal em meio fortemente alcalino usando como fonte de titânio  $\text{TiO}_2$  comercial na forma de anátase ou rútilo. A menor reactividade do rútilo exige temperaturas de síntese superiores ou tempos de reacção mais longos. A forma tubular resulta do tratamento hidrotermal e não de processos de lavagem e neutralização subsequentes. Se os NTs forem tratados após a síntese hidrotérmica em água a  $200\text{ }^\circ\text{C}$ , transformam-se em nanocilindros.

Uma das partes principais desta tese consistiu na investigação do papel dos NTs de titanato no crescimento anisotrópico de  $\text{BaTiO}_3$ . O potencial funcionamento dos NTs como “moldes” para além de precursores foi testado em reacção com hidróxido de bário em síntese em solução e por reacção com um precursor orgânico de bário em fase vapor.

Tendo por base os estudos cinéticos realizados, bem como as alterações estruturais e morfológicas das amostras, é possível concluir que a formação do  $\text{BaTiO}_3$  a partir de NTs de titanato de sódio, ocorre por dois mecanismos dependendo da temperatura e tempo de reacção. Assim, a baixa temperatura e curto tempo de reacção verifica-se que se formam partículas dendríticas de  $\text{BaTiO}_3$  cuja superfície é bastante irregular (“wild”) e que apresentam estrutura pseudo-cúbica. Estas partículas formam-se por reacção topotáctica na fronteira dos nanotubos de titanato de sódio. A temperaturas mais altas e/ou reacções mais longas, a reacção é controlada por um mecanismo de dissolução e precipitação com formação de dendrites de  $\text{BaTiO}_3$  tetragonais com superfície mais regular (“seaweed”). A microscopia de força piezoeléctrica mostrou que as dendrites “seaweeds” possuem actividade piezoeléctrica superior à das dendrites “wild”, o que confirma o papel desempenhado pela estrutura e pela concentração de defeitos na rede na coerência e ordem ferroeléctrica de nanoestruturas.

Os nossos resultados confirmam que os NTs de titanato não actuam facilmente como “moldes” na síntese em solução de BaTiO<sub>3</sub> já que a velocidade de dissolução dos NTs em condições alcalinas é superior à velocidade de formação do BaTiO<sub>3</sub>.

Assumindo que a velocidade de reacção dos NTs com o precursor de bário é superior em fase vapor, efectuou-se a deposição de um precursor orgânico de bário por deposição química de vapor sobre um filme de NTs de titanato de sódio depositados por deposição electroforética. Estudou-se a estabilidade dos NTs nas diferentes condições do reactor. Quando os NTs são tratados a temperaturas superiores a 700 °C, ocorre a transformação dos NTs em nanocilindros de anatase por um mecanismo de agregação orientada. Quando se faz a deposição do precursor de bário, seguida de calcinação a 700 °C em atmosfera oxidante de O<sub>2</sub>, verifica-se que a superfície dos NTs fica coberta com nanocristais de BaTiO<sub>3</sub> independentemente da concentração de bário. O papel dos NTs de titanato no crescimento anisotrópico de BaTiO<sub>3</sub> em fase vapor é assim descrito pela primeira vez.

Em relação à metodologias de crescimento de partículas na ausência de “moldes” mas com aditivos fez-se um estudo sistemático utilizando 5 aditivos de natureza diferente. As diferenças entre aditivos foram sistematizadas tendo em conta as diferenças estruturais e morfológicas verificadas. Está provado que os aditivos podem funcionar como modificadores de crescimento cristalino por alteração do seu padrão de crescimento ou por alteração da cinética de crescimento das faces cristalográficas do cristal. Entre os aditivos testados verificou-se que o ácido poliacrílico adsorve em faces específicas do BaTiO<sub>3</sub> alterando a cinética de crescimento e induzindo a agregação orientada das partículas. O polivinilpirrolidona, o docecil sulfato de sódio e hidroxipropilmetilcelulose actuam mais como inibidores de crescimento do que como modificadores do tipo de crescimento. A D-frutose aumenta a energia de activação da etapa de nucleação não ocorrendo formação de BaTiO<sub>3</sub> para as mesmas condições dos outros aditivos.

Esta tese clarifica o papel dos NTs de titanato de sódio enquanto precursores e “moldes” no crescimento anisotrópico de BaTiO<sub>3</sub> em solução e em fase vapor. É feita também a abordagem do controlo morfológico do BaTiO<sub>3</sub> através do uso de aditivos. As estratégias de preparação de BaTiO<sub>3</sub> propostas são de baixo custo, reprodutíveis e fáceis de efectuar. Os resultados contribuem para uma melhor compreensão da relação tamanho – morfologia – propriedade em materiais ferroelétricos nanométricos com vista à sua potencial aplicação.

**keywords**

Nanostructures, ferroelectrics , perovskites, barium titanate, titanate nanotubes, hydrothermal synthesis, additive assisted synthesis, vapour synthesis, kinetics, piezoresponse force microscopy

**abstract**

For applications as sensors, microactuators, infrared detectors, microwave phase filters and non-volatile memories, functional properties of ferroelectric materials such as switchable polarization, piezoelectricity, high non-linear optical activity, pyroelectricity, and non-linear dielectric behavior are indispensable. More recently and motivated by the industrial need of reduction of size of microelectronics devices to increase volumetric efficiency, many efforts have been dedicated to the development of micro- and nano- scale ferroelectric structures. This is because as dimensions decrease, ferroelectric materials exhibit a pronounced size effect, which is manifested in a significant deviation from bulk properties.

In this sense, interest in the fabrication of one-dimensional (1D) ferroelectric nanostructures such as nanowires (NWs) and nanotubes (NTs) has increased in the recent years for two important reasons. First, the study of these systems can provide useful information for the fabrication of the next generation, fully three-dimensional FeRAM structures with the required bit density. Second, detailed ab initio calculations have predicted a new kind of ferroelectric order in nanorods and nanodisks.

Nevertheless, the fabrication strategies proposed in the literature clearly indicate that the synthesis of 1D nanostructures is non trivial. There are two main approaches for the preparation of 1D materials. The so called **top-down** methods that consist in the size reduction until 1D nano structures are obtained and **bottom-up** methods when atoms, ions or molecules are assembled to form a 1 D nano structure. The top-down methods based on electron-beam (EB) assisted fabrication although they provide high-precision positioning and size control they are limited in resolution, time-consuming and are prone to processing damages. Among the bottom-up procedures, *template assisted* methods have been the most tried and tested for the preparation of 1D ferroelectrics. There are two main template based methods, denoted as 'physical' and 'chemical' templating. Other bottom-up approaches used for the 1D nanostructure fabrication include *non-template additive assisted* methods. In this case the assembling is achieved via the control of the crystal growth along preferential directions in the presence of specific additives.

Within this context in this work two low cost bottom-up synthesis strategies for the morphology control of BaTiO<sub>3</sub> are exploited: 1) a chemical template methodology, starting from TiO<sub>2</sub> NTs as templating agents and 2) a non template additive assisted syntheses.

For the chemical templated approach  $\text{TiO}_2$  NTs were fabricated by an hydrothermal method. Because there are still questions to be answered regarding the anisotropic growth of titanium based NTs, namely the structure and the formation mechanism, the initial part of the present work is dedicated to systematic studies of titanium based NTs to be used as template for the further growth of  $\text{BaTiO}_3$ . It is demonstrated that layered titanate nanotubes (TiNTs) with general formula  $\text{H}_2\text{Ti}_2\text{O}_5$  (and not anatase as others claimed) can be prepared by hydrothermal method in high alkaline medium starting from commercial  $\text{TiO}_2$  (anatase and rutile). Concerning the formation mechanism of the NTs it is shown that the tubular shape is formed during the hydrothermal synthesis and it is not related with the after synthesis washing process, clarifying the under going discussion on the topic. Moreover, the NTs to anatase nanorods (NRs) transformation during the post synthesis hydrothermal treatment is explained and finally the present work demonstrates that both commercial anatase and rutile are transformed in layered titanate nanotubes under high alkaline hydrothermal conditions, but because of the low reactivity of rutile, high temperatures or long reaction times were required.

As a main part of this work, the effective template role of TiNTs for the anisotropic growth of  $\text{BaTiO}_3$  is systematically addressed. For that the potential template role of TiNTs is elucidated in two low cost chemical template methods: *i*) solution based hydrothermal treatment of TiNTs in the presence of  $\text{Ba}(\text{OH})_2$  as barium precursor and *ii*) vapor phase reaction of metal-organic barium compound in the presence of TiNTs.

By a kinetic analysis and structural and morphological studies, it is demonstrated that during hydrothermal synthesis from layered titanate nanotubes, anisotropic  $\text{BaTiO}_3$  forms via two mechanisms depending on the temperature and time. At low temperatures ( $90^\circ\text{C}$ ) and short reaction time (# hours) “wild” type  $\text{BaTiO}_3$  dendritic particles with *pseudo* cubic structure are formed through a phase boundary topotactic reaction. At higher temperatures and/or for longer times, the reaction is controlled by a dissolution precipitation mechanism and “seaweed” type  $\text{BaTiO}_3$  dendrites with tetragonal structure are formed. By piezoresponse force microscopy measurements it is demonstrated that the “seaweed” type  $\text{BaTiO}_3$  dendrites have higher piezoactivity then the “wild” type and it is clearly revealed the role of the structure and the lattice defect concentration on the polarization coherency and ferroelectric order of the dendritic particles.

Our results unambiguously elucidated why TiNTs do not routinely act as templates for the hydrothermal formation of 1D BaTiO<sub>3</sub>. This is because the dissolution rate of the TiNTs under high alkaline hydrothermal conditions is higher than the barium titanate formation.

Consequently and assuming that the reaction of TiNTs with barium precursor in vapor phase is faster than the NTs transformation an original approach based on chemical vapor deposition of a metal-organic barium precursor (MoCVD) on TiNTs is proposed in this work. It is demonstrated that TiNTs are stable under MoCVD conditions and temperature. When the TiNTs are subsequently thermal treated at temperatures higher than 700 °C in O<sub>2</sub> atmosphere they transform into TiO<sub>2</sub> anatase nanorods (NRs) by an oriented attachment mechanism. After the barium precursor deposition on TiNTs and followed by annealing at 700 °C in O<sub>2</sub> atmosphere round shaped BaTiO<sub>3</sub> nanocrystals are covering the TiNTs surface independently on barium concentration. When the annealing temperature and titanium concentration increase the barium titanate nanoparticles seem to be segregated and NRs of barium deficient phases are formed. The role of the TiNTs on the anisotropic growth of barium titanate in vapor phase reaction is described for the first time in this work.

Regarding the non template additive assisted syntheses the effect of additives on the morphological control of BaTiO<sub>3</sub> particles is systematically addressed. Different types of additives were tested on the synthesis of BaTiO<sub>3</sub> and the structural changes of the nanoparticles assessed and related with the nature of the additive. It is proved that additives can be used as crystal growth modifiers by changing the growth habit or kinetically controlling the growth rate of the various crystallographic facets of the crystals. All the tested additives influence the growth of BaTiO<sub>3</sub>, but their role is distinctly different; poly(acrylic acid) (PAA) adsorbs on specific crystallographic faces changing the growth kinetics and inducing the oriented attachment of the particles; poly(vinyl pyrrolidone) (PVP), sodium dodecylsulfate (SDS) and hydroxypropylmethylcellulose (HPMC) act as growth inhibitors rather than crystal habit modifiers resulting in small crystals (26 nm); and D-Fructose appears to increase the activation energy for nucleation and no crystalline BaTiO<sub>3</sub> is formed under the same conditions used for the other additives.

In conclusion, the role of TiNTs as template agents for the growth of anisotropic BaTiO<sub>3</sub> in solution is clarified and the concept in vapour phase reaction is proved. In addition the effect of selected additives on the morphology control of BaTiO<sub>3</sub> nanoparticles is presented. The proposed preparation strategies for anisotropic BaTiO<sub>3</sub> nanostructures are low cost, reproducible and “user friendly”. The results clearly contribute to a better understanding of the size – shape - properties relationship in nano ferroelectrics envisaging future applications.

## Table of contents

LIST OF FIGURES.....	i
LIST OF TABLES .....	VIII
LIST OF SYMBOLS.....	IX
LIST OF ABBREVIATIONS.....	X
<b>1 BACKGROUND, MOTIVATION AND OBJECTIVES .....</b>	<b>1</b>
<b>1.1 Ferroelectricity and Piezoelectricity: Basic Concepts.....</b>	<b>1</b>
1.1.1 Ferroelectric phase transitions .....	3
1.1.2 Ferroelectric and ferroelastic domains .....	5
1.1.3 Polarization switching and hysteresis loop .....	6
<b>1.2 Ferroelectric materials: structure, applications and future trends.....</b>	<b>8</b>
1.2.1 Perovskite structure.....	9
1.2.2 Applications and trends .....	10
<b>1.3 Size and shape effect on ferroelectricity .....</b>	<b>16</b>
1.3.1 Instability of ferroelectricity at nano-scale .....	18
1.3.2 Concepts regarding the ferroelectricity at nanoscale.....	24
1.3.3 Intrinsic and extrinsic size effects on the ferroelectricity .....	28
<b>1.4 Synthesis strategies for morphology control of ferroelectric nanoparticles.....</b>	<b>38</b>
1.4.1 Template-directed methods .....	39
1.4.2 Additive assisted methods and other methods .....	44
<b>1.5 Summing up.....</b>	<b>47</b>
<b>1.6 Motivation and Objectives.....</b>	<b>48</b>
<b>2 EXPERIMENTAL PROCEDURES AND CHARACTERIZATION TECHNIQUES .....</b>	<b>51</b>
<b>2.1 Hydrothermal synthesis.....</b>	<b>51</b>
2.1.1 General conditions used in this work .....	53
<b>2.2 Powder X-ray diffraction .....</b>	<b>53</b>
2.2.1 Experimental conditions used in this work.....	56
<b>2.3 Vibrational spectroscopy- InfraRed and Raman.....</b>	<b>56</b>
2.3.1 Experimental conditions used in this work.....	58

<b>2.4</b>	<b><i>Electron microscopy</i></b> .....	<b>58</b>
2.4.1	Experimental conditions used in this work.....	62
<b>2.5</b>	<b><i>Piezoelectric force microscopy</i></b> .....	<b>62</b>
2.5.1	Experimental conditions used in this work.....	66
<b>2.6</b>	<b><i>Other analysis</i></b> .....	<b>67</b>
2.6.1	Thermal analysis.....	67
2.6.2	Particles size measurements.....	68
2.6.3	Chemical analysis.....	69
<b>2.7</b>	<b><i>Summing up</i></b> .....	<b>69</b>
<b>3</b>	<b>TITANIUM PRECURSORS FOR CHEMICAL TEMPLATE APPROACHES...</b>	<b>70</b>
<b>3.1</b>	<b><i>Motivation</i></b> .....	<b>70</b>
<b>3.2</b>	<b><i>Materials preparation</i></b> .....	<b>72</b>
<b>3.3</b>	<b><i>Results</i></b> .....	<b>73</b>
3.3.1	The influence of the synthesis conditions.....	73
3.3.2	The influence of post synthesis treatments.....	78
3.3.3	The influence of titanium precursor.....	86
<b>3.4</b>	<b><i>Discussion</i></b> .....	<b>89</b>
3.4.1	TiNTs structure.....	89
3.4.2	Post-synthesis neutralization.....	91
3.4.3	Anatase NRs.....	93
3.4.4	Using rutile as precursor.....	94
<b>3.5</b>	<b><i>Summing up</i></b> .....	<b>95</b>
<b>4</b>	<b>CHEMICAL TEMPLATE METHODS.....</b>	<b>97</b>
<b>4.1</b>	<b><i>Motivation</i></b> .....	<b>98</b>
<b>4.2</b>	<b><i>Solution based synthesis of BT using TiNTs precursors</i></b> .....	<b>99</b>
4.2.1	Materials preparation.....	99
4.2.2	Results.....	101
4.2.2.1	Hydrothermal Synthesis of BT.....	101
4.2.2.2	Kinetic Study.....	109
4.2.2.3	Nanoscale piezoelectric response.....	121
4.2.3	Discussion- solution based synthesis using TiNTs precursors.....	127
<b>4.3</b>	<b><i>Vapor phase synthesis of BT using TiNTs precursors</i></b> .....	<b>134</b>
4.3.1	Materials preparation.....	134
4.3.2	Results.....	137
4.3.2.1	Structural and morphological evolution of TiNTs.....	137
4.3.2.2	MoCVD synthesis.....	140
4.3.3	Discussion – MoCVD synthesis using TiNTs.....	146

<b>4.4</b>	<b>Summing up.....</b>	<b>148</b>
<b>5</b>	<b>NON TEMPLATE ADDITIVE- ASSISTED METHODS .....</b>	<b>151</b>
<b>5.1</b>	<b>Motivation.....</b>	<b>151</b>
<b>5.2</b>	<b>Materials preparation.....</b>	<b>153</b>
<b>5.3</b>	<b>Results.....</b>	<b>155</b>
5.3.1	Using Polymers .....	155
5.3.2	Using surfactants .....	160
5.3.3	Using carbohydrates .....	163
<b>5.4</b>	<b>Discussion.....</b>	<b>166</b>
5.4.1	Effect of PAA .....	168
5.4.2	Effect of PVP .....	170
5.4.3	Effect of SDS .....	170
5.4.4	Effect of HPMC .....	171
5.4.5	Effect of D-Fructose .....	172
<b>5.5</b>	<b>Summing up.....</b>	<b>173</b>
<b>6</b>	<b>GENERAL CONCLUSIONS AND FUTURE WORK.....</b>	<b>175</b>
	<b>REFERENCES.....</b>	<b>179</b>
	<b>LIST OF PUBLICATIONS.....</b>	<b>204</b>

## List of figures

Figure 1.1 The 32 crystallographic classes. <sup>5</sup> .....	2
Figure 1.2 Piezoelectric effects (direct and converse) in ferroelectric ceramics <sup>10</sup> .....	3
Figure 1.3 TiO <sub>6</sub> octahedra of a) tetragonal, b) orthorhombic and c) rhombohedral-type (structures occurring with BaTiO <sub>3</sub> crystals. The arrows show the direction of the spontaneous polarization due to the off-center displacement indicating the strong relation between the electrical response and the crystal structure <sup>15</sup> .....	4
Figure 1.4 a) Surface charge and depolarizing field ( $E_d$ ) associated with spontaneous polarization ( $P_s$ ); b) Formation of 180° domains to minimize the electrostatic energy; c) Schematic representation of 180° and 90° domain walls. <sup>20</sup> .....	6
Figure 1.5 a) P-E hysteresis and b) S-E butterfly loops used for the identification of ferroelectrics. <sup>4,5</sup> .....	7
Figure 1.6 The BT structure. At room temperature and atmospheric pressure the structure is tetragonal with Ba <sup>2+</sup> and Ti <sup>4+</sup> ions displaced relative to the O <sup>2-</sup> ions. <sup>24</sup> .....	10
Figure 1.7 Applications of bulk and film electronic ceramic materials <sup>10</sup> .....	11
Figure 1.8 Multilayer Ceramic Capacitor ( <a href="http://www.avx.com/docs/Catalogs/cdesc.pdf">http://www.avx.com/docs/Catalogs/cdesc.pdf</a> ). 12	
Figure 1.9 Schematic diagrams of high density architecture for non-volatile FeRAMs. <sup>37</sup> ..	14
Figure 1.10 3D FeCap a) pin-shaped type and b) cup-shaped type <sup>41</sup> .....	16
Figure 1.11 Relative dielectric constant $\epsilon_r$ at 104 Hz and loss $\tan\delta$ of BT ceramics as a function of temperature. $\tan\delta$ reported for 50 nm sample at three frequency values: 102, 104, and 106 Hz. The permittivity peak of fine-grained ceramics is remarkably broadened and rounded in comparison to coarse ceramics. The dielectric losses of the fine grained ceramics are rather small. <sup>49</sup> .....	19
Figure 1.12 Part of the X-ray diffraction pattern for BT ceramics with different grain size (50–1200 nm) at room temperature. The splitting of the (200)/(002) peak is no longer observed for the nanocrystalline ceramics and the patterns apparently correspond to ( $Pm3m$ ) cubic symmetry. <sup>50</sup> .....	20
Figure 1.13 Evolution of Raman spectra as a function of crystallite size obtained for the BT powders at room temperature. The average crystallite sizes are indicated in parentheses. Peaks originating from BaCO <sub>3</sub> and internal defects are marked by closed triangles ( $\blacktriangledown$ ) and diamonds ( $\blacklozenge$ ), respectively. Sharp peaks at around 100 cm <sup>-1</sup> are laser plasma lines. <sup>53</sup> .....	21
Figure 1.14 DSC data for BT ceramics illustrating the dependence of orthorhombic–tetragonal (O–T) and tetragonal–cubic (T–C) structural transitions on the grain size. With decreasing G, the DSC peaks are progressively weakened and broadened <sup>50</sup> .....	22

Figure 1.15 a) AFM-topography of the surface of a BT ceramic with average grain size of 50 nm; b) piezoelectric hysteresis loops recorded from the regions marked '1' (°) and '2' (—); Scan size:  $1 \times 1 \mu\text{m}^2$ .<sup>57,58</sup> ..... 23

Figure 1.16 Typical piezoelectric hysteresis loop of 8 nm dense BT ceramics. Ferroelectricity could remain stable in BT ceramics prepared via a two-step sintering procedure with grain size as small as 8 nm in diameter.<sup>61</sup> ..... 25

Figure 1.17 P-E loops of the heterostructures with 30, 9, and 5 nm thick BT layers are shown as filled squares, filled circle, and filled triangles, respectively. The critical thickness of the film is 5 nm.<sup>63</sup> ..... 26

Figure 1.18 a) SEM image of single nanoshell BTO tube on silicon substrate. The inset shows an SEM image of the free open ends of PZT tubes; b) Effective piezoelectric coefficient as a function of the applied voltage measured on a PZT nanoshell tube. The characteristic hysteresis loop is directly associated with the ferroelectric switching. The effective remanent piezoelectric coefficient is of about 90 pm/V and is comparable with usual values obtained on PZT thin films.<sup>65,66</sup> ..... 27

Figure 1.19 Phase diagram of the transition temperature versus grain size. Two triple points are marked with  $d_1$  and  $d_2$ . The reentrance behavior from R to C and then to R is observed as a function of grain size.<sup>69</sup> ..... 28

Figure 1.20 Charge screening and depolarization field adapted from<sup>62</sup> ..... 29

Figure 1.21 Schematic patterns of a) circular<sup>82</sup> and b) toroidal<sup>84</sup> polarizations in ferroelectrics. .... 33

Figure 1.22 The schematic representation of electrophoretic formation of nanorods. At the left, it is presented the beginning of the nanorod growth. Positively charged sol particles are moving electrophoretically towards the negative electrode, depositing at the bottom of the pore, while the negatively charged counter ions are moving in the opposite direction. The center of the diagram shows a later time, as the densely packed sol particles fill more of the pore. Lastly, the right side of the diagram shows a completely filled pore.<sup>103-105</sup> ..... 40

Figure 1.23 Schematic representation of the liquid source misted chemical deposition technique<sup>107</sup> ..... 41

Figure 1.24 The outline of the thesis ..... 50

Figure 2.1 The electromagnetic spectrum. (www.britannica.com)..... 54

Figure 2.2 Diffraction condition for a given set of lattice planes. (www.britannica.com).... 54

Figure 2.3 The six ways of vibration of a molecule. Adapted from www.wikipedia.com .... 57

Figure 2.4 Schematic representation of Transmission Electron Microscope. (www.britannica.com) ..... 59

Figure 2.5 Schematic representation of Scanning Electron Microscope. (www.britannica.com) ..... 61

Figure 2.6 A general PFM experimental setup. Adapted from the reference<sup>196</sup> ..... 63

Figure 2.7 Depiction of PFM operation. The sample deforms in response to the applied voltage. This, in turn, causes the cantilever to deflect, which can then be measured and interpreted in terms of the piezoelectric properties of the sample. Adapted from the reference <sup>200</sup> ..... 64

Figure 2.8 Schematic representation of Vertical and Lateral PFM detection. Adapted from reference <sup>195</sup> ..... 65

Figure 2.9 Switching spectroscopy PFM diagram. Adapted from the reference <sup>198</sup> ..... 66

Figure 3.1 SEM micrographs of the samples prepared at a) 130 and b) 150 °C for 48 h and c) 150 °C for 72 h with anatase-TiO<sub>2</sub>/NaOH molar ratio of 0.05. 1D particles with similar dimensions are obtained for all samples. .... 74

Figure 3.2 X-ray patterns of samples prepared from anatase showing the influence of synthesis temperature (a) and time (b). Independently on synthesis parameters the best indexation is obtained with hydrogen titanium oxide hydrate with the general formula H<sub>2</sub>Ti<sub>2</sub>O<sub>5</sub>xH<sub>2</sub>O (JCPDS no. 47-0124). .... 75

Figure 3.3 a) Raman and b) FTIR spectra of the samples prepared from anatase at 150 °C for 48 h using different TiO<sub>2</sub>/NaOH molar ratios. All samples present the O-H and H-O-H bonding vibrations indicate the bonding of hydrogen to the structure <sup>219</sup> and the presence of structural water. .... 76

Figure 3.4 DSC and TGA curves of the sample prepared at 150 °C for 48 h with TiO<sub>2</sub>/NaOH molar ratio of 0.05. .... 77

Figure 3.5 TEM images of the NT samples collected during Stage 1 at: a) pH = 13 (A13); b) pH = 11 (A11) and c) pH = 8 (A8). The images indicate that the tubular shape is formed during the hydrothermal synthesis. .... 79

Figure 3.6 X-ray patterns of samples collected in Stage I and Stage II illustrating the structural evolution during the neutralization process. .... 80

Figure 3.7 HRTEM images of samples collected at the end of Stage I at pH = 7 (A7) a) and during Stage II at pH = 2 (AC2) b) and at pH = 7 (AC7) c). The TEM micrographs show tubular morphology even at low pH. .... 80

Figure 3.8 XRD patterns of samples A7 and AC7 recorded with a step of 0.01° per minute representing the formation of H<sub>2</sub>Ti<sub>2</sub>O<sub>5</sub> xH<sub>2</sub>O (JCPDS no. 47-0124; the simulated pattern is also displayed for comparison). .... 81

Figure 3.9 Raman spectra of the samples collected at pH = 7 without and with acid treatment (A7 and AC7, respectively). .... 83

Figure 3.10 XRD patterns of the post-synthesis hydrothermal treated samples at 90, 150 and 200 °C. It is exhibiting the structural transformation from H<sub>2</sub>Ti<sub>2</sub>O<sub>5</sub> to anatase when increasing the temperature. .... 84

Figure 3.11 SEM micrographs of the post-synthesis hydrothermal treated samples at a) 90, b) 150 and c) 200 °C. It shows the morphological evolution from NTs to NRs when increasing the hydrothermal treatment temperature. .... 85

Figure 3.12 HRTEM of the sample hydrothermally treated at 200 °C representing the anatase NR. In the insets the FFT showing that the lattice spacing are not equal across rod length..... 86

Figure 3.13 XRD pattern of the samples prepared from rutile collected at pH = 7 indicating the presence of unreacted rutile, titanium aqua oxide hydroxide and hydrous dititanate acid. .... 87

Figure 3.14 Raman spectra for the samples prepared from the precursors anatase and rutile..... 88

Figure 3.15. TEM micrographs of the samples prepared from rutile. The images illustrate various stages of tubular morphology formation..... 88

Figure 4.1 X-ray diffraction patterns of the barium titanate samples prepared at 90, 110 and 200 °C for 24 h indicating the increasing in BT tetragonality and purity when increasing the synthesis temperature. .... 102

Figure 4.2 Raman spectra of the barium titanate samples prepared at 90, 110 and 200 °C for 24 h showing the tetragonal distortion of the BT lattice when increasing the synthesis temperature. .... 103

Figure 4.3 SEM micrographs of a) the titanium precursor (TiNTs) and of the barium titanate samples obtained after 24 h at b) 90 °C (BT9024), c) 110 °C (BT11024) and d) 200 °C (BT20024) illustrating the formation of BT dendritic particles. .... 104

Figure 4.4 TEM micrographs of samples prepared at 90 °C a) dark field (inset EDS) and b) bright field (inset SAED). It is indicated the single-crystal feature with growth direction along <001>..... 105

Figure 4.5 TEM micrographs of samples prepared at 200 °C for 24 h showing that “daughter” dendrons grow perpendicular to the “mother” suggesting a crystal axis orientation growth along the <001> directions..... 105

Figure 4.6 Raman spectra of the samples prepared at 90 °C for 1 h (BT901), 12 h (BT9012) and 24 h (BT9024) illustrating the formation of BT after 24h. The spectra of titanium precursor (denominated as TiNTs) is also shown for comparison. .... 106

Figure 4.7 SEM micrographs of samples prepared at 110 °C for 144h (BT110144) showing the formation of dendritic BT particles..... 107

Figure 4.8 SEM micrographs of samples prepared at 200 °C over: a) 1 h and b) 6h, in which two different particle morphologies can be clearly seen: small with round shape and big plate like particles. .... 108

Figure 4.9 X-ray diffraction patterns of the samples prepared at a) 110 °C and b) 200 °C, illustrating the gradual transformation from cubic to tetragonal BT. .... 110

Figure 4.10 Raman spectra of the samples prepared at 110 °C and 200 °C showing the easier transition from a pseudocubic to tetragonal structure at 200 °C than at 110 °C... 111

Figure 4.11 a) Trace of the (103) reflection ( $2\theta \approx 75^\circ$ ) measured at 20 °C; b) comparison of 103 traces measured at 20°C (red) and -180°C (blue) for the sample prepared at 110

°C for 18 h (BT11018). The line broadening increases with decreasing temperature suggesting a lattice distortion. .... 112

Figure 4.12 a) Temperature dependence of the FWHM for the 103 peak for the sample prepared at 110 °C for 18 h (BT11018); b) Trace of the 103 reflection recorded at 25°C (red), 50°C (blue), and 120°C (green) for the sample prepared at 110 °C for 24 h (BT11024). The broadening increasing with the temperature decreasing is attributed to a distortive phase transition. .... 113

Figure 4.13 Fraction (*f*) of BT crystalline phase represented as a function of the synthesis time for the samples prepared at a) 110 °C and b) 200 °C. The time dependence of the crystallization fraction has a sigmoidal shape for both temperatures. *f* increases with the reaction time being the reaction faster at 200 °C. .... 114

Figure 4.14 Jhonson-Mehl Avrami plots for the two different reaction temperatures a) 110 °C and b) 200 °C. The reaction take place in two stages independently on temperature. The slope values (*m*) which give indications about the mechanism are ~1 for the first stage and ~0.2 for the second. .... 116

Figure 4.15 Timeline morphological evolutions studied by SEM for the samples obtained at 110 °C after a) 6h (BT1106); b) 12h (BT11012); c) 18h (BT11018); d) 24h (BT11024); e) 96h (BT11096) and f) 144 h (BT110144). Illustrating the morphological evolution from wild-type dendrites to spherical particles to seaweed dendrites. .... 118

Figure 4.16 Timeline morphological evolutions studied by SEM for the samples obtained at 200 °C after a) 30 min (BT20030); b) 1h (BT2001); c) 24h (BT20024). Showing the wild, round shaped and seaweed morphologies. .... 119

Figure 4.17 TEM micrographs at the early stages of BT crystallization for the samples prepared at a) 110 °C and b) 200 °C. BT nuclei form on the surface of the NTs. .... 120

Figure 4.18 Structural and morphological evolution of BT particles obtained by hydrothermal treatment of titanate layered nanotubes (TiNTs) and Ba(OH)<sub>2</sub> at 110 °C. ... 120

Figure 4.19 Piezoresponse images (PFM) of the a) wild type BT dendritic particle and b) seaweed type BT dendrites (in the up insets the topography and in the down insets the SEM micrographs). More pronounced piezoresponse contrast observed for the seaweed comparing to wild. .... 122

Figure 4.20 Cross-section profiles of the wild (green) and seaweed (red) morphologies collected from the PFM images. Higher values of piezoactivity are observed for the seaweed dendrites. .... 123

Figure 4.21 The PFM response of the a) wild type BT dendritic particle and b) seaweed type BT dendrites before and after poling with + d.c. (a1 and b1) and with - d.c. (a2 and b2). The domain size for wild is smaller than for seaweed therefore can be switch. .... 124

Figure 4.22 Typical local piezoelectric coefficient as a function of the applied field measured on BT dendritic particles with wild type (a) and seaweed type (b), respectively. Different hysteresis shapes: linear with various steps for wild and squared shaped for seaweed. .... 125

Figure 4.23 FTIR spectra of the wild (sample BT1106) and seaweed (sample BT110144) morphologies, illustrating the higher OH<sup>-</sup> ions concentration of wild dendrites..... 126

Figure 4.24 Schematic representation of the proposed mechanism for the synthesis of BT under static hydrothermal conditions starting from layered titanate NTs precursors. .... 131

Figure 4.25 Schematic representation of the MoCVD experimental procedure used..... 134

Figure 4.26 Microstructures of TiNTs a) as prepared by hydrothermal treatment and b) as deposited by EPD (TiNTsEPD) representing the tubular morphology of TiNTs films after EPD. .... 137

Figure 4.27 X-Ray patterns of the TiNTs films after the CVD procedure and subsequently annealed at 700, 750, 800 and 850 °C. The formation of anatase is observed when the annealing temperature is higher than 700 °C. .... 138

Figure 4.28 SEM micrographs of TiNTs films after the CVD procedure (a) and subsequently annealed at 700 (b), 750 (c), 800 (d) and 850 °C (e). The formation of anatase NRs by oriented attachment mechanism is noticed. .... 139

Figure 4.29 X-Ray patterns of the samples obtained after MoCVD deposition of barium precursor and subsequently annealing at 700, 750, 800 and 850 °C. The formation of BT is observed after annealing at temperatures higher than 700 °C..... 140

Figure 4.30 SEM micrographs of the films obtained after MoCVD deposition of barium precursor, Ba500 (a) and subsequently annealing at 700, BT700 (b), 750 BT750 (c), 800 BT800 (d) and 850 °C BT850 (e). The formation of rough and smooth surface NRs is observed. .... 141

Figure 4.31 SEM micrographs of the samples obtained after MoCVD with various concentrations of barium followed by annealing at 700 °C, a) BT[Ba]low700, b) BT[Ba]medium700, c) BT[Ba]high700. Small crystals are formed on nanorods surface independently on [Ba]. .... 142

Figure 4.32 SEM analysis of the sample obtained after MoCVD with barium and thermal treatment at 750 °C, BT750; a) the general view presenting three zones, b) the magnification and EDX analysis of zone 1, c) the magnification and EDX analysis of zone 2 and d) the magnification of zone 3. Small crystals formed at NRs surface in zone 1 are segregated and NRs are obtained. .... 144

Figure 4.33 TEM analysis of the sample obtained at 750 °C a) image and b) EELS, highlighting the different structure between the round shape particles, NRs and plate like particles. .... 145

Figure 4.34 HRTEM analysis of the sample obtained at 750 °C- BT750; (a) particles and (b) rod and plate like particles; in the insets the Fast Fourier Transformation (FFT) analysis. The round shaped particles have BT structure. .... 146

Figure 5.1 a) X-ray diffraction patterns and b) Raman spectra of the samples prepared in the presence of polymers –PAA[low][high] and PVP[low][high] compared to the blank sample. The formation of cubic BT is observed independently on additive concentration. .... 156

Figure 5.2 SEM micrographs of : a) blank sample, BT; b) BTPAA[low]; c) BTPAA[high]; d) BTPVP[low] and e) BTPVP[high]. The images illustrate the oriented aggregation in the case of PAA and the dispersive for PVP. .... 158

Figure 5.3 TEM image of the sample prepared in the presence of PAA at high concentration; the inset presents the SAED of this sample. The crystal oriented attachment is confirmed..... 159

Figure 5.4 TGA curves of the samples prepared in the presence of PAA at [low] and [high] concentration comparing to the blank sample showing higher PAA adsorption when increasing the concentration..... 160

Figure 5.5 a) X-ray diffraction patterns and b) Raman spectra of the samples prepared in the presence of anionic surfactant –SDS[low][high] compared to the blank sample. It is illustrating the formation of BT independently on SDS concentration..... 162

Figure 5.6 SEM micrographs of a) SDS[low]; b) SDS[high]. High degree of agglomeration at high concentration of SDS. .... 163

Figure 5.7 a) X-ray diffraction patterns and b) Raman spectra of the samples prepared in the presence of carbohydrates- HPMC[low][high] and D-Fructose[low] (D-Fructose[high] in the inset) compared to the blank sample. It is showing the formation of BT in all cases except for BTFru[high]. .... 164

Figure 5.8 SEM micrographs of a) HPMC[low]; b) HPMC[high]; the inset presents the SEM X-Ray mapping of the sample HPMC[high]. Various morphologies are observed for high concentration of HPMC..... 165

Figure 5.9 SEM micrographs of a) Fru[low]; b) Fru[high]. Cocoon shaped aggregates are formed for high concentration of Fructose. .... 166

Figure 5.10 TEM micrographs of the samples prepared at 80 °C in the presence of PAA at high concentration showing the oriented aggregation of the particles..... 167

Figure 5.11 Summary of non template additive-assisted aqueous synthesis of BT. .... 173

## List of tables

Table 1.1 Classification of the nanostructures according to the quantum confinement <sup>43-45</sup> .....	17
Table 1.2 The main experimental observations regarding the instability of the ferroelectricity at sizes < 0.1 $\mu\text{m}$ . .....	24
Table 1.3 The most reported size effects on the ferroelectric polarization ( $P_s$ ).....	37
Table 3.1 The nomenclature of the 1D titanium based samples used in this study.....	73
Table 3.2 Summary of the X-ray pattern results for the samples collected at pH = 7 after Stage I and Stage II of neutralization. For comparison the values from JCPDS no. 47-0124 file of $\text{H}_2\text{Ti}_2\text{O}_5 \cdot x\text{H}_2\text{O}$ are presented. ....	82
Table 4.1 Sample labels for hydrothermal synthesis of BT starting from TiNTs. ....	100
Table 4.2 The fractional crystallinity, $f$ , at two reaction temperatures, 110 and 200 $^\circ\text{C}$ . ...	115
Table 4.3 Samples and preparation conditions for MoCVD study. ....	136
Table 5.1 Samples index for non-template additives assisted synthesis of BT .....	154
Table 5.2 The specific surface areas ( $S_{\text{BET}}$ ), the equivalent spherical particle diameters ( $d_{\text{BET}}$ ), the crystallite size ( $d_{\text{XRD}}$ ) and the factor of aggregation ( $F_{\text{agg}}$ factor) of the samples obtained at 96 $^\circ\text{C}$ . .....	157
Table 5.3 Weight loss percentages calculated from TGA curves of the samples.....	161
Table 5.4 Summary of the main results of BT synthesis by additive-assisted method....	168

## List of symbols

$P_S$	Spontaneous Polarization
$T_C$	Curie Temperature
$E_d$	Depolarizing Field
$W_{dw}$	Domain Wall Energy
$W_e$	Elastic Energy
$E_C$	Coercive Field
$P_r$	Remanent Polarization
$d_{ijk}$	Piezoelectric Coefficients
$a, b, c$	Unit Cell Parameters
$t$	Tolerance Factor
$D_i$	Electric Displacement
$E_j$	Electric Field
$\epsilon_{ij}$	Dielectric Permittivity
$\epsilon_r$	Relative Dielectric Permittivity
$\epsilon_0$	Dielectric Permittivity of the Vacuum ( $8.85 \times 10^{-12}$ F/m)
$\tan\delta$	Dielectric Loss
$\epsilon''$	Imaginary Part of the Permittivity
$\epsilon'$	Real Part of the Permittivity
$\lambda$	Wavelength
$hkl$	Miller Indexes
$d_{hkl}$	Spacing between Atomic Planes
$\theta_{hkl}$	Bragg Angle
$z$	Cantilever displacement
$V_{ac}$	ac Voltage
$V_{dc}$	dc Voltage
$\omega$	Frequency
$\varphi$	Phase of the electromechanical response
$S_{BET}$	Specific surface areas ( $m^2 \cdot g^{-1}$ )

## List of abbreviations

FE	Ferroelectric
PE	Paraelctric
BT	Barium Titanate
C	Cubic structure
T	Tetragonal structure
O	Orthorhombic structure
R	Rhombohedral structure
P-E	Polarization-Electric Field
S-E	Strain-Electric Field
FeRAMs	Ferroelectric Random Access Memories
PZT	Lead Zirconate Titanate
BLSF	Bi-Layer Structured Ferroelectrics
IC	Integrated Circuit
CMOS	Complementary Metal Oxide Semiconductor
MLCC	Multilayer Ceramic Capacitor
FeCaps	Ferroelectric capacitors
BE	Bottom Electrode
0D	Zero dimensional
1D	One dimensional
2D	Two dimensional
NTs	NanoTubes
NRs	NanoRods
NWs	NanoWires
NPs	NanoParticles
XRD	X-Ray Diffraction
FTIR	Fourier Transformed InfraRed
TEM	Transmission Electron Microscopy
SEM	Scanning Electron Microscopy
SPM	Scanning Probe Microscopy

PFM	Piezoelectric Force Microscopy
dc	Direct Current
ac	Alternating Current
TGA	Thermogravimetric Analysis
DSC	Differential scanning calorimetry
ICP	Inductively Coupled Plasma spectroscopy
TiNTs	layered titanate nanotubes
PAA	Poly(acrylic acid)
PVP	Poly(vinyl pyrrolidone)
SDS	Sodium dodecylsulfate
HPMC	Hydroxypropylmethylcellulose

# 1 Background, Motivation and Objectives

## *Summary*

It is the purpose of this chapter to provide the background and the motivations of the present work. Initially, the basic concepts and definitions of ferroelectricity and piezoelectricity such as phase transitions, ferroelectric domains and polarization switching are introduced. In the following sections the applications, including the new trends, of the ferroelectric materials with perovskite structure are presented and discussed based on their basic properties. The changes in the ferroelectric properties at the nanoscale are argued based on the effect of size and shape on the ferroelectric properties with special focus on the anisometric ferroelectrics. The most reported synthesis strategies for the morphology control of ferroelectric materials are reviewed. Finally, and within this context, the motivation and the objectives of this thesis are presented.

## **1.1 Ferroelectricity and Piezoelectricity: Basic Concepts**

*Ferroelectricity* is a phenomenon that was discovered by Joseph Valasek in 1921 during his studies of single crystals of Rochelle salt ( $\text{NaKC}_4\text{H}_4\text{O}_6 \cdot 4\text{H}_2\text{O}$ ).<sup>1</sup> Since then, many ferroelectric materials have been discovered and several essential features of the phenomenon were studied and described in several text books.<sup>2-6</sup>

Ferroelectric materials are part of the *piezoelectrics* as it is shown in the crystal classification scheme presented in Figure 1.1. For a crystal to exhibit piezoelectric effect, its crystal structure should be non-centrosymmetric. The *piezoelectric effect* was demonstrated by the brothers Jacques and Pierre Curie in 1880 during their study of the effects of pressure on the generation of electrical charge on crystals such as quartz, tourmaline and Rochelle salt.<sup>7-9</sup>

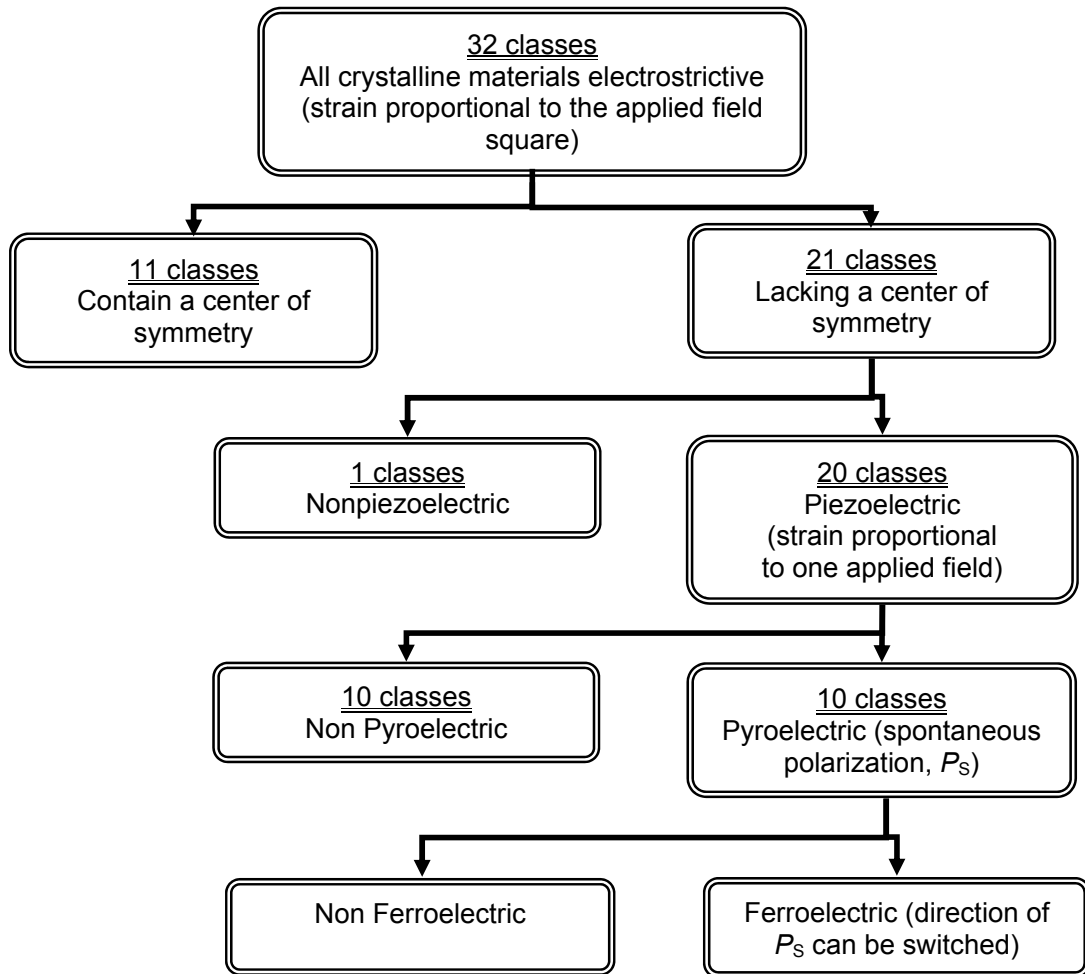


Figure 1.1 The 32 crystallographic classes. <sup>5</sup>

They found that if a certain crystal was subjected to a mechanical force, it became electrically polarized and the degree of polarization was proportional to the applied stress. Piezoelectric materials also show the inverse effect, a geometric strain is produced by the application of an electric field as illustrated in Figure 1.2.

The fingerprint of ferroelectric materials is the *spontaneous switchable polarisation* ( $P_s$ ) which is the consequence of spontaneous dipole moment created in the ferroelectric crystal by small displacements of the ions off their centrosymmetric position in the unit cell.<sup>4</sup>

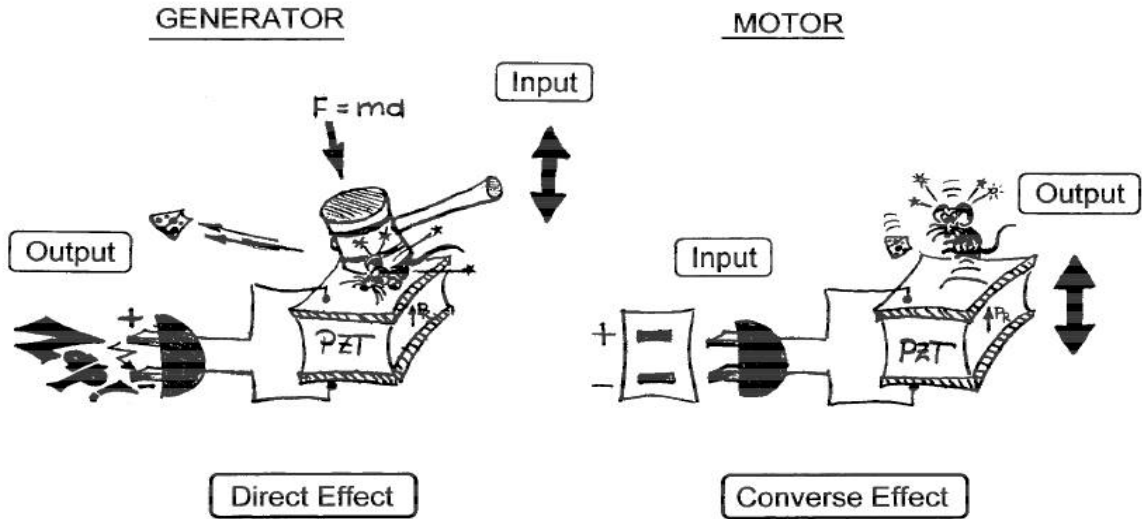


Figure 1.2 Piezoelectric effects (direct and converse) in ferroelectric ceramics <sup>10</sup>

### 1.1.1 Ferroelectric phase transitions

Most ferroelectric materials (FE) possess a transition temperature (*Curie point*,  $T_C$ ), below which they are polar (non-centro-symmetric). Above the  $T_C$ , the structure becomes centro-symmetric and loses the spontaneous polarization. In this state the material is named *paraelectric* (PE). Stated differently when the temperature decreases below the Curie point, a ferroelectric crystal undergoes a *structural phase transformation*, changing from paraelectric to ferroelectric. Early research works on ferroelectric phase transitions were described by R. E. Nettleton.<sup>11-13</sup>

If there are two or more ferroelectric phases in a crystal, the *Curie point* only specifies the temperature at which the paraelectric-ferroelectric phase transition occurs.<sup>5</sup> For example the  $T_C$  temperature of single crystalline  $\text{BaTiO}_3$  (BT), a classical ferroelectric material, is  $\sim 120^\circ\text{C}$  (or  $\sim 130^\circ\text{C}$  for polycrystalline  $\text{BaTiO}_3$ ). At this temperature the crystallographic structure passes from cubic (C) paraelectric (PE) phase to the first ferroelectric (FE) tetragonal (T) structure.  $\text{BaTiO}_3$  subsequently undergoes two further FE- FE phase transitions on cooling at  $5^\circ\text{C}$  and  $-90^\circ\text{C}$  to orthorhombic (O) and rhombohedral (R) structures, respectively.<sup>14</sup> The orientation of the spontaneous polarization usually coincides with some crystallographic axes, *i.e.*, in the tetragonal phase the polarization is

along the [001] direction and in the orthorhombic and rhombohedral structures the polarization vectors lie along the [110] and [111] directions, respectively (Figure 1.3).

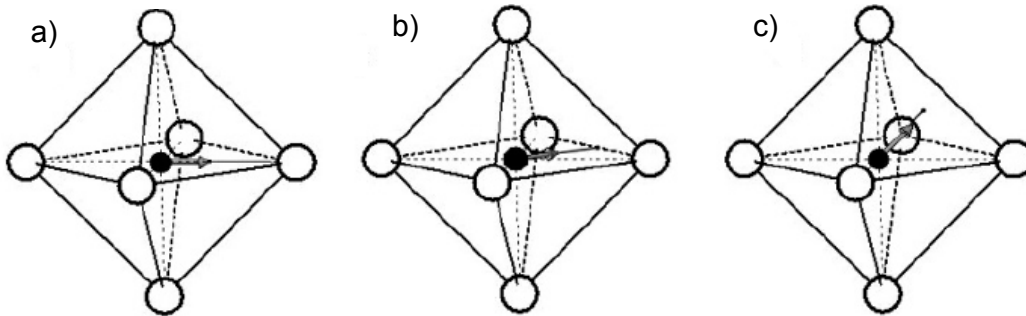


**Figure 1.3**  $\text{TiO}_6$  octahedra of a) tetragonal, b) orthorhombic and c) rhombohedral-type structures occurring with  $\text{BaTiO}_3$  crystals. The arrows show the direction of the spontaneous polarization due to the off-center displacement indicating the strong relation between the electrical response and the crystal structure <sup>15</sup>

The most important progress in the modern theory of ferroelectric phase transitions is the *soft mode concept*, which was proposed on the basis of the lattice dynamics by W. Cochran in the end of the 1950's. <sup>16-18</sup> According to this concept, for most phase transitions the structural distortions are characterized by unstable or "soft" optical phonon, whose frequency decreases substantially as the transition temperature is approached from above or below. <sup>17,18</sup> Detailed lattice dynamic calculations for several ferroelectric crystals and more rigorous mathematical treatments of the soft mode in ferroelectrics have been reported by Blinc and Zeks <sup>19</sup>. Near  $T_C$  the crystalline lattice is "soft" and can be strongly polarized with a relatively small coercive field (the intensity of the applied electric field required to reduce the polarization to zero after this has been driven to saturation - see section 1.1.3). Therefore, the dielectric permittivity of many ferroelectrics is very high in the vicinity of  $T_C$ , and can reach 10,000-80,000 at this point. <sup>5,19</sup> This phenomenon is usually called *dielectric anomaly*. The "softness" of the lattice at temperatures near  $T_C$  makes dielectric properties and other related properties

such as elastic, optical and thermal constants, to be temperature dependent in a wide range of temperatures around  $T_C$ .<sup>5</sup>

### 1.1.2 Ferroelectric and ferroelastic domains

Once the ferroelectric crystal is cooled down across the *Curie point*, an electrical polarization develops. If it develops uniformly throughout the crystal, a depolarizing field ( $E_d$ ) will appear as shown in Figure 1.4a.<sup>20</sup> To minimize the electrostatic energy related to the polarization interaction with the depolarizing field, uniform alignment of electric dipoles occurs only in certain regions of the crystal, while in other regions polarization may be oriented oppositely, as shown in Figure 1.4b. Such regions with uniform polarization value are called *ferroelectric domains*, and the interface between two adjacent domains (with thickness typically of the order of 10-100 Å) is called the *domain wall*.<sup>5</sup> Ferroelectric domains were first demonstrated in a study of spontaneous birefringence in barium titanate single crystals.<sup>21</sup> Domain walls that separate different orientations of the spontaneous polarization vector are *ferroelectric domain walls*, while those which separate different orientations of the spontaneous strain (associated with mechanical twinning) are *ferroelastic domain walls*. Inside the domain wall the dipole/strain orientation changes gradually from one domain orientation to another.

The configuration of ferroelectric domains depends on the crystal structure. The spontaneous polarization in an ideal ferroelectric crystal can be distributed with equal probability among several crystallographic directions of the centrosymmetric prototype structure (paraelectric phase). In a tetragonal phase, for example, the spontaneous polarization can be oriented only along three mutually perpendicular crystallographic directions, giving rise to two types of domain walls (as can be seen in Figure 1.4c): the walls that separate domains with oppositely oriented polarization (called 180°-walls), and those which separate domains with mutually perpendicular polarization (called 90°-walls). The 90°-walls are both ferroelectric and ferroelastic domain walls, because they separate regions with different orientation of the polarization and strain.

Since the formation of domain walls requires some energy, there is a certain amount of energy (*domain wall energy*,  $W_{dw}$ ) associated with them, in

addition to the elastic energy ( $W_e$ ) due to  $90^\circ$  domains.<sup>22</sup> The switching of polarization by  $180^\circ$  does not involve elastic deformation, while the switching of  $90^\circ$  does involve elastic deformation, and the energy of both should be different. From energy considerations, in real crystals, domain patterns depend on many factors, including the defect type and concentration, stress and electric history, temperature range relative to  $T_C$ , boundary conditions, etc.<sup>4</sup>

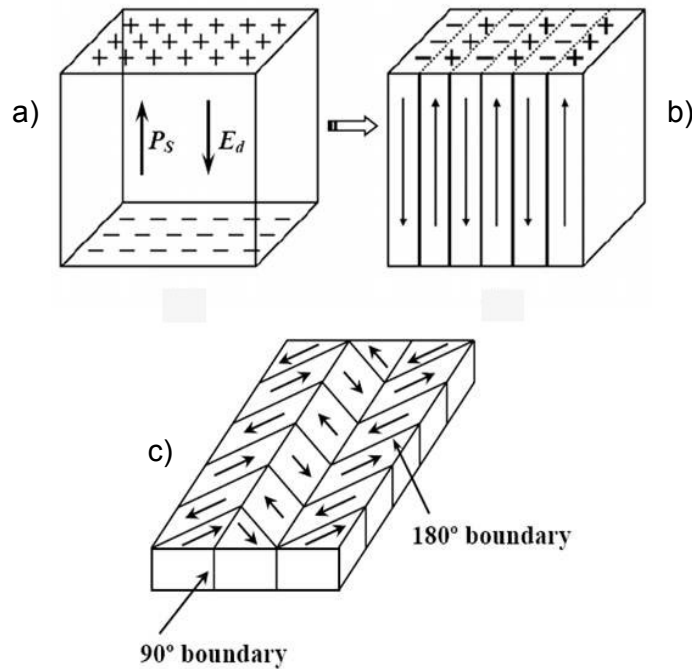


**Figure 1.4 a) Surface charge and depolarizing field ( $E_d$ ) associated with spontaneous polarization ( $P_s$ ); b) Formation of  $180^\circ$  domains to minimize the electrostatic energy; c) Schematic representation of  $180^\circ$  and  $90^\circ$  domain walls.<sup>20</sup>**

### 1.1.3 Polarization switching and hysteresis loop

As described above, ferroelectric crystal is likely to be in a polydomain state when it has just been grown and cooled down across its Curie point. However, each individual domain can be reoriented upon application of the external electric field of high enough strength. This dynamic process of domain reversal is called *domain (or polarization) switching*.<sup>5</sup> When the direction of the applied electric field

is opposite to the polarization direction of a domain, a new domain may appear inside the old one by nucleation and growth. The motion of the domain wall depends not only on extrinsic physical mechanisms but also on the stress distribution, space charges and defects in the crystal.<sup>5</sup>

When an alternating field of sufficiently high amplitude is applied to a ferroelectric material below  $T_C$ , the polarization shows a hysteretic behavior with the applied electric field, as illustrated in Figure 1.5a.<sup>4,5,7</sup> The observation of the polarization-electric field ( $P$ - $E$ ) *hysteresis loop* is often used for the identification of ferroelectrics.

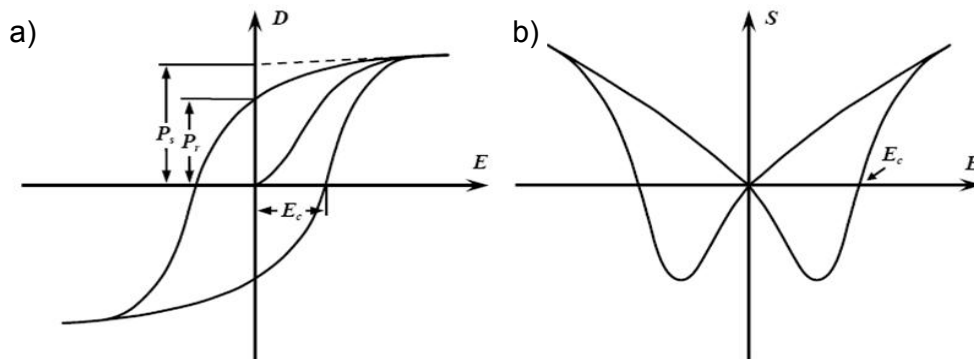


**Figure 1.5 a) P-E hysteresis and b) S-E butterfly loops used for the identification of ferroelectrics.**<sup>4,5</sup>

Application of a weak electric field generates a linear  $P(E)$  relationship (Figure 1.5a) because the field is not large enough to disturb or switch any domain. At low and at very high electric fields a ferroelectric behaves like an ordinary dielectric with a high dielectric constant, but on approaching to the *coercive field* ( $E_C$ ) the domain walls can move from their equilibrium position and domains that are oriented favorably with respect to the direction of the electric field grow rapidly at the expense of domains with opposite polarization direction, producing a switching of net polarization and a large  $P$ - $E$  non-linearity. Once most of the domains are switched, the material is said to reach its *saturation polarization*, (Figure 1.5a) where almost single domain state is attained. If the

applied electric field is then removed, some of the domains will remain aligned and the crystal will have a *remanent polarization* ( $P_r$ ) (Figure 1.5a). The extrapolation of the high field linear segment of the hysteresis loop back to the polarization axis represents the value of the spontaneous polarization ( $P_s$ ), e.g., the polarization of a single domain in the absence of electric field. Following the  $P$ - $E$  loop (Figure 1.5a), the value of the negative electric field required to return the net polarization to zero is again the (negative) coercive field. Further increase of the field in negative direction will cause an alignment of the dipoles in this direction and the cycle can be completed by reversing the field direction once again. Thus, the relation between  $P$  and  $E$  is represented by the hysteresis loop as shown in Figure 1.5a.<sup>4,5,7</sup>

In addition to the  $P$ - $E$  hysteresis loop, polarization switching by an external electric field leads to a strain-electric field ( $S$ - $E$ ) hysteresis in ferroelectric materials, as shown in Figure 1.5b.<sup>2-5,7,20</sup> The shape resembles that of a butterfly, and thus it is often referred to as the *butterfly loop*. At low electric fields, only a linear strain vs. electric field relationship is obtained due to the converse piezoelectric effect. The slope of the  $S(E)$  curve near the zero electric field represents the piezoelectric modulus ( $d_{33}$  for the longitudinal strain). As the field is increased, the strain is no longer linear with the field due to domain switching.<sup>2</sup>

## 1.2 Ferroelectric materials: structure, applications and future trends

Among the materials which exhibit piezoelectric and ferroelectric properties four main groups of materials have been considered according to their structure: the *corner sharing oxygen octahedra*, *compounds containing hydrogen bonded radicals*, *organic polymers* and *ceramic polymer composites*. One of the most important groups is the corner sharing oxygen octahedral, which includes the four following important families (structures) of materials: bronze tungsten ( $A_2B_2O_6$ ), perovskite ( $ABO_3$ ), pyrochlore ( $A_2B_2O_7$ ) and bismuth-layer ( $Bi_4Ti_3O_{12}$ ) structures.<sup>23</sup> Among these, the *perovskite* group is particularly significant, from the point of view of applications. This is because the materials belonging to this family present the highest piezoelectric coefficients and the ability to design the physical properties

required for certain applications as sensors, micro actuators, infrared detectors, microwave phase filters and non-volatile memories. The following section is dedicated to the perovskite structure.

### 1.2.1 Perovskite structure

Perovskite is a family name for a group of materials that crystallizes with the structure similar to that of the mineral calcium titanate ( $\text{CaTiO}_3$ ) which was discovered in the Ural Mountains of Russia by Gustav Rose in 1839 and was named after the Russian mineralogist, L. A. Perovski (1792-1856).<sup>24</sup> The ideal perovskite structure adopted by many oxides has the general formula  $\text{ABO}_3$ , where A and B represent cations of different sizes and O is the anion that bonds to both. A cations are surrounded by twelve anions in cubo-octahedral coordination and B cations are surrounded by six anions in octahedral coordination. The O anions are coordinated by two B-site cations and four A-site cations.<sup>24</sup>

Based on the *tolerance factor* ( $t$ )<sup>25</sup>, which takes into account the sizes of the O, A and B ions, the ideal perovskite structure adopts the cubic space group  $Pm3m$ . But factors other than the ionic size, e.g. degree of covalency, metal-metal interactions, *Janh-Teller* and ion pair effects play a role in determining the space group.<sup>24,26</sup> For example at room temperature and atmospheric pressure barium titanate  $\text{BaTiO}_3$ , which is one of the complex oxides within the perovskite family and a typical ferroelectric material, adopts a tetragonal structure with a space group  $P4mm$ <sup>14</sup>. For pure barium titanate, the tolerance factor equals 1.06. Here the tolerance factor is greater than 1 (ideal) because  $\text{Ti}^{4+}$  is smaller than its cavity and/or  $\text{Ba}^{2+}$  is larger than its cavity.<sup>27</sup>

During several years the room temperature tetragonal structure of BT was controversial. The systematic work on the structure of BT reported by Evans in 1953<sup>14</sup> was the beginning of the structural research on barium titanate. However, almost ten years after refining the BT structure in terms of four different noncubic models, Evans concluded that “it became apparent that the structure is essentially indeterminate”.<sup>28</sup> But Helen Megaw in 1962 was not so pessimistic and she said “It would be wrong if further work on this important type of structure were discouraged by the failure of one particular refinement procedure”.<sup>29</sup> Based on

these studies, the structure of barium titanate is now well known and the room temperature tetragonal structure of the BT is explained by ionic displacement of the Ti ions regarding to the oxygen ions as illustrated in Figure 1.6.

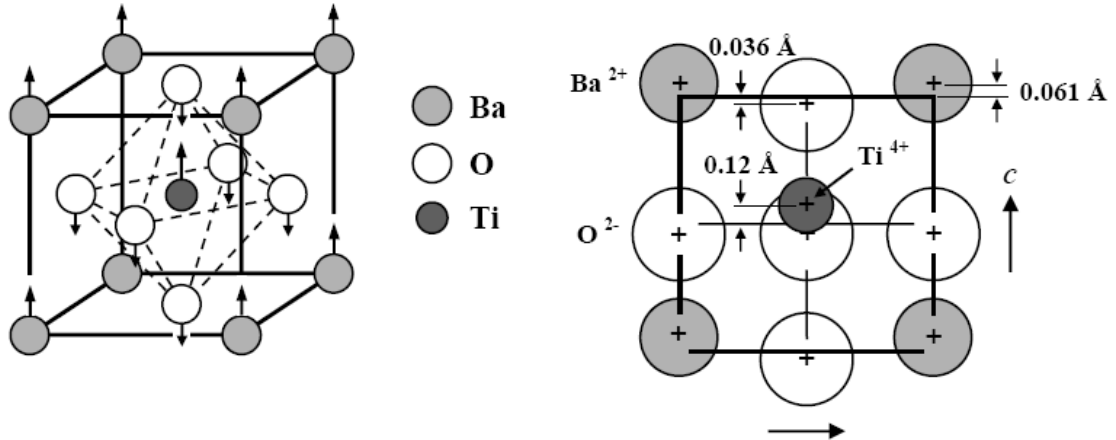


**Figure 1.6 The BT structure. At room temperature and atmospheric pressure the structure is tetragonal with  $Ba^{2+}$  and  $Ti^{4+}$  ions displaced relative to the  $O^{2-}$  ions.<sup>24</sup>**

### 1.2.2 Applications and trends

The ferroelectric materials with perovskite structure have found widespread applications as sensors, microactuators, infrared detectors, microwave phase filters and non-volatile memories (Figure 1.7), for which their functional properties such as switchable polarization, piezoelectricity, high non-linear optical activity, pyroelectricity, and non-linear dielectric behavior are indispensable<sup>4-9</sup>

According to Haertling<sup>10</sup> the discovery of non-linear dielectric properties in BT associated with very high values of the dielectric permittivity, was crucial for the development of the new generation of materials for electronic and microelectronic devices, which have occurred since the Second World War up to the current day. Hence, BT is among the most systematically studied and widely used ferroelectrics and considered as the prototype ferroelectric ceramic.

BT was firstly used as piezoelectric ceramic transducers. However, due to the discovery of better piezoelectric properties in other materials, namely the solid

solution between lead titanate and lead zirconate, BT found its main use as high permittivity dielectric in ceramic multilayer capacitors.<sup>23</sup>

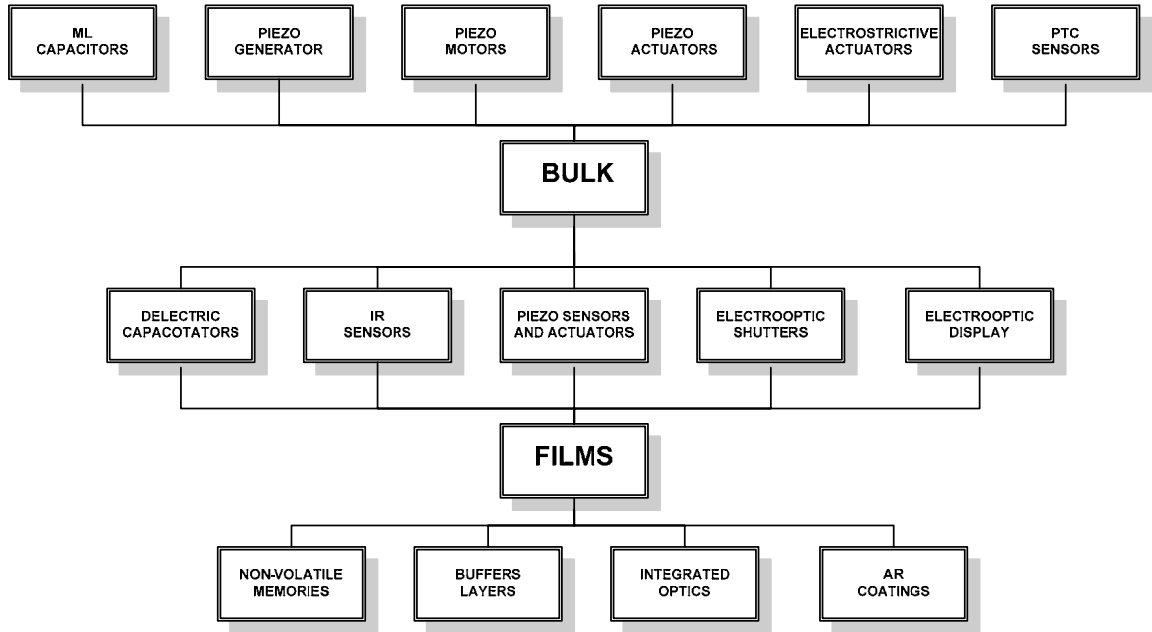
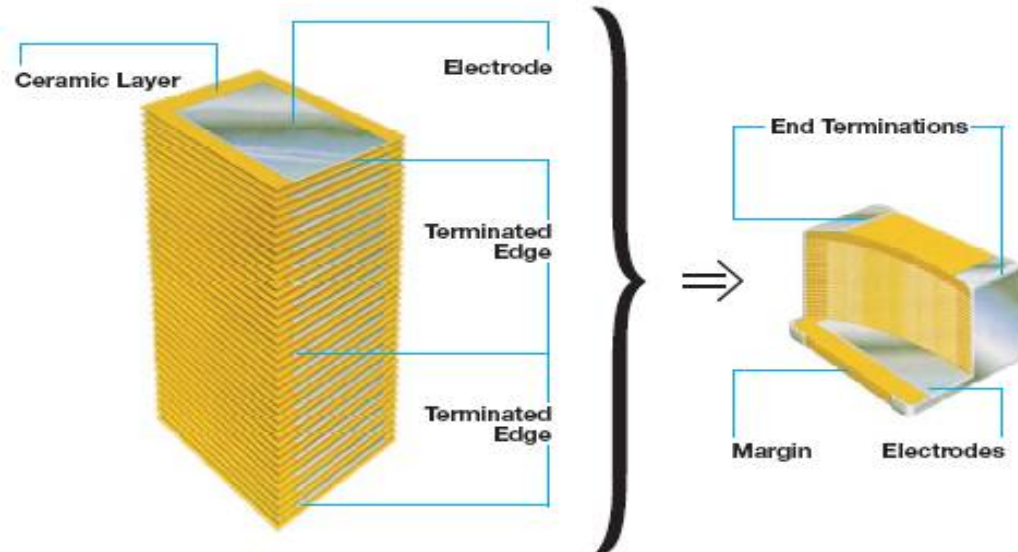


Figure 1.7 Applications of bulk and film electronic ceramic materials<sup>10</sup>

### Multilayer ceramic capacitors (MLCC)

A multilayer ceramic (MLC) capacitor is a monolithic block of ceramic containing two sets of offset, interleaved planar electrodes that extend to two opposite surfaces of the ceramic dielectric (Figure 1.8). To get a high volumetric efficiency (capacitance per unit volume) the dielectric material between the electrodes should have a large dielectric constant, a large area and a small thickness. BT based ceramics show dielectric constant values as high as 15,000 as compared to 5 or 10 for common ceramic and polymer materials. The high dielectric constant BT ceramic based disk capacitors are simple to be manufactured and have captured more than 50% of the ceramic capacitor market.<sup>30</sup> The electrode material must yield a conductive film that is continuous after firing and does not diffuse into, or react with the ceramic dielectric. This requires the use of non-oxidizing metals or alloys with high melting points. Palladium was one of the

earliest materials used. For cost reduction the nickel electrodes have been considered.<sup>31</sup>



**Figure 1.8 Multilayer Ceramic Capacitor**  
(<http://www.avx.com/docs/Catalogs/cdesc.pdf>)

The advances in tape casting technology have made it possible to make dielectric layers  $< 20 \mu\text{m}$  thick. This, combined with the use of a high dielectric constant ceramic like BT, allows large capacitance values to be achieved in relatively small volume capacitor devices. Good reviews have been written on the state of the art of the MLCC technology and the technical challenges it faces.<sup>30,32,33</sup>

### Ferroelectric Memories

Among the several applications of ferroelectrics the one that utilizes the unique characteristic of ferroelectrics, the switchable polarization under the effect of the electric field, is as a memory element, for example in *non - volatile memories*.

The concept of reversible spontaneous polarization as a memory state was one of the greatest motivations since the early days of ferroelectric research.<sup>34</sup> With the advances in thin film technology over the past 20 years, ferroelectric films

with improved properties have been receiving renewed attention for memory applications<sup>35,36</sup> in particular as *nonvolatile ferroelectric random access memory* (FeRAM).<sup>35,37</sup> FeRAMs are used in a variety of consumer products and industrial applications, such as smart cards, power meters, printers and video games, etc<sup>37</sup>.

FeRAMs base their working principle on the hysteretic behavior of the spontaneous polarization with the electric field, as described in Section 1.1.3. At zero applied electric field there are two states of remanent polarization which are equally stable,  $\pm P_r$ . Either of these two polarization states could be encoded as a "1" or a "0" (the bases of digital computing) and since no external field is required to maintain these states once reached, the memory device is nonvolatile, *i.e.* when the power is switched off the information is kept saved. Clearly, to switch the state of the device from "1" to "0" or vice versa, a threshold field greater than the coercive field is required. Additionally, in order to reduce the required applied voltage (to within a 5 V limit) for a given  $E_C$ , the ferroelectric materials need to be processed in the form of thin films.

In general, the basic structure of such high-density memory includes a thin film ferroelectric capacitor sandwiched between two chemically stable metal electrodes, integrated on a top of a semiconductor IC (integrated circuit) fabricated using existing CMOS (complementary metal oxide semiconductor) technology, as shown in Figure. 1.9.<sup>37</sup>

FeRAMs were first demonstrated in 1988 using  $\text{PbZr}_x\text{Ti}_{1-x}\text{O}_3$  (PZT) as the ferroelectric material for data storage.<sup>38</sup> Since then, many ferroelectric materials have been investigated for thin-films FeRAM, but only two families of ferroelectric materials are known to be the most important for memory applications: perovskite PZT - compositions and BLSFs, namely  $\text{SrBi}_2\text{Ta}_2\text{O}_9$  (SBT) and  $(\text{Bi},\text{La})_4\text{Ti}_3\text{O}_{12}$  (BLT).<sup>35,36</sup>

Generally, the following characteristics are desired for a ferroelectric thin film to be used as a FeRAM:<sup>36</sup>

- (1) The remanent polarization should be large, so that a relatively high polarization reversal current can be derived from a small-area capacitor.

(2) The dielectric constant should be sufficiently low, because a high dielectric constant material produces a large displacement current (linear response) and hinders detection of the polarization reversal current.

(3) The coercive field should be as low as possible for low-voltage operation of the FeRAM device.

(4) The Curie temperature should be high, much higher than the storage and operating temperature range of the device.

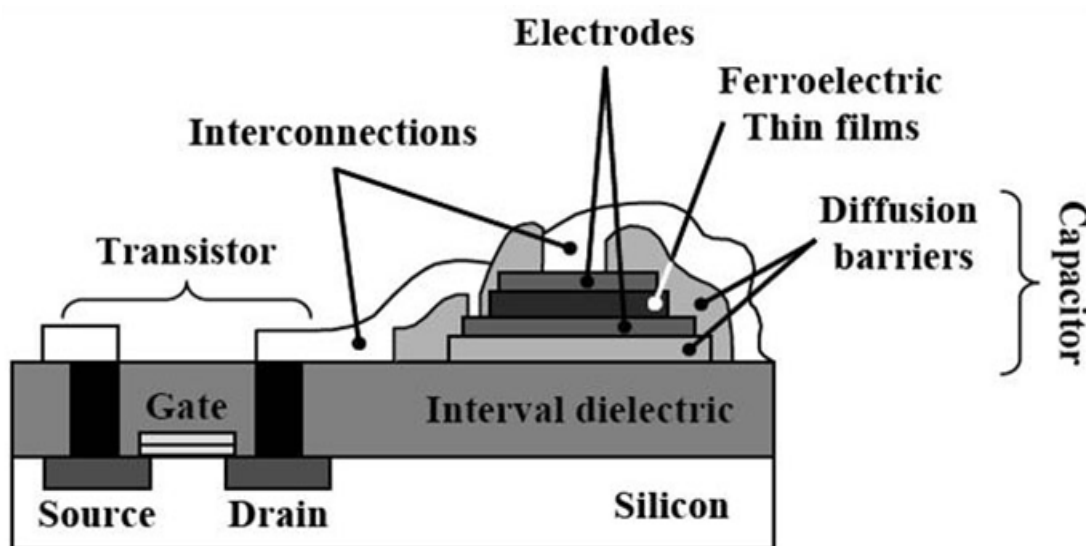


Figure 1.9 Schematic diagrams of high density architecture for non-volatile FeRAMs.<sup>37</sup>

The main advantages offered by FeRAM include non-volatile and radiation hardened compatibility with CMOS and GaAs circuitry, high speed (30ns cycle time for read/erase/rewrite) and high density ( $4 \mu\text{m}^2$  cell size).<sup>35,36</sup>

The continuing demand of electronic devices miniaturization leads to the decreasing of the dimension of ferroelectrics to the nanometer range. The “*nanostructure*” is an atomic, molecular or macromolecular structure that has at least one physical dimension of approximately 1-100 nm and possesses a special

property, provides a special function, or produces a special effect that is uniquely attributable to the nanoscale physical size.

The nanostructures are so, indispensable for the actual applications of the ferroelectric materials, for example, for future improvements in the development of highly volume-efficient which require manufacturing processes that allow for a reduced dielectric thickness well below 1  $\mu\text{m}$ . Obviously, such thin dielectric layers can only be produced if nanosized dielectric powders are applied and deposited by techniques more advanced than tape casting and screen printing. These processes require high-purity, homogeneous, weakly agglomerated ultra fine powders.

Moreover, in the particular case of the ferroelectric random access memory (FeRAM) the present roadmap for development calls for fully three-dimensional (3D) devices by 2010, *i.e.* the transition from planar to 3D capacitors.<sup>39</sup> This necessity arises because as a key requirement FeRAM capacitors must have large enough electrode surfaces to generate sufficient switched charge for the sense amplifiers to reliably discriminate between the “1” and “0” states in the memory; targeted and projected real-estate areas are not sufficient for this to be achieved using conventional 2D parallel plate capacitor arrangements, hence it is imperative to move to more complex 3D structures.<sup>40</sup>

It is possible to classify 3D ferroelectric capacitors (FeCaps) in two families, after the shape of the Bottom Electrode (BE). Pin- and cup-shaped FeCaps are represented in Figure 1.10a and b, respectively. In both cases BE must be defined before ferroelectric material deposition, meaning that 1 mask etch is no longer a viable technique to define the capacitor stack.<sup>41</sup>

However, there is little understanding of the nanodomain configurations adopted in such 3D ferroelectric devices. This is of great importance as the switching speed and operating device voltages depend upon the widths and geometries of the ferroelectric nanodomains.<sup>40</sup>

Nonvolatile polarization domains as small as 100  $\text{nm}^2$  in size can be induced on nanowires, suggesting that ferroelectric nanowires may be used to fabricate nonvolatile memory devices with an integration density approaching 1 terabit/  $\text{cm}^2$ .<sup>42</sup>

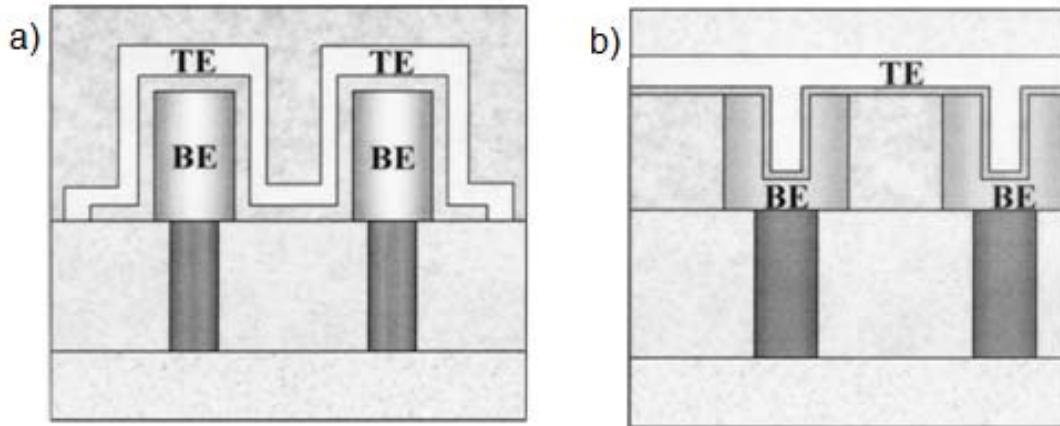


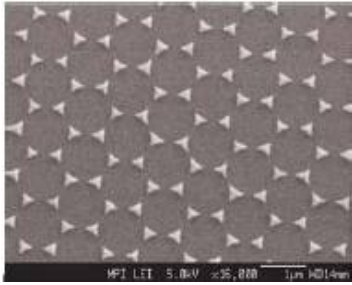
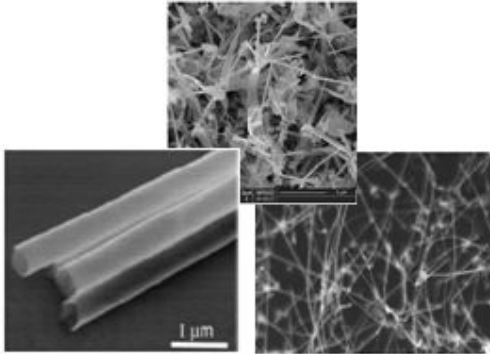
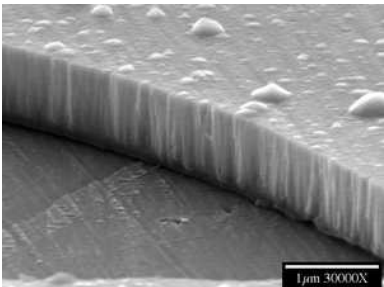
Figure 1.10 3D FeCap a) pin-shaped type and b) cup-shaped type<sup>41</sup>

It is therefore mandatory to understand how the size and shape of the ferroelectric materials can affect the properties and as a consequence the applications.

### 1.3 Size and shape effect on ferroelectricity

In a bulk crystal, the properties of the material are mainly independent on the size and are more chemical composition and defects-dependent. As the size of a crystal decreases to the nanometer regime, size starts to influence the properties of the crystal. This is because the electronic structure is altered from the continuous electronic bands to discrete or quantized electronic levels and electrons and holes are quantum confined.<sup>43</sup> *Quantum confinement* is a widely used terminology in the study of nanocrystals and the classification of the nanostructures based on this concept is presented in Table 1.1. In the particular case of ferroelectrics to understand how the quantum confinement influences the crystal structure and state of polarization, is vital to the performance of ferroelectric materials in many applications.

**Table 1.1 Classification of the nanostructures according to the quantum confinement<sup>43-45</sup>**

Quantum confinement	No of dimensions of electrons/holes confinement	Degrees of Freedom	Examples
quantum dot	3 dimensions < 100nm	0D	<p>Particles, quantum dots, hollow, spheres, etc.</p>  <p>MFI LET 5.0kV x35,000 1µm HD14nm</p>
quantum wire	2 dimensions < 100nm	1D	<p>Tubes, fibers, wires, platelets, etc</p>  <p>1 µm</p>
quantum well	1 dimension < 100nm	2D	<p>Films, coatings, multilayer, etc.</p>  <p>1µm 30000X</p>

### 1.3.1 Instability of ferroelectricity at nano-scale

The need for understanding the effect of size on the ferroelectricity arise from the experimental observation of Kazing in 1952<sup>46</sup> that the ferroelectricity is unstable when the physical dimension of the grains is decreasing similar to the phenomena observed for the ferromagnets. Nevertheless, ferroelectrics are more complicated than ferromagnets for two reasons. Most magnets have spatially localized spins whose magnitude is fixed and the mean values are in fact the mathematic average of these spin. In comparison the electric dipoles are not spatially localized, they extend over distances of order of 1 nm.<sup>36</sup> Moreover, measuring the electric properties of ferroelectrics involves metallization and or constructing a circuit. Therefore, what really is measured is in fact a system. In contrast large magnetic fields can be applied in ferromagnets in vacuum with no physical contacts.<sup>36</sup>

Kazing stated that colloidal particles of  $\text{KH}_2\text{PO}_4$  ferroelectric material with the mean diameter below 1500 Å show no measurable spontaneous polarization when cooling down from the Curie point.<sup>46</sup> Later Anliker observed that the ferroelectric to paraelectric phase transition temperature ( $T_C$ ) of BT decreases with decreasing the particle size.<sup>47</sup>

It was observed also that the *permittivity* of the ferroelectric BT strongly depends on the grain size. The *dielectric permittivity* of a material  $\epsilon_{ij}$  is the constant that relates the *electric displacement* ( $D_i$ ) in a dielectric material to the applied electric field ( $E_j$ ) by the relation,<sup>4</sup>

$$D_i = \epsilon_{ij} E_j \quad 1.1$$

The *relative dielectric permittivity*,  $\epsilon_{rij}$ , is defined as,

$$\epsilon_{ij} = \epsilon_o \epsilon_{rij} \quad 1.2$$

where  $\epsilon_o$  is the dielectric permittivity of the vacuum ( $8.85 \times 10^{-12} \text{ Fm}^{-1}$ ).

Coarse-grained ceramics of pure BT with average diameter between 20 and 50  $\mu\text{m}$  show  $\epsilon_r \sim 1500\text{-}2000$  at room temperature.<sup>30</sup> Higher values of permittivity ( $\epsilon_r$

~3500-4000) have been observed in dense, fine-grained BT ceramics with diameter  $\sim 1 \mu\text{m}$  by Arlt *et al.*<sup>48</sup> Moreover, in hot-pressed BT with the diameter  $\sim 1 \mu\text{m}$  a  $\epsilon_r$  value of  $\sim 6000$  at room temperature was found. At even smaller grain sizes, however the same authors observed a strong decrease of  $\epsilon_r$ . It was concluded then that the room-temperature permittivity of BT obviously has a maximum at a grain size of about  $\sim 1 \mu\text{m}$ . Decreasing more the BT particle size below  $1 \mu\text{m}$  it was observed that the dielectric anomaly characteristic to the temperature dependence of the permittivity (see section 1.1.1) is not longer present.<sup>48,49</sup> As can be seen in Figure 1.11 the permittivity of nanocrystalline samples is remarkably less sensitive to temperature in contrast to coarse ceramics. The permittivity peak in the case of fine-grained BT ceramics is really broadened and rounded in comparison to coarse ceramics. The *dielectric losses* of the fine grained ceramics are rather small as can be also observed in Figure 1.11. The *dielectric loss* is defined as the tangent of the loss angle,  $\tan\delta$ , *i.e.*, the ratio of the imaginary part  $\epsilon''$  to the real part  $\epsilon'$  of the permittivity,<sup>20</sup>

$$\tan \delta = \frac{\epsilon''}{\epsilon'} \quad 1.3$$

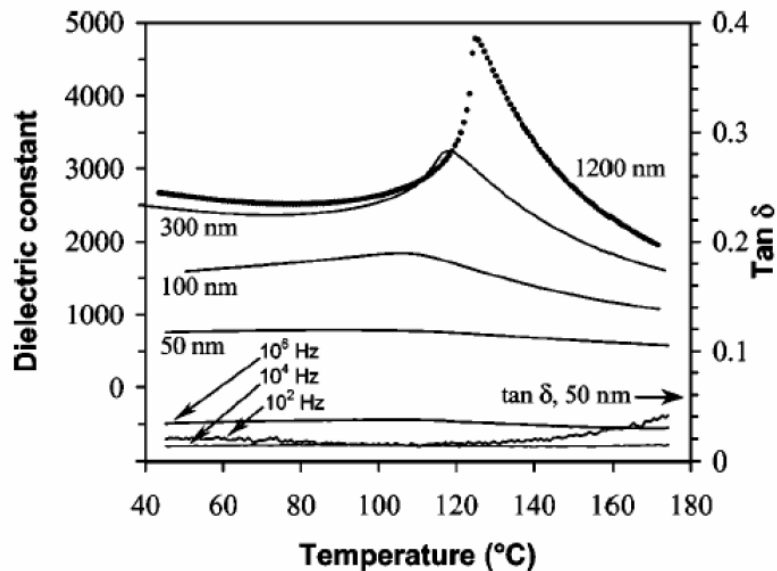


**Figure 1.11** Relative dielectric constant  $\epsilon_r$  at 104 Hz and loss  $\tan\delta$  of BT ceramics as a function of temperature.  $\tan\delta$  reported for 50 nm sample at three frequency values: 102, 104, and 106 Hz. The permittivity peak of fine-grained ceramics is remarkably broadened and rounded in comparison to coarse ceramics. The dielectric losses of the fine grained ceramics are rather small.<sup>49</sup>

Another important observation when the grain size of BT ceramics decreases to the nanometer range is related to the crystalline symmetry. X-Ray diffraction pattern corresponding to the (111) and to the (200)/(002) reflections is shown in Figure 1.12. The splitting of the (200)/(002) lines gradually decreases, meaning that the tetragonality  $c/a$  ( $a$  and  $c$  being the lattice parameters) is progressively reduced with decreasing grain size ( $G$ ).<sup>50</sup> A good fit with the tetragonal structure of the whole diffraction pattern of samples with  $G \geq 300$  nm could be obtained by Rietveld method<sup>51</sup>. The splitting is no longer observed for the nanocrystalline ceramics with  $G \approx 100$  nm and  $G \approx 50$  nm and the patterns apparently correspond to ( $Pm3m$ ) cubic symmetry<sup>50,52</sup>.

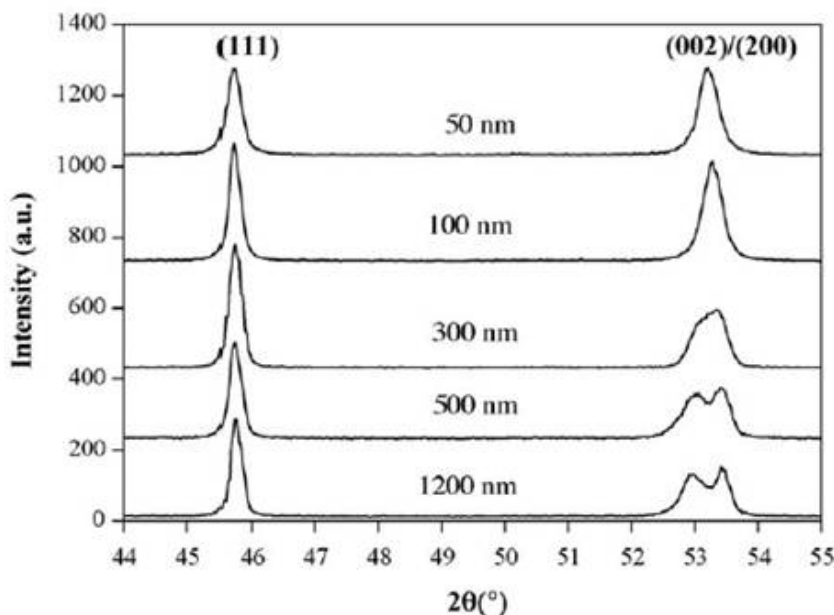


**Figure 1.12** Part of the X-ray diffraction pattern for BT ceramics with different grain size (50–1200 nm) at room temperature. The splitting of the (200)/(002) peak is no longer observed for the nanocrystalline ceramics and the patterns apparently correspond to ( $Pm3m$ ) cubic symmetry.<sup>50</sup>

However, XRD is not only limited for the crystallographic characterization of fine crystallites owing to extensive broadening of Bragg reflections but is also generally not very sensitive to transitions involving oxygen displacements.<sup>53</sup> In contrast vibrational spectroscopy is sensitive to this type of transformation. For

example Raman spectroscopy can detect local lattice distortions and crystallographic defects at a molecular level.<sup>53,54</sup>

Therefore the instability of the BT tetragonal phase at room temperature when the particle size decrease can be better evidenced by *Raman spectroscopy*. Figure 1.13 shows the typical evolution of the Raman spectra obtained for powders with different particle sizes.

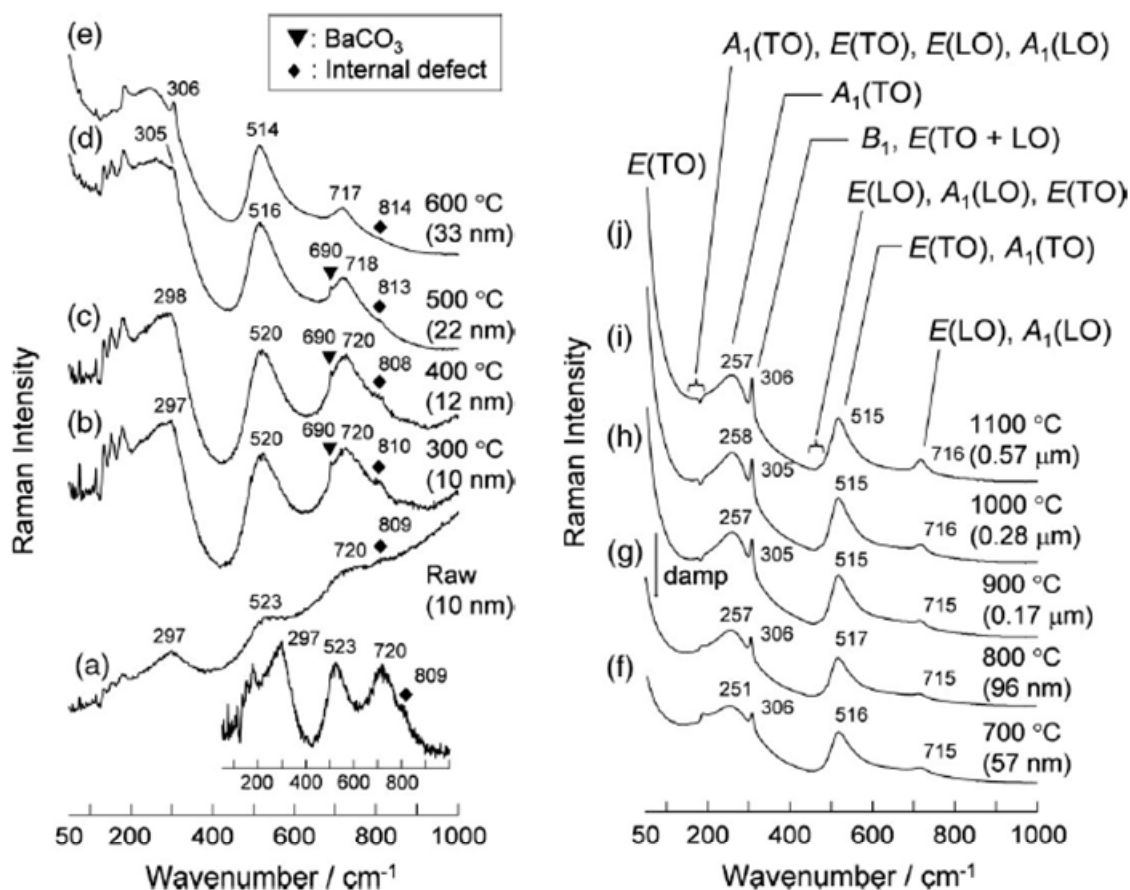


**Figure 1.13** Evolution of Raman spectra as a function of crystallite size obtained for the BT powders at room temperature. The average crystallite sizes are indicated in parentheses. Peaks originating from  $\text{BaCO}_3$  and internal defects are marked by closed triangles ( $\blacktriangledown$ ) and diamonds ( $\blacklozenge$ ), respectively. Sharp peaks at around  $100 \text{ cm}^{-1}$  are laser plasma lines.<sup>53</sup>

It was then found that the lifetime of phonons that are specifically assigned to the tetragonal phase decreased with decreasing crystallite size below a critical size of 100 nm.<sup>53</sup> In particles as fine as 100 nm, the short mean free path of

phonons, mainly due to internal pressure, causes decoupling of the coupled A1 (TO) phonons<sup>55,56</sup> and a diffuse phase transition behavior ( $T_C = 115^\circ\text{C}$ <sup>53</sup>). Coupled A1(TO) phonons, which give a spectral dip at around  $180\text{ cm}^{-1}$  were revealed for powders consisting of particles as large as  $0.17\text{ }\mu\text{m}$  ( $T_C = 123^\circ\text{C}$ ).<sup>53</sup> Further coarsening upon annealing induced the formation of aggregates, resulting in the shift of phase transition points to higher temperatures for the rhombohedral to orthorhombic and the orthorhombic to tetragonal transitions and to lower temperatures for the tetragonal to cubic transition, respectively. Moreover, it was experimentally demonstrated that the tetragonal phase is more stable in the nanograined ceramic than in powders with comparable crystallite sizes.<sup>50,54</sup>

Typical *Differential Scanning Calorimetry* (DSC) data for different grain size ceramics are presented in Figure 1.14.

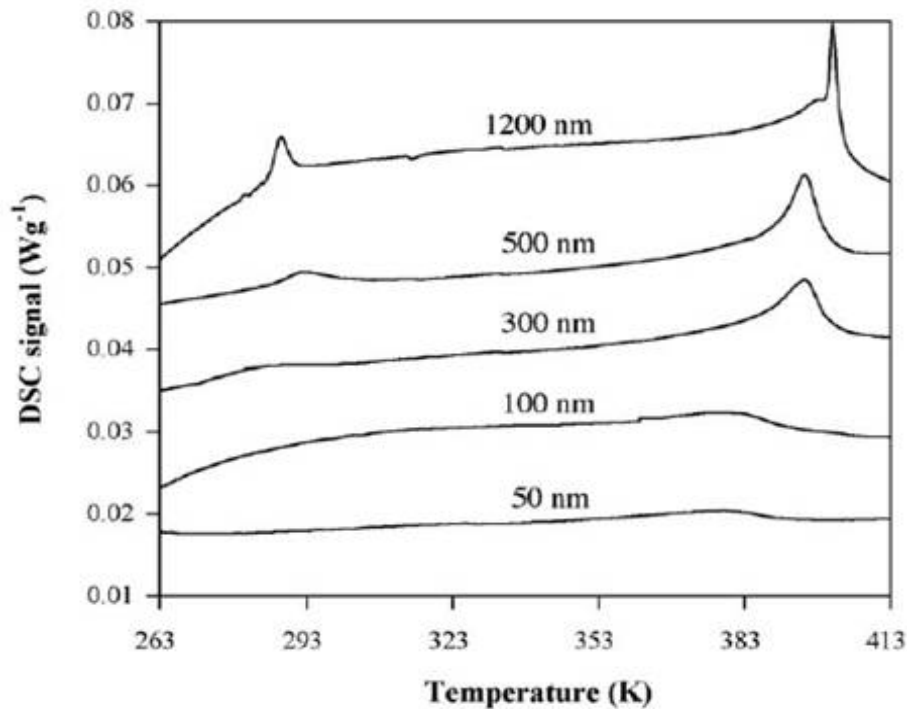


**Figure 1.14** DSC data for BT ceramics illustrating the dependence of orthorhombic-tetragonal (O-T) and tetragonal-cubic (T-C) structural transitions on the grain size. With decreasing  $G$ , the DSC peaks are progressively weakened and broadened<sup>50</sup>

For the coarser sample, the endothermic features near 283 and 403K can be attributed to the orthorhombic-tetragonal (O-T) and tetragonal-cubic (T-C)

transitions, respectively. It is evident that, with decreasing  $G$ , the DSC peaks are progressively weakened and broadened. As a result, the corresponding heat of transition is reduced. For the sample with  $G \approx 300$  nm, the enthalpies of the O–T and T–C transformations are 23 and 161 J/mol, respectively.<sup>50</sup> For the sake of comparison, the reference values reported for single-crystals are 92 and 210 J/mol, respectively.<sup>2-4</sup> For the finest ceramic ( $G \approx 50$  nm), the enthalpy of the T–C transition is reduced to only 20% of the single-crystal value, being  $\approx 45$  J/mol. The average T–C transition temperature corresponding to the maximum of the DSC peak is progressively shifted towards lower values, from 400K for  $G \approx 1200$  nm to 378K for  $G \approx 50$  nm (Figure 1.14). The O–T transition is no longer observed in the case of nanocrystalline ceramics ( $G \leq 100$  nm).

Moreover, *local switching of ferroelectric domains* probed by piezoresponse force microscopy was found to be very weak in the BT ceramics with grain size  $\sim 50$  nm.<sup>57,58</sup> Figure 1.15 shows a typical piezoresponse measurement of dense nanocrystalline BT ceramics

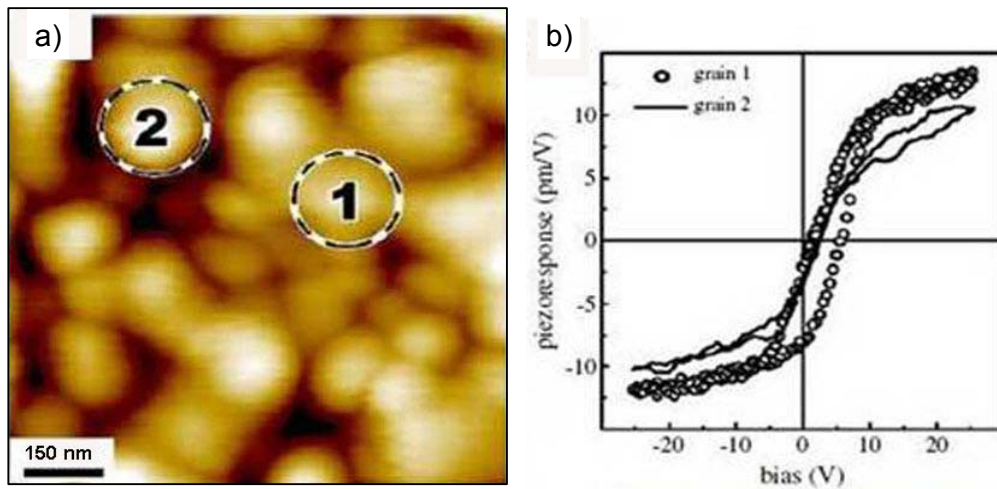


**Figure 1.15** a) AFM-topography of the surface of a BT ceramic with average grain size of 50 nm; b) piezoelectric hysteresis loops recorded from the regions marked '1' (o) and '2' (—); Scan size:  $1 \times 1 \mu\text{m}^2$ .<sup>57,58</sup>

The main behaviors regarding the instability of the ferroelectricity at nano scale are summarized in Table 1.2.

**Table 1.2 The main experimental observations regarding the instability of the ferroelectricity at sizes < 0.1  $\mu\text{m}$ .**

<b>Behaviors</b>	<b>Characterization technique</b>	<b>References</b>
Diffused dielectric anomaly, lowering of $T_C$ , or no anomaly at all	Dielectric measurements	30,48
Decrease of the $c/a$ ratio	X-Ray Diffraction	50,52
Broadening and softening of vibrational modes	Vibrational spectroscopy	53-56
Weakening or vanish of DSC signals at phase transition temperature	Differential Scanning Calorimetry	50,52
Narrowing or loss of $P$ - $E$ loops <sup>57,58</sup>	Ferroelectric measurements	57,58

### 1.3.2 Concepts regarding the ferroelectricity at nanoscale

Based on the experimental observations presented above two concepts were introduced when considering the size effect on ferroelectricity.

The first concept is the *critical size* (*critical thickness* for thin films and *critical diameter* for nanotubes or nanorods) where the dielectric anomaly is not longer present, where the phase transitions are diffuse and the spontaneous polarization of the ferroelectric materials is vanished. But the reported values for the critical size are still controversial and differ with the method of fabrication of the material. For instance, Arlt *et al.* reported a critical size value as high as 700 nm for the particle size when barium titanate is prepared by the calcination of barium-titanyl-oxalate precursor at 1000 °C.<sup>48</sup> But when the BT powders are prepared by

sol-gel process the reported values for the critical size are usually below 50 nm ( $<25$  nm<sup>52,59</sup>,  $<50$  nm<sup>60</sup>). More recently, it was demonstrated that ferroelectricity could remain stable in BT ceramics prepared via a two-step sintering procedure with grain size as small as 8 nm in diameter, as can be seen in Figure 1.16.<sup>61</sup>

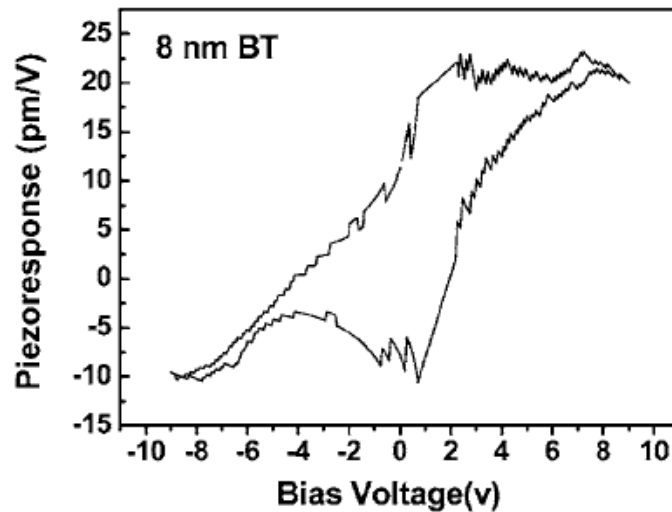


**Figure 1.16** Typical piezoelectric hysteresis loop of 8 nm dense BT ceramics. Ferroelectricity could remain stable in BT ceramics prepared via a two-step sintering procedure with grain size as small as 8 nm in diameter.<sup>61</sup>

In the case of thin films it was predicted in 2003 by first-principle simulations that the *critical thickness* related with ferroelectric instability of BT thin films is around 5 nm.<sup>62</sup> This theoretical prediction was then experimentally proved by Kim *et al.*<sup>63</sup> in SrRuO<sub>3</sub>/BT/SrRuO<sub>3</sub> (SR/BT/SR) heterostructures on SrTiO<sub>3</sub> (ST) substrates fabricated by pulsed laser deposition. Typical ferroelectric *P-E* hysteresis loops have been found for BT capacitor with thickness  $t_{\text{BT}} = 5$  nm<sup>63</sup> (Figure 1.17).

For PbTiO<sub>3</sub> thin films a critical thickness as small as 1.2 nm has been experimentally found by Fong *et al.*<sup>64</sup> which systematically investigated  $T_C$  in films with thicknesses down to a single unit cell by using synchrotron X-ray scattering for *in situ* monitoring of the film during epitaxial growth by metalorganic chemical vapor deposition.

Regarding the one-dimensional materials a *critical diameter* as high as 700 nm has been proposed in 2003 by Luo *et al.* for lead zirconate titanate tubes.<sup>65,66</sup> They found an effective remanent piezoelectric coefficient of about 90 pm/V for the tube comparable with usual values obtained on PZT thin films (Figure 1.18). Moreover, the authors pointed out the difficulty to compare the values obtained for NTs to the piezoelectric coefficients of bulk material since measurements were performed on a tube geometry that has a relatively intricate field distribution and vibrational modes.<sup>65,66</sup>

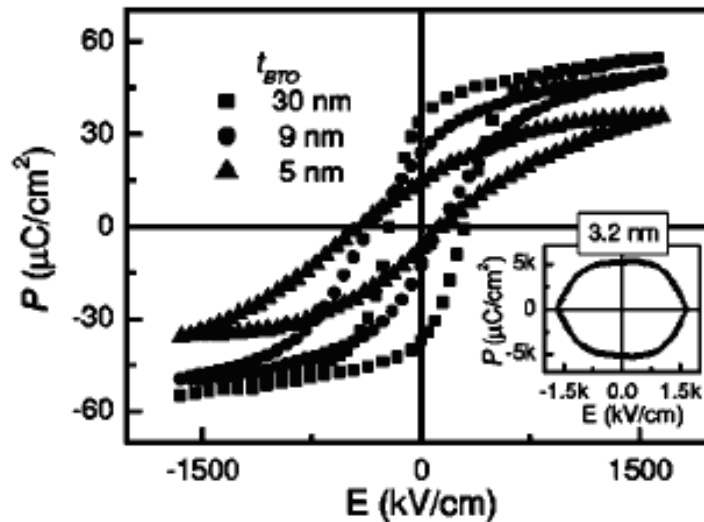
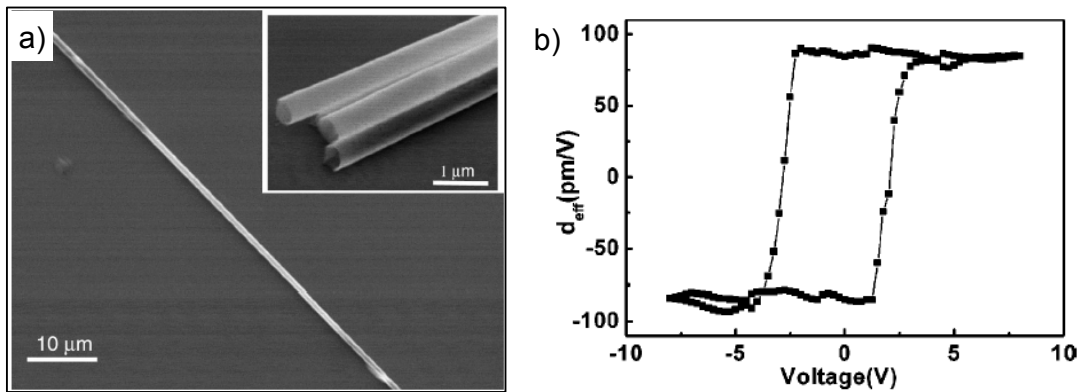


Figure 1.17 P-E loops of the heterostructures with 30, 9, and 5 nm thick BT layers are shown as filled squares, filled circle, and filled triangles, respectively. The critical thickness of the film is 5 nm.<sup>63</sup>

In 2006 it was found that the ferroelectric phase transition temperature ( $T_C$ ) of barium titanate nanowires is depressed as the nanowire diameter ( $d_{nw}$ ) decreases, following a  $1/d_{nw}$  scaling.<sup>67</sup> It was demonstrated that the diameter at which  $T_C$  falls below room temperature (critical diameter) is determined to be  $\sim 3$  nm, and extrapolation of the data indicates that nanowires with  $d_{nw}$  as small as 0.8 nm can support ferroelectricity at lower temperatures.

However, no experimental evidences of 0.8 nm critical diameter have been found till the moment. Wang *et al.* reported the existence of one-dimensional and stable formation of ferroelectric monodomains in single crystalline BT nanowires with 95 nm diameter.<sup>68</sup> Piezoresponse force microscopy operated in both vertical

and lateral modes showed ferroelectric polarization switching along the axial (lateral) direction of the nanowires, while the polarization along the transversal (vertical) direction was strongly suppressed. Such a one-dimensional polarization formation was also found to be highly stable and the switched polarization spontaneously returned to its original orientation at the instant of removing the applied poling voltage.<sup>68</sup>



**Figure 1.18 a) SEM image of single nanoshell BTO tube on silicon substrate. The inset shows an SEM image of the free open ends of PZT tubes; b) Effective piezoelectric coefficient as a function of the applied voltage measured on a PZT nanoshell tube. The characteristic hysteresis loop is directly associated with the ferroelectric switching. The effective remanent piezoelectric coefficient is of about 90 pm/V and is comparable with usual values obtained on PZT thin films.<sup>65,66</sup>**

The second concept which arises from the experimental observation is the *triple point*.<sup>69</sup> As shown above it was found that with decreasing grain size the transition temperature of C/T phase decreases, while those of T/O and O/R phases increase.<sup>50,52,54</sup> Based on this observation and by using the modified Ginsburg-Landau-Devonshire (GLD) thermodynamic theory Lin *et al.* established a theoretical phase diagram of the transition temperature versus size which predicted that the O and T ferroelectric phases are unstable and disappear at a certain critical size, respectively, and that only the R structure is stable in small dense ceramics, characterized with two triple critical points around the critical size as shown in Figure 1.19. In addition, the transition temperature from R to C varies

no monotonously with further decreasing grain size, accompanied by a reentrance behavior.<sup>69</sup>

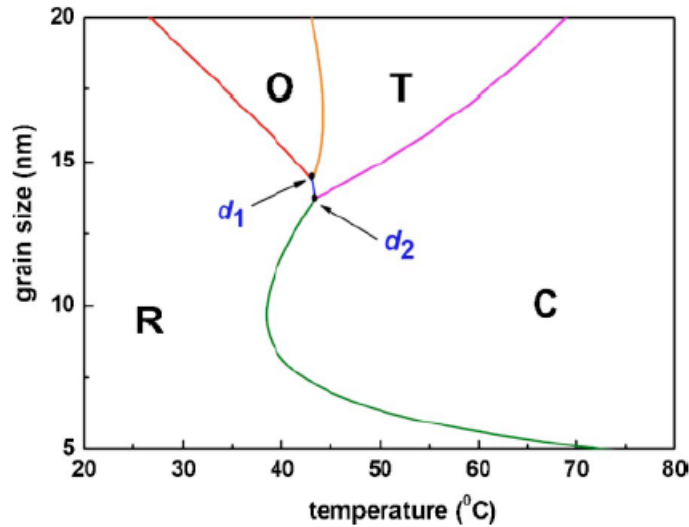


**Figure 1.19** Phase diagram of the transition temperature versus grain size. Two triple points are marked with  $d_1$  and  $d_2$ . The reentrance behavior from R to C and then to R is observed as a function of grain size.<sup>69</sup>

The various values reported for the critical size or for the triple point indicate that combination between intrinsic and extrinsic effect of the size must be considered when considering about ferroelectricity at nanoscale. In the following section the details of the most widely considered possible causes for the instability of the ferroelectricity at nanoscale are presented.

### 1.3.3 Intrinsic and extrinsic size effects on the ferroelectricity

The intrinsic effects are: depolarization effects, the absence of long-range cooperative interactions, elastic constraints and new ferroelectric polarization. The extrinsic effects are the structural defects and interface processes (grain boundary effects or adsorption).

Depolarization field

As also stated above in section 1.1.2 when a ferroelectric material spontaneously polarizes, the free surface accumulates compensating charge from the environment, from an external circuit, and/or through internal transport of charged defects (this phenomenon is called *charge screening*). After doing so, the full spontaneous polarization can be realized. In ideal cases if the charges are completely screened the spontaneous polarization is uniform as shown in Figure 1.20a. If for some reason (real cases) the spontaneous polarization would not be compensated by charges, the consequence of the necessary boundary condition of zero polarization at the free surface would be an internal electric field oriented opposite to the polarization itself as shown in Figure 1.20b. This is called the depolarization field.

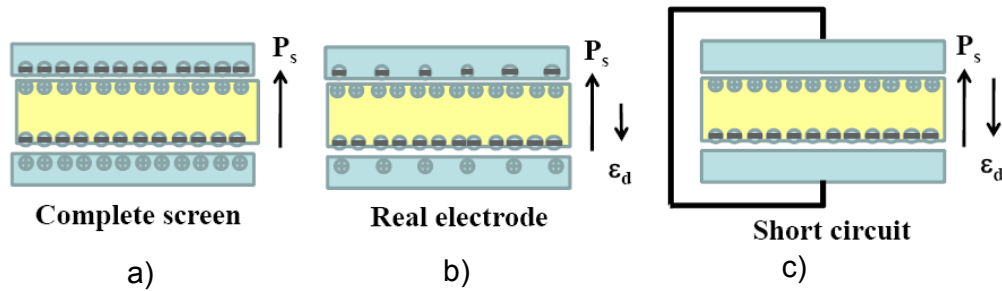


**Figure 1.20 Charge screening and depolarization field adapted from<sup>62</sup>**

Stated differently, if the surface charges are not compensated the gradient in polarization from the bulk to the surface become a source for a depolarization field. The potential difference ( $\Delta V$ ) between the two surfaces is then non zero and the depolarization field is expressed as following:<sup>4</sup>

$$\epsilon_d = \frac{2\Delta V}{l} \tag{1.4}$$

where  $l$  is the geometrical factor related to the sample dimension (grain size, film thickness, etc.). As can be noticed from the above formula the magnitude of the depolarization field is inversely proportional with the size. This is the reason why

the depolarization field becomes that important when the physical dimensions are reduced.

Kazing stated for the first time that the reduction of depolarization field in large crystals is the consequence of the split up into two or more domains.<sup>46</sup> But the depolarization factor in small ferroelectric particles is larger than the Lorentz correction and because of this is more effective than the depolarization field in small ferromagnetic particles since the magnetic dipoles are aligned by interactions which are  $10^4$  larger than the ordinary dipole-dipole interactions responsible for the spontaneous polarization.<sup>46</sup>

Beside the internal factors such as domain structure and free carriers which partly diminish the field of depolarization there are external features, namely electrodes, which can substantially decrease the field of depolarization even for single domain insulating ferroelectrics. For example, superconducting electrodes in the bulk ferroelectrics lead to complete compensation (screening) of the depolarization field.<sup>70</sup>

However, in thin ferroelectric films there is only partial compensation of the depolarization field even for superconducting electrodes<sup>71</sup>, due to the inhomogeneity of the polarization related to the contribution of surface effects (Figure 1.20b).<sup>70</sup>

Since the majority of ferroelectric materials are insulators and become single domain for thin enough films this leads to the necessity to include the contribution of electrodes when studying their ferroelectric properties. In order to extract only the contribution of the depolarization field the case of ferroelectric capacitors in short circuit, as is indicated in Figure 1.20c was simulated. In these conditions Junquera *et al.* predicted the potential drop across the film-electrode interfaces and stated that the amplitude of depolarizing field depends on (1) the screening length of the metal (electrodes) and the polarization of the thin film, which both monitor the potential drop across the interface, and (2) the film thickness.<sup>62</sup>

The smallest depolarization fields have been theoretical predicted by Moroskova *et al.*<sup>72</sup> in nanorods and nanowires where the depolarization factor tends to zero for an infinite cylinder.

Long-range order (LRO)/ short-range order (SRO)

A second view of the cause of size effects in ferroelectrics is related to the driving force for the ferroelectric transition. It is well known that the spontaneous polarization is a cooperative phenomenon of the long-range dipole-dipole interactions. But with decreasing size this LRO which supports the development of homogeneous spontaneous polarization is broken down into SRO insufficient to drive the transformation. The length factors used to describe the interaction between polar units in ferroelectric materials are the correlation lengths parallel and perpendicular to the polarization vector. Lines and Glass stated that correlation lengths parallel and perpendicular to the polar direction range from 10–50 nm and 1–2 nm, respectively.<sup>4</sup> Based on the values cited above, and as Lines and Glass explained, one might expect significant effects on phase stability when crystallite dimensions are reduced into these nanometric ranges.

It was found that metastable SRO polar regions having very low tetragonality can be turned into LRO ferroelectric regions in BT ceramics with merely  $G \sim 50$  nm but only after applying an external field.<sup>57</sup>

The update comprehension of this point of view is based on Rietveld refinement and the atomic pair distribution functions (PDF) analysis which have been used to elucidate the BT structure at room temperature with various grain sizes.<sup>15,73,74</sup> It was then found that the three-dimensional atomic ordering in small barium titanate particles is rather complex. It is cubic-like on average, but locally shows slight distortions of a tetragonal-type.<sup>15</sup> Stated differently, the loss of ferroelectricity in submicron- and nano-sized BT has an intrinsic origin related to the increased atomic positional disorder in spatially confined physical systems. It has been stated then that no particular critical size exists at which ferroelectricity in BT, in particular, and perovskites in general, is completely lost. Rather it weakens exponentially with the decreasing of their physical size.<sup>73</sup> Indeed, Rietveld and PDF analyses suggested increased distortions with decreasing particle size, although in conjunction with a tendency to a cubic average structure. These results suggest that although structural distortions are robust to changes in particle size,

what is affected is the coherency of the distortions, which is decreased in the smaller particles.<sup>74</sup>

### Elastic constrains

Below the temperature of a ferroelastic or ferroelectric structural phase transition the energy minimization is realized through the reduction of elastic energy by the formation of 90° ferroelectric and ferroelastic domains with their corresponding domain walls which separate regions with mutually perpendicular polarization and strain (see section 1.1.2). This phenomenon is designated as twinning (because it is similar to the mechanic twinning) and is related to the stress relief during the phase transition.<sup>22</sup>

The twin density depends on the grain size  $G$ ; under homogeneous stress the total elastic energy of a grain increases proportionally to  $G^3$ . Any kind of twin wall, however, increases proportionally to  $G^2$ . Below the intersection of these two curves, stress reduction by twinning cannot lower the total energy. Thus there is a critical grain size below which twinning should not occur. Above this limit the width of the twin wall increases proportionally to  $G^{1/2}$ .<sup>22</sup> For this it is believed that the elastic constrains cause such strong dependences on grain size of domain structures and dielectric properties for ceramics with  $G < 1.0 \mu\text{m}$ .

Specifically, it was already stated that BT ceramics of submicron grain size become substantially untwined as crystallite size is reduced.<sup>22</sup> It was explained that in this case, a condition of grain clamping must develop, whereby individual grains are unable to develop their full transformation strain, even if the driving force should exist. It was experimentally demonstrated by hot-stage transmission electron microscopy studies that barium titanate ceramics with fine grains are untwined at room temperature, as well as on cycling through the normal  $T_C$ , suggesting a single-domain state for individual grains.<sup>52</sup>

More than ten years ago it was predicted that the clamping of epitaxial thin films by strains from lattice mismatch increases in fact the ferroelectric properties.<sup>75</sup> Enormous strains can be created in thin films when one material is deposited on another resulting from differences in the crystal lattice parameters.<sup>76</sup>

Based on this prediction it was then experimentally proved that the Curie temperature can be adjusted in ferroelectric films by creating strains.<sup>77-79</sup>

It has been shown that epitaxial strain from the substrate can be harnessed to increase  $T_C$  by hundreds of degrees and produce room-temperature ferroelectricity in strontium titanate, a quantum paraelectric without ferroelectric anomaly.<sup>77</sup> Biaxial compressive strain has been used to markedly enhance the ferroelectric properties of BT thin films.<sup>78</sup> This strain, imposed by coherent epitaxy, can result in a ferroelectric transition temperature near 500 °C and a remanent polarization at least 250% higher than bulk BT single crystals.<sup>78</sup>

#### New ferroelectric polarization

It was stated by Fu *et al.*<sup>80</sup> that the phase transitions do in fact exist in very small nanostructures but these phase transitions differ profoundly from those occurring in bulk materials, in the sense that they lead to the formation of *spontaneous toroid moment* rather than spontaneous polarization. Ginzburg *et al.* showed for the first time that toroidal ordering should be possible in ferroelectrics, and not just rectilinear parallel or antiparallel alignment of polarizations.<sup>81</sup> This was extended more recently by Naumov *et al.*<sup>82</sup> The basic idea is illustrated in Figure 1.21, and the argument is that such structures are not stable except for very small objects (nanodots or nanowires) and at low temperatures.<sup>83</sup>

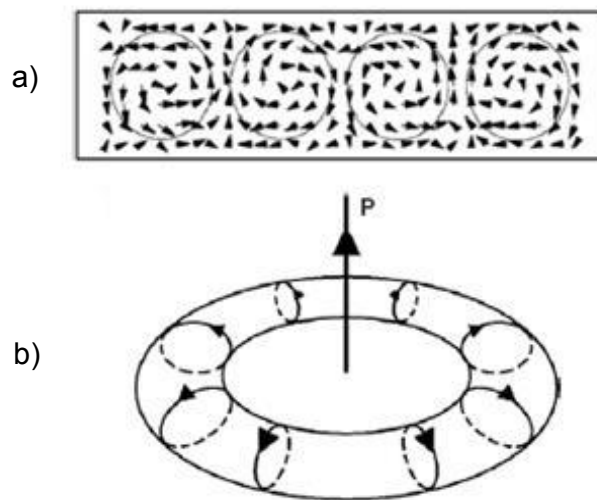


**Figure 1.21 Schematic patterns of a) circular<sup>82</sup> and b) toroidal<sup>84</sup> polarizations in ferroelectrics.**

*Lattice defects (point defects and dislocations)*

Defects exist in almost all the materials and their long-range strain fields can have a negative impact on the host materials. In materials with confined dimensions, the influence of defects can be even more pronounced due to the enhanced relative volume of the 'defective' regions.

For the particular case of chemically prepared barium titanate it is well known that hydroxyl ions can reside as defects on oxygen sites within the structure, and the resulting charged defects are probably compensated by cation vacancies.<sup>85-87</sup>

Anyway it is not well established if these point defects are intrinsic size effects on the ferroelectric polarization taking into account that if they are concentrated in small volumes they might upset the long range dipole-dipole interactions, or if they have rather an extrinsic effect on the ferroelectric properties. For instance Hennings and Schreinemacher clearly showed that the development of a room-temperature global tetragonal structure with heat treatment for BT particles of 0.2  $\mu\text{m}$  diameter, and prepared under hydrothermal conditions from acetate precursors, was associated with the elimination of hydroxyl defects, and not with particle growth.<sup>88</sup> In contrast, Begg, Vance, and Nowotny concluded that, for hydrothermal powders prepared from  $\text{Ba}(\text{OH})_2$  and hydrolyzed titanium alkoxide, the release of water from the particles on heat treatment was not at all associated with the development of a tetragonal distortion observable by XRD.<sup>89</sup>

It has been also reported that another type of defects as dislocations induced polarization instability in (001)-oriented  $\text{Pb}(\text{Zr}_{0.52}\text{Ti}_{0.48})\text{O}_3$  (PZT) nanoislands, with an average height of  $\sim 9$  nm, grown on compressive perovskite substrates.<sup>90</sup> Using quantitative high-resolution electron microscopy it has been visualized the strain fields of edge-type misfit dislocations, extending predominantly into a PZT region with a height of  $\sim 4$  nm and width of  $\sim 8$  nm. The lattice within this region deviates from the regular crystal structure. Piezoresponse force microscopy indicates that such PZT nanoislands do not show ferroelectricity.<sup>90</sup> Once again, these results suggest that misfit engineering is indispensable for obtaining nanostructured ferroelectrics with stable polarization.

### Surface effects

There is a simple model which can explain the size effect on ferroelectric ceramics and that corresponds to ferroelectric grain cores, with the same properties of a macroscopic single-crystal, separated by a non polar grain boundary layer (“dead layer”) with cubic structure. It is then assumed that the fraction of ferroelectric phase decreases with decreasing grain size. However this model is not proved, as the X-ray diffraction patterns indicate a gradual reduction of the spontaneous tetragonal distortion (directly related to the spontaneous polarization) and of the noncentrosymmetric character of the BT lattice with decreasing G.<sup>50</sup>

The same model of “dead layer” is also invoked for thin films where a drastic reduction of the effective dielectric constant in nano scale thin films is the result of a low permittivity layer formed at the film-electrode interface.<sup>91,92</sup> Nevertheless, the nature of such layer is still under investigation. The possible origins for the “dead layer” formation can be the local diffusion of electrode material or an intrinsic polarization state near the interface.<sup>93,94</sup>

An interesting idea regarding the surface process has been proposed for chemically prepared BT nanowires. By density functional theory (DFT) calculations of bare and molecule-covered surfaces Spanier *et al.* showed that ferroelectricity in nanowires is stabilized by adsorbed molecules such as OH<sup>-</sup> and carboxylates. These adsorbates are found to passivate polarization charge more effectively than metallic electrodes, explaining the observed stability of ferroelectricity in small-diameter BT nanowires.<sup>67</sup>

Table 1.3 summarizes the most reported size effects on the ferroelectricity at the nanoscale which try to explain the behaviors presented in Table 1.2. The theoretical and experimental studies clearly demonstrate that there is a strong dependence between the size and the ferroelectric properties.

As can be seen in Table 1.3 one dimension nanorods, nanowires or nanotubes enhance polarization even for very small sizes. Even so, studies aimed

at exploiting and understanding properties of one-dimensional ferroelectric nanostructures are scarce.

Very recently, the extent to which notches inhibit axial switching of polarization in ferroelectric nanowires was investigated by monitoring the switching behavior of single crystal BT wires before and after patterning triangular notches along their lengths.<sup>95</sup> Static zero-field domain patterns suggested a strong domain-notch interaction, implying that notches should act as pinning sites for domain wall propagation. Surprisingly though, notches appeared to assist, rather than inhibit, polar switching. The origin of this effect was rationalized using finite element modeling of the electric field distribution along the notched wire; it was found that the air gap associated with the notch acted to enhance the local field, both in the air, and in the adjacent region of the ferroelectric. It seems that this local field enhancement outweighs any pinning interactions.<sup>95</sup>

Experimental techniques and a first-principles- derived scheme were used to determine the phase transition sequence, in general, and reveal the unexpected low-symmetric (monoclinic) ground state, in particular, of  $\text{KNbO}_3$  and BT 1D nanostructures.<sup>96</sup> It was further discovered that the direction of the polarization in this monoclinic ground state (as well as the Curie temperature) is dramatically altered by the magnitude of the residual depolarizing field and by the nanostructures' size, implying that one can "easily" tune physical properties of these low-dimensional structures.<sup>96</sup> These observations and calculations thus demonstrate the versatility of the 1D nanoworld and the existence of apparently surprising effects of large technological promise there. Therefore there is a necessity to find easy and low cost preparation strategies for 1D materials as they are suitable systems to study the dimensionality effect in ferroelectrics. The most reported synthesis strategies are presented in the following section.

**Table 1.3 The most reported size effects on the ferroelectric polarization ( $P_s$ )**

	Intrinsic size effects								Extrinsic size effects			
	Depolarization field		LRO/SRO		Elastic constrains		New ferroelectric phenomena		Lattice defects		Surface effects	
	$P_s$	Why?	$P_s$	Why?	$P_s$	Why?	$P_s$	Why?	$P_s$	Why?	$P_s$	Why?
0D	Decreases	Non compensated surface charges <sup>70</sup>	Decreases	Affect the coherence of the dipole-dipole interactions <sup>15,73,74</sup>	Decreases	Untwined structure <sup>22</sup>	Increases /Appears	Circular polarization <sup>82</sup>	Decreases	Upset the LRO; strain fields <sup>88,90</sup>	Decreases	Polarization frozen at the interface <sup>50</sup>
1D	Increases	Depolarization factor tends to 0 for infinite cylinder <sup>72</sup>	--	--	--	--	Increases /Appears	Toroidal moment <sup>82,84</sup>	--	--	Increases	Passivate surface charge by adsorbed molecules. <sup>67</sup>
2D	Decreases	Non compensated surface charges. <sup>62</sup>	--	--	Increases	Strains from lattice mismatch <sup>75,77-79</sup>	--	--	--	--	Decreases	"dead layer" with low permittivity <sup>93,94</sup>

## 1.4 Synthesis strategies for morphology control of ferroelectric nanoparticles

According to Gruverman and Kholkin<sup>97</sup> there are two main approaches for the preparation of 1D materials. The so called *top-down* methods that consist in the size reduction until 1D nano structures are obtained and *bottom-up* methods when atoms, ions or molecules are assembled<sup>98</sup>.

The top-down methods based on electron-beam (EB) assisted fabrication involve patterning the ferroelectric structures either by milling of the ferroelectric layer using a focused ion beam (FIB)<sup>99</sup> or by maskless EB lithography<sup>100</sup>. Top-down methods are currently widely used in modern commercial nanotechnology because they provide high-precision positioning and size control. However, they are limited in resolution (very small structures are difficult to obtain), time-consuming and are prone to processing damage<sup>97</sup>.

Bottom-up methods include: the use of the intrinsically anisotropic crystallographic structure of a solid to accomplish 1D growth; introduction of a liquid-solid interface to reduce the symmetry of a seed; use of various templates with 1D morphologies to direct the formation of 1D nanostructures; use of supersaturation control to modify the growth habit of a seed; use of appropriated capping reagents to kinetically control the growth rates of various facets of a seed; and self assembly of 0D nanostructures<sup>98</sup>.

Among the bottom-up procedures, *template assisted methods* have been the most tried and tested for the preparation of 1D ferroelectric materials. In general, there are two main template based methods; denoted as 'physical' and 'chemical' templating. *Physical template* methods use templates with 1D morphologies in order to direct the growth of 1D product. After synthesis, the template must be removed either by thermal or chemical etching. *Chemical template* methods utilize 1D particles, which act as both template and precursor.

Other bottom-up approaches used for 1D nanostructure fabrication include *additive assisted methods*. It has been demonstrated that additives can be used as crystal growth modifiers by changing the growth habit or kinetically controlling the growth rate of various crystallographic facets<sup>101,102</sup>.

### 1.4.1 Template-directed methods

Template-based techniques are conceptually simple to implement. The template basically serves as a scaffold within (or around) a different material is *in situ* generated and shaped with the morphology complementary to that of the template.

#### Physical template methods for perovskite 1D preparation

The most efficient template methods are the physical sol-gel template techniques. In general, the sol-gel template procedures are initiated by filling on the template with precursor sol pores. The templates are porous membranes as poly(carbonate)-PC, anodized aluminum oxide-AAO or macro porous silicon. After the template is filled, the crystallization process takes place at elevated temperatures. The template is removed either during the annealing process by pyrolysis (as in the case of PC) or after the annealing step by chemical etching (as in the case of AAO).

It was demonstrated that depending on the process of filling the pores of the template NRs<sup>103-105</sup> or NTs<sup>106</sup> can be formed. For instance nanorods of TiO<sub>2</sub>, SiO<sub>2</sub>, BT, Sr<sub>2</sub>Nb<sub>2</sub>O<sub>7</sub>, Pb(Zr<sub>0.52</sub>Ti<sub>0.48</sub>)O<sub>3</sub> were grown in PC membranes when the template pores were filled by *electrophoresis* (sol-gel electrophoresis - Figure 1.22).<sup>103-105</sup> Limmer and coworkers claimed that the driving force of the template pores filling is the mobility of the nanoclusters under the electric field. This depends on the surface charge, zeta potential and nanocluster concentration.<sup>103,104</sup> It was demonstrated that nanotubes (NTs) of different ferroelectric materials can be obtained if the precursor mixture forms a thin layer on the pores walls during the pores filling.<sup>65,66,106-109</sup> NTs of PT and BT were obtained for the first time by Hernandez *et al.* in 2002<sup>106</sup> and NTs of BiFeO<sub>3</sub> were obtained by Park *et al.* in 2004<sup>108</sup> using the phenomenon of *capillarity* to fill the templates (PC and AAO) pores with sol precursor. The mechanism of formation of the NTs by this method was clarified by Morrison who claimed that in fact the positively charged sol nanoclusters<sup>110</sup> formed a uniform layer on the template pore wall by electrostatic interactions.<sup>107</sup> In other words the sol is wetting the pore wall.

By a method that consists in wetting the pore walls of porous templates (macroporous silicon) Luo *et al.* prepared in 2003 ferroelectric NTs ( $\text{PbZr}_{0.52}\text{Ti}_{0.48}\text{O}_3$  and BT) with sizes tunable over a relatively large mesoscopic range.<sup>65,66</sup> Instead of using sols they used organic polymers containing the precursors. These organic polymers are among the materials with low surface energy and because of this they can wet the pore walls under ambient conditions at room temperature and led to a reduction of the whole energy of the system. As a prerequisite, the pore walls must have a high surface energy.<sup>111</sup> In this way a mesoscopic film wets the walls of the pores in a manner analogous to the formation of precursor films on flat substrates.

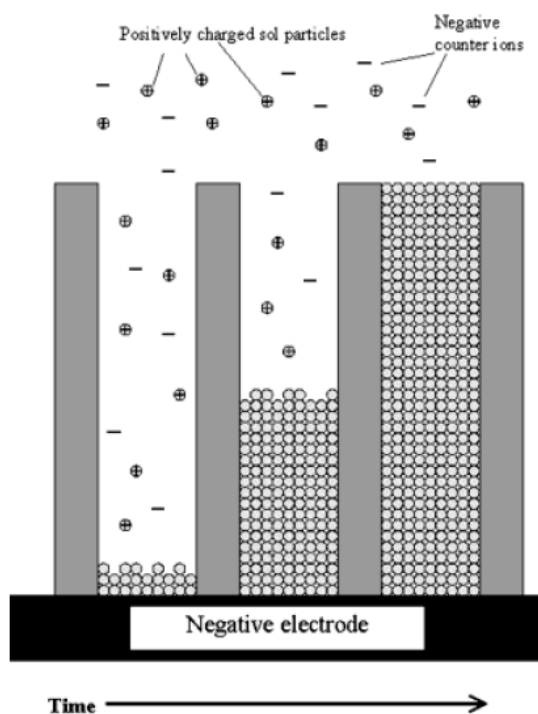


**Figure 1.22** The schematic representation of electrophoretic formation of nanorods. At the left, it is presented the beginning of the nanorod growth. Positively charged sol particles are moving electrophoretically towards the negative electrode, depositing at the bottom of the pore, while the negatively charged counter ions are moving in the opposite direction. The center of the diagram shows a later time, as the densely packed sol particles fill more of the pore. Lastly, the right side of the diagram shows a completely filled pore.<sup>103-105</sup>

In the same manner Zhao *et al.* prepared  $\text{LiNbO}_3$  nanotubes when ordered porous alumina templates (AAO) were wetted with solutions of a single source precursor.<sup>109</sup> The precursor solution spread on the alumina surface, and the pores were thus filled with the liquid. As the solvent evaporated, a layer of adsorbed molecules remains at the pore walls.

Another method of covering the template pore walls with a very thin layer of precursors mixtures is the chemical solution deposition (CSD) proposed and developed by Morrison *et al.*<sup>107</sup> The authors reported the use of liquid source misted chemical deposition<sup>112</sup> for filling porous Si substrates. The schematic representation of the misted CSD is shown in Figure 1.23.

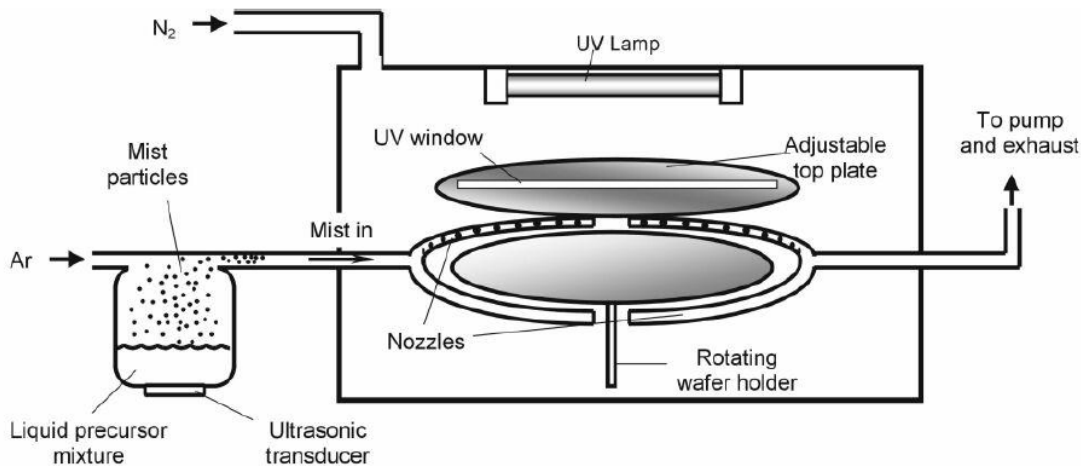


**Figure 1.23 Schematic representation of the liquid source misted chemical deposition technique<sup>107</sup>**

The system utilizes a precursor solution with the correct stoichiometry that is driven through a multiple nozzle type delivery system in close proximity to the rotating Si wafer. The main advantage comparing to the spin-on rotation for sol-gel precursors is that this method can achieve excellent step coverage. Moreover, the high speed spin on rotation for the sol-gel precursors would be completely inappropriate for NTs deposition.

For the sol-gel template method besides the parameters related to the pore filling or pore wall wetting the characteristics of the starting sol are very important specially because on these depend the subsequent crystallization process. For

instance Limmer *et al.* obtained at 700 °C for 15 min BT NRs starting from barium acetate in glacial acetic acid and titanium(IV) isopropoxide as barium and titanium sources, respectively. After the precursor mixture was stirred for about 30 min ethylene glycol was added, and the sol was stirred at 90 °C for 1 h. The resultant sol is stable at room temperature for a period of months, and has a pH ~ 5.<sup>104,113</sup> BT NTs were also obtained at 700 °C but after 6h by Hernandez *et al.* using a 0.8 M sol made by dissolving the barium acetate in hot acetic acid (62 °C). Titanium isopropoxide and ethanol were added to the barium acetate solution.<sup>106</sup> Luo *et al.* obtained crystalline barium titanate NTs at 850 °C for 1h by using commercial polymeric precursors (BATIO 9101 Polymer from Chemat Technology, INC).<sup>65,66</sup> First, the polymeric precursor in the template pores was transformed in an amorphous oxide layer by annealing in air at 300°C. This amorphous layer was subsequently crystallized by a thermal treatment in air.

Although physical template methods have the advantage of producing periodic arrays of 1D nanostructures, the main drawbacks are that the dimensions of the 1D structures are confined to the sizes of the template (usually larger in diameter than the required nanoparticle dimension) and the need of a post-deposition annealing process (often at high temperature).

#### *Chemical template methods for BT 1D preparation*

To overcome the abovementioned drawbacks chemical template methods using 1D nanostructures as both precursors and templates have been proposed.

The use of this approach was reported by Mao *et al.* for the synthesis of BT in which titanium oxide (TiO<sub>2</sub>) nanotubes were used as “bona fide” precursor material to generate the perovskite transition metal oxide BT and SrTiO<sub>3</sub> nanotubes.<sup>114</sup> Many aspects remain unclear in this work. The chemical nature of the nanotubes was not clearly identified at that time and the obtained powders contained amorphous phases, unreacted titania nanotubes and carbonate impurities.<sup>115</sup>

Later Bao *et al.* reassessed this approach and reported the hydrothermal synthesis of barium titanate nanostructures using Na<sub>2</sub>Ti<sub>3</sub>O<sub>7</sub> nanotubes and nanowires as synthetic precursors.<sup>116</sup> The shapes of the various BT products were

found to be dependent on the concentration of  $\text{Ba}(\text{OH})_2$ , the temperature, and the nature of the precursors. Various nanoblocks, including nanosheets and nanorods formed from the  $\text{Na}_2\text{Ti}_3\text{O}_7$  nanotubes and nanowires, respectively, grow and assemble to form nanowires, nanosheets, nanocubes, and hexagonal nanoparticles or ordered architectures of coral-like nanostructures of assembled nanorods, starfish-like nanostructures, and sword-like BT nanostructures.<sup>116</sup> However, the reported formation of barium titanate nanowires is questionable as no X-Ray diffraction data of the samples is presented and the reported microstructures do not sufficiently support the claimed results.

Buscaglia *et al.* also reported the synthesis of single crystal BT nanowires with tetragonal structure by topochemical solid-state reaction at 700 °C using layered  $\text{TiO}_2$  nanowires as reactive templates coated with  $\text{BaCO}_3$  nanocrystals<sup>117</sup>. According to the authors, the initial morphology of the titania nanowires was retained in the final product and the BT NWs exhibited strong piezoactivity and a striped domain structure.

Layered titanates ( $\text{K}_2\text{Ti}_4\text{O}_9$ ) were used as precursor for the formation of BT nanorods.<sup>118</sup> Layered structures were dispersed in aqueous solution of  $\text{Ba}(\text{OH})_2 \cdot 8\text{H}_2\text{O}$  and hydrothermal treatment at 90 °C without stirring for various times. After 42 h of reaction, single-crystal BT (cubic) nanorods with flat surface of facets and defined crystal axis were obtained. As the reaction time was extended to 50 h, a certain volume of nanorods converted to nanoparticles. When the reaction time was further elongated to 72 h, the volume of nanoparticles in the product notably increased. The proposed mechanism is based on an ion exchange ( $\text{K}^+$  ions in the interlayer spaces are ion-exchanged with  $\text{Ba}^{2+}$  ions) and the structural transformation from the layer structure of the precursor into the perovskite structure at the early stages of the reaction. At longer times of reaction (over 42 h) the nanorods changed to nanoparticles following a dissolution-precipitation mechanism.<sup>118</sup>

Following a different approach, well-ordered nanotubes of titania were fabricated by anodic oxidation of pure titanium foils in HF aqueous solution. Using these ordered nanotubes as templates, nanotube arrays of barium titanate<sup>119-121</sup> and barium strontium titanate<sup>121</sup> were synthesized under hydrothermal condition at

200 °C. The possible mechanism of 1D nanostructure formation is likely to be based on the wetting of the titania NTs surface and the topotactic reaction with formation of BT.

Although the chemical template methods are not straightforward and different mechanisms can nullify the template role of 1D precursors, small 1D ferroelectrics may be obtained at lower temperatures via these methods.

#### **1.4.2 Additive assisted methods and other methods**

It has been demonstrated that additives can be used as crystal growth modifiers by changing the growth habit or kinetically controlling the growth rate of various crystallographic facets<sup>101,102</sup>

##### Additive methods

Single-crystalline perovskite nanorods composed of BT (tetragonal) and SrTiO<sub>3</sub> have been prepared by Urban *et al.*<sup>67,122,123</sup> based on the solution-phase decomposition of bimetallic alkoxide precursors in the presence of coordinating ligands. In a typical reaction, H<sub>2</sub>O<sub>2</sub> was added at 100 °C to a heptadecane solution containing bimetallic alkoxide precursors and oleic acid. The reaction mixture was subsequently heated to 280 °C for 6 h, resulting in a white precipitate composed of nanorod aggregates. The authors claimed that the anisotropic nanorod growth is most likely due to precursor decomposition<sup>124</sup> and crystallization in a structured inverse micelle medium (water in oil)<sup>125</sup> formed by precursors and oleic acid under these reaction conditions.<sup>67,122,123</sup>

Mao *et al.* reported a large-scale molten salt synthesis for the preparation of single-crystalline BT NWs and nanocubes of SrTiO<sub>3</sub> in a NaCl medium at 820 °C in the presence of a nonionic surfactant.<sup>126</sup> In a typical synthesis, barium or strontium oxalate (depending on the desired nanostructure), TiO<sub>2</sub> (anatase), NaCl, and NP-9 (nonylphenyl ether) were mixed, ground, and sonicated. The authors observed that initially cubic shape nuclei were formed which subsequently growth into NWs. If the initial barium or strontium precursor was omitted altogether, identical experimental protocols all yield cubes, consisting of a mixture of anatase and rutile.<sup>126</sup> Moreover the authors observed that if NaCl is removed from the synthesis

of BT nanowires, the product is randomly particulate in shape distribution.<sup>127</sup> Recall that the shape of a nanocrystal may be determined by the relative specific surface energies associated with the facets of the crystal.<sup>128</sup> In addition, the preferential adsorption of molecules and ions to different crystal faces likely directs the growth of nanoparticles to their ultimate product morphology by controlling the growth rates along the different crystal faces.<sup>128-130</sup>

Therefore, what determines the final shape in the case of BT NWs may be the relative growth rates on the (100) vs. the (111) crystallographic planes due to preferential adsorption of the chloride ions (from NaCl) as also observed in the case of copper nanorods<sup>131,132</sup>. It seems like the role of the nonionic surfactant is only to facilitate the mixing and grinding of the precursors and is not influencing the growth of the perovskite NWs.<sup>127</sup>

In 2005 using poly(vinyl alcohol) (PVA) and poly(acrylic acid) (PAA) as additives Xu *et al.* prepared by hydrothermal synthesis Pb(Zr,Ti)O<sub>3</sub> NWs.<sup>101,133</sup> The authors observed that the morphology of Pb(Zr,Ti)O<sub>3</sub> nanocrystals develops from a particle to a rod by an oriented attachment and then to a wire by adjusting the ratio of PVA/PAA and the synthesis reaction time. The mechanism of the NWs formation can be explained as follows. The largest space of the crystalline plane in the tetragonal PZT structure occurs in the direction of [001], and the exposed (001) crystalline plane has the largest surface energy. In the presence of PVA and PAA, the difference in the surface energy between the exposed (001) plane and the other exposed planes of PZT particles is enlarged due to the different modes of adsorption of PVA and PAA on them.<sup>133</sup> PVA molecules are considered to adsorb on the ceramic particle surface by hydrogen bonds, whereas the adsorption of PAA on the particle surface is realized by chemical bond rather than a hydrogen bond.<sup>134-136</sup>

Similar oriented attachment mechanism<sup>137-139</sup> has been invoked by Zhang *et al.* for the formation of single-crystalline BT nanorods.<sup>102</sup> The synthesis was accomplished by using barium acetate and tetrabutyl titanate as starting materials and laurylamine as surfactant. The surfactant adsorbed on some special crystalline surfaces of the BT nanoparticles inducing the oriented attachment of

the primary nanoparticles. Depending on the orientation, further oriented attachment will result in the formation of rod-shaped structures.<sup>137-139</sup>

#### Other methods

Predominately tetragonal single crystalline BT NWs have been prepared by a surfactant free hydrothermal synthesis starting from TiO<sub>2</sub> crystalline anatase with spherical morphology as titanium source and Ba(OH)<sub>2</sub> as barium precursor in the presence of ammonia at pH ~13.<sup>140,141</sup> The main experimental observation was that at the early stages of reaction irregular BT particles formed but after longer reaction time NWs were obtained. Moreover the authors observed that the formation of nanowires with a high aspect ratio depended critically on pH and temperature of the synthesis solution. At a lower concentration of ammonia only particle aggregates of BT were obtained<sup>140</sup> The authors claimed that the morphology evolution might be governed by the well-known Ostwald ripening process.<sup>142,143</sup> Due to the absence of a stabilizing agent, the spherical particles undergo aggregation and rupturing (as a result of Rayleigh instability<sup>144</sup>) and finally start to dissolve due to higher free energy. At the same time, the TiO<sub>2</sub> particles act as a seed. The authors claimed that the reduction in surface energy is the primary driving force for the crystal growth and morphology evolution, due to the difference in solubility between the large particles and the small particles,<sup>140</sup> according to the well-known Gibbs–Thomson law.<sup>145</sup> But the authors did not give a good explanation about how the Ostwald ripening mechanism is responsible for the formation of the 1D morphology. This mechanism is the most probable growth mechanism for round shaped particles,<sup>146</sup> therefore, an oriented attachment mechanism<sup>137-139</sup> seems to be more likely.

The growth kinetics of one-dimensional single-crystalline KNbO<sub>3</sub> nanostructures (nanowires and nanofingers, the latter understood as defective nanowires) prepared by hydrothermal processing routes has been theoretically studied by Vasco *et al.*<sup>147</sup> A detailed inspection of nanofinger morphology reveals the following: (i) The nanofingers are made up by slightly distorted cubes, which are uniaxially attached to each other along [011] KN (Amm2 orthorhombic KN unit cell). (ii) The cube size ( $r$ ) decreases in a stepped way with random step heights

toward the nanofinger tip. These findings suggested that: (1) cubes constitute the nanofinger/nanowire building blocks, (2) the previous cubes act as substrates or base surfaces for the nucleation and epitaxial growth of the next cubes and (3) the nucleation of a new cube takes place only on a substrate cube larger than a certain critical size ( $r_c$ ), which is probably determined by the cube superficial tension.<sup>147</sup> Moreover, their results indicate that the morphology of KN nanostructures strongly depends on the temperature-pressure conditions and the starting composition. Nanowires with a well defined structure, a narrow diameter distribution, high aspect ratio, and high density have been obtained in a narrow window of the ternary phase diagram of KOH-Nb<sub>2</sub>O<sub>5</sub>-H<sub>2</sub>O.<sup>148</sup>

In 2007 Yuh *et al.* obtained for the first time by electrospinning combined with sol-gel process single crystalline tetragonal BT nanofibres with 50 nm in diameter and 1  $\mu$ m in length.<sup>149</sup> Starting from barium acetate and titanium isopropoxide, the viscosity of the precursor was controlled by poly(vinyl pyrrolidone) in 2-methoxyethanol. Tetragonality was confirmed by XRD, TEM and Raman spectroscopy and it was observed that perovskite tetragonal structures were developed with increased heat treatment temperature and time.<sup>149</sup>

As well stated in this section there is a current need and interest in the synthesis of anisometric ferroelectric perovskites, for applications in which optimized performance of the ferroelectrics is required. Due to the simplicity and costs of bottom-up synthesis, the chemical template growth of anisometric ferroelectric nanoparticles from nanotubes is highly promising, and deserves deep exploitation and study as well as the effect of additives on the morphological control of BT particles.

## **1.5 Summing up**

In this chapter the background of the present work has been introduced and discussed. The fundamental issues of ferroelectricity phenomena such as phase transitions, ferroelectric domains and polarization switching have been related to the basic properties of the perovskite structure. Based on the experimental observation of the decreasing of the spontaneous polarization with the size, size

and shape effect on ferroelectricity has been discussed for the confined nanostructures (0D, 1D, 2D), with special focus on the one-dimension ferroelectrics for which it was theoretically predict an increase of the ferroelectric performance when the size decreases. Nanowires of barium titanate with ca. 1.2 nm of radius possess the minimal critical volume that allows the ferroelectricity to be conserved above room temperature ( $T_C \approx 400$  K).<sup>72</sup>

Therefore, BT, a typical ferroelectric material, can be a good candidate to study the dimensionality and size reduction on the ferroelectricity. But the synthesis of anisometric nanostructures of complex oxides by chemical methods is not a trivial task (chapter 1.4). Indeed systematic studies on the synthesis of anisometric ferroelectric nanostructures and rigorous characterization are required.

## **1.6 Motivation and Objectives**

It was described in section 1.1 that ferroelectric oxides exhibit spontaneous electric polarization that can be reoriented by an external electric field (*i.e.* ferroelectricity) and other related properties such as piezoelectricity and pyroelectricity, in addition they possess large dielectric constants. Due to these properties ferroelectric oxides find currently application in a wide range of electronic and microelectronic devices (section 1.2.2). However, the continuous tendency for the scaling down has been imposing the decreasing size of electronic devices. In microelectronics, the concept “smaller” means greater performance in less space; for the case of integrated circuits represents more components per chip, faster operation, lower cost and less power consumption what implies the decrease of the size of the active and passive components of the circuitry. Nevertheless the physical properties of ferroelectric materials are critically dependent on the particle size and shape or, in other words, on the dimensionality.<sup>98,150-152</sup>

### *Why 1D ferroelectrics?*

The dimensionality effect on the nanoferroelectric materials has received special attention in the last decades<sup>50,52,60,64,73,153-155</sup> It has been introduced the

concept of critical size for 0D, critical diameter for 1D and critical thickness for 2D nanostructures below which ferroelectricity may no longer exist (see section 1.3).

The more recent interest in the fabrication of 1D ferroelectric nanostructures such as nanowires (NWs) and nanotubes (NTs) is owing to the following important motives. On the one hand, the study of these systems can provide useful information for the fabrication of next generation, fully three-dimensional FeRAM structures with the required bit density<sup>39,40</sup>. On the other hand, detailed *ab initio* calculations have predicted a new kind of ferroelectric order in nanorods and nanodisks<sup>72,82</sup>.

#### *Why bottom-up approaches?*

As stated in section 1.4 there are two main approaches for the preparation of 1D materials: top-down and bottom-up methods.<sup>97</sup> Top-down methods are widely used in modern commercial nanotechnology because they provide high-precision positioning and size control. However, they are limited in resolution, time-consuming and are prone to processing damage. Bottom-up approaches represent an alternative route for fabrication of ferroelectric nanostructures. Self-assembling processes governed by physicochemical interactions overcome the low throughput and processing damage of the top-down methods. In addition, the bottom-up methods are expected to produce structures with the dimensions much smaller than those achievable in the top-down approaches.

#### *Why BT?*

BT is one of the most widely used ferroelectric ceramic materials in passive electronic components, particularly in multilayer ceramics capacitors (MLCCs)<sup>30</sup>. In addition, there is currently renewed interest in BT with optimized piezoelectric performance as a possible lead free substitute for PZT<sup>156</sup>. Consequently, it was considered an ideal material upon which to base the activity of this PhD work.

Within this context, the main purpose of this research effort is to study low cost chemical routes for the preparation of anisotropic barium titanate particles. For that, two bottom-up approaches, chemical template method starting from layered titanate nanotubes (TiNTs) and additive assisted synthesis, were investigated since they match the objective of low-cost and offer the advantage of morphological control of BT nanostructures. This research was directed towards

the understanding the anisotropic growth and the role of dimensionality on the ferroelectric properties of barium titanate nanoparticulates. The specific objectives of this work include the following aspects:

- 1) Preparation of 1D titanium based materials to be use as templates for the anisotropic growth of BT.
- 2) Chemical template hydrothermal synthesis of anisotropic BT
- 3) Chemical template vapor phase synthesis of BT starting from TiNTs.
- 4) Assesment of the effect of various additives on the anisotropic growth of BT.

The outline of the thesis is schematically represented in Figure 1.24.

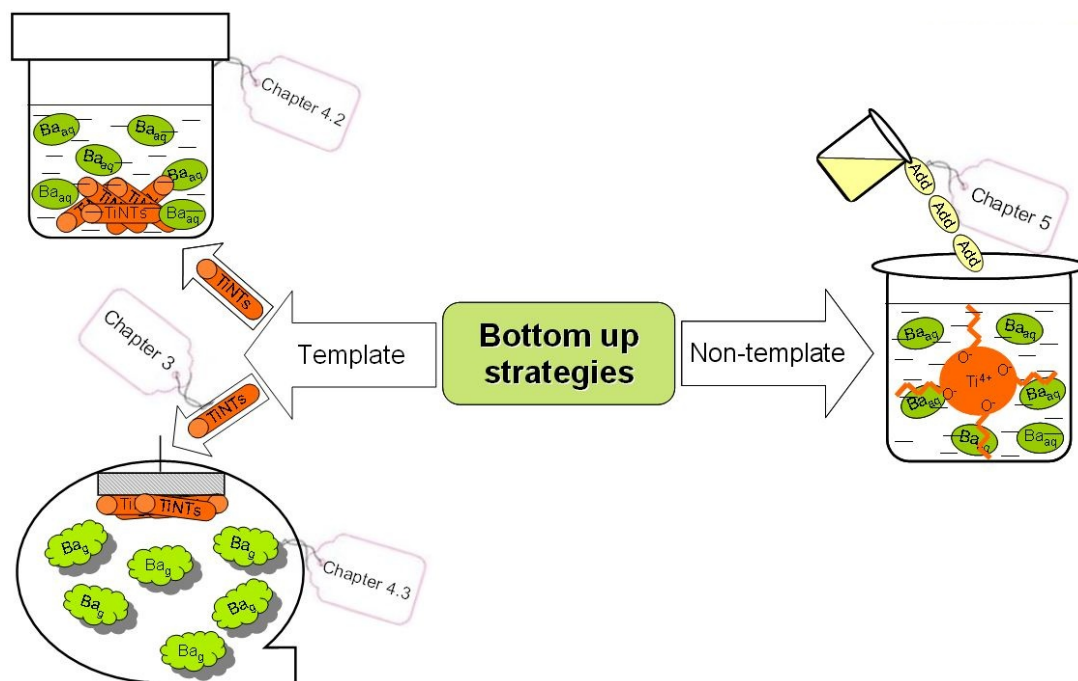


Figure 1.24 The outline of the thesis

## 2 Experimental Procedures and Characterization Techniques

### *Summary*

In this chapter, a detailed description of the principal experimental procedure used in this work, namely hydrothermal synthesis is presented. In addition, the main characterization techniques utilized to study the structural, microstructural and ferroelectric properties of the obtained nanoparticles such as powder X-ray diffraction (XRD), Fourier Transformed InfraRed (FTIR) and Raman spectroscopies, Scanning and Transmission Electron microscopies (SEM and TEM) and Piezoelectric Force Microscopy (PFM) are described.

### 2.1 Hydrothermal synthesis

Hydrothermal synthesis usually refers to any heterogeneous reactions occurring under the conditions of high-temperature–high-pressure ( $>100^{\circ}\text{C}$ ,  $>1$  atm) in aqueous solutions in a closed system.<sup>157</sup> Heating water in a sealed vessel (bomb, autoclave, etc) produces thermodynamic conditions and transport behavior that are remarkably different from those in ambient conditions. For instance, the solubility of nonpolar species increases, whereas that of ionic and polar compounds decreases. As a result of the drop of the polarity of water, the molecular mobility increases due to a decrease in the solvent viscosity ( $\eta$ ). Drastic changes of ionic hydration are brought about by the decrease in the dielectric constant ( $\epsilon$ ) and density ( $\rho$ ).<sup>157</sup>

Hydrothermal crystal growth has been well studied and described in many reviews and books.<sup>157-160</sup> As known, crystallization is governed by thermodynamic and kinetic rules, however there are few fundamental studies concerning the hydrothermal physical chemistry. This is possibly due to the lack of proper data on the type of solvents, the solubility, and solvent-solute interaction.

Nonetheless, in the particular case of BT, the main compound of this work, the thermodynamics of formation under hydrothermal conditions has been studied by Lencka *et al.*<sup>161</sup>. The authors reported stability diagrams which indicate the

optimum synthesis conditions (temperature, pressure, reactant concentration, pH, etc.) at which the barium titanate product is thermodynamically favorable. Hydrothermal reaction equilibria for multicomponent perovskite oxides typically involve a large number of independent reactions consisting of many species<sup>162</sup>. A substantial thermodynamic database is required to examine these equilibria. For the Ba-Ti hydrothermal system 20 relevant equilibria can be taken into account<sup>161</sup>.

Among the relevant species present in the Ba-Ti hydrothermal system there is a lack of standard state properties of the hydrous titanium species. This can be a limitation of thermodynamic modeling of hydrothermal systems based on titanium precursors. However, according to their calculations the predominant aqueous species of titanium in alkaline conditions is  $\text{Ti}(\text{OH})_4$ , whereas for barium, both  $\text{Ba}^{2+}$  and  $\text{BaOH}^+$  ionic species are important at  $\text{pH} > 12$  and  $t = 90^\circ\text{C}$ .

The general conclusions of their thermodynamic studies can be summarized as follows:

- the formation of BT requires high pH ( $> 12$ ) as at low pH the solubility of barium titanate increases;
- although the increase of barium concentration leads to a high yield of BT, this must be avoided due to the formation of a secondary  $\text{BaCO}_3$  product;
- despite the possibility that the barium carbonate can be removed by subsequent washing with acid solution, this process causes leaching of  $\text{Ba}^{2+}$  ion<sup>163</sup> from the perovskite phase;
- the more concentrated the solution of barium, the lower the necessary Ba/Ti ratio in order to obtain a good yield (note that ratios  $< 1$  cannot be used due to contamination with  $\text{TiO}_2$ );
- if the pH is very high barium hydroxide can precipitate as an impurity;
- the reaction can take place at pH lower than 12 if the reaction temperature is increased.

Regarding the kinetics of the hydrothermal crystallization of barium titanate two concurrent nucleation and growth mechanisms were proposed.<sup>164-166</sup> Hertl<sup>165</sup> suggested an *in-situ* transformation model which assumes that the dissolved  $\text{Ba}^{2+}$

and  $\text{Ba}(\text{OH})^+$  ions react topochemically with the titanium precursor at its surface with formation of BT by heterogeneous nucleation<sup>165,167</sup>. The second mechanism, the dissolution-precipitation mechanism<sup>164,166</sup> assumes that barium and titanium sources are rapidly dissolved and homogeneous nucleation of BT takes place. The thermodynamic and kinetics of BT hydrothermal formation is principally dictated by the properties of the titanium precursor<sup>85,161,164-166,168-170</sup>, as most of the barium sources are readily soluble in aqueous media. Recently, layered titanates were found to act as highly reactive titanium precursors suitable for the preparation of BT particles due to their enhanced ion-exchange capacity<sup>167</sup>. Moreover, it has been proposed that the morphology of the layered structured titanium precursor might be maintained if the topotactic reaction mechanism is favored and enhanced<sup>167,171</sup>.

### **2.1.1 General conditions used in this work**

All hydrothermal syntheses were performed in home made Teflon lined autoclaves. After mixing the different reagents by magnetic stirring to achieve good homogeneity, the autoclaves were closed and treated at temperatures ranging from 90 to 200 °C. After 1 to 144 h, the samples were removed from the oven, cooled, filtered and washed with distilled water. The powders were dried overnight at 60 °C.

## **2.2 Powder X-ray diffraction**

Powder X-ray diffraction (XRD) has been used in order to determine the crystallographic nature of the obtained samples. XRD analysis is commonly used to identify unknown substances, by comparing diffraction data against a database provided by the *International Centre for Diffraction Data*.<sup>172</sup>

The discovery of X-rays in 1895 by Wilhelm Conrad Röntgen (electromagnetic waves occurring between gamma-rays and the ultraviolet in the electromagnetic spectrum region (Figure 2.1) with the wavelength about 1 Å ( $10^{-10}$  m)) enables probing crystalline structures at the atomic level.

X-ray diffraction for the crystalline structure identification is based on the *Bragg's diffraction* from a three dimensional periodic structure such as atoms in a

crystal and is a consequence of the interference between waves reflecting from different crystal planes as shown in Figure 2.2.

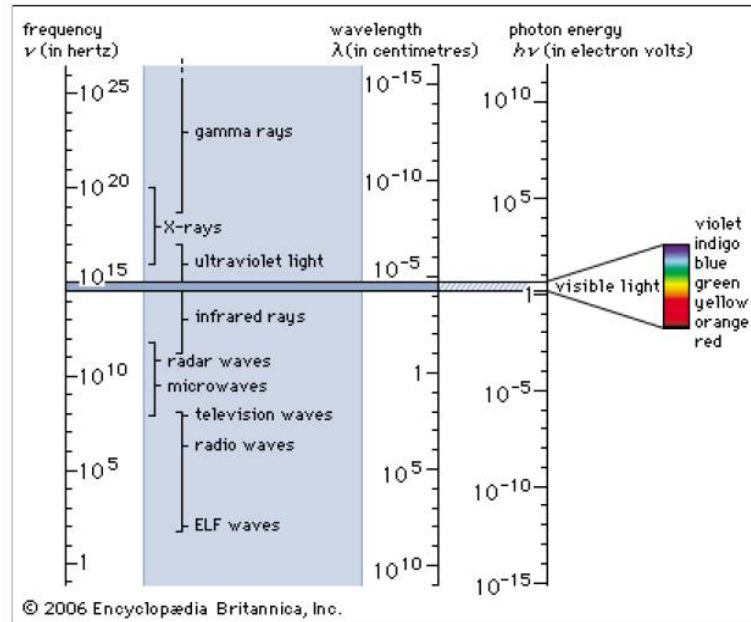


Figure 2.1 The electromagnetic spectrum. (www.britannica.com)

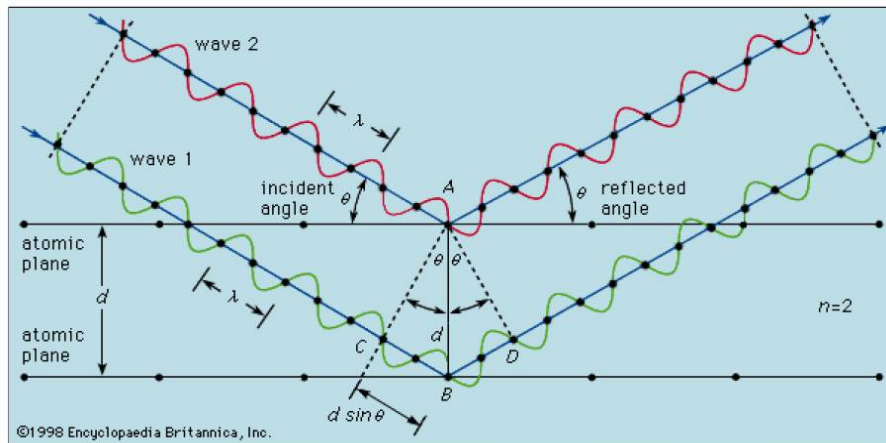


Figure 2.2 Diffraction condition for a given set of lattice planes. (www.britannica.com)

For a given set of lattice planes, Bragg's law (equation 2.1) relates the spacing between the planes in the atomic lattice,  $d_{hkl}$ , to a particular Bragg angle,  $\theta_{hkl}$ , at which reflections from these planes are observed:<sup>173,174</sup>

$$n \lambda = 2 d_{hkl} \sin \theta_{hkl} \quad \mathbf{2.1}$$

where  $\lambda$  states for the wavelength of incident monochromatic X-ray radiation,  $n$  for the number of planes (which is always an integer number) and  $hkl$  for the Miller indexes.

In other words Bragg's law indicates that diffraction is only observed when a set of planes makes a very specific angle (Bragg angle) with the incoming X-ray beam. This angle depends on the inter-plane spacing  $d_{hkl}$ , which itself depends on the size of the molecules/ions in the structure.

A characteristic pattern for each compound is produced by plotting the angular positions and intensities of the resultant diffracted peaks and the result is called powder X-ray diffraction pattern which contains the following information: the peak position which is related to the position of the atoms; the peak intensity closely related to the structure; the shape of the peak which is mostly related to the size of the crystal and the strain in the crystalline lattice and the background which can give indications about the short range order in the crystal.

A very useful concept proposed by crystallographers as a simple and convenient representation of the physics of diffraction by a crystal is the *reciprocal lattice*. The reciprocal space lattice is a set of imaginary points constructed in such a way that the direction of a vector from one point to another coincides with the direction of a normal to the real space planes and the separation of those points (absolute value of the vector) is equal to the reciprocal of the real interplanar distance.<sup>175</sup> The reciprocal lattice concept is useful for the crystal structure determination from powder diffraction data. Indeed, based on this concept crystal structures of known materials can be refined using the *Rietveld method*.<sup>51</sup> The Rietveld method is a so-called full pattern analysis technique. A crystal structure, together with instrumental and microstructural information is used to generate a theoretical diffraction pattern that can be compared to the observed data. A least squares procedure is then used to minimize the difference between the calculated

pattern and each point of the observed pattern by adjusting model parameters. There are various computer softwares which apply the Rietveld method<sup>176</sup>.

### **2.2.1 Experimental conditions used in this work**

The phase identification of the obtained samples was conducted by X-ray diffraction (XRD) using mainly a Rigaku diffractometer with Cu-K $\alpha$  radiation filtered by Ni. In general, the diffraction patterns were acquired from 5 to 130 ° ( $2\theta$ ) with a step length of 0.02 and a fixed counting time of 7 s. The X-ray patterns were processed afterward using *Jade* software.<sup>177</sup>

Philips X'Pert diffractometer and Cu-K $\alpha$  radiation was also used. In this case the diffraction patterns were acquired from 20 ° to 50 ° ( $2\theta$ ) with a step length of 0.04 ° and a fixed counting time of 20 sec/step. In order to obtain reliable quantitative data for kinetic analysis presented in section 4.2. The scan time and the samples weight were always the same.<sup>178</sup>

Variable-temperature X-Ray diffraction measurements were performed using Panalytical X'pert-Pro powder diffractometer equipped with an incident beam monochromator (Cu K $\alpha_1$  radiation), Pixcel position sensitive detector, and Anton Paar TTK-450 temperature stage having an operating range from -190 °C to +450 °C. The measurements were conducted in vacuum. The sample powder was mixed with a small amount of vacuum grease to improve thermal conductivity.

## **2.3 Vibrational spectroscopy- InfraRed and Raman**

Once the sample long range order structure was estimated by X-Ray Diffraction Analysis, other characterization techniques as vibrational spectroscopies InfraRed and Raman were used in order to refine structural details of the synthesized materials, such as estimating short range order and distinguishing between various crystalline phases.

Basically, the infrared (or Raman) spectrum is formed as a consequence of the absorption of electromagnetic radiation at frequencies that correlate to the vibration of specific sets of chemical bonds within the molecule / compound.<sup>179</sup>

A unit commonly used in vibrational spectroscopy is the *wavenumber*, which is expressed in  $\text{cm}^{-1}$ . This is the number of waves in a length of one centimeter and is given by the following relationship:

$$\bar{\nu} = \frac{1}{\lambda} = \frac{\nu}{c} \quad 2.2$$

where  $\lambda$  stands for the wavelength and  $c$  for the speed of the light in vacuum ( $c = 2.997925 \times 10^8 \text{ ms}^{-1}$ ).

The number of fundamental *modes of vibration* of a molecule can be predicted by the degrees of freedom of the vibrational energy which for linear and non linear polyatomic molecules containing  $N$  atoms are  $3N-5$  and  $3N-6$ , respectively.<sup>179</sup> For example the molecule of BT have 5 atoms per unit cell and is non-linear and therefore has  $3 \times 5 - 6 = 9$  vibrational degrees of freedom.

There are different possible modes of vibration. If a molecule is regarded as atoms joined by bonds with spring like properties the *stretching vibration* can be described by the movement when the bond length vary, and the *bending vibration* is the movement when one atom can move out of plane and so the bond angle is changed. Some bonds can stretch in-phase (*symmetric stretching*) or out-of-phase (*asymmetric stretching*). For more detailed description of modes of vibration see Figure 2.3.<sup>180</sup>

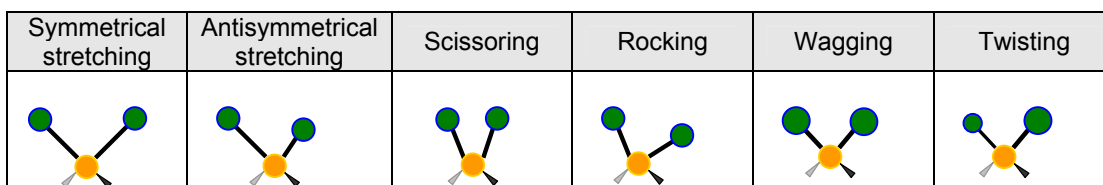


Figure 2.3 The six ways of vibration of a molecule. Adapted from [www.wikipedia.com](http://www.wikipedia.com)

IR and Raman spectra of solids are plots of intensity of absorption (IR) or scattering (Raman) as a function of frequency or wavenumber and are usually complex with a large number of peaks, each corresponding to a particular vibrational transition. The IR and Raman spectra of a particular solid are quite different since the two techniques are governed by different selection rules of the

vibrational modes. For instance, in order for a particular mode to be IR active, the associated dipole moment must vary during the vibrational cycle. The larger this change, then the more intense the absorption band will be. Consequently, centrosymmetric vibrational modes are IR active. The principal selection rule for a vibrational mode to be Raman active is that the nuclear motions involved must produce a change in its polarizability.<sup>181,182</sup> For example, the cubic phase of BT is IR active but in Raman spectroscopy only the non-centrosymmetric phases of barium titanate, namely tetragonal, orthorhombic and rhombohedra can be identified.<sup>183,184</sup>

### **2.3.1 Experimental conditions used in this work**

In this work Fourier Transformed Infrared (FTIR) spectra in transmittance mode were acquired with a Mattson Mod 7000 FTIR spectrometer using KBr pellets in a range 400-4000  $\text{cm}^{-1}$ . The pellets were prepared by sample dispersion (0.2 mg) in KBr matrix (150 mg) and pressed. The spectra were typically an average of 64 scans with 4  $\text{cm}^{-1}$  resolution.

Raman spectra were recorded on a Bruker RFS 100/S FT Raman spectrometer using a 1064 nm excitation of the Nd/YAG laser. The spectra were collected on powder samples in a range of wavenumber 100 and 1500  $\text{cm}^{-1}$ .

## **2.4 Electron microscopy**

Once the structure of the obtained samples has been determined the microstructural characterization by *Scanning* and *Transmission Electron microscopy* was considered.

An electron microscope is a type of microscope that uses an *electron beam* to illuminate a specimen and create a highly-magnified image. The high magnification up to 2 million times which can be achieved by an electron microscope compared to only 2000 times of a light microscope is due to the wavelength of an electron: *de Broglie wavelength* is much smaller than that of the photon in the visible light.<sup>185</sup>

The original form of electron microscope, the *transmission electron microscope* (TEM), illustrated in Figure 2.4, uses a high voltage electron beam to create an image.

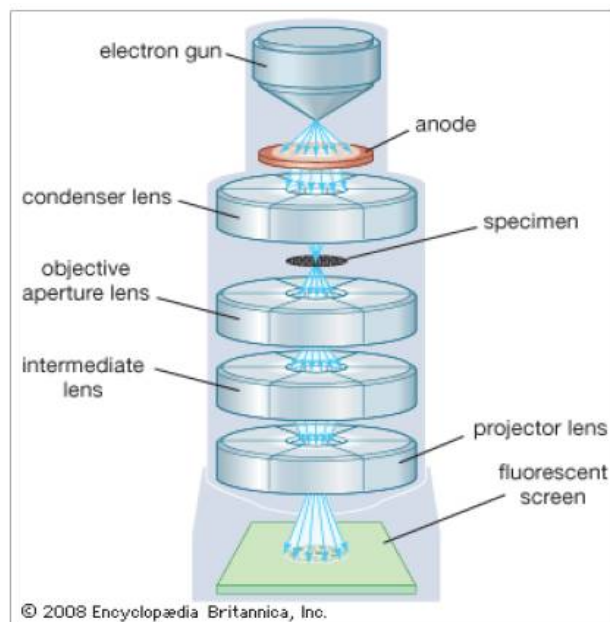


**Figure 2.4 Schematic representation of Transmission Electron Microscope.**  
([www.britannica.com](http://www.britannica.com))

A TEM consists of an illumination system, specimen stage and imaging system.<sup>186</sup> The electrons are emitted by an *electron gun*, commonly fitted with a tungsten filament cathode as the electron source. The electron beam is accelerated by an anode typically at +100 keV (40 to 400 keV) with respect to the cathode, focused by electrostatic and electromagnetic lenses (similar to how a light microscope uses glass lenses to focus light), and transmitted through the specimen that is in part transparent to electrons and in part scatters them out of the beam.<sup>186</sup> The contrast is mainly formed by the elastic scattering of electrons with matter and can be used to obtain real-space as well as diffraction information. The inelastic scattering of some of the electrons can be helpful in obtaining chemical information from very small regions in the specimen. The spatial variation in this information (the "image") is viewed by projecting the magnified electron image onto a fluorescent viewing screen coated with a phosphor or scintillator

material such as zinc sulfide. The image can be photographically recorded by exposing a photographic film or plate directly to the electron beam, or a high-resolution phosphor may be coupled by means of a lens optical system or a fiber optic light-guide to the sensor of a CCD (charge-coupled device) camera. The image detected by the CCD may be displayed on a monitor or computer.<sup>186</sup>

The resolution of the TEM is limited primarily by *spherical aberration*. By the reduction of the spherical aberration (by aberration correctors), an increase of the mechanical stability and the use of high voltages has led to the development of *High Resolution TEM* (HRTEM) which allowed the production of images with sufficient resolution to show carbon atoms in diamond separated by only 0.89 Å and atoms in silicon at 0.78 Å.<sup>187,188</sup> at magnifications of 50 million times.<sup>189</sup> The ability to determine the positions of atoms within materials has made the HRTEM an important tool for nano-technologies research and development.

Unlike the TEM, where electrons of the high voltage beam carry the image of the specimen, the electron beam of the *Scanning Electron Microscope* (SEM-Figure 2.5)<sup>190,191</sup> does not at any time carry a complete image of the specimen.

The SEM produces images by probing the specimen with a focused electron beam that is scanned across a rectangular area of the specimen.<sup>190</sup> At each point of the specimen the incident electron beam loses some energy, and that lost energy is converted into other forms, such as heat, emission of low-energy secondary electrons, light emission (cathodoluminescence) or X-ray emission.<sup>190</sup>

Generally, the image resolution of an SEM is about an order of magnitude lower than that of a TEM. However, because SEM image relies on surface processes rather than transmission it is able to image bulk samples up to several centimeters in size (depending on instrument design) and has a much greater depth of view, and so can produce images that are a good representation of the 3D structure of the sample.<sup>186,190</sup>

An important structural characterization technique used in this work is *electron diffraction* performed by TEM. This has the main advantage over the X-ray diffraction of wavelength of electrons which is much smaller than that of the X-

ray.<sup>186</sup> Moreover, the electron diffraction in TEM can be combined with direct imaging of the sample.<sup>186</sup>

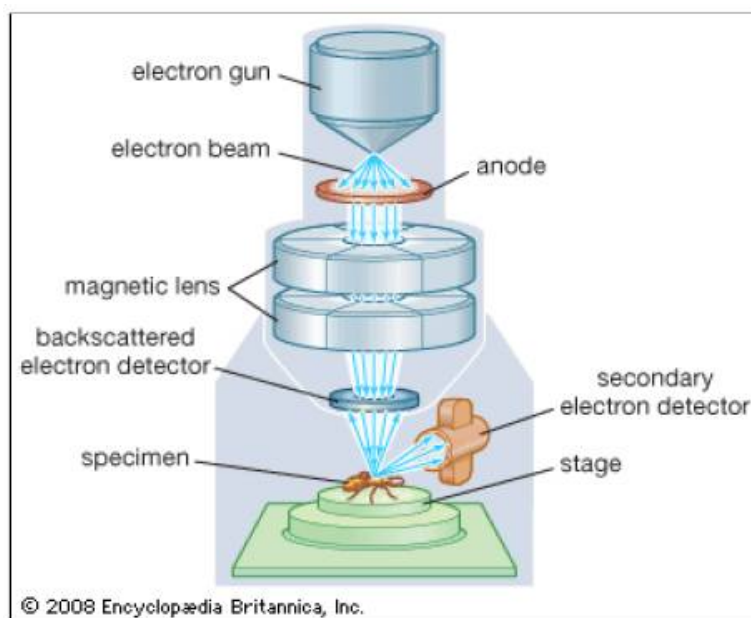


**Figure 2.5 Schematic representation of Scanning Electron Microscope.**  
([www.britannica.com](http://www.britannica.com))

However the electron diffraction in TEM has several important limitations. First, as a general requirement for TEM experiment, the sample to be studied must be electron transparent, meaning the sample thickness must be of the order of 100 nm or less.<sup>186</sup> Furthermore, taking into account that the electron diffraction is interacting with a small portion of the sample it is often regarded as a qualitative technique suitable for symmetry determination, but too inaccurate for determination of lattice parameters and atomic positions of all the sample.

Electron energy-loss spectroscopy is exploited in this work as a powerful analytical technique that can be utilized to obtain information on the structure, bonding, and electronic properties of a material.<sup>186,192</sup> The interactions of fast electrons with the specimen result in excitations of electrons into unoccupied energy levels in the conduction band as well as collective excitations of valence electrons. When a spectrum is obtained by analyzing the energy lost by the

incident electrons, the region up to an energy loss of ~50 eV is dominated by collective excitations of valence electrons (plasmon) and by interband transitions. At higher-energy losses, ionization edges occur due to excitation of core electrons into the conduction band. Interband transitions originate from the excitation of electrons in the valence band to empty states in the conduction bands, so these can be identified as transitions in a band structure model.<sup>186,192</sup>

#### **2.4.1 Experimental conditions used in this work**

In this work, the microstructures were analyzed by SEM with a Hitachi SU-70 (S-4100) (*FCT: REDE/1509/RME/2005*) microscope, and by TEM with a 300 kV Hitachi H9000-NA instrument or a Jeol 2200FS microscope. A Philips XL 30 FEG microscope was also used in some cases.

The samples to be characterized by SEM were prepared as follows. Powder samples were dispersed in ethanol and few drops of the suspension were added onto the Al sample holder. After drying the samples were covered with a thin layer of carbon in order to make them conductive. The carbon deposition process was performed using an Emitech K950 carbon deposition chamber equipped with a turbo pump. The outgas time and evaporated time were 30 and 2 seconds, respectively.

For TEM analysis powder samples were dispersed in ethanol. One drop of the formed suspension was then added to a holey carbon film supported on a copper grid (Agar Scientific 400 Mesh Cu).

### **2.5 Piezoelectric force microscopy**

The local ferroelectric properties of the samples obtained in this work have been evaluated by *Piezoelectric Force Microscopy* (PFM) which belongs to the group of techniques called *Scanning Probe Microscopy* (SPM).

The concept of SPM is based on using the interaction of a small physical probe (*tip*) with a solid surface to obtain spatially resolved information about the sample surface. The (small) probe is scanned with respect to the sample, and the interaction is monitored. The spatial position (x, y) of the monitored interaction is

combined with the interaction information to construct a map of the probe-sample interactions.<sup>193</sup>

PFM is a scanning probe technique based on the detection of the electromechanical response of a material to an applied electrical bias and it has been developed due to the necessity for probing electromechanical functionalities. Electromechanical coupling is one of the fundamental mechanisms underlying the functionality of many systems ranging from non-volatile computer memories and micro electromechanical systems to electromotor proteins and cellular membranes.<sup>194</sup> The PFM is a tool for local nanoscale imaging, spectroscopy, and manipulation of piezoelectric and ferroelectric materials.<sup>194,195</sup> A general PFM experimental setup is presented in Figure 2.6.<sup>196</sup>

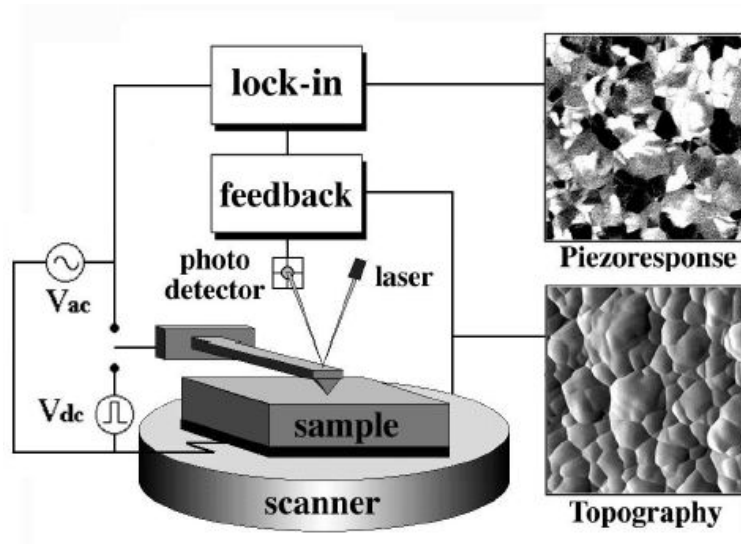


Figure 2.6 A general PFM experimental setup. Adapted from the reference<sup>196</sup>

As shown in Chapter 1 the relationship between the strain and the applied electric field (referred to as the “inverse piezo effect”) in piezoelectric materials are described by a rank-3 tensor. The most important component of this tensor for typical “vertical” PFM is the  $d_{33}$  component of the piezoelectric tensor,<sup>197</sup> since it couples directly into the vertical motion of the cantilever. The voltage applied to the tip is:

$$V_{tip} = V_{dc} + V_{ac} (\cos \omega t) \quad 2.3$$

where  $V_{dc}$  states for the dc bias voltage applied to the bottom electrode and  $V_{ac}(\cos \omega t)$  for the ac voltage applied to the tip with  $\omega$  first harmonic signal. This voltage results into a piezoelectric strain in the material due to piezoelectric effect that causes a cantilever displacement of<sup>198</sup>:

$$z = z_{dc} + A(\omega, V_{ac}, V_{dc}) \cos(\omega t + \varphi) \quad 2.4$$

where  $z_{dc}$  states for the dc component of the cantilever displacement,  $A(\omega, V_{ac}, V_{dc})$  for piezoresponse amplitude and  $\varphi$  for the phase of the electromechanical response. When the voltage is driven at a frequency well below that of the contact resonance of the cantilever, this expression becomes:

$$z = d_{33}V_{dc} + d_{33}V_{ac} \cos(\omega t + \varphi) \quad 2.5$$

where it is implicitly assumed that the piezoelectric coefficient,  $d_{33}$ , depends on the polarization state of the material. In reality, the component  $d_{33}$  in Equation 2.5 is an “effective” piezoelectric coefficient that depends on the contribution from other tensor elements and on the crystallographic and real space orientation of the piezo material, as well as details of the tip-sample contact.<sup>199</sup>

PFM measures therefore the mechanical response when an electrical voltage is applied to the sample surface with a conductive tip. In response to the electrical stimulus, the sample then locally expands or contracts as shown in Figure 2.7.

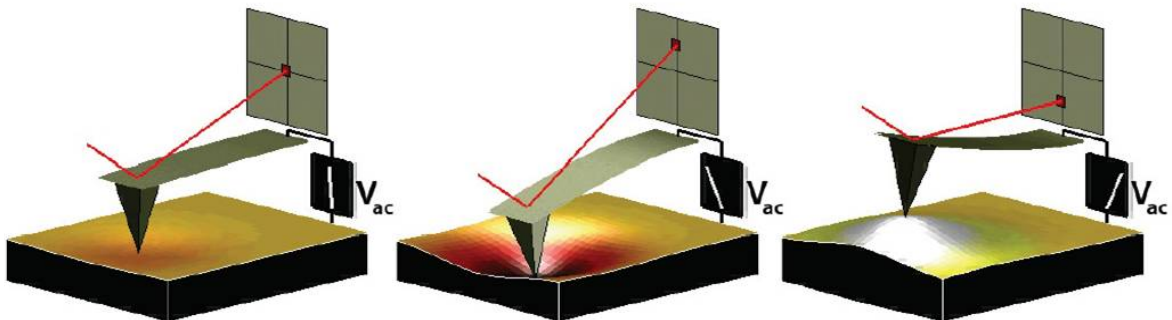


**Figure 2.7** Depiction of PFM operation. The sample deforms in response to the applied voltage. This, in turn, causes the cantilever to deflect, which can then be measured and interpreted in terms of the piezoelectric properties of the sample. Adapted from the reference<sup>200</sup>

Three typical PFM techniques have been used in the present work: vertical PFM, lateral PFM and PFM spectroscopy. In vertical PFM imaging, out-of-plane polarization is measured by recording the tip-deflection signal at the frequency of modulation. Lateral PFM is a technique where the in-plane component of polarization is detected as lateral motion of the cantilever due to bias-induced surface shearing. Eng *et al.*<sup>201,202</sup> have shown that the in-plane component of the polarization can be observed by following the lateral deflection of the AFM cantilever, and have applied this technique to reconstruct the three-dimensional distribution of polarization within domains of ferroelectric single crystals. The schematic representation of vertical and lateral PFM detection is presented in Figure 2.8.

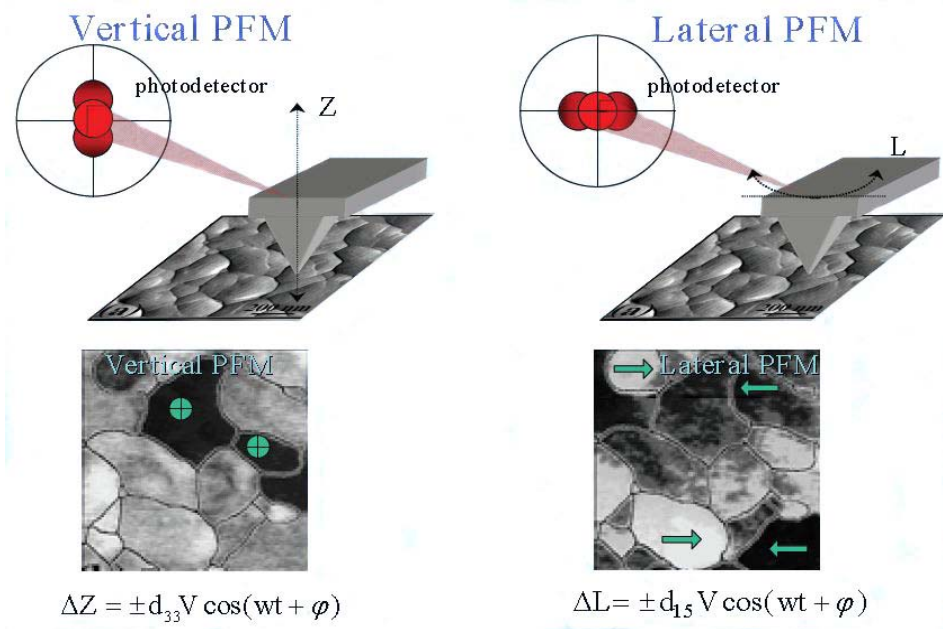


**Figure 2.8 Schematic representation of Vertical and Lateral PFM detection. Adapted from reference<sup>195</sup>**

Switching Spectroscopy PFM (SS-PFM) refers to locally generating hysteresis loops in ferroelectric materials. From these hysteresis loops, information on local ferroelectric behavior such as imprint, local work of switching, and nucleation biases can be obtained.<sup>198</sup> In SS-PFM, a sine wave is carried by a square wave that steps in magnitude with time, as illustrated in Figure 2.9.

Between each ever-increasing voltage step, the offset is stepped back to zero with the AC bias still applied to determine the bias-induced change in polarization distribution (e.g. the size of the switched domain). It is then possible to see the hysteresis curve of the switching of the polarization of the surface (bottom diagram in Figure 2.9).<sup>198</sup>

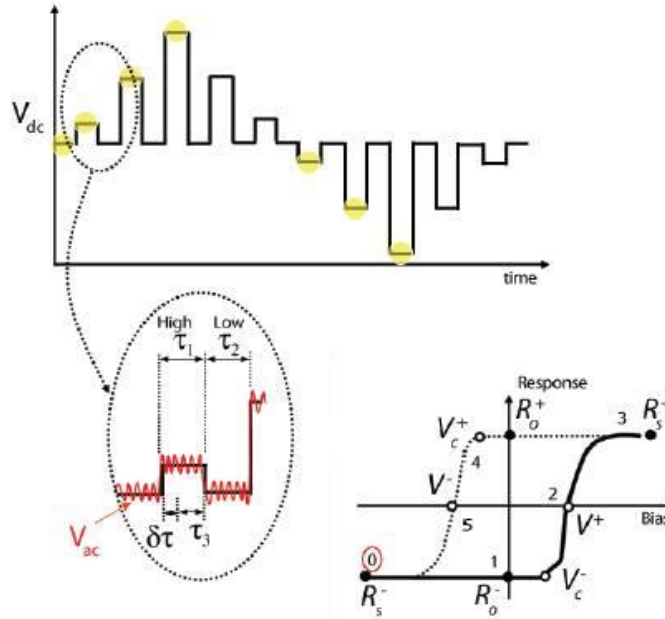


Figure 2.9 Switching spectroscopy PFM diagram. Adapted from the reference <sup>198</sup>

### 2.5.1 Experimental conditions used in this work

In this work the room temperature piezoelectric response was evaluated by SPM using NanoScope III, Digital Instruments VEECO. The vertical PFM was obtained when the mechanical oscillations were induced by alternating current (ac) voltage at 50 kHz to the tip. Two types of tips were used according to the samples features. NANOWORLD point probe silicon Pt/Ir coated with the spring constant of the cantilever of 2.8N/m and the free resonance frequency of 75 kHz has been used in same cases. In other cases NANOSENSORS silicon probes with force constant of 55 N/m and free resonance frequency of 350 kHz have been used. The lateral PFM measurements with the ac voltage at 5 kHz and 0 degree scan angle of the tip.

It is better to remark here that the PFM measurement procedure requires mechanical contact between the tip and the investigated material. This means that the particles under study have to sustain lateral forces during the scanning of the AFM tip. It is for this that the sample preparation for this type of measurements is very challenging. In this work barium titanate powders were dispersed in a solution of polyvinyl pyrrolidone in ethanol<sup>203</sup> and spin coated afterwards on Pt/Ti/SiO<sub>2</sub>/Si substrates. The as prepared samples were annealed at 450 °C to eliminate the polymer and glued afterwards on a conductive substrate with Ag paste as the bottom electrode.

The switching of barium titanate samples was evaluated by poling a selected area with an appropriated dc bias. The local hysteresis measurements on individual grains were performed by scanning a dc bias in 20 steps, with 0.3 s duration of each step and 0.2 s delay after the step.

## **2.6 Other analysis**

### **2.6.1 Thermal analysis**

Whenever it was necessary to evaluate structural phase transitions thermal analyses have been considered. Thermal analysis consists of a group of techniques in which a physical property of a substance is analyzed as a function of temperature, while the substance is subjected to a controlled temperature programmer.

*Thermogravimetric Analysis* (TGA) determines the changes in sample weight in relation to the change in temperature. Such analysis relies on a high degree of precision in three measurements: weight, temperature, and temperature change.<sup>204</sup>

*Differential scanning calorimetry* (DSC) is a thermoanalytical technique in which the difference in the amount of heat required to increase the temperature of a sample and reference are measured as a function of temperature. Both the sample and reference are maintained at nearly the same temperature throughout the experiment. The main application of DSC is in studying phase transitions, such as melting, glass transitions, or exothermic decompositions. These transitions

involve energy changes or heat capacity changes that can be detected by DSC with high sensitivity.<sup>205</sup>

In this work thermogravimetric (TGA) curves were measured with a TGA-50 Shimadzu or Mettler TGA/DSC/TMA analyzer from room temperature to 800 °C under air at a heating rate of 10 °C/min. Differential scanning calorimetry (DSC) patterns were collected using a DSC-50 Shimadzu analyzer at a rate of 10 °C/min.

### **2.6.2 Particles size measurements**

The *Particle Size Distribution* (PSD) was collected using a laser diffraction method (Malvern Mastersizer S) based on *Dynamic Light Scattering* (DLS) technique. When the light hits small particles the light scatters in all directions (Rayleigh scattering) as long as the particles are small compared to the wavelength (< 250 nm). If the light source is a laser, and thus is monochromatic and coherent, then one observes a time-dependent fluctuation in the scattering intensity. These fluctuations are due to the fact that the small molecules in solutions are undergoing Brownian motions and so the distance between the scatterers in the solution is constantly changing with time. This scattered light then undergoes either constructive or destructive interference by the surrounding particles and, within this intensity fluctuation information is contained about the time scale of movement of the scatterers. A review of the DLS methods has been reported by Pecora<sup>206</sup>.

For DLS measurements 0.4 g of material was dispersed in 40 g of a PAA solution (0.1 wt %, pH = 10) using an ultrasonic horn, before being analyzed (refractive index  $n = 2.4$ ).

The size of the primary particles,  $d_{\text{BET}}$  (nm) was estimated starting from Brunauer-Emmett-Teller (BET) specific surface areas  $S_{\text{BET}}$  ( $\text{m}^2 \cdot \text{g}^{-1}$ ) which were estimated from  $\text{N}_2$  adsorption isotherms using a Micromeritics Gemini 2375 equipment. The *adsorption isotherms* are plots which show the quantity of the gas adsorbed at constant temperature and indicate the concentration of the adsorbate in equilibrium with the solid surface versus the partial pressure of the gas.<sup>207</sup> The BET method is an extension of the Langmuir theory to multilayer adsorption with the following hypotheses: (a) gas molecules physically adsorb on a solid in infinite

layers; (b) there is no interaction between each adsorption layer; and (c) the Langmuir theory can be applied to each layer.<sup>207</sup> Before BET measurements the samples were dried at 200 °C in flowing nitrogen for 1 h.

### **2.6.3 Chemical analysis**

The chemical content of the samples were determined by Inductively Coupled Plasma spectroscopy (ICP). Prior to analysis, 10 mg of sample was added to 1 ml HNO<sub>3</sub> and 0.1 ml HF. After complete dissolution by microwave treatment the sample was diluted to 100 ml and analyzed.

## **2.7 Summing up**

This chapter provided the general conditions of the experimental procedures and the main characterization techniques used in this work.

The samples studied herein were prepared mainly by the hydrothermal method, as described above. Further details of the experimental procedures are presented in the following chapters.

Phase identification of the obtained samples was routinely conducted with powder X-ray diffraction (XRD). As supplementary methods to refine the phase identification Raman and IR spectroscopies were utilized. The microstructures were analyzed by electron microscopy (SEM and TEM). The local electrical properties were evaluated by SPM (PFM). The PSD was estimated by DLS and the specific surface area by N<sub>2</sub> adsorption (BET method). Some thermal analysis techniques were used for the evaluation temperature behavior of the samples. Chemical analysis by ICP was also described.

### 3 Titanium precursors for chemical template approaches

#### *Summary*

This chapter is dedicated to the results and discussion of titanium based 1D nanostructures prepared by hydrothermal synthesis. Initially, systematic structural and morphological studies, demonstrated that during hydrothermal treatment of TiO<sub>2</sub> anatase in the presence of concentrated NaOH aqueous solution, layered structured titanate nanotubes form independent of synthesis temperature, time or molar ratio of reagents. In subsequent investigations, the effect of post synthesis neutralization and hydrothermal processes was assessed in order to evaluate the morphological stability of the nanotubes. It is established that the driving force for the formation of tubular shape is the alkaline treatment and that layered structured sodium titanate nanotubes transform to anatase nanorods during the after synthesis hydrothermal treatment. Finally it is confirmed that rutile is less efficient than anatase to form pure phase nanotubes due to its higher stability and low reactivity in alkaline conditions.

#### 3.1 Motivation

In the last 20 years much work has been dedicated to develop 1D TiO<sub>2</sub> and titanate nanomaterials due to their potential applications in catalysis<sup>208,209</sup>, photocatalysis<sup>210,211</sup>, electrocatalysis, lithium batteries<sup>212</sup>, hydrogen storage<sup>213</sup>, and solar-cell technologies<sup>214,215</sup> where the aspect ratio of the materials is important.

In 1996, Hoyer<sup>216</sup> reported for the first time the formation of titanium dioxide nanotube arrays. The tubular structure was formed by an electrochemical deposition in a polymer mold, obtained from porous aluminium oxide. The inner diameter of the tubes decreased from ca. 100 nm to 70 nm during the crystallization. In 1998, Kasuga *et al.*<sup>217,218</sup> reported the synthesis of TiO<sub>2</sub> nanotubes with 8 nm in diameter and ~ 100 nm in length by the hydrothermal

method. In the absence of a template and with a potential for high-volume production, the authors, using a highly concentrated sodium hydroxide (NaOH) solution, developed an easy and low cost method to produce TiO<sub>2</sub> NTs through a chemical method.

The unanswered questions from the work of Kasuga and co-workers<sup>217,218</sup> have been the driving force for the later research in the field of Ti NTs<sup>219-224</sup>. The first issue to arise from their works was related to the crystallographic structure of the NTs. Kasuga *et al.*<sup>218</sup> claimed that under hydrothermal conditions anatase NTs are formed. Other authors<sup>219,220</sup> contested this indexation due to absence of a lamellar features in the anatase phase, suggesting instead that the tubular materials were layered titanates with the general formula H<sub>2</sub>Ti<sub>3</sub>O<sub>7</sub><sup>219</sup> or H<sub>x</sub>Ti<sub>2x/4</sub>□<sub>x/4</sub>O<sub>4</sub> (x ≈ 0.7, □: vacancy<sup>220</sup>). Later on, Yang *et al.*<sup>225</sup> questioned the formation of trititanate and reported the formation of a dititanate layered structure, Na<sub>2</sub>Ti<sub>2</sub>O<sub>4</sub>(OH)<sub>2</sub>. The second problem under debate was the moment and the formation mechanism of the nanotubes. According to Kasuga *et al.*<sup>218</sup> the water washing step and the post-treatment with acid are essential processes for the formation of the tubes, because they allow the elimination of sodium cations and dehydration, with subsequent formation of the NTs. The same idea was claimed by Tsai *et al.* when dititanate (H<sub>2</sub>Ti<sub>2</sub>O<sub>5</sub>) NTs were obtained.<sup>222</sup> The authors reported that the transformation into the nanotubular shape occurs during the post-treatment acid washing and the driving force for this process is the Na<sup>+</sup>/H<sup>+</sup> ion exchange. On the contrary, Du *et al.*<sup>226</sup>, using high-resolution transmission electron microscopy, observed that the trititanate (H<sub>2</sub>Ti<sub>3</sub>O<sub>7</sub>) NTs were formed during alkaline treatment with NaOH and not during washing and acid treatment processes.

Nevertheless, as shown in Chapter 1 the growth of titanate based ferroelectrics starting from TiO<sub>2</sub> NTs has been evaluated. It was claimed that TiO<sub>2</sub> based nanotubes act as both template and precursors for the preparation of BT 1D nanostructures.<sup>114,117,227</sup> Within this context we studied the titanium based 1D materials and the results obtained are presented and discussed in the following sections.

### **3.2 Materials preparation**

The commercial titanium dioxide precursors used for this study were anatase (Merck, 99%) and rutile (Johnson Matthey - Alfa, 99.8%). The preparation was initiated by treating a certain amount of each titania precursor with 10 M NaOH (Fluka, 97%) solution. The  $\text{TiO}_2/\text{NaOH}$  molar ratio was varied from 0.05 to 0.4. After stirring for 30 minutes, the mixtures were transferred into 100 mL Teflon-lined autoclaves and hydrothermal treatments were performed at various temperatures (from 110 °C to 150 °C) for various periods of time (20 to 72h). The samples were washed after the synthesis with distilled water until pH = 7. Each sample was dried overnight in air at 50 °C. The samples were indexed with "A7" and "R7" indicating the samples prepared with anatase and rutile, respectively and collected at pH = 7 after water washing. In the study of the influence of the synthesis conditions reference to the temperature and duration of the synthesis have been added to the label. For example the sample prepared from anatase at 130 °C for 48 h is indexed as A7-130-48.

In order to study the effect of the post-synthesis process, the sample synthesized at 150 °C for 48 h ( $\text{TiO}_2/\text{NaOH}$  molar ratio = 0.05) was divided in two portions and treated as follows: (i) Stage I (neutralization after hydrothermal synthesis at high pH) consisted in decreasing pH from 14 to 7 by washing the obtained precipitate with distilled water at room temperature; (ii) the Stage II (acid treatment + neutralization) was performed by decreasing the pH from 7 to 2. Therefore, part of the suspension obtained in Stage I was treated with 50 mL of an aqueous solution of hydrochloric acid (Panreac, 0.1 M) and was ultra-sonicated for 20 minutes. The as obtained suspension with pH = 2 was then neutralized to pH = 7 by successive washing cycles with distilled water at room temperature. During the washing steps, samples at different values of pH were collected for further analysis. Each sample was dried in air at 60 °C for 12 h. In this case the samples were indexed with A from anatase and a number denoting the pH value at which the sample was collected. "C" indicates the washed samples with hydrochloric acid. As an example, the sample prepared starting from anatase and collected in Stage I at pH 7 was indexed as A7. The correspondent sample after the Stage II was denoted by AC7.

The effect of post synthesis hydrothermal treatment was also studied. For this, samples obtained from anatase as described above after the first stage of washing (A7) were redispersed in deionized water and hydrothermally treated at 90, 150 and 200 °C for 24 h. The samples were denominated as for example A7→200, in which the number “200” indicates the temperature of the post-synthesis hydrothermal treatment.

Table 3.1 summarizes the sample indexes used in this study.

**Table 3.1 The nomenclature of the 1D titanium based samples used in this study.**

Synthesis conditions			Post-synthesis		Titanium precursor	
Temperature	Time	TiO <sub>2</sub> /NaOH Molar ratio (A715048)	Stage and pH of sample collection	Hydrothermal	Anatase	Rutile
A7-130-48	A7-150-48	0.05	A13	A7→90	A7	R7
A7-150-48	A7-150-72	0.125	A11	A7→150	AC7	RC7
			A8	A7→200		
			A7			
			AC2			
			AC7			

### 3.3 Results

#### 3.3.1 The influence of the synthesis conditions

Figure 3.1 shows the SEM micrographs of the samples prepared at a) 130 and b) 150 °C for 48 h and c) 150 °C for 72 h with TiO<sub>2</sub>/NaOH molar ratio of 0.05.

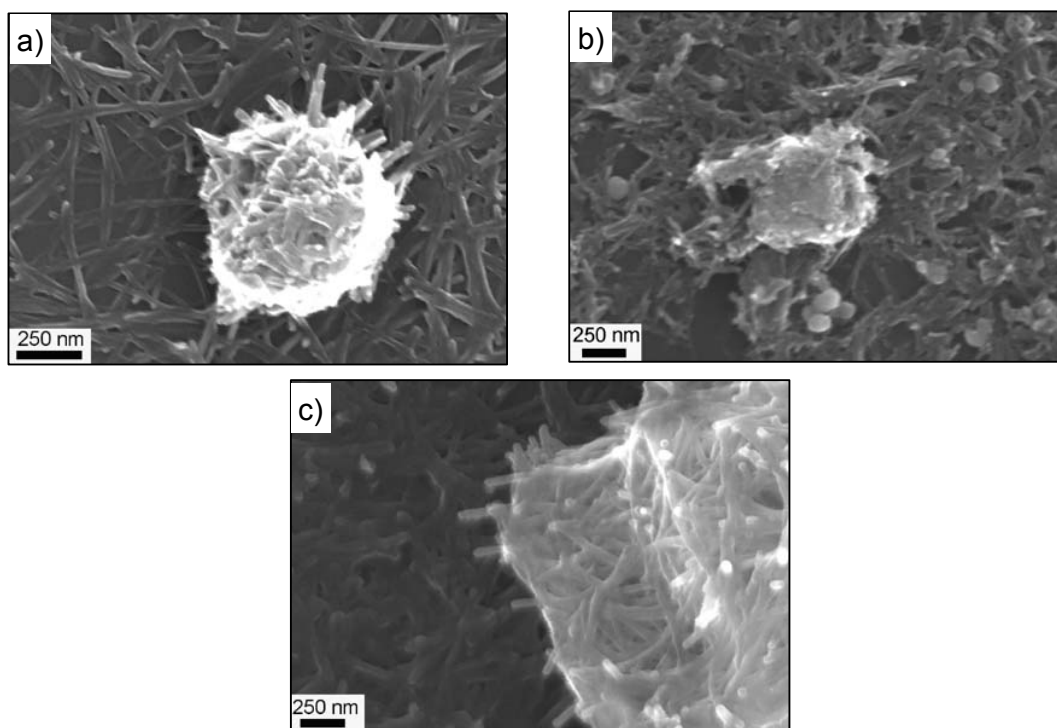


**Figure 3.1 SEM micrographs of the samples prepared at a) 130 and b) 150 °C for 48 h and c) 150 °C for 72 h with anatase-TiO<sub>2</sub>/NaOH molar ratio of 0.05. 1D particles with similar dimensions are obtained for all samples.**

As can be noticed, 1D particles with similar dimensions are obtained for all samples. Comparing the samples prepared at 130 and 150 °C the tubes seem to be less agglomerated when the synthesis temperature is lower. No evident morphological changes can be observed when increasing the synthesis time (please compare Figure 3.1 b and c).

Figure 3.2 presents the X-ray patterns of the samples prepared from anatase at different temperatures (130 and 150 °C) for 48 h (Figure 3.2a) and at different reaction times (48 and 72 hours) at 150 °C (Figure 3.2b). As can be readily noticed, the patterns are similar for all investigated synthesis conditions and the appearance of the following sequence of peaks:  $2\theta \sim 9.5^\circ, 24.5^\circ, 28^\circ, 48^\circ, 62^\circ$  can be assigned to A<sub>2</sub>Ti<sub>n</sub>O<sub>2n+1</sub> titanate phase (A= Na<sup>+</sup> or H<sup>+</sup>), as described in other works.<sup>219,222</sup> However the best indexation is obtained with hydrogen titanium oxide hydrate with the general formula H<sub>2</sub>Ti<sub>2</sub>O<sub>5</sub>·xH<sub>2</sub>O (JCPDS no. 47-0124).

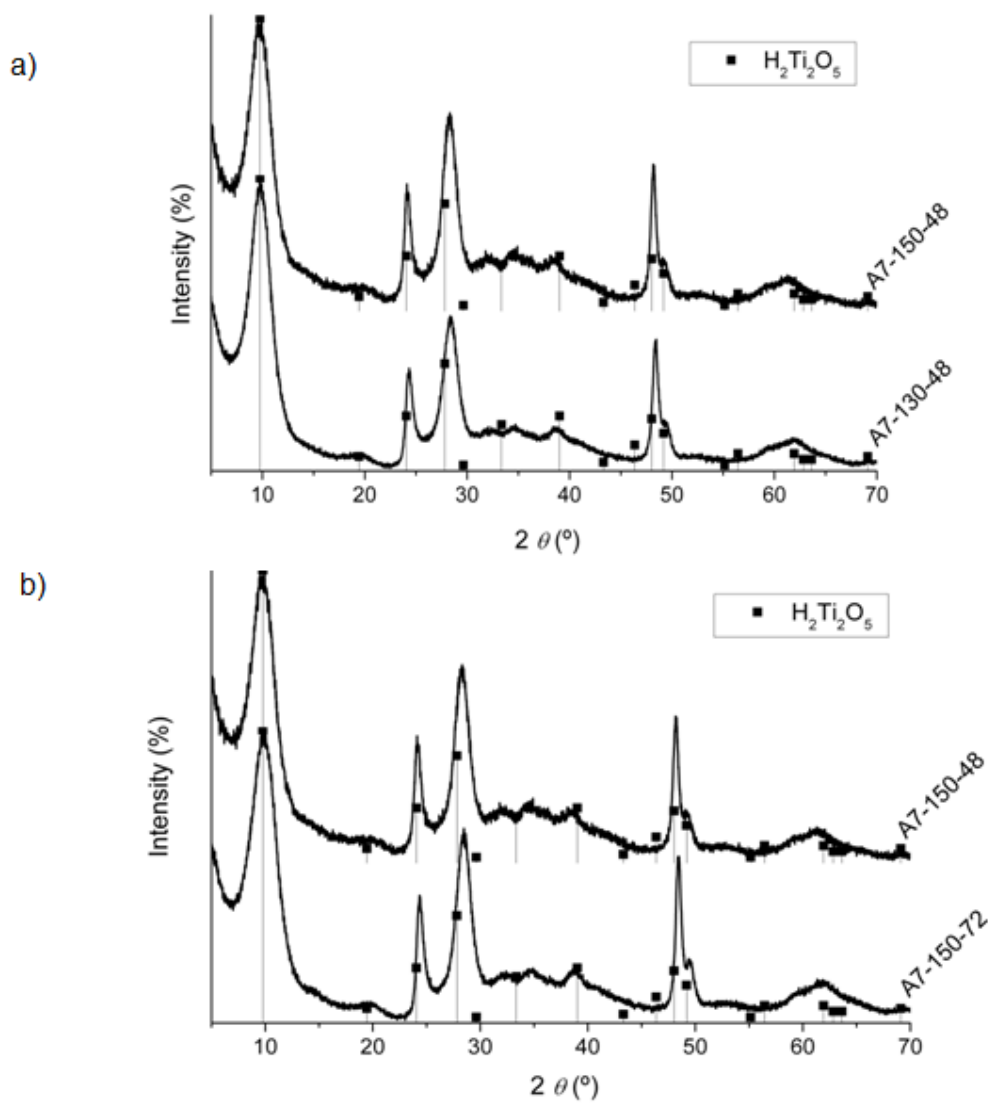


**Figure 3.2 X-ray patterns of samples prepared from anatase showing the influence of synthesis temperature (a) and time (b). Independently on synthesis parameters the best indexation is obtained with hydrogen titanium oxide hydrate with the general formula  $H_2Ti_2O_5 \cdot xH_2O$  (JCPDS no. 47-0124).**

Figure 3.3 presents the Raman (Figure 3.3a) and FTIR (Figure 3.3b) spectra of the samples prepared from anatase at 150 °C for 48 h using different  $TiO_2/NaOH$  molar ratios (0.05, 0.125 and 0.4).

For the three  $TiO_2/NaOH$  molar ratios used, similar Raman spectra were collected presenting the following bands:  $190\text{ cm}^{-1}$ ,  $278\text{ cm}^{-1}$ ,  $450\text{ cm}^{-1}$ ,  $665\text{ cm}^{-1}$  and  $910\text{ cm}^{-1}$ . In spite of many works regarding the structural characterization of the

titanium based NTs the complete assignment of the vibrational mode of titanate nanotubes it is not defined.

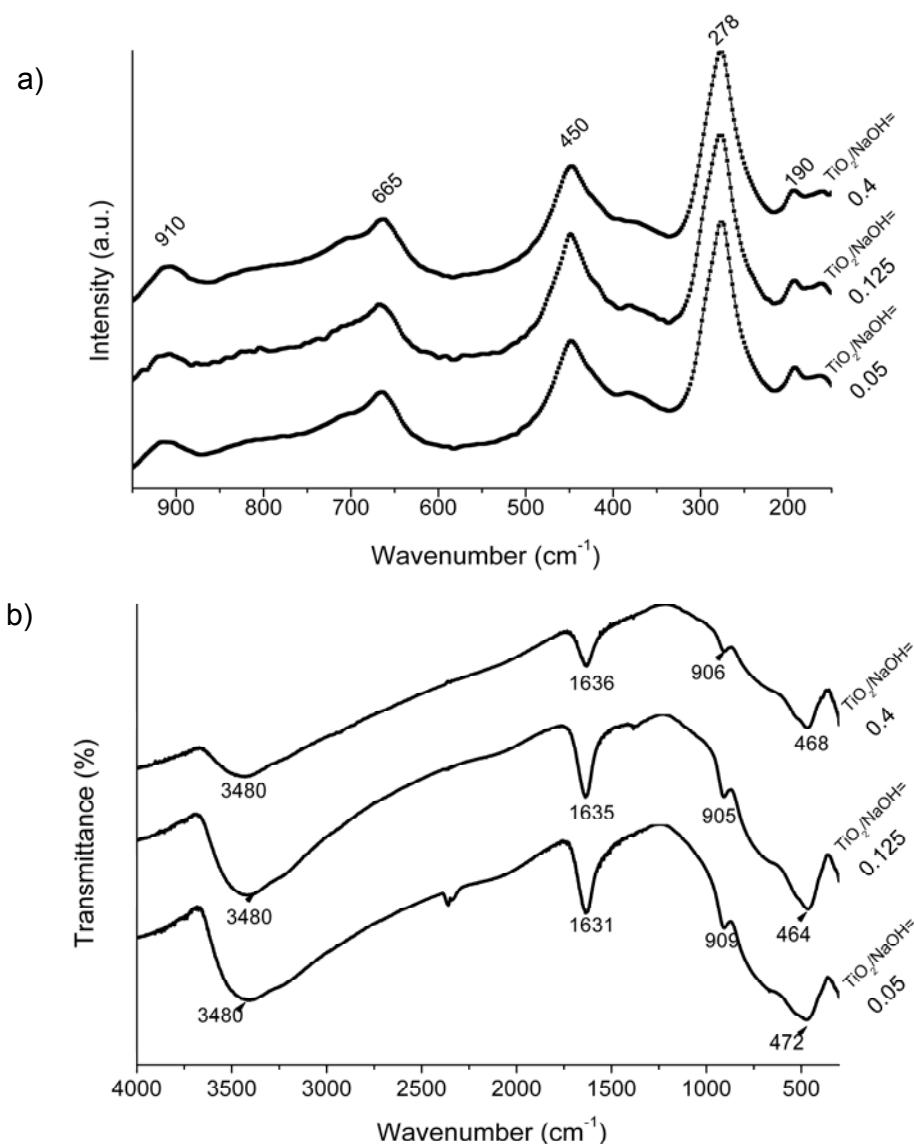


**Figure 3.3 a) Raman and b) FTIR spectra of the samples prepared from anatase at 150 °C for 48 h using different  $\text{TiO}_2/\text{NaOH}$  molar ratios. All samples present the O-H and H-O-H bonding vibrations indicate the bonding of hydrogen to the structure<sup>219</sup> and the presence of structural water.**

Anatase presents a tetragonal symmetry and has the space group  $D_{4h}$  ( $I4_1/amd$ ) containing two formula units per primitive unit cell. From the group analysis, there are six Raman active modes,  $A_{1g}+2B_{1g}+3E_g$ , which were identified at 144  $\text{cm}^{-1}$  ( $E_g$ ), 197  $\text{cm}^{-1}$  ( $E_g$ ), 399  $\text{cm}^{-1}$  ( $B_{1g}$ ), 513  $\text{cm}^{-1}$  ( $A_{1g}$ ), 519  $\text{cm}^{-1}$  ( $B_{1g}$ ) and 639  $\text{cm}^{-1}$

( $E_g$ ).<sup>228</sup> Comparing the Raman spectra of the anatase with the one of the obtained samples one can be readily seen that the  $144\text{ cm}^{-1}$  band of anatase disappeared and a shoulder at  $\sim 160\text{ cm}^{-1}$  appears (Figure 3.3a). The  $197\text{ cm}^{-1}$  band of anatase suffers a red shift (shift to lower frequencies) to  $192\text{ cm}^{-1}$ . In the nanotubes samples, a broad band at  $278\text{ cm}^{-1}$  appears. The  $399\text{ cm}^{-1}$  band of anatase disappeared while a band at  $\sim 450\text{ cm}^{-1}$  appears. The bands at  $513\text{ cm}^{-1}$  ( $A_{1g}$ ) and  $519\text{ cm}^{-1}$  ( $B_{1g}$ ) of the anatase are absent in the spectrum of the NTs. The anatase band at  $639\text{ cm}^{-1}$  has a blue shift (shift to higher frequencies) to  $\sim 665\text{ cm}^{-1}$  for the NT samples and a new band at  $\sim 910\text{ cm}^{-1}$  appears.

The FTIR spectra in Figure 3.3b are all similar. A stretching vibration around  $3400\text{ cm}^{-1}$  which is assigned to O-H bond and an absorption band around  $1630\text{ cm}^{-1}$  assigned to H-O-H bending vibrations indicate the bonding of hydroxide ions to the structure<sup>219</sup> and the presence of structural water.

DSC analysis (Figure 3.4) of the sample prepared at  $150\text{ }^\circ\text{C}$  for 48 h with  $\text{TiO}_2/\text{NaOH}$  molar ratio of 0.05 shows a large endothermic peak at  $\sim 80\text{ }^\circ\text{C}$  followed by a smaller one at around  $150\text{ }^\circ\text{C}$ .

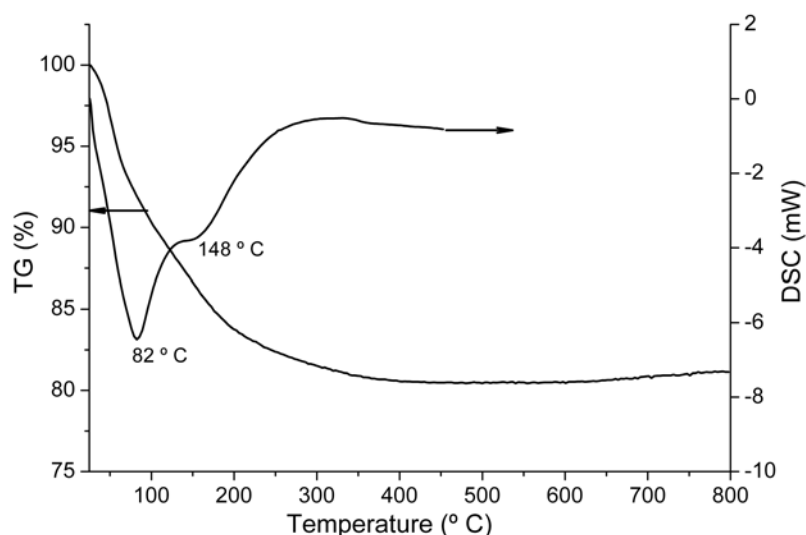


**Figure 3.4 DSC and TGA curves of the sample prepared at  $150\text{ }^\circ\text{C}$  for 48 h with  $\text{TiO}_2/\text{NaOH}$  molar ratio of 0.05.**

The TGA curves show the corresponding decrease in weight (Figure 3.4). The total weight loss at 500 °C is ~ 20%, comprising of 9.3 % between 25 and 100 °C and ~ 10.3% in the temperature range from 100 to 500 °C. The weight loss between 25 and 100 °C can be attributed to the loss of water that was adsorbed at the surface and the weight loss between 100 and 500 °C can be attributed to the loss of structural water.

The results presented above show that layered titanate nanotubes (TiNTs) can be obtained by hydrothermal treatment of anatase with highly alkaline NaOH aqueous solution independent of the synthesis temperature, time or TiO<sub>2</sub>/NaOH ratio.

### **3.3.2 The influence of post synthesis treatments**

#### *Influence of the neutralization process*

The post-synthesis washing process was evaluated in order to clarify the role of the neutralization and cation exchange reaction in the formation of titanium based NTs by hydrothermal synthesis starting from commercial anatase precursor as described in section 3.1.

Morphological analysis during Stage I (Figure 3.5) show the presence of nanotubular shaped particles at high pH. The A13 sample (Figure 3.5a) shows elongated particles immersed in rounded agglomerates. This indicates that the tubular shape is formed during the hydrothermal synthesis. With the reduction of pH the amount of agglomerates decreases (Figure 3.5b, sample A11) and only tubular shaped particles are observed at pH = 8 (Figure 3.5c).

Figure 3.6 presents the X-ray patterns of samples collected at Stage I and Stage II. The main crystalline phase of A13 sample (Figure 3.6a) was identified as sodium carbonate (Na<sub>2</sub>CO<sub>3</sub>, JCPDS no. 37-0451). As pH decreases, the amount of Na<sub>2</sub>CO<sub>3</sub> unquestionably decreases (Figure 3.6b). The peaks at 2θ = 17° and 32° correspond to hydrated sodium carbonate (thermonatrite - JCPDS no. 08-0448). Another type of hydrated sodium carbonate (trona - JCPDS no. 29-1447) was identified by the presence of the peaks at 2θ = 18° and 29° (Figure 3.6b). At pH = 8 (sample A8, Figure 2c) the peaks at 2θ = 9.5°, 24.5°, 28°, 48°, 49.5°, 62° are assigned to A<sub>2</sub>Ti<sub>n</sub>O<sub>2n+1</sub> titanate phase (A= Na<sup>+</sup> or H<sup>+</sup>), as described above

(see section 3.3). During the decrease of the pH to 7, the reflection peaks at  $9.5^\circ$  and  $24.5^\circ$  maintain the same intensity and width. The peaks at  $2\theta = 28^\circ$  and  $48^\circ$  become more intense and narrow with the neutralization.

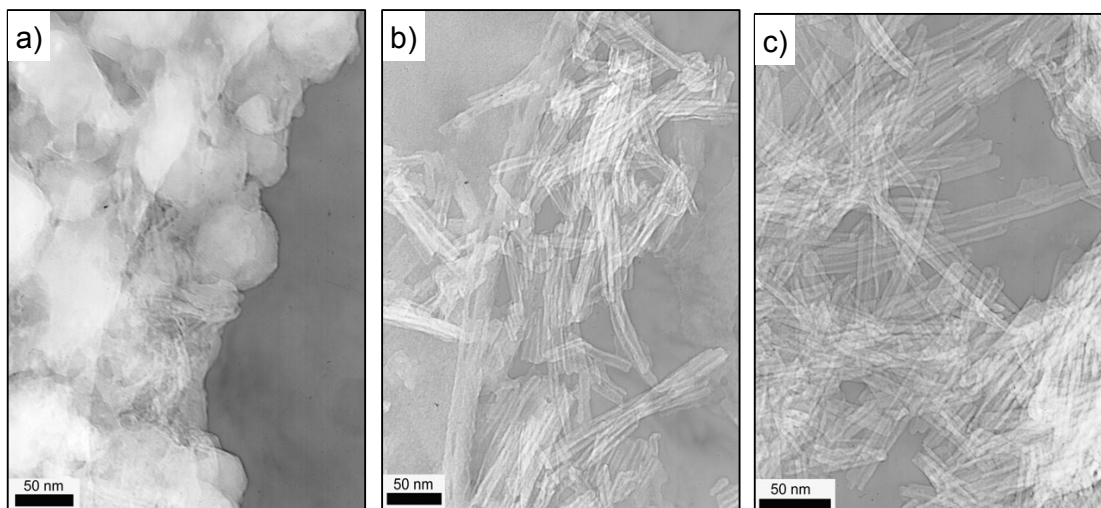


**Figure 3.5 TEM images of the NT samples collected during Stage 1 at: a) pH = 13 (A13); b) pH = 11 (A11) and c) pH = 8 (A8). The images indicate that the tubular shape is formed during the hydrothermal synthesis.**

Figure 3.7 presents HRTEM images of samples collected at the end of Stage I (Figure 3.7a) and during Stage II. A7 sample shows well defined NTs with internal and external diameters of ca. 6 nm and ca. 13 nm, respectively. The in-plane layer spacing parallel and perpendicular to the tube are  $\sim 0.9$  nm and 0.17 nm respectively (Figure 3.7a). HRTEM image of sample AC2, after acid treatment (Figure 3.7b) shows the presence of the tubes at low pH, indicating that NTs morphology is not dependent on the acid treatment. The main diffraction peaks of sodium chloride (NaCl, JCPDS no. 05-0628) are present in the X-ray pattern of this sample (Figure 3.6d). This observation indicates that the acid treatment released  $\text{Na}^+$  retained in the interlayer titanate structure. The neutralization process after the acid addition led to an increase of the pH from 2 to 7. HRTEM image of samples collected after the subsequent neutralization (AC7) is shown in Figure 3.7c. When comparing A7 (Figure 3.7a) with AC7 (Figure 3.7c) HRTEM

images, it is possible to observe that the layered structure of the titanate with the higher Na content is better defined than the protonated one.

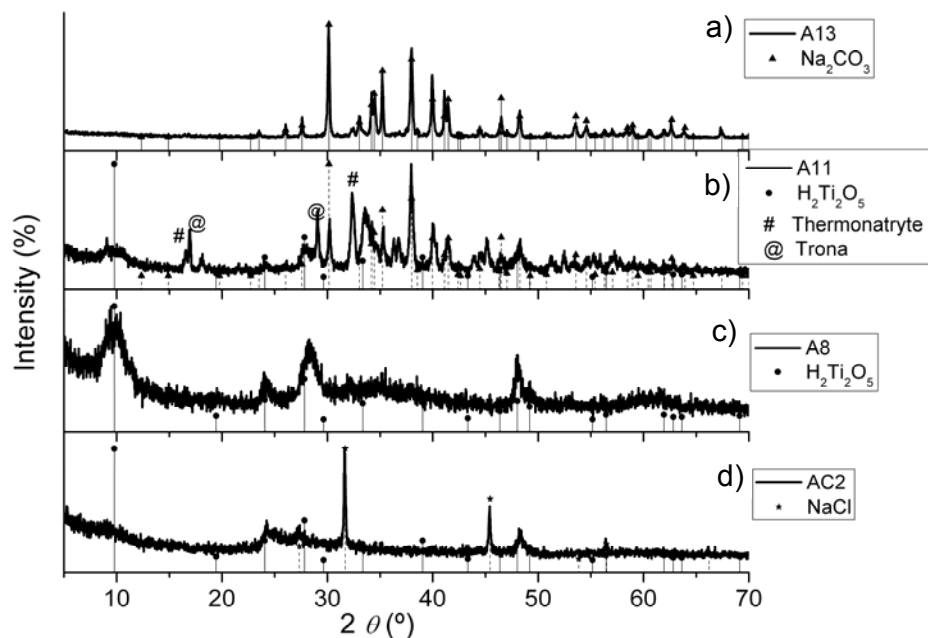


Figure 3.6 X-ray patterns of samples collected in Stage I and Stage II illustrating the structural evolution during the neutralization process.

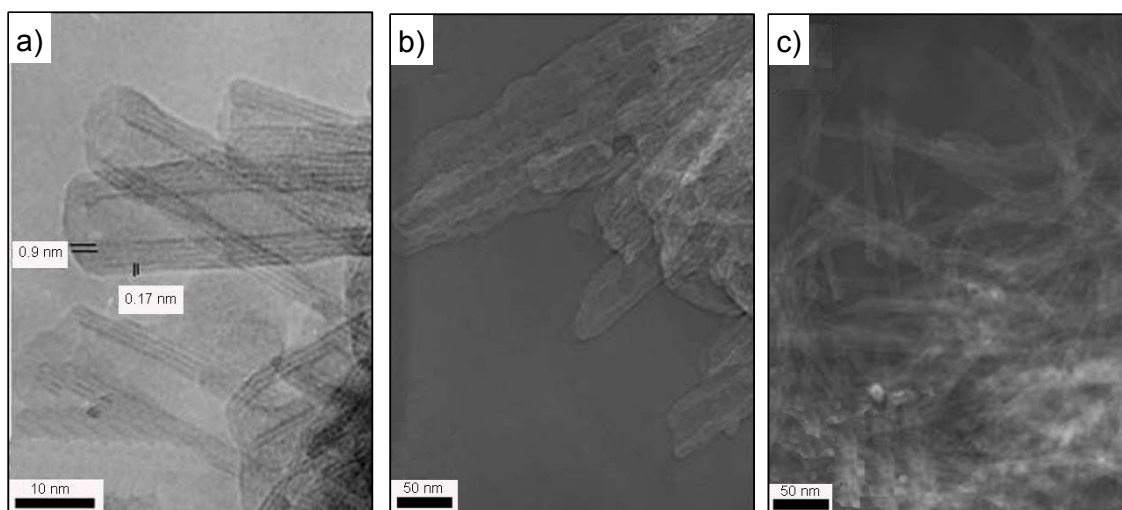
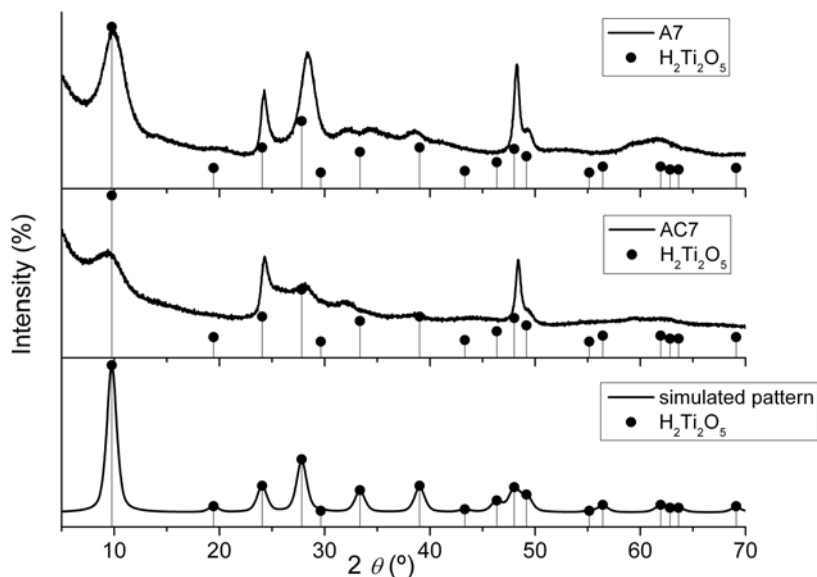


Figure 3.7 HRTEM images of samples collected at the end of Stage I at pH = 7 (A7) a) and during Stage II at pH = 2 (AC2) b) and at pH = 7 (AC7) c). The TEM micrographs show tubular morphology even at low pH.

The X-ray patterns of the A7 and AC7 samples recorded with a step of  $0.01^\circ$  and a fixed counting time of 7 s (Figure 3.8) present similar diffraction peaks. No significant differences were observed.



**Figure 3.8** XRD patterns of samples A7 and AC7 recorded with a step of  $0.01^\circ$  per minute representing the formation of  $\text{H}_2\text{Ti}_2\text{O}_5 \cdot x\text{H}_2\text{O}$  (JCPDS no. 47-0124; the simulated pattern is also displayed for comparison).

Because XRD patterns of NTs display very broad reflections associated with their small size, the indexation of the crystallographic phase is especially difficult. As stated in section 3.3.1 the best indexation of X-ray patterns of these samples was obtained with the JCPDS no. 47-0124 file that corresponds to hydrous dititanate acid with the general formula  $\text{H}_2\text{Ti}_2\text{O}_5 \cdot x\text{H}_2\text{O}$ . The simulated XRD profile using dititanate model (*Jade5* software<sup>177</sup>) is created assuming that 5% of the sample is amorphous and the crystallite size is in the nanometer range ( $\sim 50$  nm). The simulated pattern is presented for comparison (see Figure 3.8) and a good match to the experimental patterns of the titanate NTs can be observed. The absence of some peaks, and the different intensities when compared to the JCPDS file, can be justified by the limited number of titanate layers in tubular shape as well as to the size effect. In order to evaluate the differences between the X-ray patterns of these samples, peak profile fitting was performed<sup>177</sup> and the results are presented in Table 3.2. The increase of  $d$  spacing of (200) planes from 8.86 Å to 9.24 Å,

observed for sample A7 when compared with sample AC7, can be explained based on the  $\text{Na}^+/\text{H}_3\text{O}^+$  ion-exchange reaction as the ionic radius of  $\text{Na}^+$  is 1.02 Å compared to 1.40 Å of  $\text{H}_3\text{O}^+$  <sup>229</sup>. Another noticeable difference in the spectra occurs in the (310) planes. The AC7 sample has a double value of the Full Width at Half Maximum (FWHM) of the (310) peak compared to the value for the A7 sample. This observation points to the decrease of the number of diffracting planes and to the reduction of sample crystallinity after the acid attack.

**Table 3.2 Summary of the X-ray pattern results for the samples collected at pH = 7 after Stage I and Stage II of neutralization. For comparison the values from JCPDS no. 47-0124 file of  $\text{H}_2\text{Ti}_2\text{O}_5 \cdot x\text{H}_2\text{O}$  are presented.**

$\text{H}_2\text{Ti}_2\text{O}_5 \cdot x\text{H}_2\text{O}$			A7 *			AC7		
hkl	2θ	d (Å)	2θ	d (Å)	FWHM	2θ	d (Å)	FWHM
200	9.7	9.04	9.9	8.86	2.46	9.2	9.24	2.07
110	24.0	3.70	24.0	3.70	0.77	24.1	3.68	0.995
310	27.8	3.20	28.3	3.15	1.70	28.1	3.17	3.935
020	48.0	1.89	48.2	1.89	0.56	48.3	1.88	0.51
220	49.2	1.85	49.2	1.85	0.985	49.3	1.84	1.37

\* Residual Error of Fit: SI-7- 10.5 % and SII-7 -9.3%

The Raman spectra of A7 and AC7 collected at pH = 7 are shown in Figure 3.9, and the bands at around 190, 275, 450, 660 and 910  $\text{cm}^{-1}$  can be identified. As stated before in section 3.3, the full assignment of the Raman spectrum of titanate NTs is not available in the literature. However, the bands at 190 and 660  $\text{cm}^{-1}$  are assigned to the  $E_g$  Raman active modes of anatase and the band at 450  $\text{cm}^{-1}$  is attributed to the  $E_g$  mode of rutile <sup>228</sup>. The bands at ~ 275 and 910  $\text{cm}^{-1}$  for sample A7 are characteristic of sodium titanates with layered structures <sup>230</sup> and are assigned to the symmetric stretching mode of a short Ti-O bond. After the acid

treatment the band at  $277\text{ cm}^{-1}$  became less intense, a shoulder at  $269\text{ cm}^{-1}$  appears and the band at  $910\text{ cm}^{-1}$  cannot be identified.

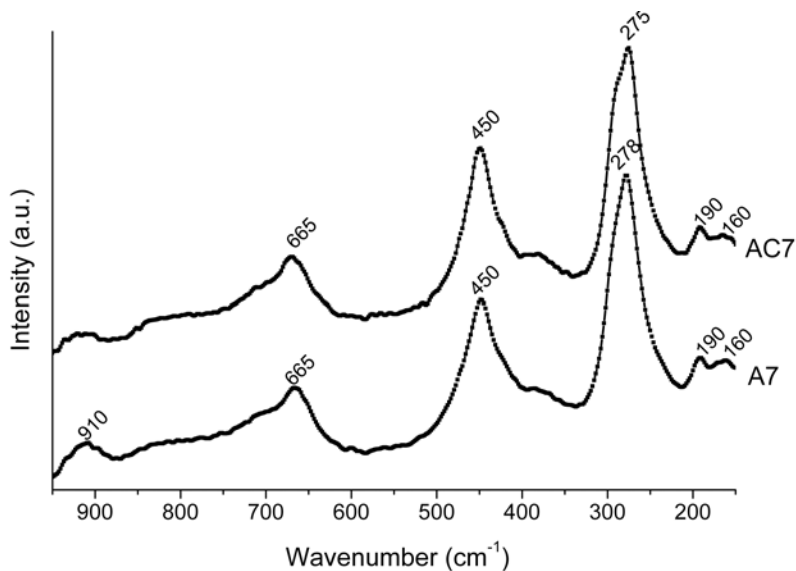


**Figure 3.9 Raman spectra of the samples collected at pH = 7 without and with acid treatment (A7 and AC7, respectively).**

The values of Ti/Na ratios for the A7 (3.5) and AC7 (7.9) obtained by ICP confirmed that the  $\text{Na}^+/\text{H}^+$  ion exchange was performed and support the previous observations above reported.

#### Influence of the post-synthesis hydrothermal treatment

The influence of the post-synthesis hydrothermal treatment was studied in order to evaluate the stability of the as prepared NTs for further processes. For this, samples prepared at  $150\text{ }^\circ\text{C}$  for 48 h and collected at the end of Stage I of neutralization (A7) were hydrothermally treated at 90, 150 and  $200\text{ }^\circ\text{C}$  respectively as described in section 3.2.

Figure 3.10 presents the X-ray diffraction patterns of the post-synthesis hydrothermal treated samples at 90, 150 and  $200\text{ }^\circ\text{C}$  for 24 hours. When the titanate NTs were hydrothermal treated at  $90\text{ }^\circ\text{C}$  no structural transformation

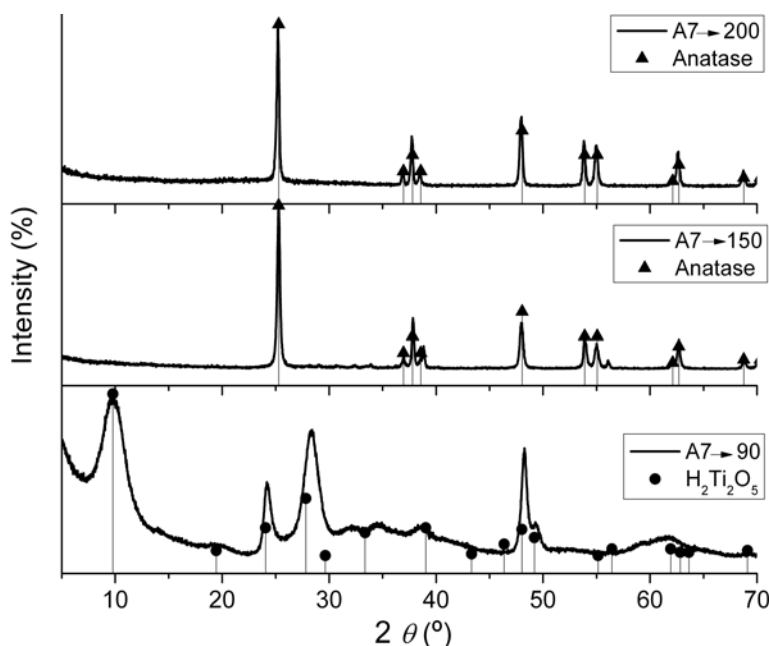


**Figure 3.10 XRD patterns of the post-synthesis hydrothermal treated samples at 90, 150 and 200 °C. It is exhibiting the structural transformation from  $H_2Ti_2O_5$  to anatase when increasing the temperature.**

occurs and the pattern can be indexed with hydrogen titanium oxide hydrate with the general formula  $H_2Ti_2O_5 \cdot xH_2O$  (JCPDS no. 47-0124). When the post-synthesis hydrothermal treatment temperature increases the formation of pure anatase (JCPDS no. 21-1272) can be observed for both investigated temperatures (150 and 200 °C).

The morphological evolution of the post-synthesis hydrothermal treated samples at 90, 150 and 200 °C is presented in Figure 3.11. When comparing the SEM morphology of the starting sample A15048 (Figure 3.1b) with the SEM of A7→90 (Figure 3.11a) it is possible to observe that similar 1D morphologies are obtained after the post-synthesis hydrothermal treatment at 90 °C. When increasing the post-synthesis treatment temperature to 150 or 200 °C the morphological transformation from NTs to nanorods (NRs) is noticed (Figures 3.11 b and c). Relating this observation with the X-ray diffraction data (Figure 3.10), it is possible to assign the NRs morphology to the anatase crystallographic phase.

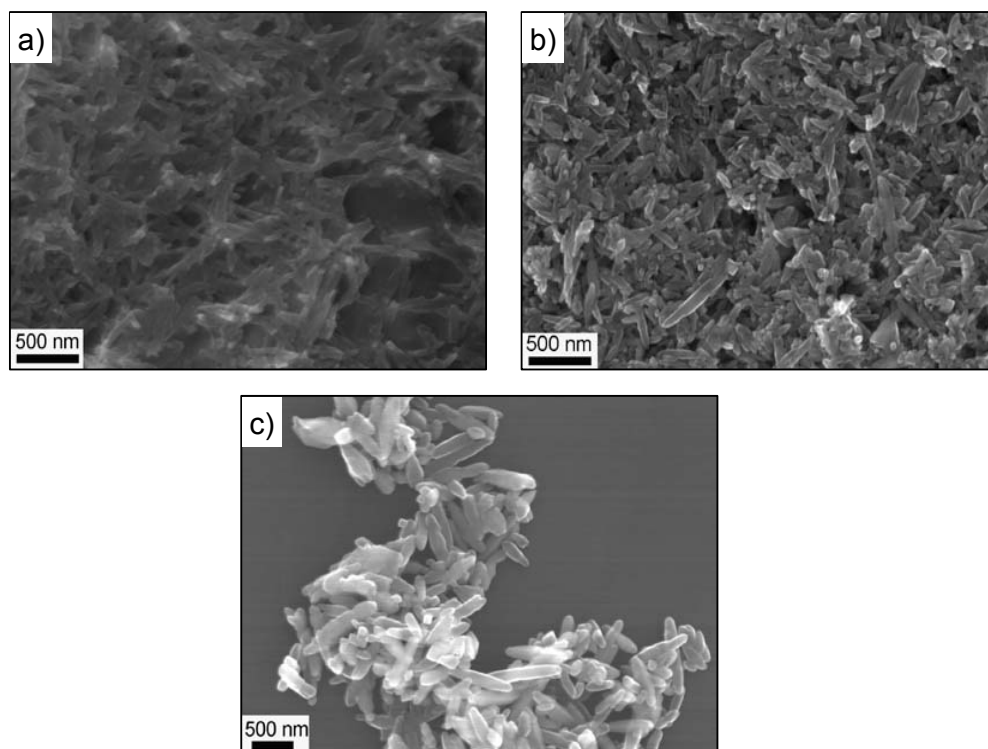


**Figure 3.11 SEM micrographs of the post-synthesis hydrothermal treated samples at a) 90, b) 150 and c) 200 °C. It shows the morphological evolution from NTs to NRs when increasing the hydrothermal treatment temperature.**

Figure 3.12 presents the HRTEM of the sample hydrothermally treated at 200 °C. As it can be noticed the diameter of the nanorods is ~ 60 nm. By Fast Fourier Transformation (FFT) analysis of the HRTEM image it was observed that rods show lattice spacings that are not equal across their length. In the lower right part (Figure 3.12 down inset), the spacing fits within an error of less than 5% to the (002) spacing of anatase (which is the fast growing direction of these rods), and the zone axis (viewing direction) corresponds to the  $\langle 010 \rangle$  direction.

In the middle region, the contrast is pretty strong and in the upper left part, there is mainly a broad intensity in the FFT (Figure 3.12 up inset) suggesting that the lattice spacing is widened significantly perhaps due to defects incorporation.

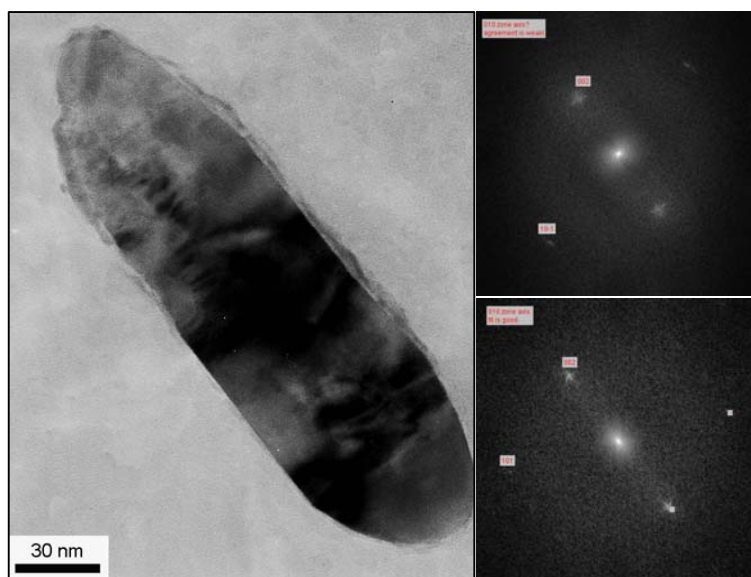
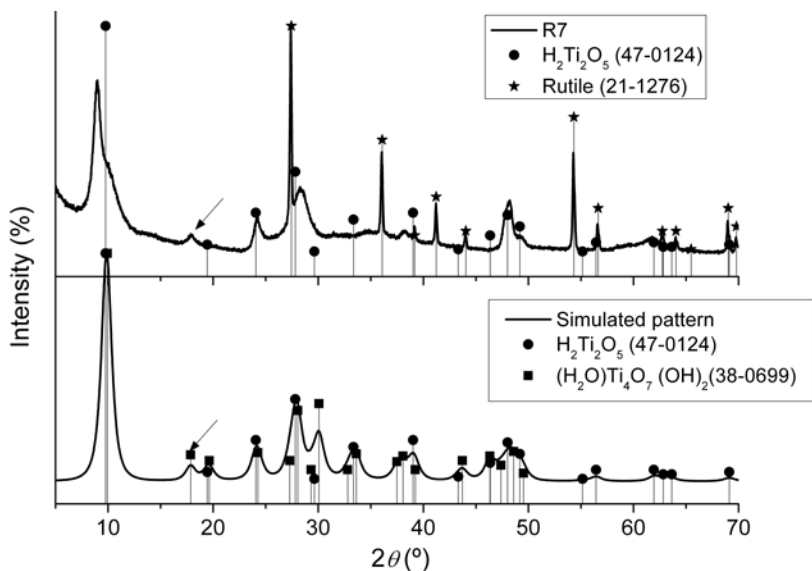


Figure 3.12 HRTEM of the sample hydrothermally treated at 200 °C representing the anatase NR. In the insets the FFT showing that the lattice spacing are not equal across rod length.

### 3.3.3 The influence of titanium precursor

Figure 3.13 illustrates the XRD pattern of samples prepared from rutile and collected at pH = 7 (R7). The collected patterns show peaks corresponding to the dititanate phase ( $\text{H}_2\text{Ti}_2\text{O}_5$ ) and also peaks attributed to the rutile structure (JCPDS = 21-1276). When comparing the X-ray patterns of R7 with A7 (samples prepared starting from anatase - Figure 3.8), two main differences can be noticed regarding the indexation of  $\text{H}_2\text{Ti}_2\text{O}_5$  phase. Firstly, the peak at around  $2\theta = 9.5^\circ$  of the A7 samples is split in the case of R7 into two peaks (one peak at  $2\theta = 8.9^\circ$  and a small shoulder at  $2\theta = 9.9^\circ$ ). Secondly, a peak at  $2\theta = 18.0^\circ$  appears in the case of the R7 sample which can not be attributed to the dititanate phase. The best indexation of the different peaks can be obtained with (201) and (402) reflections of titanium aqua oxide hydroxide with general formula  $(\text{H}_2\text{O})\text{Ti}_4\text{O}_7(\text{OH})_2$  (JCPDS = 38-0699). In order to better define the XRD pattern of the sample prepared from rutile a simulated XRD pattern was created using both titanate phases, namely  $\text{H}_2\text{Ti}_2\text{O}_5$  and  $(\text{H}_2\text{O})\text{Ti}_4\text{O}_7(\text{OH})_2$  respectively.



**Figure 3.13 XRD pattern of the samples prepared from rutile collected at pH = 7 indicating the presence of unreacted rutile, titanium aqua oxide hydroxide and hydrous dititanate acid.**

The simulated pattern, presented for comparison in Figure 3.13, was created using *Jade5* software<sup>177</sup> and assuming that 5 % of the sample is amorphous and the crystallite size is around 50 nm. The simulated pattern matches well to the XRD diffractogram of the sample prepared from rutile, indicating that titanium aqua oxide hydroxide can form together with hydrous dititanate acid.

The Raman spectra of the samples prepared from anatase and rutile are presented in Figure 3.14. Although the spectra are similar and can be attributed to layered titanates structures<sup>230</sup> two important differences can be noted. The first is the appearance of small bands at around 613 cm<sup>-1</sup> and 700 cm<sup>-1</sup> for the sample prepared from rutile. The second observation is the shift of the 910 cm<sup>-1</sup> band of the sample prepared starting from anatase to 900 cm<sup>-1</sup> when rutile is used as a starting precursor.

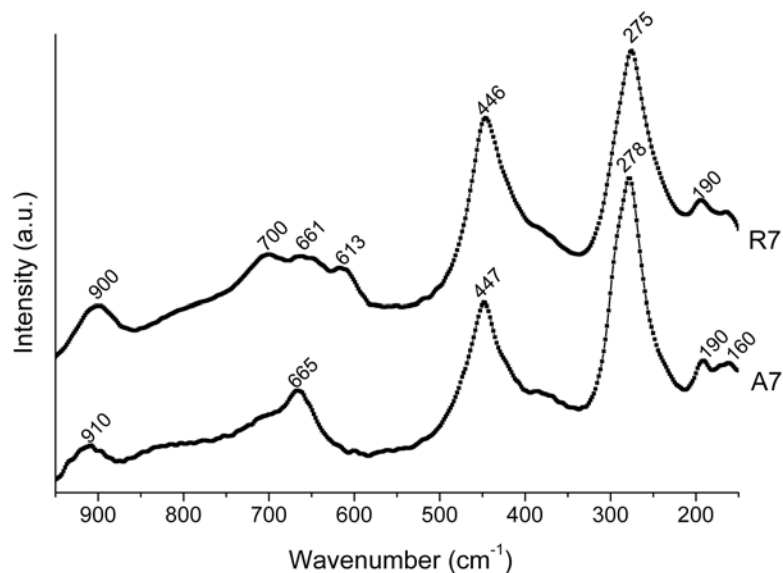


**Figure 3.14 Raman spectra for the samples prepared from the precursors anatase and rutile.**

The TEM micrographs of the sample prepared from rutile (R7) are presented in the Figure 3.15 showing various stages of nanotubes formation.

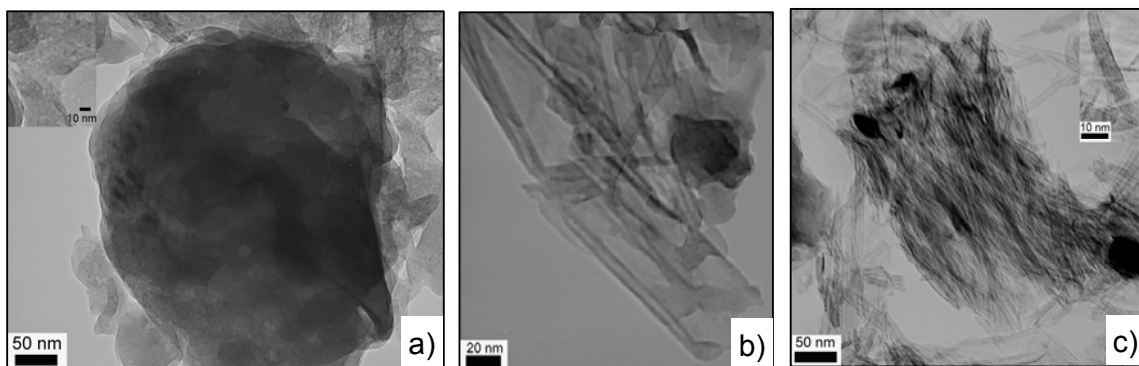


**Figure 3.15. TEM micrographs of the samples prepared from rutile. The images illustrate various stages of tubular morphology formation.**

In Figure 3.15a round shaped particles with some degree of porosity can be observed. Moreover, the presence of sheet like particles formed by the exfoliation of rutile is also noticed (inset of Figure 3.15a). Figure 3.15b shows one of these sheets which are rolling and generated the tubes. A bench of aligned NTs is presented in Figure 3.15c.

### 3.4 Discussion

Four main points result from the data presented above. The first one is that independent of the investigated synthesis conditions (temperature, time, reagents molar ratio) 1D, namely nanotubular particles, are obtained when starting from anatase. The structure of these particles is predominantly layered titanate with general formula  $A_2Ti_nO_{2n+1}$  rather than anatase. The second important point is that the nanotubular shape is formed during the alkaline treatment and that the neutralization step is not related to the tubular morphology. The third point is that the post-synthesis hydrothermal treatment at 150 and 200 °C results in the formation of anatase NRs, but no transformation in shape or structure was observed when the nanotubes were treated at 90 °C. The last important point is that using rutile as starting precursor the layered titanate nanotubes are more slowly formed. In this case the NTs are not pure  $A_2Ti_nO_{2n+1}$  phase but contain unreacted rutile and  $Ti_4O_7$  phases.

#### 3.4.1 TiNTs structure

The formation of nanotubular titanium based materials in the presence of concentrated NaOH aqueous solution under hydrothermal conditions has been intensively reported in the last years.<sup>219,220,225,231,232</sup> As clearly shown in Figure 3.1 nanotubular morphology is also obtained in the present study independently on the hydrothermal synthesis variables like temperature, time or reagent molar ratios.

However, as stated in section 3.1 the crystallographic nature of titanium based NTs and the formation mechanism of nanotubes are still topics under debate. The suggested structures for the layered (lamellar) titanates reported in the literature can be divided in two crystalline systems: 1) the monoclinic trititanate with general formula  $A_2Ti_3O_7$ ,<sup>219,226,233-237</sup> and 2) the orthorhombic system of lepidocrocite- type phase as  $A_xTi_{2-x/4}\square_{x/4}O_4$  where A is Na and/or H and  $\square$  is vacancy<sup>220,238</sup>, and  $A_2Ti_2O_4(OH)_2$  (or  $A_2Ti_2O_5 \cdot H_2O$ )<sup>222,225,231,232,239</sup>.

The trititanate layered structure<sup>219</sup> is composed of corrugated ribbons of edge-sharing  $TiO_6$  octahedra. The ribbons are three octahedra wide, and these

octahedra join corners to form stepped sheets. The sheets are separated by H<sup>+</sup> ions creating an inter-sheet spacing of  $d_{200} \sim 0.786$  nm. However, the trititanate nanotubes model<sup>219</sup> is questionable for the present study. For example, in the XRD patterns of the trititanate nanotubes, the strongest reflection peak was observed at  $d = 0.926$  nm<sup>219</sup> and it was assigned to the (001) reflection ( $d = 0.901$  nm) of the trititanate phase. However, the 001 reflection of trititanate should be very weak compared with the (200) peak ( $d = 0.786$  nm). But this (200) reflection peak, supposed to be the strongest, actually does not appear in the XRD pattern of the titanate nanotubes with trititanate structure.<sup>219</sup> As stated before, regarding the crystal structure, the X-ray powder patterns of NTs display very broad reflections associated with their small size. Therefore, the indexation of the crystallographic phase is especially difficult.

In the present study the XRD patterns of the NTs obtained starting from anatase present the main peak at  $2\theta \sim 9.56^\circ$  (Figure 3.2) which corresponds to an interplanar distance  $d = 0.924$  nm (Table 3.1). This result is sustained by HRTEM results (Figure 3.7a) in which a interlayer space of  $\sim 0.9$  nm was found and not 0.78 nm as reported for trititanate ( $\text{H}_2\text{Ti}_3\text{O}_7$ ) model<sup>219,226,234</sup>. Therefore, the best indexation is obtained with hydrous titanate with the general formula  $\text{H}_2\text{Ti}_2\text{O}_5$  (JCPDS no. 47-0124) for which the  $d_{200}$  is 0.9 nm.

Taking into account the above considerations it is more probable that the titanate nanotubes structure, obtained in the present study when starting from anatase as precursor, is predominately orthorhombic  $\text{A}_2\text{Ti}_2\text{O}_5$  layered titanate as also reported by others<sup>222,225,231,232,239</sup> rather than trititanate. The orthorhombic structure contains lepidocrocite type host layers that are two-dimensional sheets in which  $\text{TiO}_6$  octahedra are linked with each other via edge-sharing.

The layered structure of the titanate NTs obtained from anatase is also sustained by the Raman study (Figure 3.3a). Although the complete assignment of the titanium based nanotubes Raman spectra is not yet reported, the present results clearly show that the obtained samples are not anatase, as Kasuga *et al.*<sup>218</sup> claimed. Indeed, when comparing the Raman spectra of the anatase to the spectra of the obtained samples bands at ca.  $278\text{ cm}^{-1}$  and  $910\text{ cm}^{-1}$  cannot be assigned to any Raman active modes of anatase (Figure 3.3a). These bands are

rather characteristic of layered structures of sodium titanates and are assigned to the vibrational modes of the short Ti-O bond (distorted  $\text{TiO}_6$  octahedra) in sodium titanates.<sup>230</sup>

The infrared absorption (Figure 3.3b) band at  $1640\text{ cm}^{-1}$  and the water desorption below  $100\text{ }^\circ\text{C}$  (Figure 3.4) indicate that the compound contains interlayer water and the total mass loss at  $800\text{ }^\circ\text{C}$  (Figure 3.4) indicates a structural water content of 1.8 molecules per formula unit.

The structural analysis clearly points out that  $\text{A}_2\text{Ti}_2\text{O}_5 \cdot 1.8\text{ H}_2\text{O}$  (A= Na/H) is the layered structure of titanate nanotubes in the present study.

### 3.4.2 Post-synthesis neutralization

As mentioned in section 3.1, the moment of formation of nanotubular morphology is still a subject under debate. In this study, morphological analysis in the alkaline stage (Stage I-Figure 3.5a) shows the presence of nanotubular shaped particles at high pH, clearly indicating that the tubular shape is formed during the hydrothermal synthesis. The presence of the  $\text{Na}_2\text{CO}_3$  phase at high pH (Figure 3.6a) is due to the drying of the samples in air and also to the excess sodium cations. It does not influence the nanotubular titanate formation, however, it contributes to the agglomeration of NTs. Due to their low degree of crystallinity when compared with the sodium carbonate phase, the presence of titanate-based phases is not clear.

Consequently, in accordance with the work of Zhang *et al.*<sup>233</sup>, the results of the present work confirm the formation of the tubular shape during the hydrothermal synthesis as follows: a) crystalline  $\text{TiO}_2$  raw material (anatase in this case) undergoes a high degree of hydration (swelling via hydration<sup>240</sup>) in highly concentrated alkaline solution leading to the formation of a layered structure of  $[\text{Ti}_n\text{O}_{2n+1}]^{2-}$  species, where n is depending on the synthesis conditions such as temperature or time; b) by an osmotic swelling type mechanism<sup>240</sup> the interlayer space increases. The top layers are balanced by positive charge of  $\text{Na}^+$  which permanently interacts with  $\text{OH}^-$  of the alkaline solution leading to some degree of contraction in the relevant Ti-O bonds on the layer surface; c) when the positive charge deficiency reaches a certain limit, the surface layer may peel off, taking into

account that the surface tension becomes larger than the coupling energy between the adjacent layers.

The role of the first stage of neutralization was to gradually wash out the excess of sodium ions, decreasing the agglomerate particle size and finally releasing the tubes. The ion exchange of  $\text{Na}^+/\text{H}^+$  starts in the first stage, however, it is confirmed that it is not essential for the formation of the tubular structure, as claimed by Kasuga *et al.*<sup>218</sup> and Tsai *et al.*<sup>222</sup>.

Ion exchange processes are constrained by both kinetic and thermodynamic factors. The rate of ion-exchange depends on kinetic factors, which are largely influenced by the mobility of the ions. Therefore, the most intrinsically located  $\text{Na}^+$  ions cannot be liberated just by water washing and requires acid attack of the layers for the ion exchange to take place. The HRTEM images (Figures 3.7) indicate that the layered structure of the titanate with higher Na content (Figure. 3.7a) is better defined than the protonated one (Figure. 3.7c), clearly suggesting the importance of  $\text{Na}^+$  in the interlayer space, as reported by Du *et al.*<sup>226</sup>. The layered structure and the tubular shape are maintained even at pH = 2 (Figure 3.7b), indicating that the tubular morphology is not dependent on the washing process. This result somehow supports the observation of Kim *et al.*<sup>241-243</sup> that there are two different sodium bonding states in nanotubular titanates: the weakly bonded sodium adsorbed at the tube surface and the strongly bonded sodium intercalated into the tubular structure.

When comparing the X-ray diffraction patterns of the A7 and the AC7 samples, it is clear that the interlayer ion exchange takes place under the acid attack. The increase of  $d$  spacing of (200) planes observed for samples AC7 when compared with samples A7 can be explained based on the  $\text{Na}^+/\text{H}_3\text{O}^+$  ion exchange reaction. These results are in accordance with the FTIR spectra. The infrared spectra (Figure 3.3b) of the samples, collected at neutral pH, present a stretching vibration around  $3400\text{ cm}^{-1}$  which was assigned to O-H bond and the absorption band around  $1640\text{ cm}^{-1}$  assigned to H-O-H bonding vibrations, indicating the bonding of hydrogen to the structure<sup>229</sup> and the presence of interlayer water as  $\text{H}_3\text{O}^+$ . The intercalation of water molecules into the proton layer is also suggested by the disappearance of a Raman band at around  $910\text{ cm}^{-1}$

(Figure 3.9). This change in the Raman spectra is related to the partial replacement of Ti-O-Na bonds by Ti-O-H, suggesting the transition of Na-O ionic bond to hydrogen bond. This probably results in an intralayer structural rearrangement with a change of Ti<sub>2</sub>O<sub>5</sub> host layers, also reflected in the FWHM values of (310) peak.

The presence of the interlayer water decreases the covalent character of O-H bond, and consequently the Brønsted acidity increases, resulting in a high ion-exchange capacity of the layered structure and easy acid catalyzed condensation of OH groups during the heat treatment <sup>244</sup>.

### 3.4.3 Anatase NRs

The transformation of the layered titanate NTs into 1D anatase nanoparticles during the post-synthesis thermal treatments has been reported <sup>221,232,245</sup> but the transformation mechanism is still under debate. Nian and Teng <sup>232</sup> claimed that the key step of transformation is the local shrinkage of the tube walls which results into the formation of anatase crystallites and the subsequent oriented attachment of these crystallites lead to the formation of the anatase NRs. The authors stated that layered titanate NTs (H<sub>2</sub>Ti<sub>2</sub>O<sub>5</sub>·H<sub>2</sub>O) to anatase NRs transformation needs an acidic environment. Boercker *et al.* <sup>245</sup> claimed that nanowires of anatase are obtained from H<sub>2</sub>Ti<sub>2</sub>O<sub>4</sub>(OH)<sub>2</sub> nanotubes by a topotactic transformation. The sheets made of edge bonded TiO<sub>6</sub> octahedra in the H<sub>2</sub>Ti<sub>2</sub>O<sub>4</sub>(OH)<sub>2</sub> nanotubes dehydrate and move towards each other to form anatase crystals oriented along the nanotube axis which creates a polycrystalline nanowire. Moreover Yoshida *et al.* <sup>221</sup> stated that by post-heat-treatment above 350 °C, some of the nanotubes with nominal composition of ~H<sub>1.5</sub>Na<sub>0.5</sub>Ti<sub>3</sub>O<sub>7</sub> began to break into particles (not 1D) of anatase phase, and the others remained as nanotubes where a lot of Na existed, indicating the remnant Na stabilized nanotube structure.

The present study clearly demonstrates that NRs of anatase are formed when the post-synthesis hydrothermal temperature is 150 °C or 200 °C (Figure 3.10 and Figure 3.11b and c). The shapes of the NRs is similar to that reported by Nian and Teng <sup>232</sup>. However in our case no acidic environment is needed to transform the NTs into NRs. Moreover the present study shows the formation of

anatase NRs at 150 °C for 24 h on contrary to the Nian and Teng which use higher temperature (175 °C) and longer time (48h) <sup>232</sup>.

The observation in the present study that the dimensions of the NTs (diameter ~9 nm) cannot be related to the dimensions of the NRs (diameter size ~60 nm) excludes the 1/1 topotactic transformation as claimed by others <sup>245</sup>. We believe that the mechanisms of NTs to NRs transformation is rather a dehydration of the titanate layers into a bench of NTs aligned in the same direction as shown in the Figure 3.15c. The HRTEM analysis (Figure 3.12) does not exclude the possibility of NRs formation by oriented attachment of anatase crystallite. It is supposed that at the defective regions of the TiNTs, nanocrystals of anatase are nucleated because the zigzag pattern formed by the TiO<sub>6</sub> octahedra in the TiNTs along the [010] direction is similar to the zigzag pattern formed by the TiO<sub>6</sub> octahedra in the anatase along the [100]. <sup>245</sup> Therefore, the formation of the polycrystalline anatase nanorods (NRs) is the result of an oriented attachment process when two adjacent anatase particles come into the same crystallographic orientation, with high-energy faces, fuse and eliminate these faces and the result is a particle with directed orientation <sup>232,246-249</sup>

Moreover it is shown in the present study that the presence of Na does not influence the formation of the NRs as the formation of the NRs is observed in the samples containing Na (before Na<sup>+</sup>/H<sup>+</sup> ion exchange) (Figure 3.11b and c). So in the present study experimental conditions the NRs are formed independently when Na ions are present in the interlayer space on contrary to Yoshida *et al.* claimed <sup>221</sup>.

#### 3.4.4 Using rutile as precursor

The different TiO<sub>6</sub> octahedra sharing make anatase and rutile distinctive structures despite having the same symmetry (tetragonal). Each TiO<sub>6</sub> octahedron in anatase connected with two edge-sharing octahedron and eight corner-sharing octahedron. In rutile each TiO<sub>6</sub> octahedron connected with four edge-sharing octahedron and four corner-sharing octahedron. With c axis longer than a, anatase is preferred to form nanotubes rather than the rutile. The explanation for the presence of the rutile X-ray peaks (Figure 3.13) is based on the lower reactivity of

this oxide. The temperature and reaction time involved on the osmotic swelling of rutile, and subsequent exfoliation and rolling in order to form nanotubes (Figure 3.15) is higher and respectively longer than in the case of the anatase.

The  $\text{Ti}_4\text{O}_7$  structure of the nanotubes noticed for the sample prepared from rutile (Figures 3.13 and 3.14) is one of the substoichiometric titanium oxides,  $\text{Ti}_n\text{O}_{2n-1}$  called Magnéli phases where  $n$  is a number between 4 and 10. The Magnéli phases are made up of two-dimensional chains of octahedral  $\text{TiO}_2$ , with every  $n^{\text{th}}$  layer missing oxygen atoms to accommodate the loss in stoichiometry.<sup>250</sup>

It was claimed that from a practical point of view, synthesis of nanotubes containing significant Magnéli phases would be of great interest since it would dramatically increase the electrical conductivity and then the photovoltaic efficiency of titanium based materials.<sup>224</sup>

Magnéli phases derivate from rutile have been obtained by two steps method combining sol-gel process and laser treatment by Langlade *et al.*<sup>251</sup> More recently triclinic  $\text{Ti}_8\text{O}_{15}$  nanowires and  $\text{Ti}_4\text{O}_7$  quasi-one-dimensional fibers were obtained by heat-treating thick  $\text{H}_2\text{Ti}_3\text{O}_7$  nanowires under hydrogen atmospheres at 850 and 1050 °C, respectively.<sup>252</sup>

In the present study the indexation of the X-Ray patterns of the sample prepared from rutile (Figure 3.13) with  $\text{Ti}_4\text{O}_7$  structure and the appearance of the Raman band at  $612\text{ cm}^{-1}$  (Figure 3.14) characteristic to the Magnéli phase<sup>253</sup> can be the indication that the NTs obtained from rutile contains certain amount of Magnéli phase. It is then demonstrated by the present study that these types of nonstoichiometric titanium oxides can be prepared by a simple one-step method. However more investigation is needed in order to increase the amount of this phase in the NTs structures.

### 3.5 Summing up

Nanotubes of  $\text{H}_2\text{Ti}_2\text{O}_5$  layered structured were successfully prepared by hydrothermal synthesis starting from  $\text{TiO}_2$  precursors in the presence of NaOH aqueous solution. The systematic study of the neutralization process performed after hydrothermal synthesis showed that the driving force for the formation of tubular shape is the alkaline treatment. In a high concentrated sodium alkaline

solution for 48 hours and at 150 °C, anatase undergoes a high degree of hydration, which leads to the formation of a layered structure of  $[\text{Ti}_2\text{O}_5]^{2-}$  species by an osmotic swelling type mechanism.

Although anatase and rutile are both suitable precursors to get titanate nanotubes under hydrothermal alkaline conditions, rutile is less efficient than anatase to form pure titanium based NTs because of its low reactivity.

The above-mentioned results contribute to a better understanding of the structure and morphological evolution during 1D structure formation, which may be important for the functionalization of one-dimensional titanates nanostructure for future advanced applications.

For the present work the achievements presented in this chapter help for the evaluation of template role of the titanium based nanotubes for the anisotropic growth of BT.

## 4 Chemical Template Methods

### *Summary*

In this chapter the results and discussion of the use of two chemical templating preparation methods (solution and vapor based) of BT, starting from layered titanate nanotubes (TiNTs) as precursors are presented

Concerning the solution based approach, by kinetic analysis and systematic structural and morphological studies, it is demonstrated that the formation of BT occurs via two different mechanisms depending on the temperature and time. At low temperature and short reaction time, “wild” type BT dendritic particles with cubic structure are formed through a phase boundary topotactic reaction. At higher temperatures and/or for longer reaction time, the reaction is controlled by a dissolution precipitation mechanism and “seaweed” type BT dendrites are formed. By PFM measurements it is demonstrated that the “seaweed” type BT dendrites have higher piezoelectric activity than the “wild” type.

Concerning the vapor based approach, an original procedure based on the chemical vapor deposition of a metalorganic barium precursor (MoCVD) on TiNTs at 500 °C is proposed. The potential template effect of TiNTs in the vapor state reaction for the anisotropic growth of BT is assessed and discussed. In terms of stability of the TiNTs under MoCVD conditions in the absence of barium precursors it is demonstrated that TiNTs are stable at the MoCVD temperature transforming in TiO<sub>2</sub> anatase nanorods (NRs) by an oriented attachment mechanism when thermal treated at temperatures higher than 700 °C. The deposition of barium precursor on the top of the TiNTs followed by annealing at 700 °C in O<sub>2</sub> atmosphere lead to the formation of round shaped BT nanocrystals at the TiNTs surface independently on barium concentration. When the annealing temperature and titanium concentration increase the barium titanate nanoparticles seem to segregate and NRs of barium deficient phases are formed. More studies are required to optimize the barium and titanium stoichiometry necessary to obtain a pure barium titanate perovskite phase.

## 4.1 Motivation

As stated in Chapter 1, the interest in the fabrication of anisotropic ferroelectric nanostructures such as one-dimensional (1D) nanowires (NWs), nanotubes (NTs) or nanorods (NRs) has increased in the recent years for two important reasons. On one hand, the study of these systems can provide useful information for the fabrication of next generation, fully three-dimensional FeRAM structures with the required bit density<sup>254</sup>. On the other hand, detailed *ab initio* calculations have predicted a new kind of ferroelectric order in nanorods and nanodisks<sup>72,82</sup>

In addition it is well known that the shape and size of particles are highly dependent on the preparation method and controlled by the synthesis parameters. From this point of view, there is a strong need to develop synthetic methods to produce anisotropic ferroelectric nanostructures to achieve a major breakthrough in understanding the effect of scaling and dimensionality on electric properties and eventually in transferring this knowledge to practical applications.

Chemical template methods using 1D nanostructures as both precursors and templates have been proposed for the anisotropic growth of ferroelectric nanostructures (more details in Chapter 1). Although these methods are not straightforward and different mechanisms can nullify the template role of 1D precursors, smaller 1D ferroelectrics may be obtained at lower temperatures via these methods. Within this context the growth of titanate based ferroelectrics starting from TiO<sub>2</sub> NTs was studied. It was claimed that TiO<sub>2</sub> based nanotubes act as precursors for the hydrothermal preparation of BT 1D nanostructures<sup>114</sup>. However, the chemical nature of the nanotubes was not clearly identified and the obtained powders contained a mixture of barium titanate, amorphous phases, anatase and carbonate impurities<sup>115</sup>. More recently, Bao *et al.* reassessed this approach but the reported formation of BT NWs is questionable as no XRD data of the samples is presented and the microstructures do not sufficiently support the claimed results.<sup>116</sup> Buscaglia *et al.* also reported the synthesis of single crystal BT nanowires with tetragonal structure by topochemical solid-state reaction at 700 °C using layered TiO<sub>2</sub> nanowires as reactive templates coated with BaCO<sub>3</sub> nanocrystals<sup>117</sup>. According to the authors, the initial morphology of the TiO<sub>2</sub>

nanowires was retained in the final product and the BT NWs with strong piezoactivity are formed.

In our opinion the growth of barium titanate particles starting from layered titanate nanotubes has not been yet addressed systematically. Moreover the use of titanate layered templates for vapor reactions with barium precursors for the synthesis of BT have not been reported. This chapter presents the main results and discussion of systematic studies of two chemical template approaches starting from layered titanate nanotubes with general formula  $\text{Na}_{2-x}\text{H}_x\text{Ti}_2\text{O}_5 \cdot 1.8\text{H}_2\text{O}$  (TiNTs): the reaction of barium precursor with TiNTs under solution based hydrothermal conditions and in vapor phase, constituting this last one an original approach.

## 4.2 Solution based synthesis of BT using TiNTs precursors

In the last years the interest for the chemical solution routes for the preparation of BT powder had increased. Several such routes have been reported in the literature and reviewed by Hennings.<sup>255</sup> Among these methodologies, the hydrothermal procedure has been referred to as a versatile, low cost and environmentally friendly method for the preparation of barium titanate nanoparticles with different sizes and morphologies.

### 4.2.1 Materials preparation

All the syntheses were performed in Teflon lined autoclaves. A layered titanate precursor with the general formula  $\text{Na}_{2-x}\text{H}_x\text{Ti}_2\text{O}_5 \cdot 1.8\text{H}_2\text{O}$  (see Chapter 3) and  $\text{Ba}(\text{OH})_2 \cdot 8\text{H}_2\text{O}$  (Merck, 98% purity) were used as titanium and barium source, respectively. Briefly, the Ti precursor was made by mixing 2 g of anatase (Merck, 99%) with 40 mL of 10 M NaOH (Fluka, 97%) solution. After stirring, the mixture was autoclaved for 48 h at 150 °C. The product was filtered, washed with distilled water until pH 7 and dried at 60 °C (section 3.2). The titanium precursor is indexed as TiNTs. The barium titanate preparation was initiated by mixing barium and

titanium precursors in a 1.01 Ba/Ti molar ratio with the necessary quantity of deionized distilled water in order to prepare a 0.1 M solution of Ba(OH)<sub>2</sub>. In this way, the pH of the starting mixture was above 13. These experimental conditions were chosen based on the thermodynamic studies of Lencka *et al.*<sup>161</sup> After stirring for 30 min, the mixtures were transferred into Teflon-lined autoclaves and the hydrothermal syntheses were performed at 90, 110 and 200 °C for several periods of time. The synthesis products were washed with distilled water for various periods of time and dried overnight at 50 °C. The labels of the samples studied in this section are presented in Table 4.1.

**Table 4.1 Sample labels for hydrothermal synthesis of BT starting from TiNTs.**

Temp. (°C) \ Time (h)	90	110	200
0.5	--	--	BT20030'
1	BT901	--	BT2001
2.5	--	BT1102.5	BT2002,5
4	--	--	BT2004
6	--	BT1106	BT2006
12	BT9012	--	--
15	--	BT11015	--
18	BT9018	BT11018	--
21	BT9021	BT11021	--
24	BT9024	BT11024	BT20024
36	--	BT11036	--
72	--	BT11072	BT20072
96	--	BT11096	--
120	--	BT110120	--
144	BT90144	BT110144	--

For simplification the samples are identified by “BT” followed by the indication of the temperature and time of synthesis. For example, the sample prepared at 90 °C for 24 h was indexed as BT9024. For the kinetic study of the

formation of barium titanate starting from TiNTs, the hydrothermal syntheses were performed at 110 and 200 °C for several periods of time. Similar nomenclature as described above was used. The samples were characterized by XRD, Raman, FTIR, SEM, TEM, PFM and TG as described in Chapter 2.

## 4.2.2 Results

### 4.2.2.1 Hydrothermal Synthesis of BT

#### The influence of temperature

Figure 4.1 presents the X-ray diffraction patterns of the samples prepared at 90, 110 and 200 °C for 24 h. All the samples can be indexed with both tetragonal (JCPDF no. 05-0626) and cubic (JCPDF no. 31-0174) BT structures. The X-ray patterns of the samples obtained at 90 °C indicates that barium titanate is predominantly cubic ( $c/a = 1.0005$ ). An increase in the tetragonality is noted when the synthesis temperature is enhanced to 110 °C and 200 °C ( $c/a = 1.006$ ). The insets in Figure 4.1 show the reflections around  $2\theta 45^\circ$  [(200) and (002)] denoting the splitting of the peaks in this region as a result of the distortion of the unit cell, characteristic of the tetragonal structure. For comparison the (200) reflection of cubic BT (JCPDF no. 31-0174) is also presented. In addition, it can be observed (Figure 4.1) that the samples prepared at 90 and 110 °C for 24 h contain residual  $\text{BaCO}_3$ . No  $\text{BaCO}_3$  was obtained after 24 h of reaction at 200 °C.

Figure 4.2 shows the Raman spectra of the samples prepared at 90, 110 and 200 °C for 24 h. Eight Raman active modes are expected for tetragonal BT with a space group  $P4mm$ ,  $3A_{1g}+B_{1g}+4E_g$ <sup>256</sup>. The peaks at around 517, 253 and 185  $\text{cm}^{-1}$  are assigned to the fundamental TO modes (transverse component of the optical mode) of  $A_1$  symmetry and the peak at 307  $\text{cm}^{-1}$  is assigned to the  $B_1$  mode, indicating an asymmetry within the  $\text{TiO}_6$  octahedra of BT at a local scale. The broad band at around 715  $\text{cm}^{-1}$  is related to the highest frequency longitudinal optical mode (LO) of  $A_1$  symmetry. If the sharpness of the peak at 307  $\text{cm}^{-1}$  is reduced and it becomes indistinct then the tetragonal phase is not dominant<sup>141</sup>.

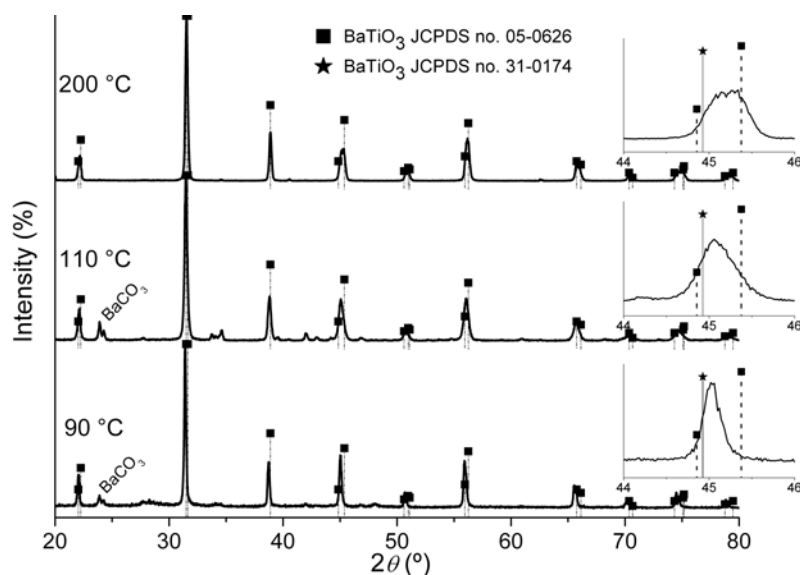


**Figure 4.1** X-ray diffraction patterns of the barium titanate samples prepared at 90, 110 and 200 °C for 24 h indicating the increasing in BT tetragonality and purity when increasing the synthesis temperature.

The sample synthesized at 90 °C presents bands at around 184, 274 (a small shoulder at  $\sim 300$ ), 448, 517, 663 and 712  $\text{cm}^{-1}$ . Increasing the synthesis temperature to 110 °C sharp bands at 136, 154, 185, 307 and 517  $\text{cm}^{-1}$  appeared. Two broad peaks at 264 and 712  $\text{cm}^{-1}$  were also present. The sample obtained at 200 °C contained peaks of predominantly tetragonal barium titanate identified by the bands around 184 (shoulder), 253 (broad) and by the three sharp peaks at 307, 519 and 718  $\text{cm}^{-1}$  <sup>257</sup>. The main difference between the Raman spectra of these samples consists in a band shift from 274  $\text{cm}^{-1}$  for the sample prepared at 90 °C, to lower frequencies of 264  $\text{cm}^{-1}$  for the sample prepared at 110 °C, and to 253  $\text{cm}^{-1}$  for the sample prepared at 200 °C.

Figure 4.3 shows SEM micrographs of a) titanium precursor (TiNTs) and barium titanate samples obtained after 24 h at b) 90 °C (BT9024), c) 110 °C (BT11024) and d) 200 °C (BT20024). It can be readily noticed the modification of the titanium precursor morphology during the hydrothermal treatment.

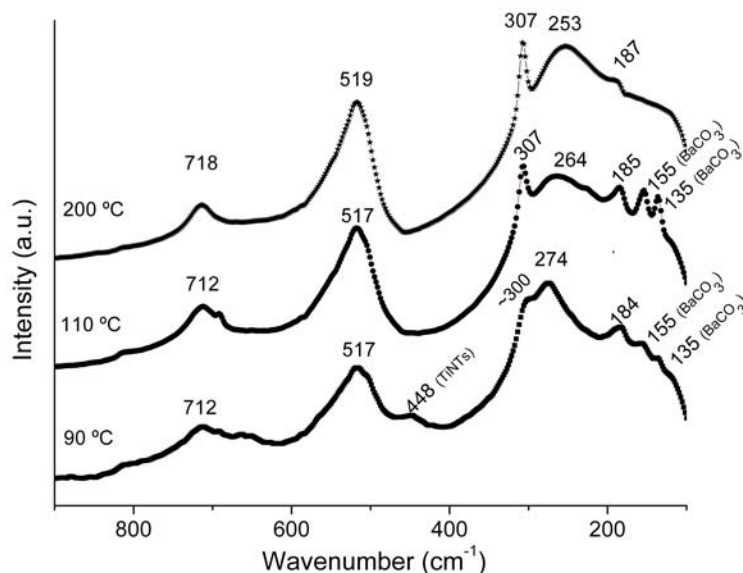


**Figure 4.2** Raman spectra of the barium titanate samples prepared at 90, 110 and 200 °C for 24 h showing the tetragonal distortion of the BT lattice when increasing the synthesis temperature.

When the synthesis temperature is 90 and 200 °C dendritic morphologies are observed. Partially disordered dendrites with mostly planar structure are detected for the samples prepared at 90 °C. The average dendron size is  $\sim 2.5 \mu\text{m}$  in length and  $\sim 200 \text{ nm}$  in diameter with a rough surface. Unreacted precursor can be also noticed. In the case of the samples prepared at 200 °C, the frequency of dendritic branching increased resulting in three-dimensional aggregates of disordered dendrites. The surfaces of the dendrons are smooth and the average dendron length is  $\sim 1 \mu\text{m}$  and diameter  $\sim 150 \text{ nm}$ . The situation is completely different when the synthesis is performed at 110 °C. A general low magnification view reveals round-shaped particles with small sizes ( $\sim 80 \text{ nm}$ ), but the inset of Figure 4.3c shows regions of inhomogeneous growth with the nucleation of branched structures.

TEM micrographs of the sample prepared at 90 °C are presented in Figure 4.4. The dark field TEM image (Figure 4.4a) suggests, as anticipated, that each dendrite is a single crystal. EDS reveals that the particles are composed of Ba, Ti and O (see Figure 4.4a, down inset). A faceted growth of the dendrons is evidenced in the bright field TEM image of the same sample (Figure 4.4b). It is

also indicated that the angle between the “mother” dendron and the “daughter” dendron<sup>258</sup> is 90°. This result is corroborated by the Selected Area Electron Diffraction (SAED) pattern in Figure 4.4b- inset that demonstrates that the crystal growth directions are along  $\langle 001 \rangle$  direction of the barium titanate lattice. This is typical for the growth of perovskite crystals where A and B cations have +2 and +4 valence states, respectively since the  $\{001\}$  facets are neutral and have the lowest interfacial energy with the surrounding media.

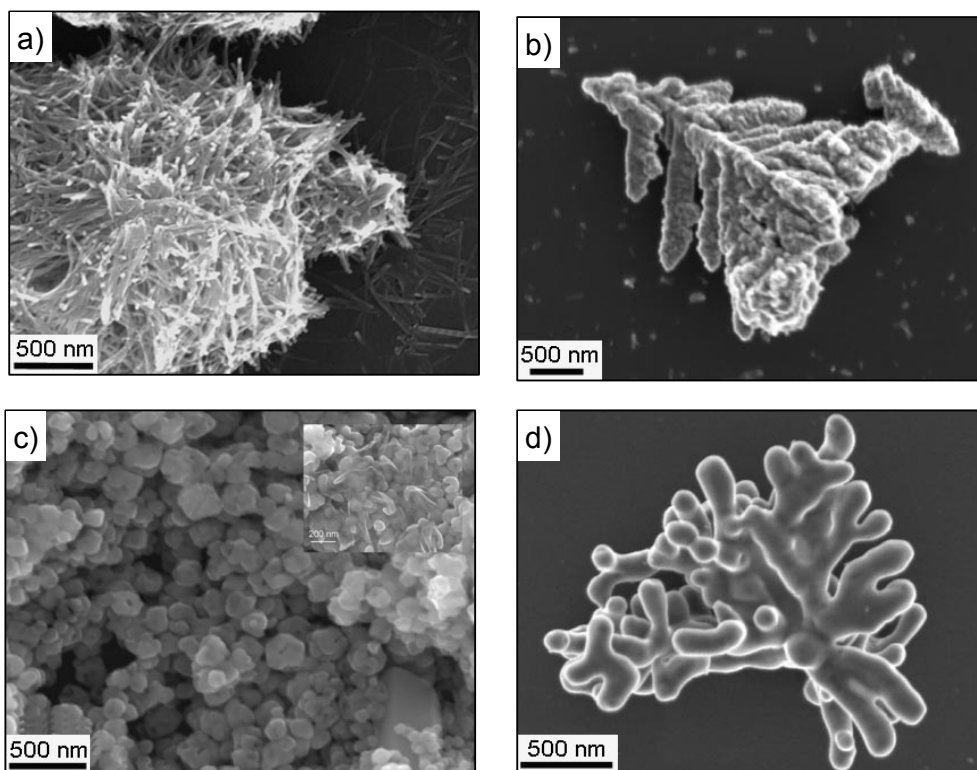


**Figure 4.3** SEM micrographs of a) the titanium precursor (TiNTs) and of the barium titanate samples obtained after 24 h at b) 90 °C (BT9024), c) 110 °C (BT11024) and d) 200 °C (BT20024) illustrating the formation of BT dendritic particles.

The morphology of the particles prepared at 200 °C for 24 h was also analyzed by TEM and is shown in Figure 4.5. Differences in the contrast along the seaweed dendron can be detected, but SAED patterns taken from multiple locations of the dendrons (see inset of Figure 4.5a) indicate only slight changes in

the orientation of the order of 1 to 2 degrees. It is concluded therefore that they are essentially single crystals.

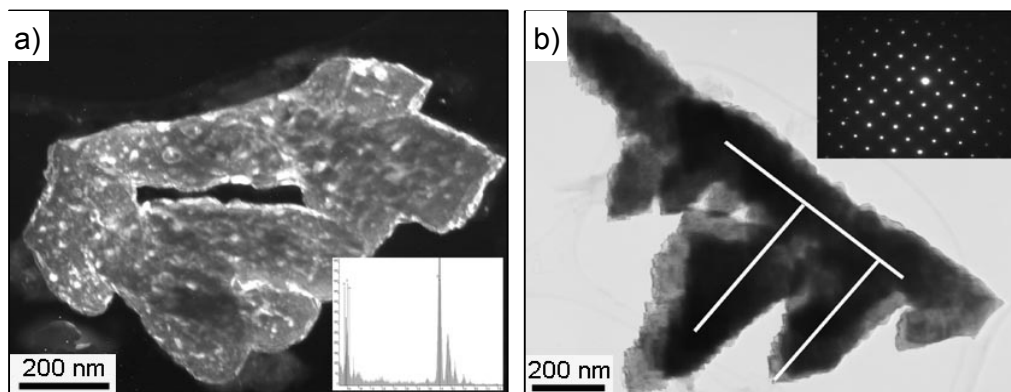


**Figure 4.4** TEM micrographs of samples prepared at 90 °C *a)* dark field (inset EDS) and *b)* bright field (inset SAED). It is indicated the single-crystal feature with growth direction along  $\langle 001 \rangle$ .

In addition, “daughter” dendrons once again grow perpendicular to the “mother” suggesting a crystal axis orientation growth along the  $\langle 001 \rangle$  directions, Figure 4.5*b*.

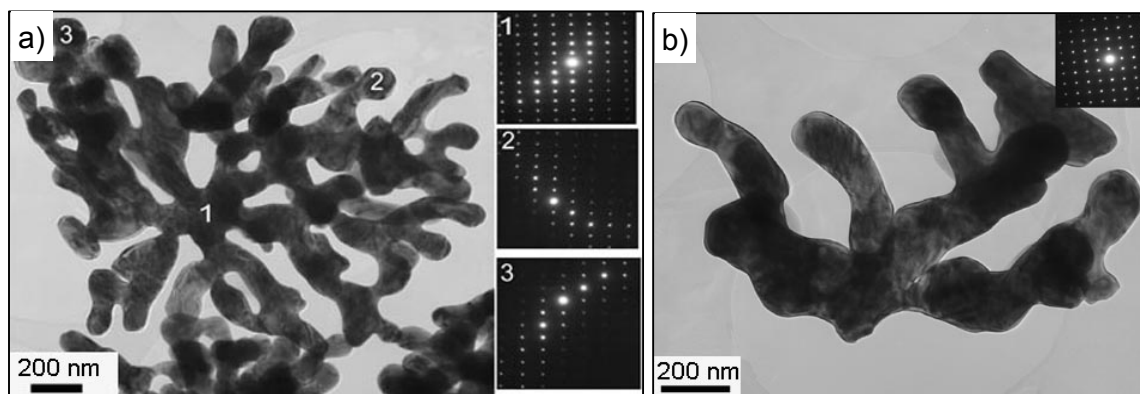


**Figure 4.5** TEM micrographs of samples prepared at 200 °C for 24 h showing that “daughter” dendrons grow perpendicular to the “mother” suggesting a crystal axis orientation growth along the  $\langle 001 \rangle$  directions.

#### The influence of time

At 90 °C hydrothermal treatment, X-ray diffraction revealed that BT was absent until 24 h of reaction time. This is in contrast with hydrothermal treatment at

200 °C, at which BT phase is formed after 1 h. However, a substantial quantity of BaCO<sub>3</sub> is present which decreases monotonously until only BT is present for hydrothermal treatments longer than 24h.

Figure 4.6 shows the Raman spectra of the samples prepared at 90 °C for 1 h (BT901), 12 h (BT9012) and 24 h (BT9024). The spectrum of titanium precursor (denominated as Ti-NTs) is also included for comparison. The Raman spectra of the samples collected after 1 and 12 h illustrate the characteristic bands of the titanium precursor at around 166, 191, 276, 450, 663 cm<sup>-1</sup> and the broad peak at ~910 cm<sup>-1</sup>.

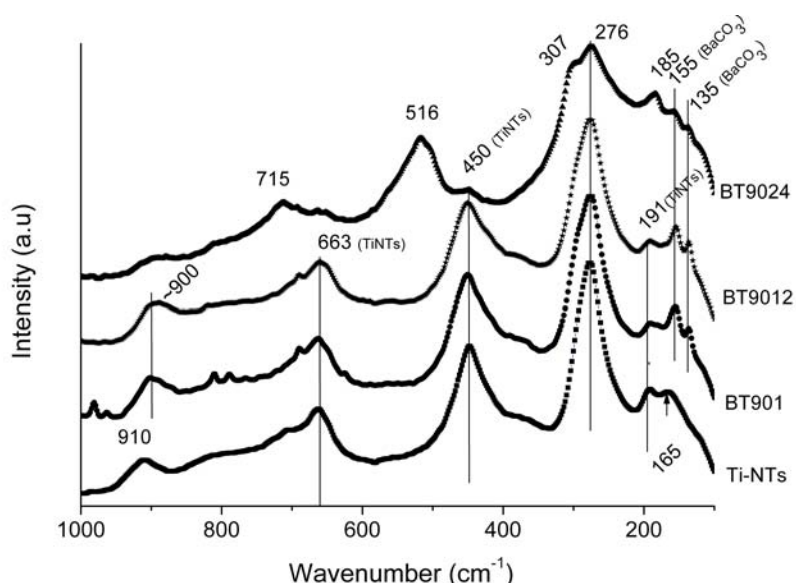


**Figure 4.6** Raman spectra of the samples prepared at 90 °C for 1 h (BT901), 12 h (BT9012) and 24 h (BT9024) illustrating the formation of BT after 24h. The spectra of titanium precursor (denominated as TiNTs) is also shown for comparison.

When comparing the Raman spectra of titanium precursor with the one of BT901 sample the appearance of two new bands at around 135 and 155 cm<sup>-1</sup> can be noticed which according to Shiratori *et al.*<sup>53</sup> can be assigned to orthorhombic BaCO<sub>3</sub>, what corroborates well the previous observations. The spectra of samples collected after 24 h of reaction show the characteristic bands of barium titanate (185, shoulder at ~300, 516, 715 cm<sup>-1</sup>). It is worth noting here that the

characteristic band at  $276\text{ cm}^{-1}$  of titanium precursor does not change during the reaction for all the samples prepared at  $90\text{ }^{\circ}\text{C}$  suggesting a slow conversion to BT.

No morphological differences were apparent for the samples prepared at  $90\text{ }^{\circ}\text{C}$  when examined by SEM and TEM. However, obvious differences were observed for the samples prepared at  $110\text{ }^{\circ}\text{C}$  for different synthesis times. Figure 4.7 depicts the SEM micrographs of samples prepared at  $110\text{ }^{\circ}\text{C}$  for 144 h (BT110144).

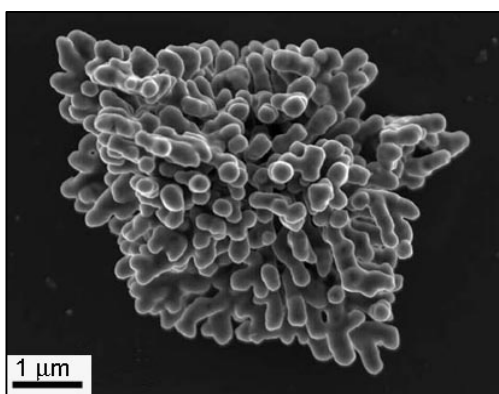


**Figure 4.7 SEM micrograph of samples prepared at  $110\text{ }^{\circ}\text{C}$  for 144h (BT110144) showing the formation of dendritic BT particles.**

After 24h mostly round-shaped particles were obtained, as depicted in Figure 4.3c), in which an incipient dendritic growth is suggested. The dendritic growth becomes obvious after 144h at this temperature.

Figure 4.8 presents the SEM micrographs of samples prepared at  $200\text{ }^{\circ}\text{C}$  for 1 and 6h respectively. Samples obtained after 1h (Figure 4.8a) show two morphologies: small particles with round shape and big plate like particles. TEM micrographs illustrate the round-shaped particles with  $\sim 110\text{ nm}$  in size as presented in the inset of Figure 4.8a. After 6 h of reaction (Figure 4.8b) the big particles remain present, the small particles are not observed anymore but seaweed dendritic particles with a dendron diameter of  $\sim 175\text{ nm}$  appeared.

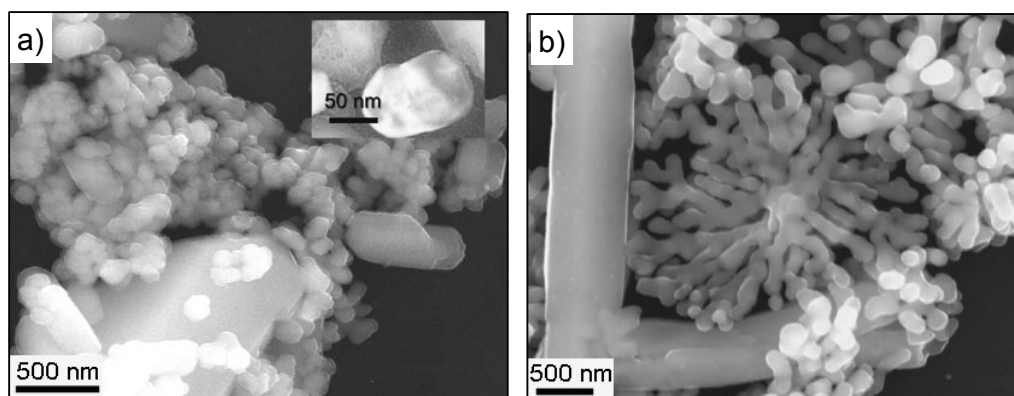


**Figure 4.8 SEM micrographs of samples prepared at 200 °C over: a) 1 h and b) 6h, in which two different particle morphologies can be clearly seen: small with round shape and big plate like particles.**

The aforementioned results and others recent studies<sup>116,118,171</sup> obviously showed that titanate layered structures in general and nanotubes in particular, do not easily act as templates for the 1D growth of BT. Although it has been claimed that anatase nanotubes can behave as growth directing agents to obtain BT NTs,<sup>114,115</sup> in the present work anisotropic growth of barium titanate particles was observed instead. When the synthesis temperature was 90 °C pseudo-cubic BT particles with a “wild”-type dendritic shape were formed. At 200 °C, barium titanate “seaweed”-type dendritic particles with a predominantly tetragonal structure were obtained. To better understand the role of the titanate nanotubes in the crystallization of BT under hydrothermal conditions, a detailed kinetic study is required.

The kinetics of hydrothermal (and aqueous) synthesis of round shaped barium titanate have been thoroughly studied and two concurrent mechanisms have been proposed<sup>164-166,170,178,259,260</sup>. Hertl suggested an in-situ transformation mechanism that assumes that the dissolved  $\text{Ba}^{2+}$  and  $\text{Ba}(\text{OH})^+$  ions react topochemically with the titanium precursor and BT is formed by heterogeneous nucleation on its surface<sup>165</sup>. The second mechanism, dissolution-precipitation,<sup>164,170,178,259</sup> assumes that Ba and Ti sources are rapidly dissolved and homogeneous nucleation of BT takes place. However, none of these studies reported the kinetics of the crystallization of anisotropic BT particles. Moreover the kinetics of BT crystallization starting from titanate NTs has never been described.

A detailed kinetic analysis (at 110 °C and 200 °C) of the morphogenesis of anisotropic BT under hydrothermal conditions using layered titanate nanotubes as a precursor source is performed in this work and presented in the following section.

#### 4.2.2.2 Kinetic Study

The kinetic analysis were carried out at 110 and 200 °C based on the method described by Hancock and Sharp<sup>261</sup> and using the Johnson-Mehl-Avrami equation<sup>262,263</sup>. The fraction of crystallized barium titanate as a function of reaction time was extracted from the XRD patterns presented in Figure 4.12. The degree of crystallization of a material can be represented by the gross intensity ( $I_{\text{gross}}$ ) of a diffraction peak determined by the area of the peak and defined as<sup>178</sup>:

$$I_{\text{gross}} = (\text{integrated phase counts/scan time}) \times (\Delta 2\theta) \quad 4.1$$

The gross intensity of the (110) reflection in the  $2\theta$  range from 30.2 to 32.5° for each sample at the two reaction temperatures 110 and 200 °C was determined.

Crystallization fractions ( $f$ ) were calculated taking into account that at time 0 (pure titanium precursor) the BT crystallization fraction is 0. The maximum extent of the reaction ( $f = 100\%$ ) is obtained from a BT sample fabricated by solid state reaction at 1100 °C and is denominated as BT standard. The BT crystallization fraction at time  $t$  was calculated by the ratio between the gross intensity ( $I_{\text{gross}}$ ) at the specific time of each sample and the gross intensity ( $I_{\text{gross}}$ ) of the standard sample.

#### Structural evolution

Figure 4.9 presents the X-ray diffraction patterns from samples prepared at 110 °C (Figure 4.9a) and 200 °C (Figure 4.9b). Crystalline BT is formed after ~ 6h and after 30 minutes at 110 °C and 200 °C, respectively. For comparison, (200)/(002) XRD peaks from BT fabricated by solid state reaction at 1100 °C are also included. A gradual transformation from a cubic to a predominantly tetragonal structure is observed at both reaction temperatures as the synthesis time

increases. At short reaction times,  $\text{BaCO}_3$  is detected particularly at 200 °C for 30 minutes and 1 h (Figure 4.9b) but the volume fraction decreases as the reaction time increases and a single BT phase is formed after 2.5 h.

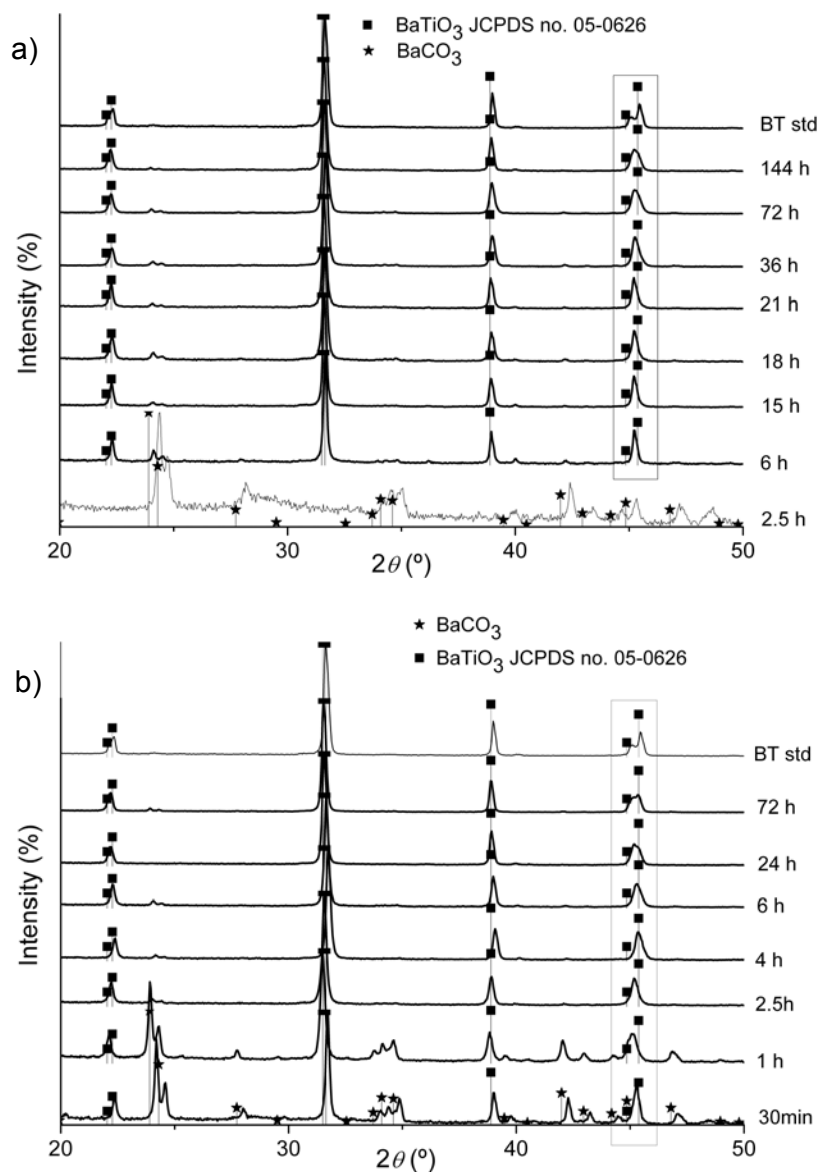


**Figure 4.9** X-ray diffraction patterns of the samples prepared at a) 110 °C and b) 200 °C, illustrating the gradual transformation from cubic to tetragonal BT.

The Raman spectra of the samples prepared at 110 °C and 200 °C are illustrated in Figures 4.10a and b, respectively. In the Raman spectra from samples collected after 18 h at 110 °C (Figure 4.10a) and 30 minutes at 200 °C

(Figure 4.10b) the band at  $307\text{ cm}^{-1}$  is broad and indistinct but with increasing time it sharpens, suggesting a transition from a pseudocubic to tetragonal structure. The transition occurs more rapidly at  $200\text{ }^{\circ}\text{C}$  than at  $110\text{ }^{\circ}\text{C}$ .

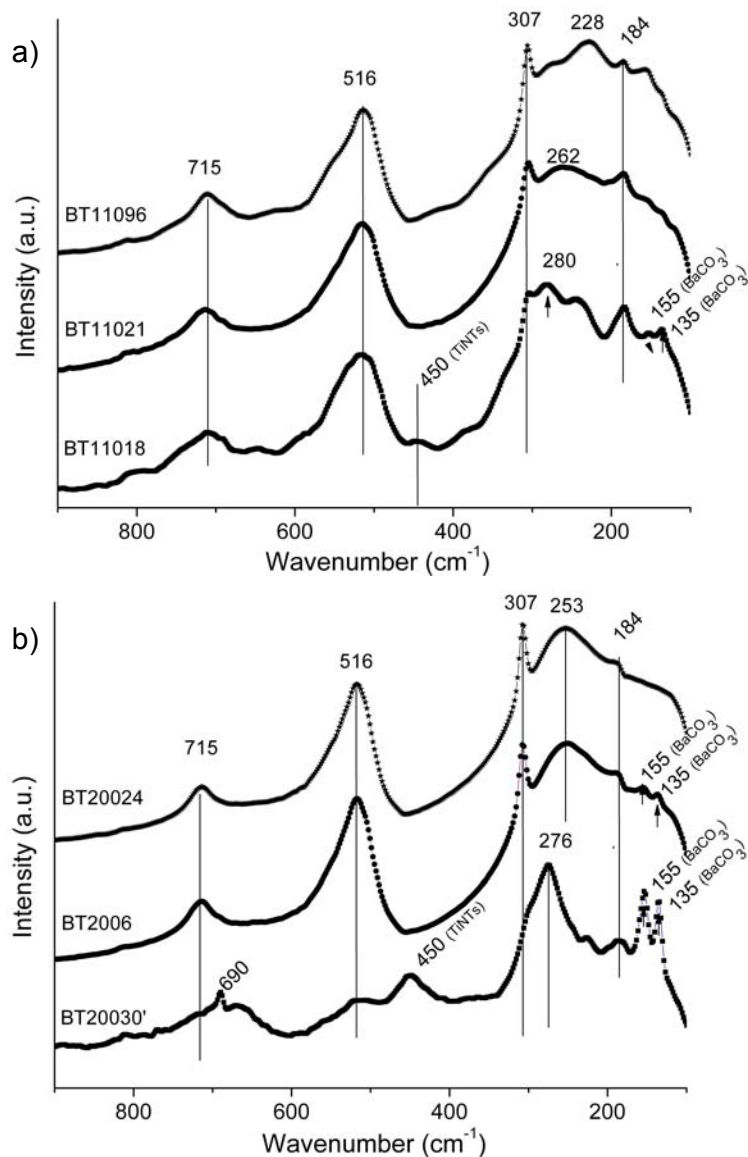


**Figure 4.10** Raman spectra of the samples prepared at  $110\text{ }^{\circ}\text{C}$  and  $200\text{ }^{\circ}\text{C}$  showing the easier transition from a pseudocubic to tetragonal structure at  $200\text{ }^{\circ}\text{C}$  than at  $110\text{ }^{\circ}\text{C}$ .

The transition from pseudocubic to tetragonal structure was studied using variable-temperature XRD for the samples prepared at  $110\text{ }^{\circ}\text{C}$  for 18 h and 24 h. Figure 4.11a and b shows traces of the 103 reflection ( $2\theta \approx 75^{\circ}$ ) recorded at  $20\text{ }^{\circ}\text{C}$

(red) and 180 °C (blue), respectively, for the 18 h sample. The peak is relatively narrow but asymmetric and exhibits a broadened base likely due to heterogeneities within the sample (Figure 4.11a). The line broadening increases significantly with decreasing temperature suggesting a lattice distortion (Figure 4.11b).

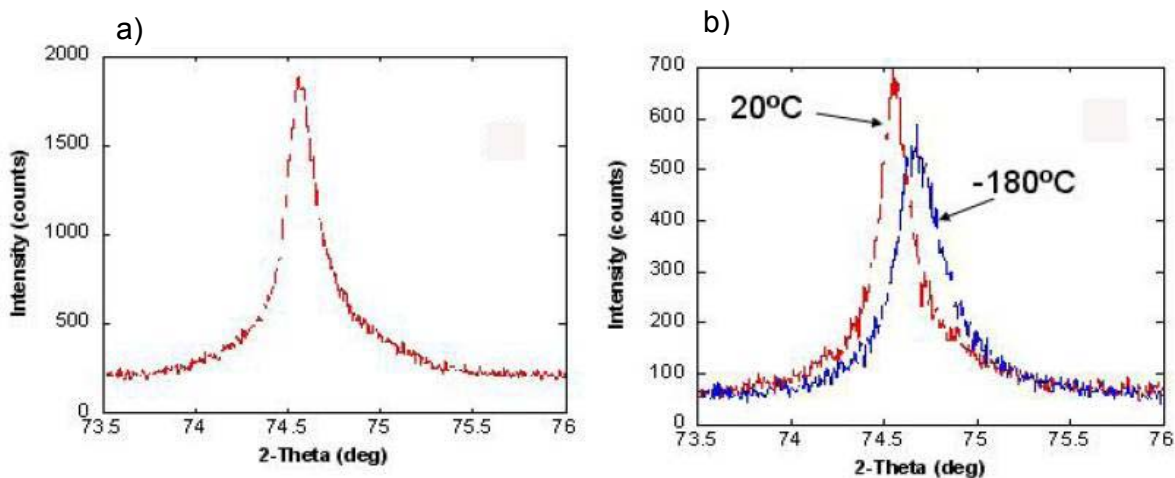


**Figure 4.11 a) Trace of the (103) reflection ( $2\theta \approx 75^\circ$ ) measured at 20 °C; b) comparison of 103 traces measured at 20°C (red) and -180°C (blue) for the sample prepared at 110 °C for 18 h (BT11018). The line broadening increases with decreasing temperature suggesting a lattice distortion.**

Figure 4.12a displays the temperature dependence of the FWHM for the 103 peak of the same sample (BT11018). A clear onset of the strong line broadening is observed below -80°C; the broadening increases progressively with decreasing temperature. This trend is attributed to a distortive phase transition, most likely from cubic to tetragonal. The error bars reflect statistical uncertainties associated with profile fitting.

The results of a similar analysis performed on the sample synthesized at 110 °C for 24 h are presented in Figure 4.12b. In this case the 103 reflection was recorded at 25°C (red), 50°C (blue), and 120°C (green). The peak exhibits a clear splitting as expected for a tetragonal phase. The splitting decreases progressively upon heating consistent with occurrence of the tetragonal to cubic transition at higher temperatures.

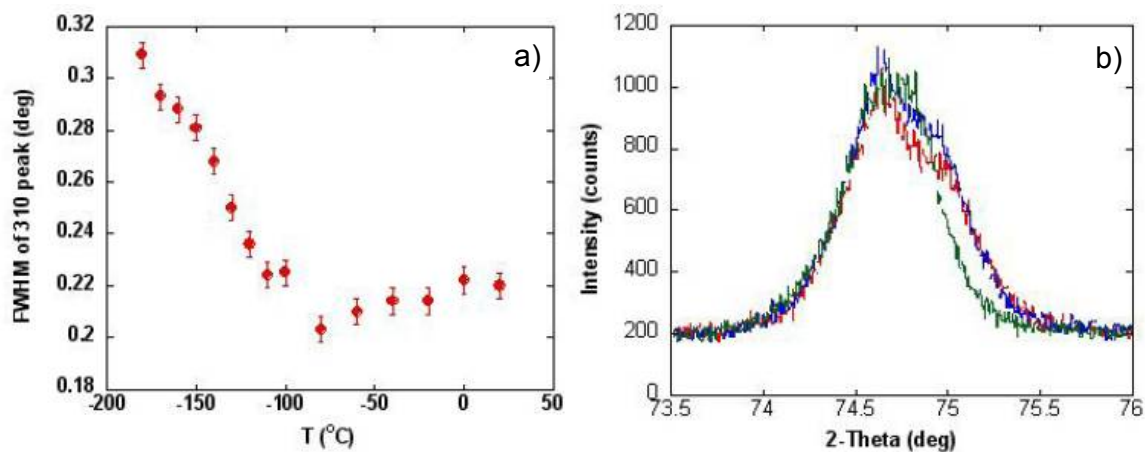


**Figure 4.12** a) Temperature dependence of the FWHM for the 103 peak for the sample prepared at 110 °C for 18 h (BT11018); b) Trace of the 103 reflection recorded at 25°C (red), 50°C (blue), and 120°C (green) for the sample prepared at 110 °C for 24 h (BT11024). The broadening increasing with the temperature decreasing is attributed to a distortive phase transition.

### Kinetic Analysis

The crystalline fraction of BT ( $f$ ) as a function of the synthesis time,  $t$ , is represented in Figure 4.13a and b at for 110 °C and 200 °C, respectively. The  $f$  values calculated from the raw XRD data are presented in Table 1.

It is evident that  $f$  increases with the reaction time but that the reaction is faster at 200 °C than at 110 °C. After 24 h at 110 and 200 °C,  $f = 0.75$  and  $0.85$ , respectively. The maximum extent of the reaction (100% of BT) is reached after  $\sim 24$  h at 200 °C and 96 h at 110 °C. The time dependence of the crystallization fraction has a sigmoidal shape. From the Avrami-Erofe'ev equation<sup>262,263</sup>, Hancock and Sharp derived equation 4.2 from which the kinetic parameters of the crystallization in a solid state reaction can be extracted.<sup>261</sup>

$$\ln[-\ln(1-f)] = \ln(k) + m \ln(t) \quad 4.2$$

where  $f$  stands for the fraction isothermally crystallized at the time  $t$ ,  $k$  for the rate constant which partially depends on the nucleation frequency and growth rate and is very sensitive to the temperature, and  $m$  for an exponent which is independent

of the temperature but responsive to the time of nucleation and growth rate and to the geometry of the particles.

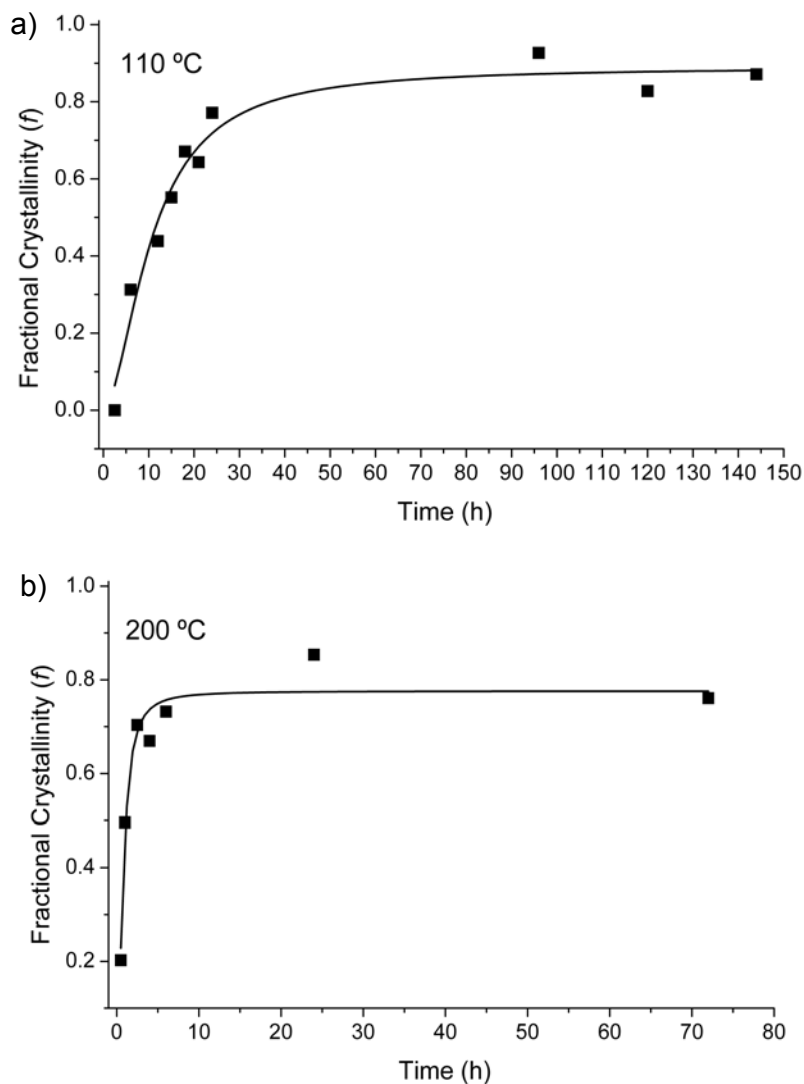


**Figure 4.13** Fraction ( $f$ ) of BT crystalline phase represented as a function of the synthesis time for the samples prepared at a) 110 °C and b) 200 °C. The time dependence of the crystallization fraction has a sigmoidal shape for both temperatures.  $f$  increases with the reaction time being the reaction faster at 200 °C.

Hancock and Sharp<sup>261</sup> reported that for reactions obeying a single theoretical rate equation Johnson-Mehl Avrami plots,  $\ln[-\ln(1-f)]$  versus  $\ln(t)$ , over the range  $f = 0.15 - 0.50$  yields approximately straight lines, with slope ( $m$ ) characteristic of three distinct reaction mechanisms<sup>261</sup>; for  $m = 0.54 - 0.62$ ,

diffusion is the rate limiting step, for  $m = 1.0 - 1.24$ , a zero-order, first-order, or phase boundary controlled mechanism is indicated and when  $m = 2.0 - 3.0$  nucleation is rate controlling.

**Table 4.2 The fractional crystallinity,  $f$ , at two reaction temperatures, 110 and 200 °C.**

110 °C			200 °C		
Sample index	Time(h)	$f$	Sample index	Time(h)	$f$
Ti NTs	0	0	Ti NTs	0	0
BT110	2.5	0.00	BT20030'	0.5	0.20
BT1106	6	0.31	BT2001	1	0.50
BT11012	12	0.44	BT2002,5	2.5	0.70
BT11015	15	0.55	BT2004	4	0.67
BT11018	18	0.67	BT2006	6	0.73
BT11021	21	0.64	BT20024	24	0.85
BT11024	24	0.77	BT20072	72	0.76
BT11096	96	0.93			
BT110120	120	0.83			
BT110144	144	0.87			
BTstrd	-	0.1	BTstrd	-	0.1

In the current study, from the kinetic analysis based on the Johnson-Mehl Avrami model for the two different reaction temperatures (Figure 4.14a and b) it is indicated that the crystallization of BT takes place in two stages, in a manner similar to that previously reported<sup>164,170,178</sup>.

In the first regime ( $f < 0.70$ ) at both temperatures,  $m \approx 1$  which corresponds to a phase boundary mechanism<sup>261</sup>. This value was also obtained for *in-situ* study reported by Walton *et al.* in which BT was synthesized in a static hydrothermal cell starting from barium hydroxide and amorphous titanium oxide<sup>259</sup>. For the

synthesis of BT via aqueous co-precipitation or in non-static hydrothermal cells<sup>164,170,178</sup> values as high as  $m = 2.63$  have been reported and attributed to nucleation dominated mechanisms. This data implies that there is a fundamental different rate determining step in static hydrothermal synthesis of BT compared to other methods.

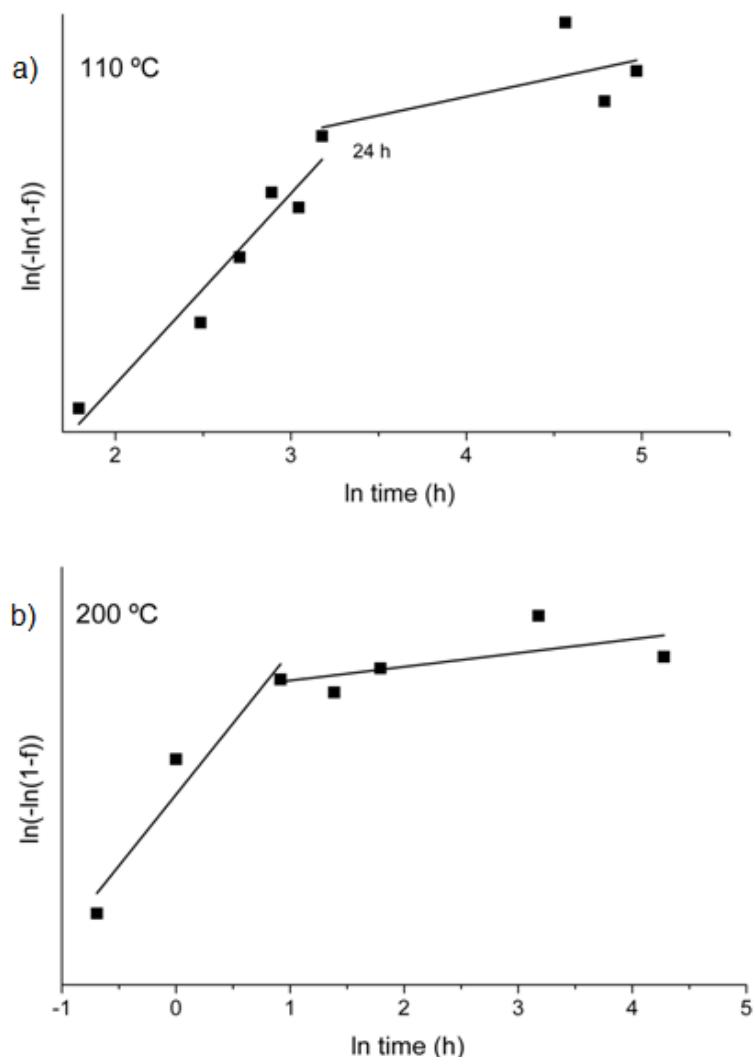


**Figure 4.14** Johnson-Mehl Avrami plots for the two different reaction temperatures a) 110 °C and b) 200 °C. The reaction take place in two stages independently on temperature. The slope values ( $m$ ) which give indications about the mechanism are  $\sim 1$  for the first stage and  $\sim 0.2$  for the second.

For the second regime, a value of  $m \approx 0.2$  is obtained for both temperatures. According to the table of Hancock and Sharp this value does not fall into any of the three listed exponent ranges.<sup>261</sup> However, the method of kinetic

analysis proposed by Hancock and Sharp is only valid for  $f \leq 0.5$  and no attempt has ever been made to rationalize kinetic data for such large crystalline fractions. Therefore, to understand further the crystallization process, a detailed morphological study was performed and is presented in the following section.

#### Morphological evolution

SEM micrographs of the timeline of morphological evolution at 110 °C are presented in Figure 4.15. At the early stages of the reaction, 6 h (Figure 4.15a), dendrites with a rough surface are detected along with wild-type dendrites. These morphologies are similar to those observed for the BT synthesis at 90 °C (see section 4.2.2.1)<sup>258</sup> As  $t$  increases more wild type dendrites are formed (Figure 4.18b for 12 h) but unreacted titanium precursor is still observed up to 18 h of reaction (Figure 4.15c). It is worthwhile to note that the unreacted titanium precursor can not be detected by XRD due to its low crystallinity. Concomitantly, for this synthesis time (18h) spherical barium titanate particles are formed (see inset Figure 4.15c). After 24 h of reaction the presence of spherical particles is noticeable in Figure 4.15d. After 96 h of reaction when the maximum extent of crystallization is attained (~ 75%) (Figure 4.13a) two types of barium titanate dendritic morphologies are observed (Figure 4.15e). Wild type dendrites coexist with small and large seaweed type dendritic aggregates characterized by a smooth surface. The percentage of the round shaped particles seems to be reduced compared to the sample obtained after 24 h. The coexistence of the wild and seaweed type dendritic particles is also verified after 144 h of reaction, Figure 4.15f.

A similar morphological evolution, wild-type dendrites to spherical particles to seaweed dendrites is also observed at 200 °C (Figure 4.16). At this temperature, the wild-type dendrites are formed after only 30 minutes and, at the same time, large quantities of unreacted titanium precursor are observed, Figure 4.16a. Spherical particles and small 'seaweed' dendrites are formed after 1 h (Figure 4.16b). After 24 h at 200 °C ( $f \sim 85\%$ ) only large seaweed-type dendritic aggregates are apparent (Figure 4.16c).

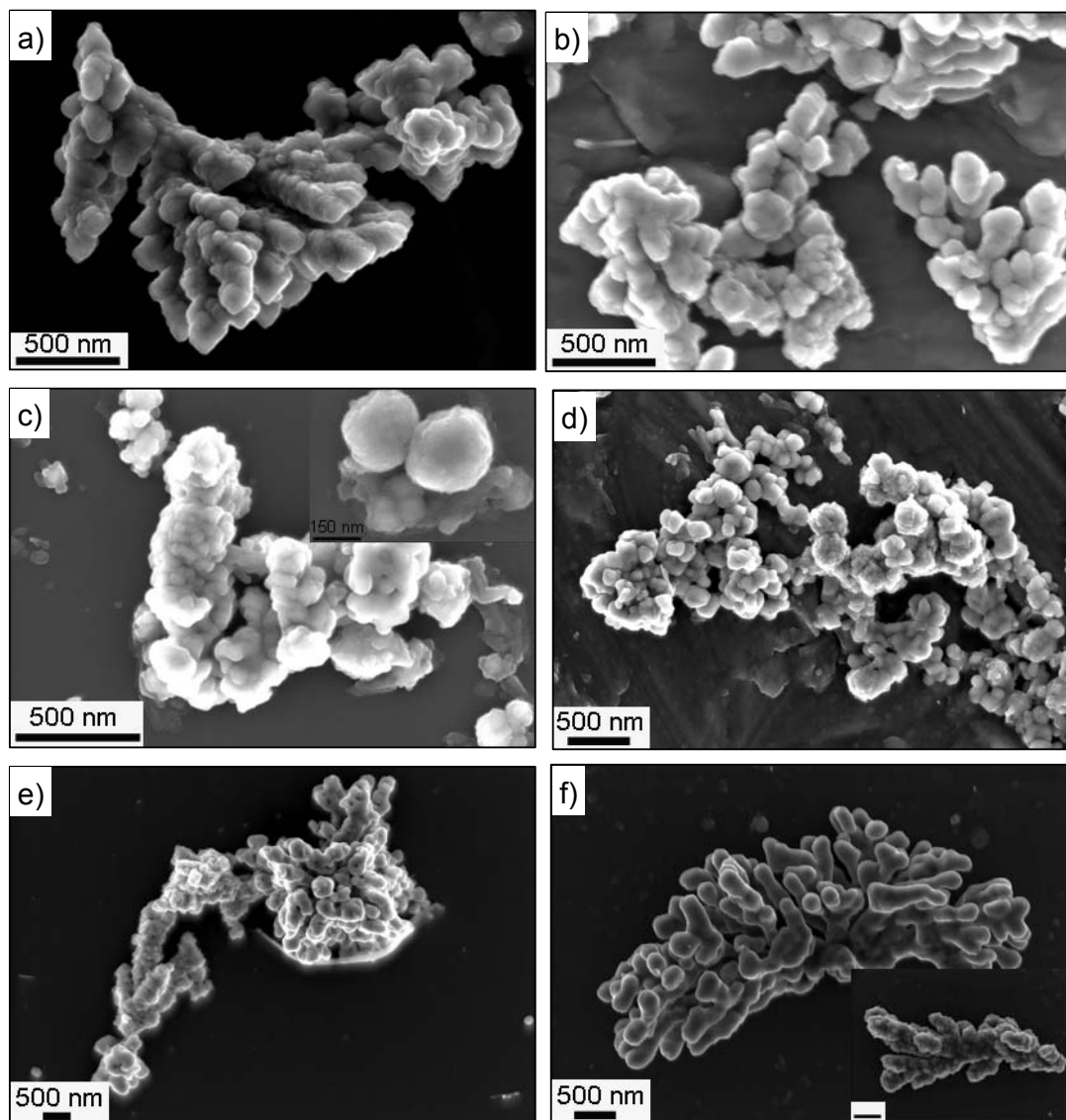


**Figure 4.15** Timeline morphological evolutions studied by SEM for the samples obtained at 110 °C after a) 6h (BT1106); b) 12h (BT11012); c) 18h (BT11018); d) 24h (BT11024); e) 96h (BT11096) and f) 144 h (BT110144). It is illustrating the morphological evolution from wild-type dendrites to spherical particles to seaweed dendrites.

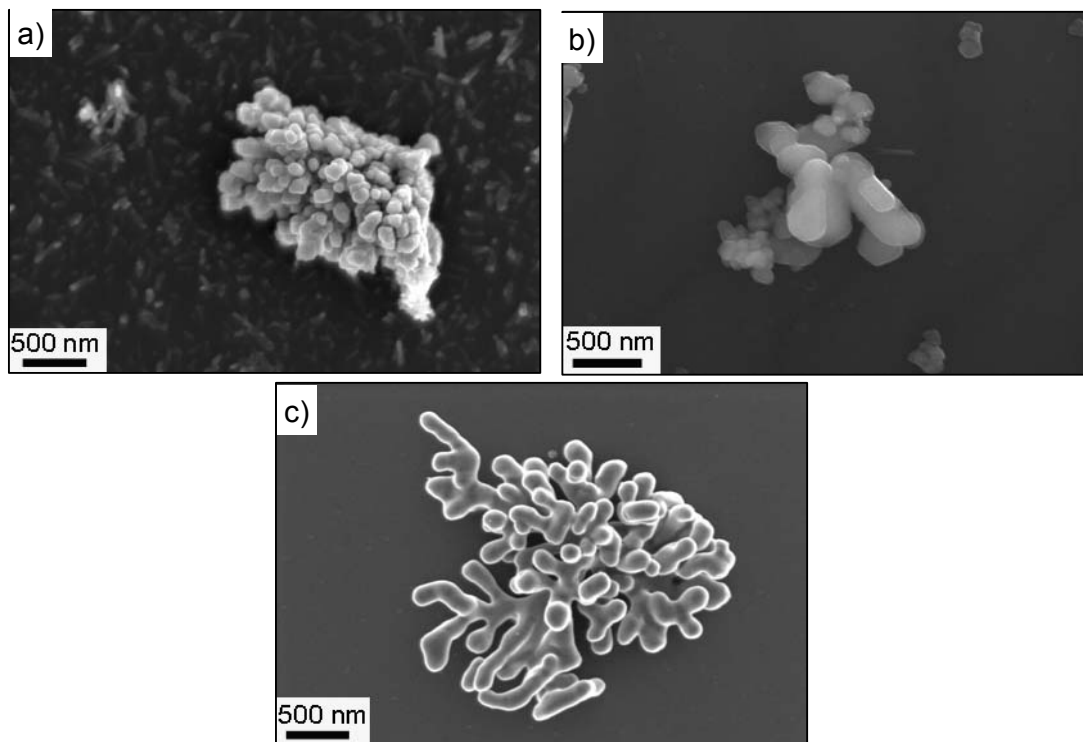


**Figure 4.16** Timeline morphological evolutions studied by SEM for the samples obtained at 200 °C after a) 30 min (BT20030); b) 1h (BT20001); c) 24h (BT20024). Showing the wild, round shaped and seaweed morphologies.

Figure 4.17a and b shows the TEM micrographs of BT particles synthesized at 110 and 200 °C, respectively. Irrespective of temperature, BT nuclei form on the surface of the NTs at the early stages of synthesis. The ensuing particle morphologies mirror those observed by SEM. However, diffraction patterns from dendrites oriented with the  $\langle 001 \rangle$  direction parallel to the electron beam, confirmed that the dendritic arms occupied  $\{001\}$  growth habits.

The main achievements regarding the hydrothermal synthesis of BT by hydrothermal treatment of titanate layered nanotubes (TiNTs) and  $\text{Ba}(\text{OH})_2$  are schematically represented in Figure 4.18. The anisotropy of BT particles is dependent on the synthesis temperature and time. Pseudo-cubic BT particles with a “wild”-type dendritic shape are formed at low temperatures and short reaction time by a phase boundary mechanism with BT nucleating at TiNTs surface. At longer reaction times and high temperatures BT forms by a dissolution-

precipitation mechanism, exhibits also a dendritic morphology but “seaweed”-type with a tetragonal structure.

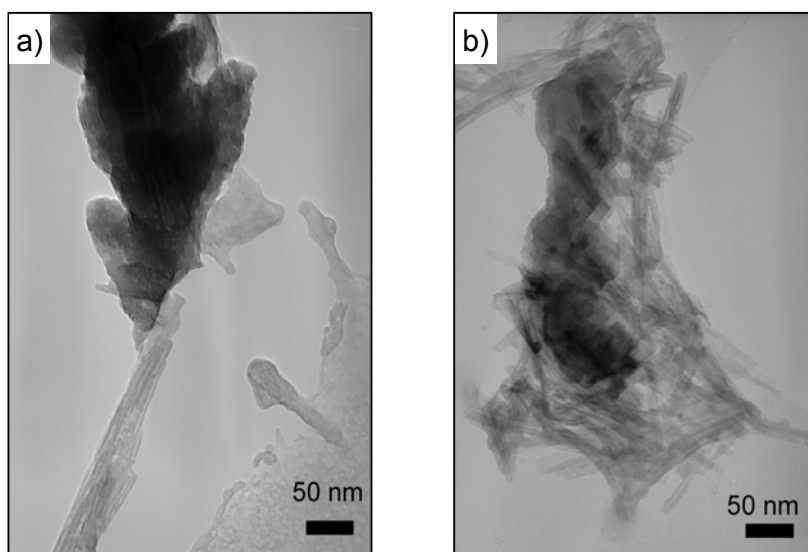


Figure 4.17 TEM micrographs at the early stages of BT crystallization for the samples prepared at a) 110 °C and b) 200 °C. BT nuclei form on the surface of the NTs.

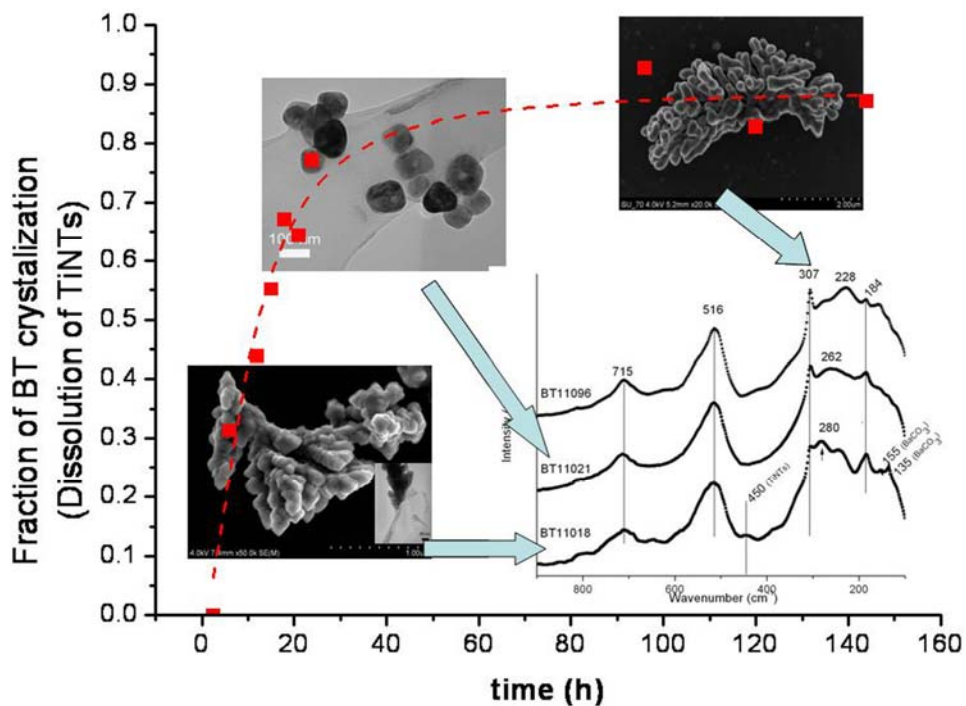


Figure 4.18 Structural and morphological evolution of BT particles obtained by hydrothermal treatment of titanate layered nanotubes (TiNTs) and  $\text{Ba}(\text{OH})_2$  at 110 °C.

But the effect of the morphology on the electric response of these nanoferroelectrics is still to be explained. Therefore the study of the nanoscale piezoresponse of dendritic BT was considered interesting and is reported in the next section.

#### 4.2.2.3 Nanoscale piezoelectric response

The piezoelectric (domain) images acquired simultaneously with topography (up insets) of BT morphologies *a*) “wild”-type and *b*) “seaweed”-type are represented in Figure 4.19. The SEM micrographs are also included in the right lower corner insets. The comparison of simultaneously acquired topographic and piezoresponse images allows one to establish an apparent correlation between the sample morphology and domain population. In the piezoelectric image, domains with opposite polarities exhibit different contrast. Dark regions (negative domains) correspond to domains with polarization head terminates at the bottom electrode, and bright regions (positive domains) to domains with polarization terminated at the free surface of the sample. As depicted in Figure 4.19a very weak piezoresponse contrast was observed for the wild type dendritic particles. On contrary seaweed type dendritic ones show a clear and pronounced piezoresponse contrast (Figure 4.19b). Moreover it is observed that the domain size of the wild type is around 50 nm and is smaller than the seaweed type, which is around 125 nm.

However, both cross-section profiles collected in the darkest zones of the PFM images and depicted in Figure 4.20 present a distribution of the piezoelectric contrast trough the negative part suggesting a downwards preferred orientation of the ferroelectric domains referred as negative domains (note the predominately dark contrast in the piezoresponse images Figures 4.19a and 4.19b, respectively). However, the predominately dark contrast is more typical for wild particles, while seaweed exhibits domains of both polarities. Moreover, the cross-section profiles of the seaweed type show higher values of piezoactivity regarding to the wild type (Figure 4.20).

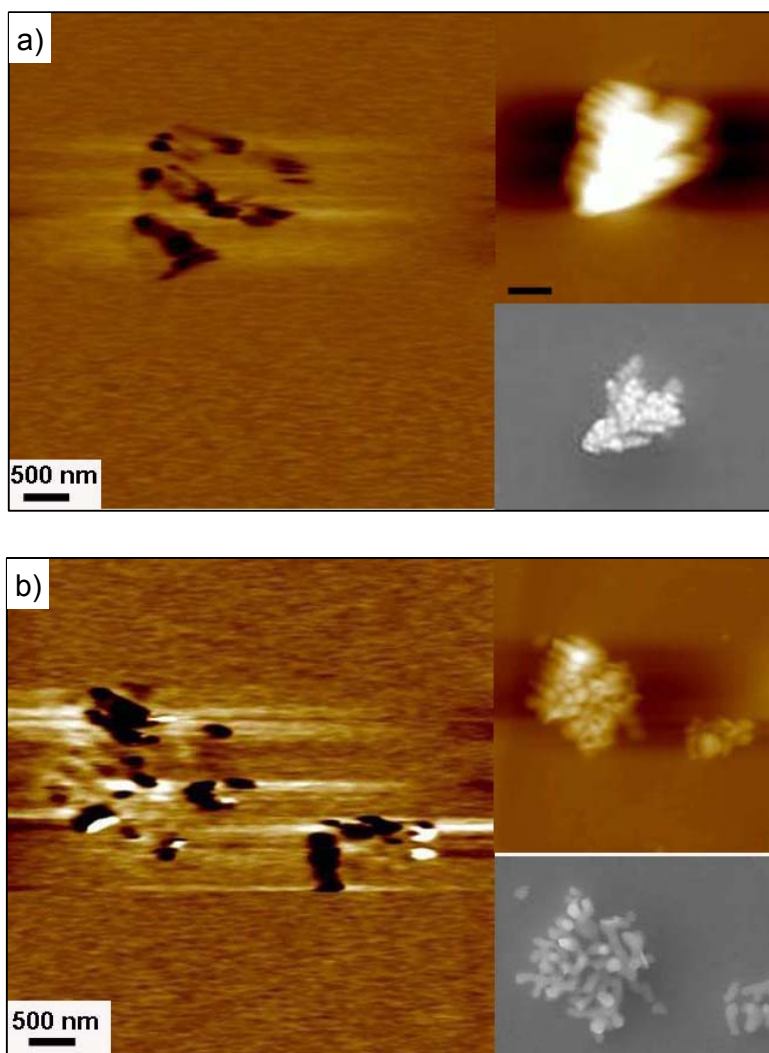


**Figure 4.19 Piezoresponse images (PFM) of the a) wild type BT dendritic particle and b) seaweed type BT dendrites (in the up insets the topography and in the down insets the SEM micrographs). More pronounced piezoresponse contrast observed for the seaweed comparing to wild.**

The polarization switching behavior can be evaluated by applying a relatively large dc field between the tip and sample (poling). Figures 4.21a and 4.21b present the obtained piezoresponse images before and after poling (4.21a1 and 4.21b1 dc = +20 V and 4.21a2 and 4.21b2 dc = -20 V).

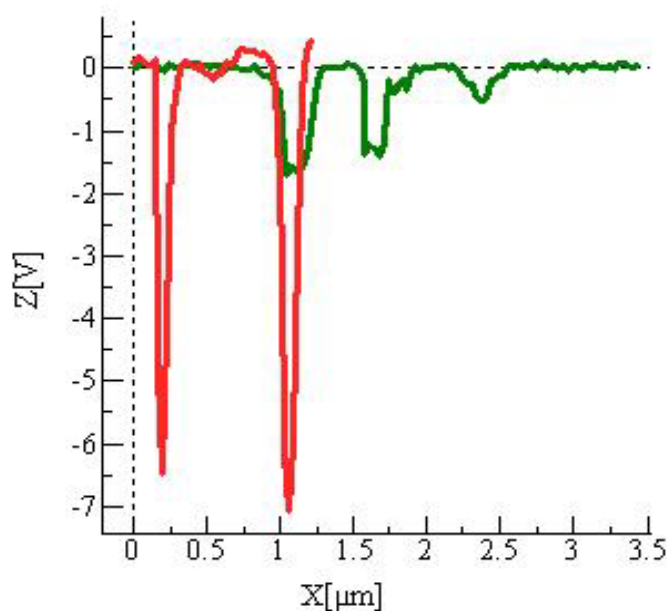


**Figure 4.20** Cross-section profiles of the wild (green) and seaweed (red) morphologies collected from the PFM images. Higher values of piezoactivity are observed for the seaweed dendrites.

Comparing Figures 4.21a and 4.21a1 one can notice that one small domain of the wild type particles switched from dark to bright (square marked area in Figure 4.21a) when changing from positive to negative poling. On the contrary, in the case of seaweed type particles there is no obvious switching under identical poling conditions. This can be due to the instability of the poled state during the ac scanning or to the insufficient applied electric field taking into account that the domain size of seaweed particles is larger than the wild type and because of that more difficult to switch. However, there are some regions (square marked areas in Figure 4.21b) where the former dark regions fade after poling of negative dc due to the realignment of the ferroelectric domains, in seaweed type particles (Figures 4.21b1 and b2).

It is better to say here that an evident switching could not be obtained even at higher dc field ( $\pm 50$  V) due to the following possible reasons. As described in the PFM sample preparation (section 2.5.1) particles are embedded in a non-piezoactive polymeric matrix and it is very probable that the dielectric permittivity of this matrix to be lower than that of BT. Therefore a larger voltage drop occurs

through the non-ferroelectric layer. As a result only a part of the external voltage is effectively applied to the ferroelectric particle and might be not enough to induce polarization switching. Moreover, if the self-polarization phenomenon appears due to accumulated charge, a relatively large self-built electric field should be also overcome.

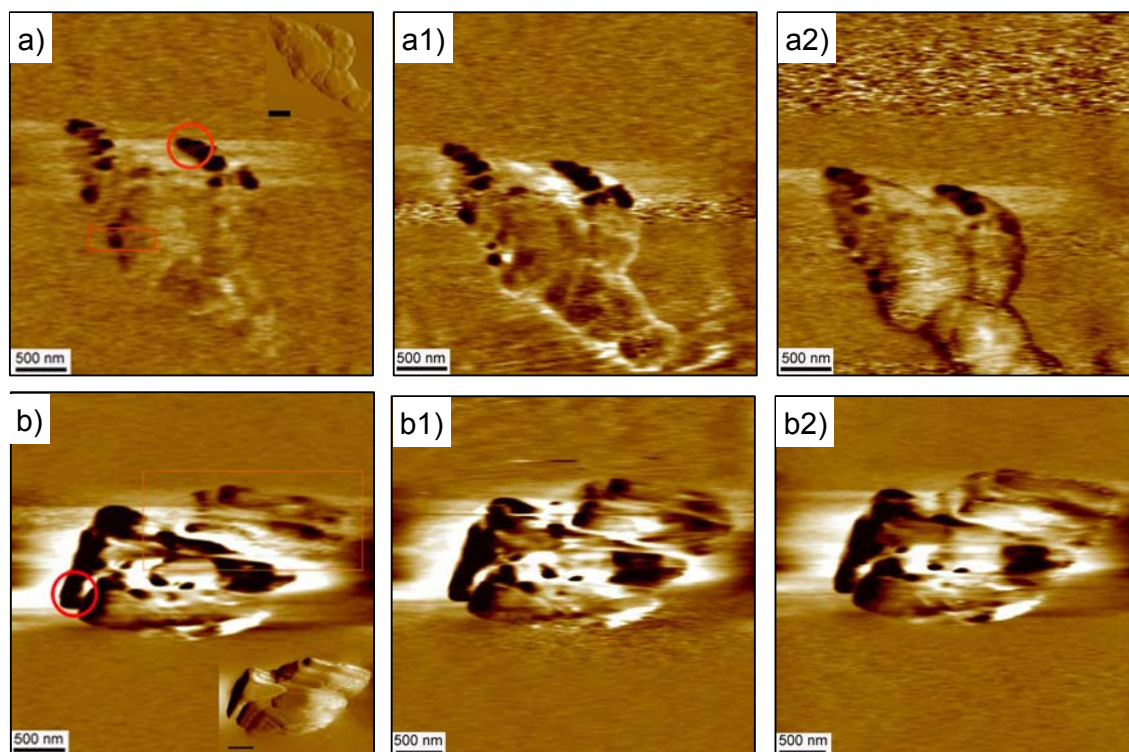


**Figure 4.21** The PFM response of the *a)* wild type BT dendritic particle and *b)* seaweed type BT dendrites before and after poling with + d.c. (*a1* and *b1*) and with - d.c. (*a2* and *b2*). The domain size for wild is smaller than for seaweed therefore can be switch.

The local effective piezoelectric coefficient as a function of the applied field measured on individual grains (circles marked in Figures 4.21a and 4.21b) of wild type BT dendritic aggregates and seaweed dendrites is presented in Figure 4.22a and 4.22b, respectively. The grains were chosen in the zones with dark contrast in the PFM images and with height  $\sim 800$  nm. It is important to note here that a larger dc field was applied in this case,  $\pm 35$  V comparing to  $\pm 20$  V previously used. Both types of dendritic particles present polarization switching although the hysteresis loop shapes are quite different. For the wild type (Figure 4.22a) the shape is almost linear and presents various steps, suggesting intermediate

metastable polarization states<sup>199</sup>, *i.e.* the ferroelectric polarization of the domains of wild type particles are not stable and have the tendency to revert during the pulse duration. On the contrary an abrupt polarization switching from one state to another (typical square shaped hysteresis loop) is observed for seaweed particles (Figure 4.23b).

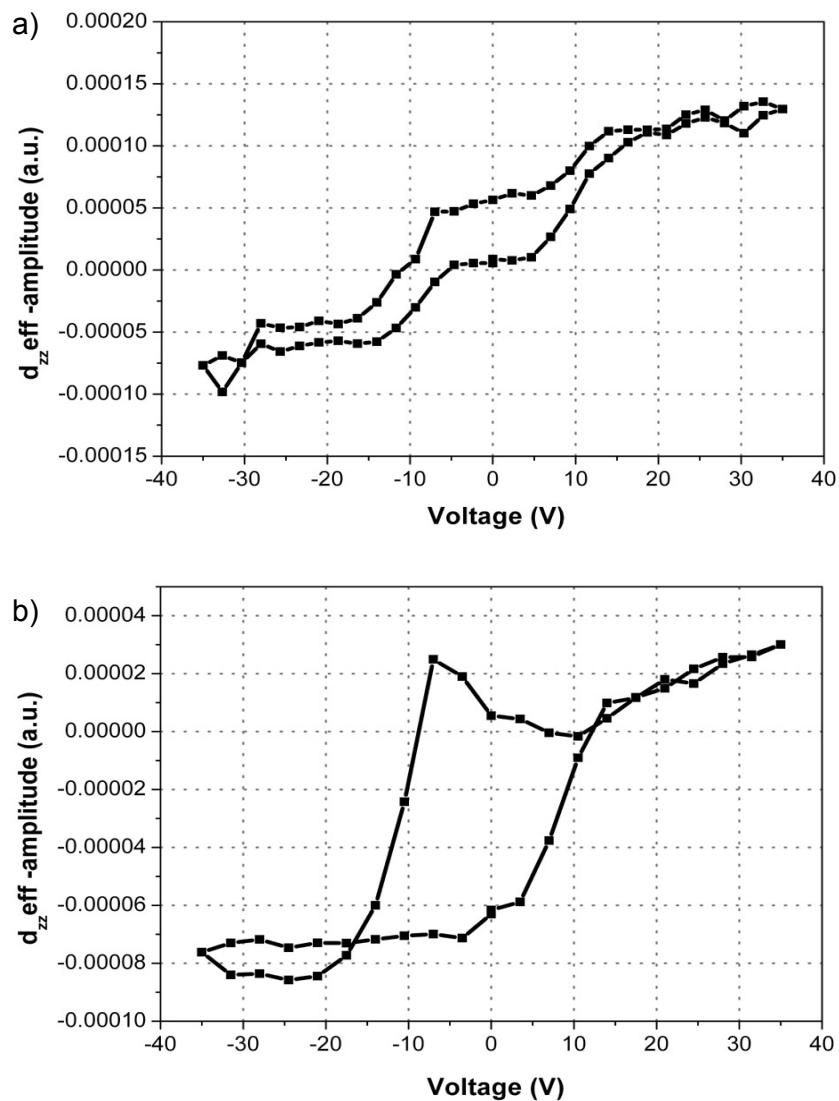


**Figure 4.22** Typical local piezoelectric coefficient as a function of the applied field measured on BT dendritic particles with wild type (a) and seaweed type (b), respectively. Different hysteresis shapes: linear with various steps for wild and squared shaped for seaweed.

The polarization switching through various metastable states of wild type particles can be related with their average *pseudo* cubic type structure. As stated above the stabilization of BT cubic structure at room temperature is due to the incorporation in the lattice of  $\text{OH}^-$  ions.<sup>85</sup> The  $\text{OH}^-$  concentration can be estimated by Fourier Transformed Infrared spectroscopy (FTIR). Indeed the FTIR spectra (Figure 4.23) of the wild type dendritic particles present at  $\sim 3480\text{ cm}^{-1}$  the characteristic absorption band assigned to the  $\text{OH}^-$  stretching mode of internal hydroxyl ions<sup>264</sup>, not present in the case of seaweed particles. In addition, the high frequency band centered at  $535\text{ cm}^{-1}$  and a shoulder near  $650\text{ cm}^{-1}$ , characteristic bands of BT cubic structure are also visible. The  $650\text{ cm}^{-1}$  shoulder disappears in the case of seaweed dendrites according to their tetragonal symmetry.

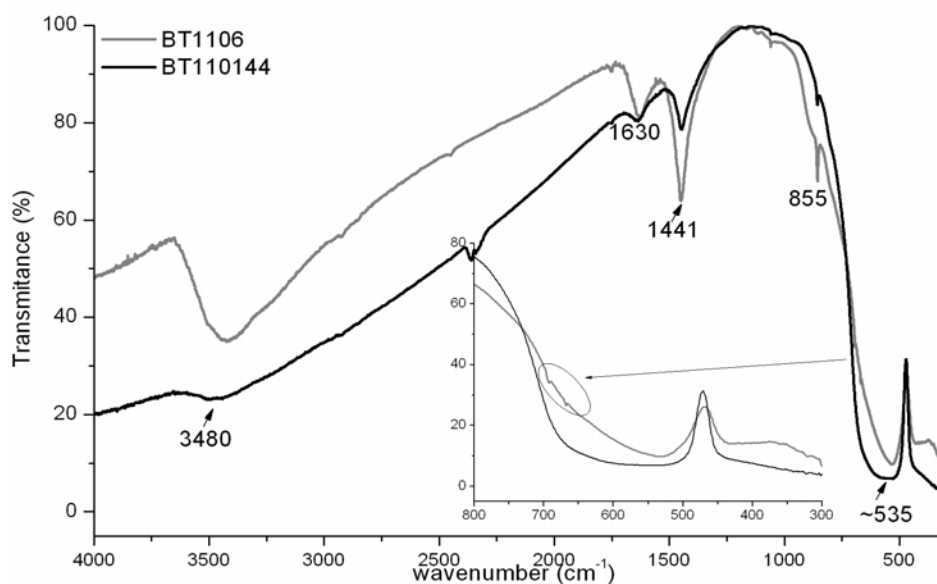


**Figure 4.23 FTIR spectra of the wild (sample BT1106) and seaweed (sample BT110144) morphologies, illustrating the higher  $\text{OH}^-$  ions concentration of wild dendrites.**

### 4.2.3 Discussion- solution based synthesis using TiNTs precursors

The results presented above indicate that crystalline BT can be prepared at temperatures ranging from 90 to 200 °C by hydrothermal treatment using layered nanotubes and Ba(OH)<sub>2</sub> as Ti and Ba sources, respectively. However, there is a marked difference in morphology of the particles depending on the temperature and reaction time. Low temperatures (90 °C) favor rough dendrites whereas at 110 °C and 200 °C either round-shaped particles or dendrites are observed. There is no resemblance with the microstructures reported by Mao<sup>114</sup>.

Hertl<sup>165</sup>, in part, explained some of the observed differences by considering that the solubility of the Ti precursor increases with increasing temperature. He postulated that at some critical temperature (>90 °C in this study), the Ti precursor dissolves prior to reaction with Ba(OH)<sub>2</sub>. Below this value the mechanism is topochemical and BT effectively grows on the surface of the Ti precursor. In the first hours of topochemical synthesis, Ba<sup>2+</sup> ions partially exchange with Na<sup>+</sup> and proton ions existent between the nanotube layers are also adsorbed at the surface of the titanate nanotubes. The formation of BT occurs simultaneously with dehydration which is a slow process in superheated fluids<sup>85</sup>. Residual hydroxyl ions are retained in the oxygen sublattice and are compensated by cation vacancies. As claimed by Vivekanandan *et al*<sup>85</sup>, these lattice defects lead to the presence of a metastable BT pseudo-cubic phase at room temperature. The presence of defects on the crystal lattice can be supported by the single diffraction peak at 45° 2θ (Figure 4.1) and by the absence of a clear band at 307 cm<sup>-1</sup> (characteristic of tetragonal BT) in the Raman spectrum (Figure 4.2).

For reactions at > 90 °C, the Ti precursors dissolve creating Ti rich regions in the aqueous medium which acts as a nucleation site for BT.<sup>164</sup> The mechanism of dissolution appears to occur via an intermediate anatase phase formed by the dehydration of the nanotubes after 1h of thermal treatment, Figure 4.7. Subsequently, the Ti-O bonds of the anatase are broken by hydrolytic reaction to form [Ti(OH)<sub>x</sub><sup>4-x</sup>] soluble species that reacts with the Ba<sup>2+</sup> and BaOH<sup>+</sup> ions in solution to precipitate BT. The high solubility of the Ti precursor may be attributed to the layered structure of the titanate nanotubes which originates from a zigzag

chainlike structure of the basic structural  $\text{TiO}_6$  octahedral units<sup>222</sup>. Within the layers  $\text{Na}^+$  or  $\text{H}^+$  ions exist to balance the electric charge leaving the nanotubes vulnerable to a particularly high ion-exchange capacity and degree of hydration in aqueous media at low temperature<sup>240</sup>. Similar levels of solubility were achieved by Clark *et al*<sup>265</sup> who utilized an amorphous Ti precursor ( $\text{H}_2\text{TiO}_3$ ), commercially referred to as titanitic acid.

The large number of defects present at the BT nucleus creates a high surface energy and a strong anisotropic curvature of the surface, giving rise to high surface tension anisotropy of the solid-liquid interface. Together with diffusion limited aggregation phenomena, surface tension anisotropy are the driving forces for the observed dendritic growth. In this work two types of dendrites are observed: *i*) the wild-type as in the particles prepared at 90 °C (Figures 4.3b and Figure 4.4) and *ii*) the seaweed-type obtained for particles synthesised at 200 °C (Figures 4.3d and Figure 4.5).

At 90 °C, the BT nuclei, obtained mainly by the topochemical reaction mechanism on the nanotube surface, possess a high concentration of lattice defects. Molecular motion is limited and dendritic growth is consequently controlled by the high surface energy. Consequently, a rough surface with faceted growth (wild type dendritic growth) is observed (Figure 4.3b and Figure 4.4). At 200 °C, a combination of relatively fast molecular motion and the occurrence of dissolution – precipitation mechanism, results in fewer surface defects and a lower surface energy. The growth of “daughter” dendrons is favoured and the sharp tips of the dendrons are eliminated. Under such conditions seaweed-type dendritic particles with smooth surfaces are formed (Figure 4.3c and Figure 4.5).

At 110 °C, round-shaped particles (80 nm) are generally observed after 24 h (Figure 4.3c) (although some preliminary branching is evident (Figure 4.8)) whereas at 200 °C large single crystal dendrites (1  $\mu\text{m}$ ) with rounded arms are present (Figure 4.3c). The round-shaped particles obtained at 110 °C after 24 h (Figure 4.3c) are similar to the ones observed for samples prepared at 200 °C after 1h (Figure 4.9a). It is believed therefore that they represent the early stages of the dissolution-precipitation reaction in which the round-shaped particles are effectively nuclei for subsequent dendritic growth. Similar, but less extreme

conditions for growth occur at 110 °C (Figure 4.3c) as opposed to 200 °C and therefore after prolonged thermal treatment at 110 °C (Figure 4.8) some evidence of burgeoning dendrites are observed which appear to possess seaweed type branches (Figure 4.3b). At 110 °C, the crystals are formed in a temperature regime where nucleation dominates within the aqueous medium and growth of the BT particles is restricted. Conversely, at 200 °C, growth dominates and upon formation of a stable nucleus a large dendritic crystal rapidly forms. The presence of round-shaped particles after 2h at 200 °C confirms this hypothesis; the reaction to form BT is incomplete and only nuclei are present which will ultimately grow to form the dendrites.

From a simplistic perspective, the conditions occurred at 110 °C and 200 °C appear to correspond to two different regimes for the precipitation of BT comparing to the reaction at 90 °C. For that the detailed kinetic study has been performed.

The kinetic analysis presented above lead to the four key points that need to be considered. First, at the early stages of crystallisation, BT nucleates on the surface of the Ti-nanotubes. Second, there is a gradual transition with reaction time from pseudocubic to tetragonal barium titanate (Figures 4.9 - 4.12). Third, the transition from pseudocubic to tetragonal is accompanied by a change in the particle morphology from “wild”-type dendrites to spherical particles and seaweed dendrites (Figures 4.15 and 4.16). Finally, an exponent,  $m = 1$  is obtained by fitting Johnson-Mehl Avrami plots ( $f < 0.7$ ) to the reaction which suggests that the kinetics are dominated by a phase boundary rather than a classic diffusion or nucleation controlled mechanism.

The movement of the solid-liquid interface within the reacting medium is physically unimpeded so it is reasonable to assume that the slowest step occurs within the chemical reaction to form BT at the phase boundary.

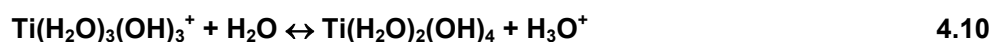
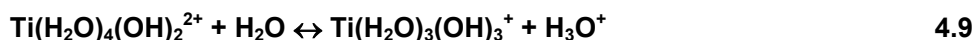
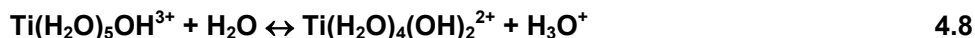
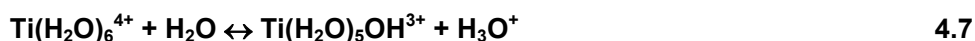
The overall reaction for the formation of BT is given below (equation 4.3):



but as with all complex reactions there are multiple steps within the mechanism, one of which will be rate determining. Based on the thermodynamic study of Lencka and Riman <sup>161</sup>, the aqueous chemistry of Ba<sup>2+</sup>, Ti<sup>4+</sup> cations and O<sup>2-</sup> is represented by:



and indicates that formation of stoichiometric BT requires hydrated Ti(OH)<sub>4</sub> (Ti(H<sub>2</sub>O)<sub>2</sub>(OH)<sub>4</sub>) species. As illustrated below, dissolution of Ti is accompanied by a sequence of reactions to form hydrous titanium cations (Ti(OH)<sub>x</sub><sup>(4-x)+</sup>). Since each step generates H<sub>3</sub>O<sup>+</sup> ions, the isothermal stability of the Ti(OH)<sub>x</sub><sup>(4-x)+</sup> species is related to pH which decreases with increasing titanium concentration <sup>161</sup>.



Therefore, the protons released during Ti dissolution and hydrolysis result in a decrease in pH as the titanate NTs dissolve. It is postulated therefore that, under the current static synthesis conditions, the local concentration of Ti increases and therefore local pH decreases at the surface of the NTs. The decrease in local pH shifts the equilibrium of reactions 4.7 to 4.10 to the left, thereby suppressing the formation of Ti(H<sub>2</sub>O)<sub>2</sub>(OH)<sub>4</sub> which according to reaction 4.5 is critical for the formation of BT. The proposed rate-determining step (RDS) therefore relates not to nucleation or diffusion but to hydrolysis of the Ti precursor at the surface of the titanate NTs. This RDS corresponds directly to the phase boundary mechanism

indicated by the exponent,  $m \approx 1$  obtained from fitting the kinetic data, Figure 4.14a and b. Figure 4.24 schematically illustrates the proposed RDS.

Walton *et al.*<sup>259</sup> also reported a phase boundary mechanism ( $m \approx 1$ ) for the crystallization of BT. The main similarity between the results presented here and the study by Walton *et al.*<sup>259</sup> is that each was performed under static conditions. Therefore, a dissolution of the Ti precursor would locally decrease pH in a similar manner to that postulated and reaction rate will be controlled by the formation of  $\text{Ti}(\text{H}_2\text{O})_2(\text{OH})_4$  at the solid liquid interface. Under non-static conditions, percolation of the aqueous solution eradicates the local decrease of pH at the precursor surface and much higher exponents are observed ( $m > 2.5$ ) corresponding to nucleation as the RDS.

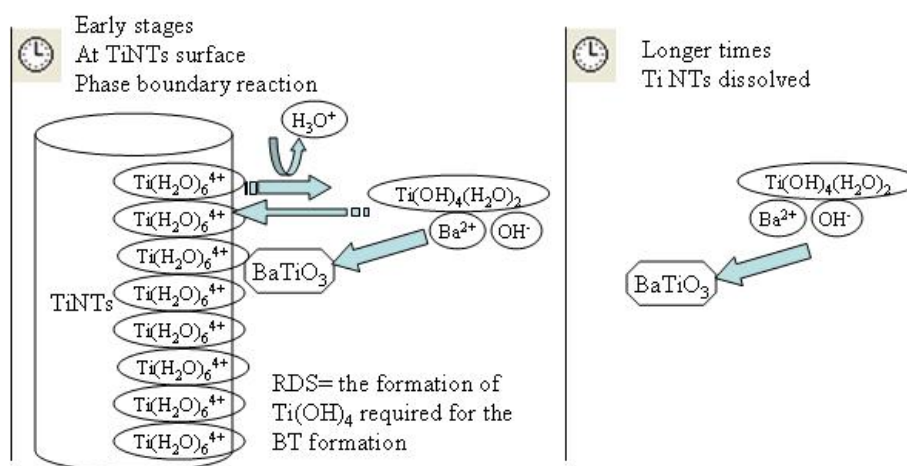


**Figure 4.24 Schematic representation of the proposed mechanism for the synthesis of BT under static hydrothermal conditions starting from layered titanate NTs precursors.**

However, only in the present study the dendritic particles are observed at early stages of the reaction<sup>170,266</sup>. The apparent difference between the experimental conditions described by Walton *et al.*<sup>259</sup> and in the present study is in the titanium precursor which may be an indication that titanate NTs play a crucial role in the formation of anisotropic BT at the early stages of the reaction. This effect may simply relate to the 1D geometry of the NTs and to multiple nucleation events on their surface.

As the reaction progresses, the nanotubes fully dissolve ( $f > 0.7$ ) and the aqueous solution becomes enriched in hydrated Ti ions. There are no longer any local conditions inhibiting the formation of  $\text{Ti}(\text{H}_2\text{O})_2(\text{OH})_4$  and the homogeneous precipitation of BT is observed.

In the early stages, BT nucleated on the surface of the NTs is pseudocubic, implying that defects are incorporated within the perovskite lattice. In contrast, BT nucleated in the latter stages of the reaction is tetragonal, implying a lower concentration of impurity ions or defects. Moreover, the BT formed on the surface NTs has a wild-type dendritic morphology with a rough surface with evidence of nanoscale planar defects in high resolution TEM micrographs. The particles of homogeneously nucleated BT observed in the latter stages of the reaction have a smooth surface and no evidence of planar defects within its microstructure. The change in structure, microstructure and morphology of the BT is entirely consistent with change in kinetics and reaction mechanism at  $f \cong 0.7$ .

As stated in Chapter 1 device size reduction is requiring the study of size-property relations in ferroelectrics. Besides, morphology of nanoscale ferroelectrics is becoming an essential aspect and 3-D geometries of nanoferroelectrics are currently being exploited for High-Density-Memories<sup>267</sup>. First studies showed that spontaneous polarization of BT (BT) decreases with grain size decrease<sup>155</sup>. The concept of critical size below which spontaneous polarization of ferroelectrics would vanish was introduced. However, discrepancies reported for the critical size clearly indicate that besides so-called intrinsic effects (depolarization fields, absence of long-range dipole-dipole interactions or elastic constrains<sup>52</sup>),-extrinsic effects (point defects and dislocations<sup>268</sup> or grain-boundaries<sup>50</sup>) play definitely a role on the ferroelectricity at nanoscale, if not the dominant one. Hence, a dependence of dimensionality on materials processing is expected. Indeed, critical size for BT varies markedly [120-8nm] with the synthesis method<sup>61,155</sup>. Further studies and understanding is required. Moreover, the effect of the morphology of nanoferroelectrics is still to be explained. In addition, to ours best knowledge the nanoscale ferroelectric properties of the dendritic BT particles have never been reported.

In this work the dependence of the domain configuration and piezoresponse on the dendritic morphology was evaluated. It was observed in the piezoelectric domain images a predominately dark contrast for both morphologies (Figure 4.19 and 4.20). The asymmetry of the contrast distribution is a manifestation of the so-called self-polarization effect, *i.e.*, the average piezoresponse of negatively polarized domains is different from that of positive ones. Self-polarization occurs due to the presence of internal electric fields which are at least as large as the coercive field at the Curie temperature<sup>269</sup>. This phenomenon may be related *e.g.* to a charge accumulated on an interface between the particles and the non-ferroelectric matrix, where they are embedded. One can suggest that self-polarization and charge accumulation depend on crystallographic orientation of particles. Therefore effect for wild and seaweed particles are expected to be different.

The hysteresis loops measured on individual wild and seaweed particles have different shapes (Figure 4.21a and b). This suggests that domain nucleation and growth mechanisms are different in wild type and seaweed particles resulting indeed in a different ferroelectric response. Once the local threshold field has been reached, nucleation and growth of an opposite domain takes place in the whole probed volume within some nanoseconds, giving rise to square shaped hysteresis loop<sup>199</sup> as in the case of wild type dendrites.

The polarization switching through various metastable states of wild type particles is an experimental evidence of a low local coherency of the tetragonal type distortions<sup>74</sup> in good agreement with their average pseudo cubic type structure. The stabilization of BT cubic structure at room temperature is commonly reported for particles prepared by hydrothermal method<sup>85</sup>. The retention of OH<sup>-</sup> ions in the BT lattice results in the formation of lattice defects (oxygen vacancies) creating lattice strains responsible for the stabilization of the cubic structure at room temperature<sup>85</sup>. The FTIR spectra (Figure 4.23) and the higher total thermogravimetric weight loss of 6.25% of wild type dendrites compared to 1.93% for the seaweed type supports the high concentration of OH<sup>-</sup> ions in the first case.

### 4.3 Vapor phase synthesis of BT using TiNTs precursors

The results and discussion presented above show that the template role of TiNTs in hydrothermal synthesis is limited due to their dissolution compromising the template role of the NTs. Considering that the chemical reactions in vapour phase are faster the potential role of TiNTs as template for the synthesis of BT in the presence of barium rich vapor is worthwhile to be studied. Under such conditions may be drastic morphological changes of the TiNTs will be avoided.

#### 4.3.1 Materials preparation

The schematic representation of all experimental steps is presented in Figure 4.25. Table 4.2 summarizes the samples prepared and the correspondent preparation conditions under this study.

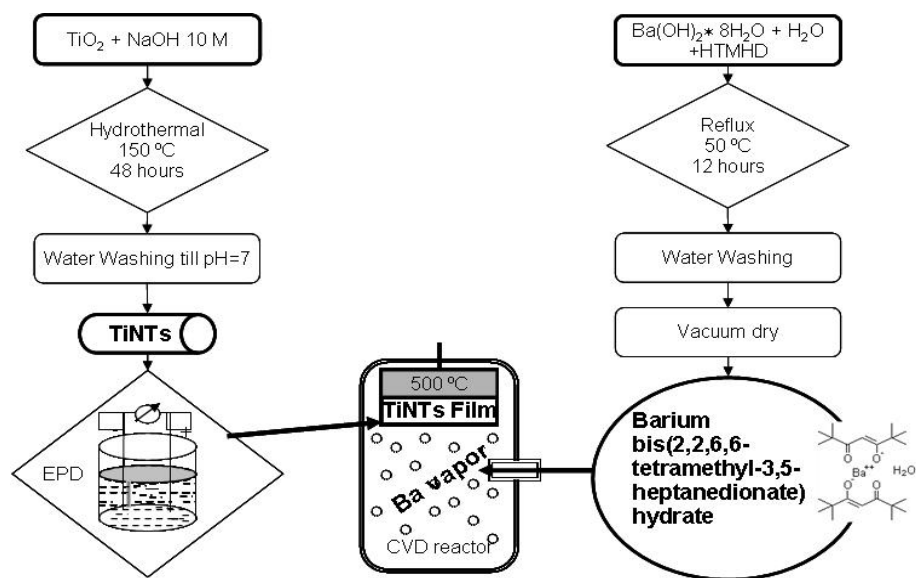


Figure 4.25 Schematic representation of the MoCVD experimental procedure used.

Titanate nanotubes were prepared as describe in Chapter 3 section 3.1 and were indexed as TiNTs. For the vapor phase reaction TiNTs films were prepared. TiNTs were deposited by electrophoretic deposition (EPD) on a Pt/Si/TiO<sub>2</sub>/Pt substrate following the method proposed by Kim *et al.*<sup>243</sup>. Firstly the TiNTs were dispersed in a mixture of methanol and distilled water (proportion 30/70 v/v). The suspension was sonicated for 4 h before the electrodeposition. Substrates were used as an anode, while Pt foils were used as a counter cathode electrode. The electrodeposition was carried out at an optimized voltage between 40 and 100 V at room temperature. The obtained films were dried at room temperature and annealed at 300 °C for 60 min. The TiNTs films were indexed as TiNTsEPD.

The barium 2,2,6,6-tetramethyl-3,5-heptanedionate was prepared following the patented procedure<sup>270</sup>. Briefly, 1.3 g (0.004 mol) of Ba(OH)<sub>2</sub>•8H<sub>2</sub>O (Merck, 98% purity) dissolved in water were added drop by drop to 1.7 ml of 2,2,6,6-tetramethyl-3,5- heptadione (HTMHD). The mixture was refluxed at 50 °C overnight. The obtained powder was filtered and washed with water. The powder drying took palce in a oven at 60 °C overnight and in vacuum line at 70 °C for four hours.

The chemical vapor deposition of the metal-organic compound of barium on the TiNTs films was performed using the Pulsed Injection Metal-Organic Chemical Vapor Deposition technique (MoCVD). This procedure was conducted at the Departamento de Física da Faculdade de Ciências da Universidade de Lisboa, Centro de Física da Matéria Condensada (CFMC/FC/UL), Portugal in collaboration with Dr. Rui Borges and Prof. Margarida Godinho. In this technique a solution containing the barium precursor is kept at room temperature in a pressurized container in order to avoid the thermal decomposition of the precursors. An electrically driven valve allows the controlled injection of small droplets of the solution into the reactor. The size of the droplets can be controlled by changing the pressure in the container and the opening times of the valve. Injected droplets are flash vaporized forming a stable gas-phase composition that is carried by a stream of Ar and O<sub>2</sub> towards a heated substrate where the deposition takes place.

All depositions were carried out under a pressure of 667 Pa with oxygen partial pressure of 267 Pa. Ar was used as a carrier gas with a flow rate of 900

ml/min and the flow rate of O<sub>2</sub> was 600 ml/min. The total amount of Ba injected into the reactor was controlled by the number of droplets and the solution injector valve was operated with an opening frequency of 2 Hz and an opening time of 2 ms. Three barium concentrations have been investigated in this study by introducing 140, 700 and 1400 droplets into the reactor. The temperature of the evaporator was 280 °C and the substrate temperature was 500 °C. After each deposition the films were slowly cooled down to room temperature under 1 bar of O<sub>2</sub>.

**Table 4.3 Samples and preparation conditions for MoCVD study.**

Sample Index	CVD conditions	Annealing Temperature
TiNTsEPD	----	---
TiNTsCVD	500 °C; without Ba	---
700-TiNTsCVD	500 °C; without Ba	700 °C
750-TiNTsCVD	500 °C; without Ba	750 °C
800-TiNTsCVD	500 °C; without Ba	800 °C
850-TiNTsCVD	500 °C; without Ba	850 °C
Ba-TiNTsCVD	500 °C; with Ba	---
BT700	500 °C; with Ba	700 °C
BT750	500 °C; with Ba	750 °C
BT800	500 °C; with Ba	800 °C
BT850	500 °C; with Ba	850 °C
BT[Ba] <sub>low</sub> 700	500 °C; with low Ba concentration	700 °C
BT[Ba] <sub>medium</sub> 700	500 °C; with medium Ba concentration	700 °C
BT[Ba] <sub>high</sub> 700	500 °C; with high Ba concentration	700 °C

The stability of the TiNTs was evaluated by conducting the same experimental procedure as presented above without introducing the barium

precursor into the reactor. The samples obtained in this step were indexed as TiNTsCVD.

After the CVD procedure some films were thermal treated under O<sub>2</sub> atmosphere at 700, 750, 800, and 850 °C, respectively. The sample obtained after the CVD step without barium and thermal treated at 850 °C is indexed as 850-TiNTsCVD and the sample treated at the same temperature but with barium is indexed as BT850.

The samples were characterized by XRD, SEM, TEM and PFM as described in Chapter 2.

### 4.3.2 Results

#### 4.3.2.1 Structural and morphological evolution of TiNTs

Figure 4.26a presents the morphology of the titanate nanotubes prepared by hydrothermal treatment of anatase in the presence of NaOH, as previously described in Chapter 3, analysed by SEM and TEM. The tubular morphology of the TiNTs is maintained after deposition by EPD (Figures 4.26a and 4.26b) although arranged in big agglomerates, as a consequence of the deposition process (inset of Figure 4.26b).

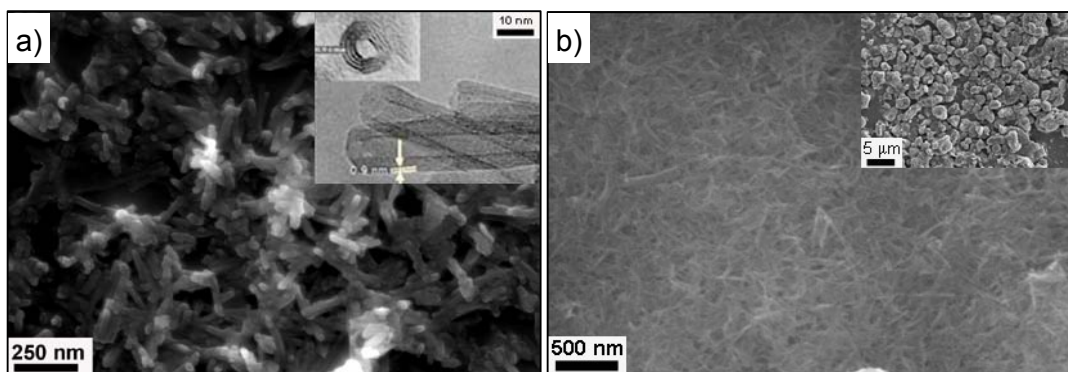
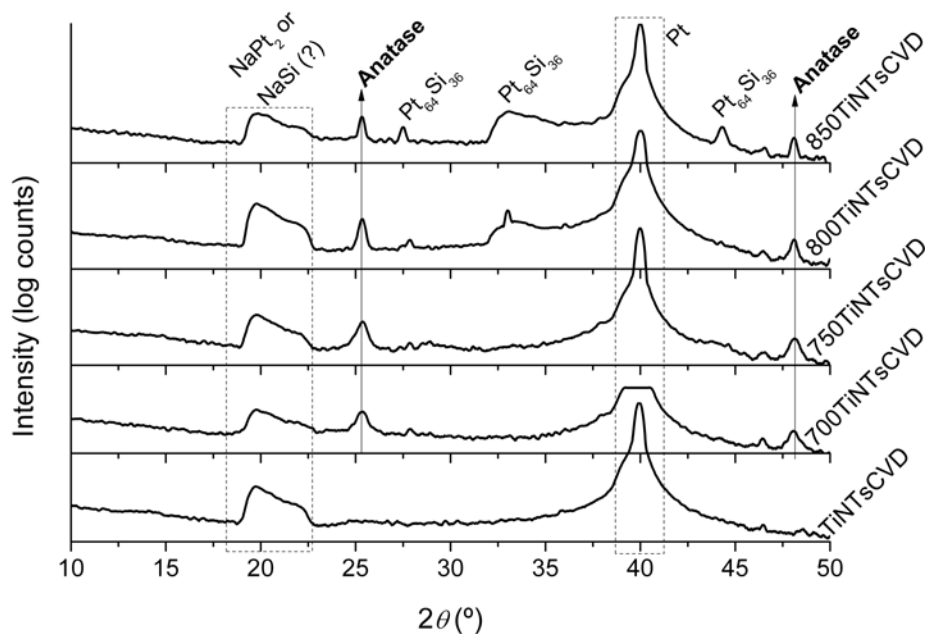


**Figure 4.26** Microstructures of TiNTs *a*) as prepared by hydrothermal treatment and *b*) as deposited by EPD (TiNTsEPD) representing the tubular morphology of TiNTs films after EPD.

Figure 4.27 presents the structural evolution determined by XRD of the TiNTs films after the CVD procedure without barium and subsequently annealed at

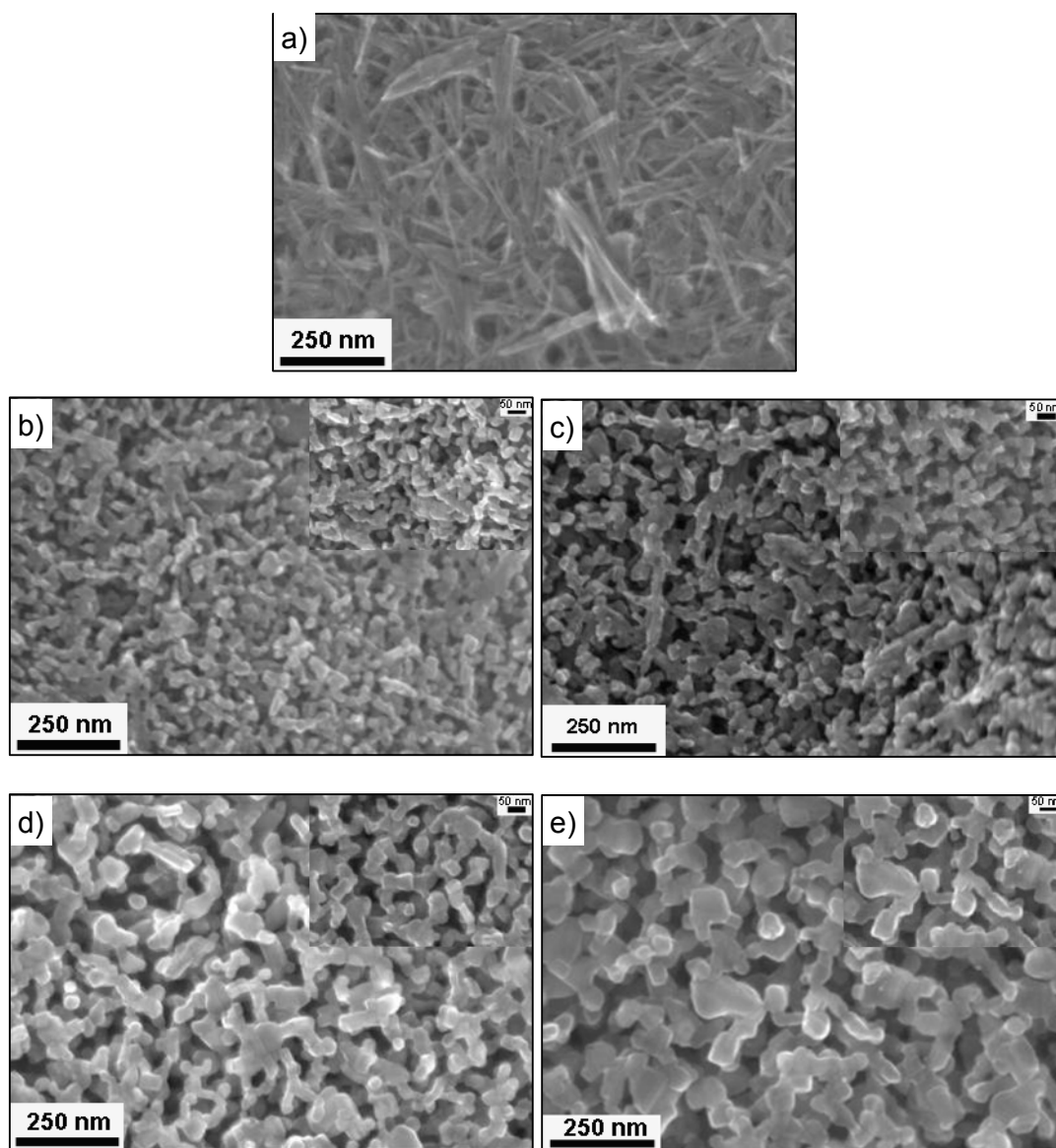
700, 750, 800 and 850 °C. Before the thermal treatment only the peaks corresponding to the film substrate are observed. It is better to recall here that the TiNTs have a pseudo-crystalline phase (see Chapter 3 for more details) and because of this the peaks corresponding to the layered titanate NTs are not visible here. Regarding the films obtained after thermal treatment the principal remark is the formation of TiO<sub>2</sub> anatase (JCPDS no. 21-1272) after annealing at temperatures higher than 700 °C, as also reported by others after thermal treatment of layered titanate nanotubes<sup>232,247,248</sup>.

Figure 4.28 presents the morphological evolution of the TiNTs after the CVD procedure in absence of barium and subsequently thermal treatment at 700, 750, 800 and 850 °C as imaged by SEM. Comparing Figure 4.26b and 4.28a no evident morphological transformation of the nanotubes can be observed right after the CVD process. However, after the thermal treatment at 700 °C formation of nanorods (NRs) with rough surface can be noticed (Figure 4.28b). At higher magnification it can be noticed that the NRs are formed in fact by the oriented aggregation of small crystals (see inset of Figure 4.28b).



**Figure 4.27** X-Ray patterns of the TiNTs films after the CVD procedure and subsequently annealed at 700, 750, 800 and 850 °C. The formation of anatase is observed when the annealing temperature is higher than 700 °C.

The same features of the morphological transformation from NTs to NRs can be noticed when increasing the annealing temperature to more than 750 °C (Figures 4.28c, d and e). The oriented aggregation of small crystals is observed for all the studied temperatures as indicated in the insets of Figures 4.28c, d and e.

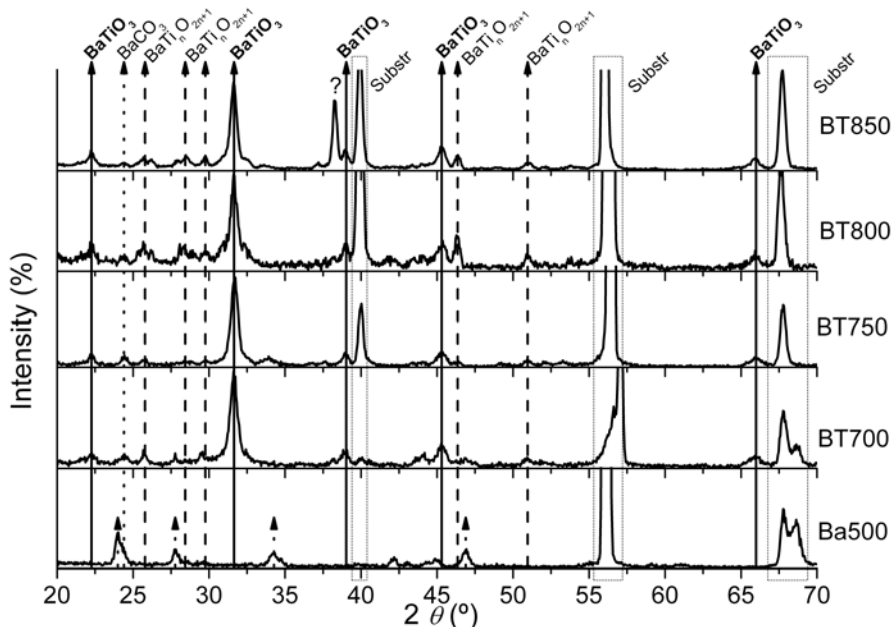


**Figure 4.28** SEM micrographs of TiNTs films after the CVD procedure (a) and subsequently annealed at 700 (b), 750 (c), 800 (d) and 850 °C (e). The formation of anatase NRs by oriented attachment mechanism is noticed.

## 4.3.2.2 MoCVD synthesis

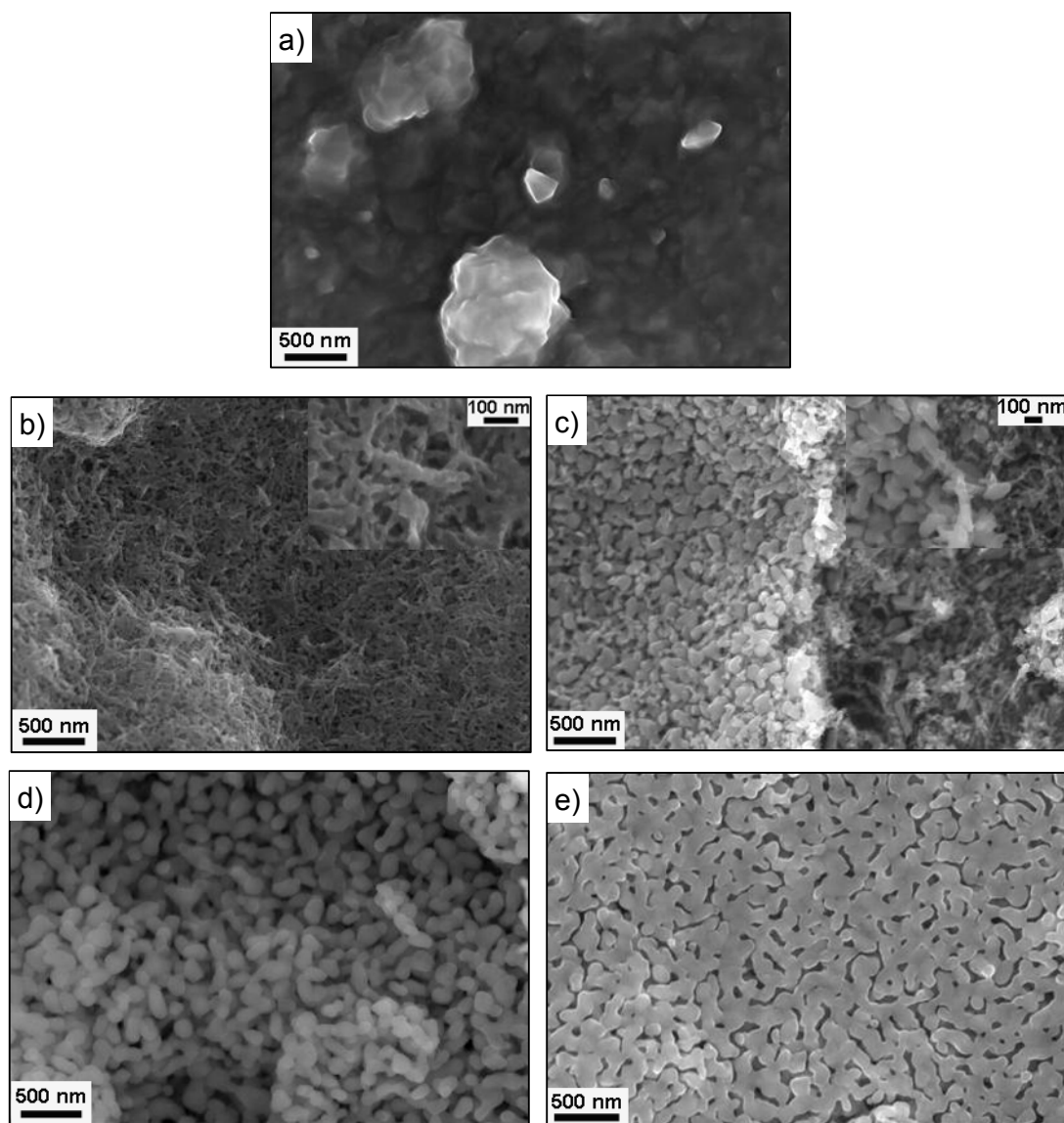
The influence of thermal treatment temperature

Figure 4.29 presents the X-Ray patterns of the films obtained after the MoCVD deposition of barium precursor on the TiNTs films and subsequently annealed at 700, 750, 800 and 850 °C. The patterns of the samples obtained right after MoCVD of barium precursor present mainly peaks of BaCO<sub>3</sub>, which is the common secondary product in the synthesis of barium titanate. After annealing at 700 °C, a pronounced peak at  $2\theta \sim 31^\circ$  appears suggesting the formation of BT (JPCDS no 31-0174) as major phase. It is also observed the formation of intermediary phases of barium and titanium with general formula BaTi<sub>n</sub>O<sub>2n+1</sub> as orthorhombic BaTi<sub>2</sub>O<sub>5</sub> or BaTi<sub>4</sub>O<sub>9</sub>. The coexistence of these phases of barium and titanium is also noticed at higher annealing temperatures (750, 800 and 850 °C). However, it is better to remark here, that the pattern identification is rather difficult due to the formation of various phases of barium and titanium commonly reported in the synthesis of barium titanate by solid state reaction<sup>156,271,272</sup>



**Figure 4.29** X-Ray patterns of the samples obtained after MoCVD deposition of barium precursor and subsequently annealing at 700, 750, 800 and 850 °C. The formation of BT is observed after annealing at temperatures higher than 700 °C.

Figure 4.30 presents the SEM morphological evolution of the films obtained after MoCVD of barium precursor and subsequently annealed at 700, 750, 800 and 850 °C. For the samples obtained right after the MoCVD procedure (Figure 4.30a) faceted particles of amorphouse phases are formed.



**Figure 4.30 SEM micrographs of the films obtained after MoCVD deposition of barium precursor, Ba500 (a) and subsequently annealing at 700, BT700 (b), 750 BT750 (c), 800 BT800 (d) and 850 °C BT850 (e). The formation of rough and smooth surface NRs is observed.**

When the samples are thermal treated at 700 °C the formation of 1D nanoparticles with rough surface is noticed (Figure 4.30b) and at higher magnification one can observe that small crystals are nucleated at their surface (see inset Figure 4.30b). The formation of smooth surface NRs is seen when increasing the annealing temperature at 750 °C (Figure 4.30c), moreover it was observed at this temperature that these NRs seem to be the result of the surface nanocrystals segregation as is indicated in the inset of Figure 4.30c. Similar NRs morphologies are also visible at temperatures as high as 800 °C (Figure 4.30d). After the thermal treatment at 850 °C the obtained sample seems to be densified (Figure 4.30e).

#### The influence of barium and titanium concentrations

Figure 4.31 presents the SEM micrographs of the samples obtained after MoCVD with various concentrations of barium followed by annealing at 700 °C, a) BT[Ba]<sub>low</sub>700, b) BT[Ba]<sub>medium</sub>700, c) BT[Ba]<sub>high</sub>700.

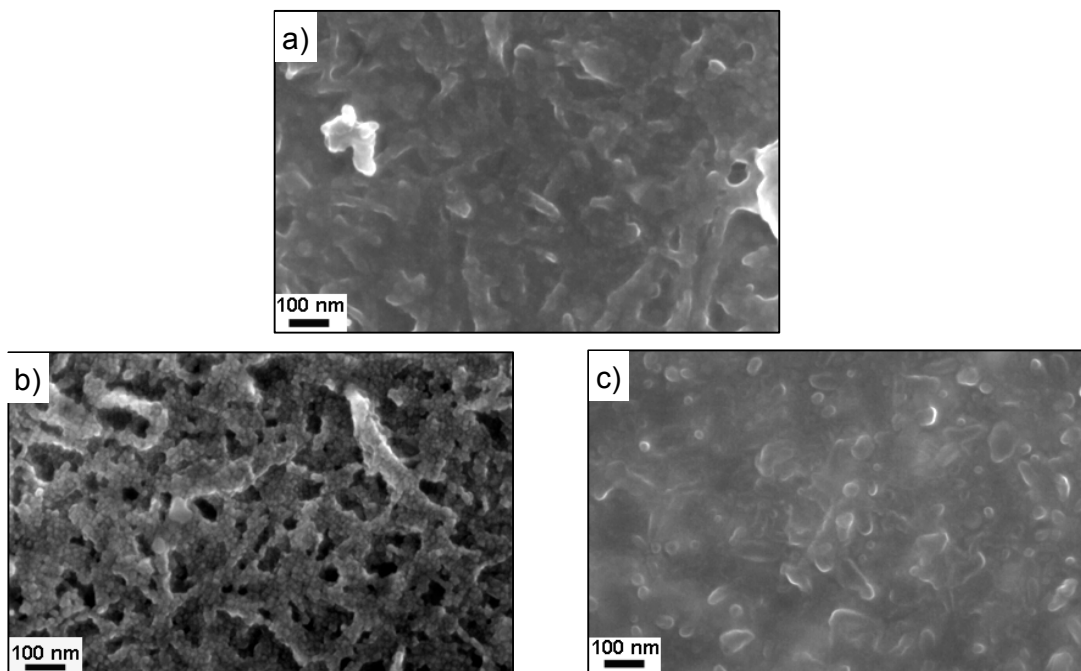


**Figure 4.31 SEM micrographs of the samples obtained after MoCVD with various concentrations of barium followed by annealing at 700 °C, a) BT[Ba]<sub>low</sub>700, b) BT[Ba]<sub>medium</sub>700, c) BT[Ba]<sub>high</sub>700. Small crystals are formed on nanorods surface independently on [Ba].**

Similar morphologies with the ones observed in Figure 4.30b were noticed for all the studied concentrations. Thus, it can be said that 1D nanoparticles with small nanocrystals nucleated on their surface are formed independently on the barium concentration (Figure 4.31a-c).

Figure 4.32 presents the SEM analysis of the samples obtained after chemical vapor deposition of barium precursor and thermal treated at 750 °C afterwards (BT750). Various morphologies are formed as a function of film thickness (Figure 4.32a). The variation of the film thickness is in fact the variation of Ti quantity available for the vapor reaction with Ba ions. As can be observed close to the substrate (marked with 1 in Figure 4.32a) where less Ti is available for the reaction, nanorods with rough surface are formed as presented in Figure 4.32b similar to the ones obtained at 700 °C (compare the insets of Figure 4.30b and Figure 4.32b). When increasing the film thickness (zones marked with 2 and 3 in Figure 4.32a), i.e. the titanium concentration is higher, big anisotropic particles with smooth surface like NRs (Figure 4.32c) or plate-like shape (Figure 4.32d) are formed. Comparing the EDX collected in zones 1 and 2, respectively (down insets of Figure 4.32b and c) Ba/Ti ratio decreases as the film thickness increases indicating that the anisotropic particles formed in zones 2 or 3 are barium deficient.

Various morphologies were also observed by TEM analysis of the same samples obtained after MoCVD procedure with barium and subsequently annealed at 750 °C as indicated in Figure 4.33a. The presence of small nanoparticles with round shapes (up inset of Figure 4.33a) and the coexistence with nanorods and plate-like particles (down inset of Figure 4.33a) was confirmed. The electron energy loss spectra (EELS) collected in two different regions, NPs and NRs, are presented in Figure 4.33b. The spectra are similar and contain two peaks for Ti-L energy level, and two well defined Ba-M peaks. Only the O-K edge is slightly different when comparing the spectra collected from the NPs zone to the NRs one. The NPs spectra present the characteristic shape peaks of BT<sup>273</sup> and the different shape of O-K edge comparing to the NRs suggests that the oxygen coordination into the crystalline lattice is different from the nanoparticles to the nanorods and consequently the structure of the NPs is different from the one of the NRs.

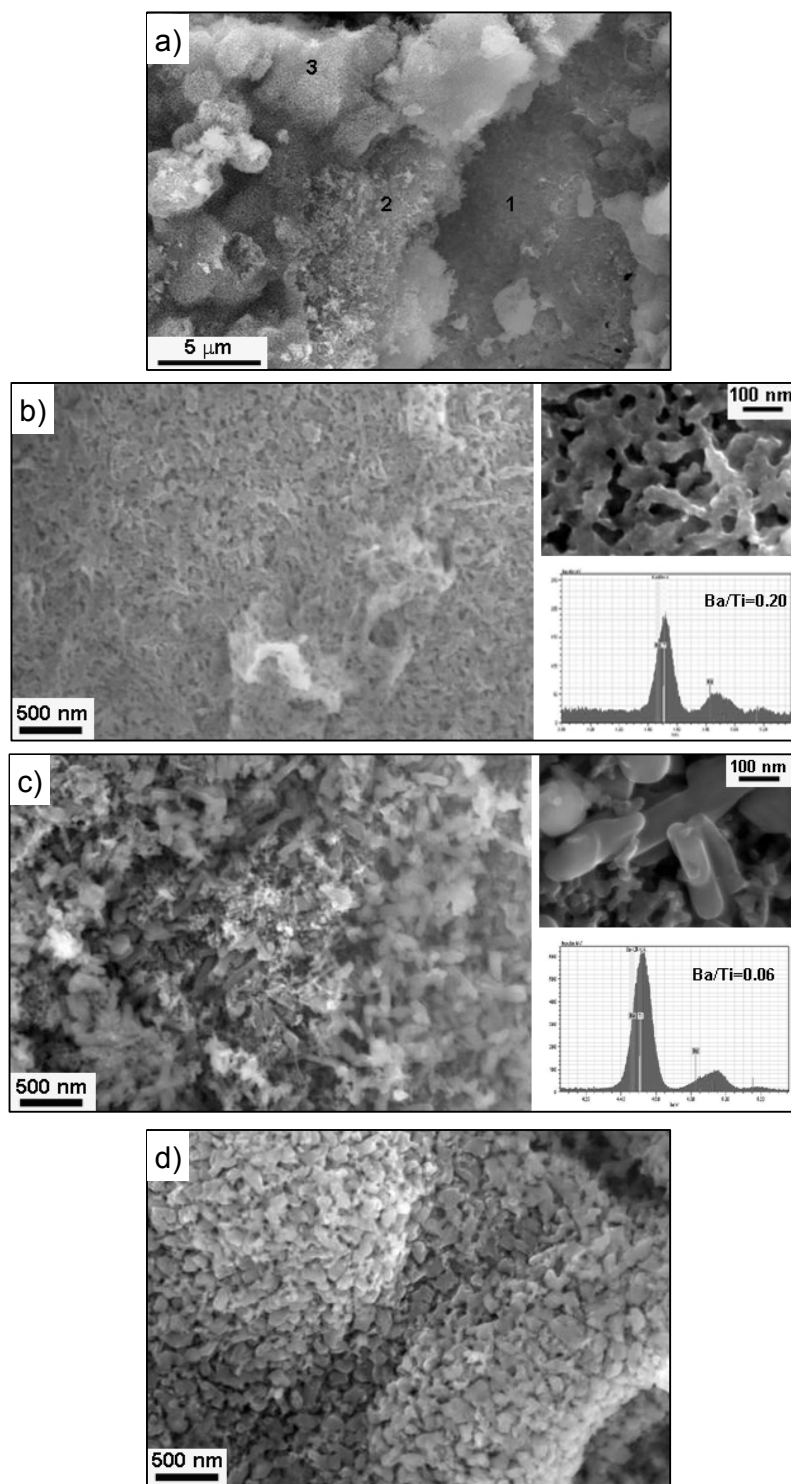


**Figure 4.32 SEM analysis of the sample obtained after MoCVD with barium and thermal treatment at 750 °C, BT750; a) the general view presenting three zones, b) the magnification and EDX analysis of zone 1, c) the magnification and EDX analysis of zone 2 and d) the magnification of zone 3. Small crystals formed at NRs surface in zone 1 are segregated and NRs are obtained.**

The structure of the NPs and the NRs was investigated by HRTEM and is presented in Figures 4.34. By Fast Fourier Transformation (FFT) analysis of the HRTEM image (Figure 4.34a) it was observed that NPs show lattice spacing which fits within an error of less than 5% to the (100) spacing of cubic barium titanate, and the zone axis (viewing direction) corresponds to the  $\langle 012 \rangle$  direction. The same FFT analysis has been performed for the NRs and plate like particles (Figure 4.34b). Although in some cases the distances between NRs fringes correspond to  $\langle 132 \rangle$  zone axis of orthorhombic  $\text{BaTi}_2\text{O}_5$ , the pattern and the spots distribution do not really match to this structure. More studies are need for the identification of the NRs structure.

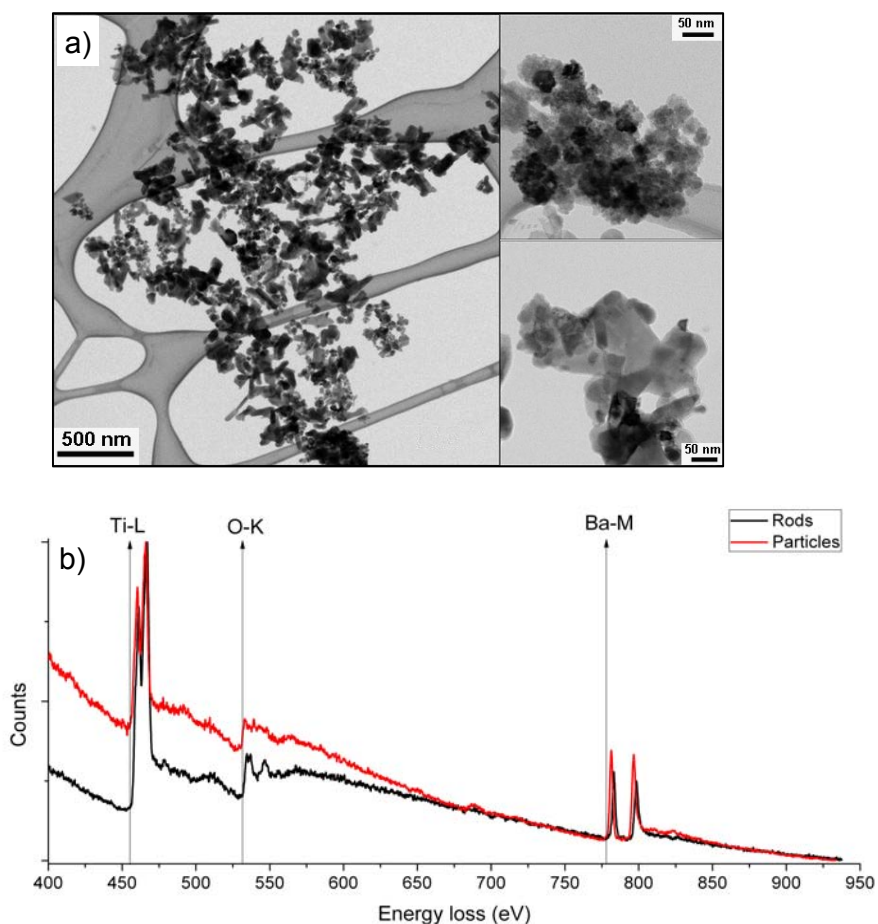


**Figure 4.33** TEM analysis of the sample obtained at 750 °C a) image and b) EELS, highlighting the different structure between the round shape particles, NRs and plate like particles.

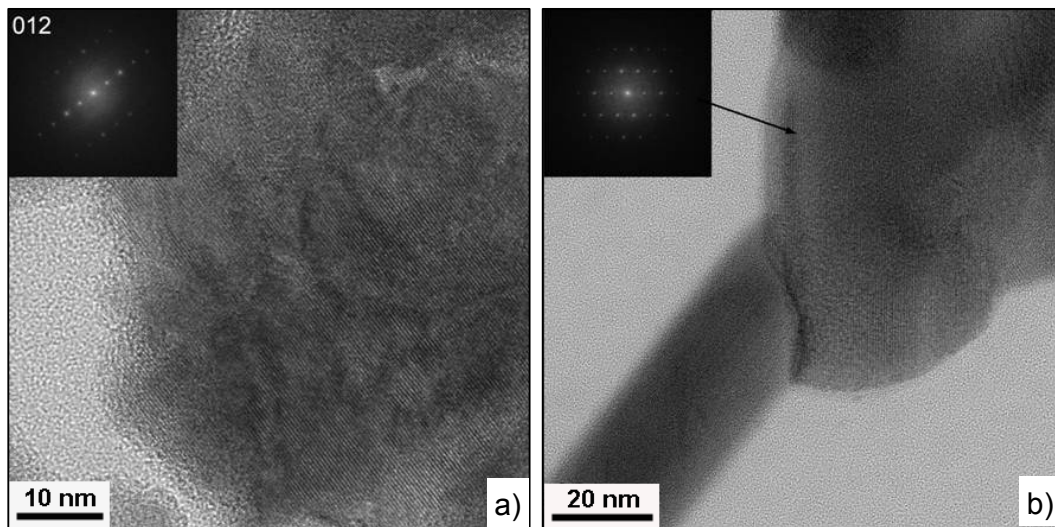


**Figure 4.34** HRTEM analysis of the sample obtained at 750 °C- BT750; (a) particles and (b) rod and plate like particles; in the insets the Fast Fourier Transformation (FFT) analysis. The round shaped particles have BT structure.

### 4.3.3 Discussion – MoCVD synthesis using TiNTs

The results presented above lead to four key points that need to be considered:

1. The TiNTs are stable at temperatures as high as 500 °C but the thermal treatment at higher temperature results in morphological transformation from NTs to NRs;
2. The structure of the NRs obtained just by CVD in the absence of barium precursor can be assigned to anatase phase;
3. The round shaped nanoparticles of BT are nucleated at the surface of the TiNTs independently on the barium concentration;
4. The increase of the temperature of the thermal treatment led to the segregation of BT round shape nanocrystals and to the formation of NRs of non-stoichiometric barium titanate.

As shown in Chapter 3 the structure of the TiNTs precursors is attributed to dititanate structures with general formula  $A_2Ti_2O_5$  (where  $A = Na^+$  or  $H_3O^+$ ). Moreover, the transformation from TiNTs to anatase NRs has been observed

when the nanotubes were hydrothermal treated at temperatures higher than 150 °C (see sections 3.4.2 and 3.6.3). The NTs to NRs conversion has been already reported in the literature<sup>232,247,248</sup> and it is consensually accepted that the process is taking place in three steps. First the TiNTs dehydrate with acid or heat resulting into a defective structure created by the approaching of the layered structure sheets. Second, at the defective regions nanocrystals of anatase are nucleated because the zigzag pattern formed by the TiO<sub>6</sub> octahedra in the TiNTs along the [010] direction is similar to the zigzag pattern formed by the TiO<sub>6</sub> octahedra in the anatase along the [100].<sup>245</sup> Finally, the formation of the polycrystalline anatase NRs is the result of an oriented attachment process when two adjacent anatase particles come into the same crystallographic orientation, with high-energy faces, fuse and eliminate these faces and the result is a particle with directed orientation

232,246-249

In the present study TiNTs are stable at 500 °C (the temperature of the CVD reactor- Figures 4.28a) and transform to anatase NRs after thermal treatment at temperatures higher than 700 °C (Figures 4.28b-e), confirming the previous observations. Moreover, corroborated by XRD and SEM analyses (Figures 4.27 and 4.28b-e) it is suggested that under the present conditions anatase NRs are formed by an oriented attachment mechanism after the thermal treatment of the TiNTs at temperatures higher than 700 °C.

When the barium precursor is added to the process a thin layer of barium is deposited on the TiNTs (Figure 4.30a). After annealing at 700 °C BT nanocrystals are nucleated on the TiNTs surface independently on the barium concentration (Figures 4.30b and 4.31a-c). During the MoCVD procedure barium vapors adsorb on the TiNTs surface. As described above when the TiNTs are annealed at temperatures higher than 700 °C they undergo a dehydration process and a defective structure is formed due to the nanotube layered structure collapsing.<sup>245</sup> At these defective sites BT is most likely to nucleate.

Increasing the thermal treatment temperature and the titanium concentration the round shape particles of BT seem to segregate from the NTs surface and NRs and plate like particles of barium deficient phases are formed (Figures 4.30c-e and 4.32). Why BT crystals do not follow the oriented

attachement growth as anatase nanoparticles do, is still an issue to be clarified. This can be related to the crystallographic differences between anatase and perovskite structures. Moreover, the crystal habit dictates that under equilibrium conditions crystal growth with isotropic morphology will take place for  $ABO_3$  perovskite crystals and round or cubic shaped particles will be easily grown.<sup>128</sup> In addition, barium is more volatile than titanium having the heat of vaporization equal of  $140.3 \text{ kJ mol}^{-1}$  compared to  $425 \text{ kJ mol}^{-1}$  of titanium.<sup>274</sup> This means that when increasing the annealing temperature it is probable that the BT growing sites to be scarce in barium.

Another issue to be clarified is the formation of NRs and platelike particles of barium deficient phases at high temperature and titanium concentration. It is known that the diffusion rate increases as the temperature increases and thus barium ions can go deeply into the TiNTs film. Moreover, as stated above, the TiNTs undergo dehydration when increasing the annealing temperature and structural defects are formed. Therefore it can be said that when increasing the titanium concentration in fact the defects concentration increases. Summarizing, when increasing the temperature and titanium concentration the diffusion rate and the defect concentration are high. In these conditions it is likely that barium ions transport through the film to be accelerated. However, the Ba/Ti ratio in the inner parts of the TiNTs films is not adequate for the formation of BT (Figure 4.32), being a titanium rich region, therefore NRs and plate like particles of barium deficient titanates are formed.

#### 4.4 Summing up

The template role of the layered titanate nanotubes of general formula  $\text{Na}_{2-x}\text{H}_x\text{Ti}_2\text{O}_5 \cdot 1.8\text{H}_2\text{O}$  (TiNTs) on the preparation of anisotropic BT nanoparticles has been investigated by two chemical template approaches.

The present work demonstrates that, for the formation of BT by chemical template hydrothermal synthesis starting from layered titanate nanotubes two mechanisms take place depending on the temperature and time. At the early stages of crystallization (low temperature and short time), the reaction taking place at the solid-liquid interface was considered to be the rate-determining step. The

reaction is controlled by concentration of  $\text{Ti}(\text{H}_2\text{O})_2\text{OH}_4$  which is limited in the vicinity of the NTs by a local decrease of pH. As the reaction proceeds, the NTs fully dissolve ( $f > 0.7$ ), the bulk of the solution becomes enriched in hydrated Ti ions, and homogeneous nucleation of BT occurs.

The BT formed when the kinetics are controlled by reaction at the phase boundary is pseudocubic with a rough surface morphology and a microstructure containing planar defects. In contrast, in the later stages of the reaction, the BT is tetragonal with a smooth surface and a microstructure free from planar defects.

Dendrites are formed throughout the reaction but the morphology differs depending on  $f$ . In the early stages ( $f < 0.7$ ), dendrites are 'wild-type' but in the later stages 'seaweed-type' are observed. The changes in structure and microstructure are consistent with a change in the kinetics at  $f \sim 0.7$ .

The different ferroelectric properties observed in the wild and seaweed BT dendritic particles can be explained by the different crystallographic nature and concentration of defects and not so related with the size of the particles. The cubic structure of BT wild type dendritic particles with the size in the micrometric range is stabilized due to the strains created by the lattice defects. The present study is the clear evidence that the instability of the ferroelectricity is due to extrinsic effects such as point defects and not an intrinsic effect of the size.

The hydrothermal study here conducted clearly shows that TiNTs can not easily act as directing growth agents or as template for hydrothermal synthesis of 1D BT. Although at low temperature and low time topotactic reactions on the NTs surface takes place, their instability in the high alkaline solution results in a dissolution rate faster than that of BT nucleation.

Therefore the second approach implied the reaction in vapor phase of a metal-organic barium precursor with TiNTs, assuming that the reaction is faster than the structural and morphological transformation of nanotube precursors. The original BT synthesis method was based on the chemical vapor deposition of barium 2,2,6,6-tetramethyl-3,5-heptanedionate metal-organic compound (MoCVD) on TiNTs film obtained by EPD. In the first set of experiments the stability of the TiNTs in MoCVD conditions without barium and after subsequently thermal treatments at 700, 750, 800 and 850 °C in  $\text{O}_2$  atmosphere was evaluated. TiNTs

are stable under the MoCVD conditions but when thermal treated at temperatures higher than 700 °C transform into TiO<sub>2</sub> anatase nanorods (NRs) by an oriented attachment mechanism. Further structural and morphological studies demonstrated that after barium precursor deposition on TiNTs and followed by annealing at 700 °C in O<sub>2</sub> atmosphere round shaped BT nanocrystals are formed at the TiNTs surface independently on barium concentration. We believe that the mechanism of nucleation is based on a topotactic reaction similar to the one observed at low temperatures and low reaction times in the hydrothermal conditions. When the annealing temperature and titanium concentration increase the barium titanate nanoparticles seem to segregate and NRs of barium deficient phases are formed.

A lesson to be learned from the present work is that although the synthesis of 1D nanostructures of complex oxide by chemical methods is not a trivial mission the TiNTs influenced the growth of the BT and anisotropic particles can be obtained at low temperatures.

## 5 Non Template Additive- Assisted Methods

### *Summary*

In this chapter the results and discussion of the effect of poly(acrylic acid) (PAA), poly(vinylpyrrolidone) (PVP), sodium dodecylsulfate (SDS), hydroxypropylmethylcellulose (HPMC) and D-fructose additives on the growth of BT particles by aqueous synthesis is presented. It is demonstrated that, though via different mechanisms, all the tested additives influence the growth of BT. It is shown that for high concentrations, PAA is adsorbed on specific crystallographic faces, changing the growth kinetics and inducing the oriented attachment of the particles, acting as a crystal growth modifier. PVP, SDS and HPMC behave as growth inhibitors rather than crystal habit modifiers and barium titanate crystals as small as 26 nm are obtained. D-fructose appeared to increase the activation energy for barium titanate nucleation when the additive concentration increases.

### 5.1 Motivation

Although no 1D barium titanate particles were obtained by chemical template method (Chapter 4), it was shown that the morphology of anisotropic dendritic particles depends heavily on the synthesis method. This observation can be related to the fact that the processes involved on the synthesis of one-dimensional perovskite oxide particles using hydrothermal and related methods are far from being trivial. Indeed, the crystal habit dictates that, under equilibrium conditions, crystal growth with isotropic morphology will take place for  $ABO_3$  perovskite crystals and round or cubic shaped particles will be easily grown<sup>128</sup>. However, it is believed that a modification of the crystal growth may occur if the growth on some of the crystal faces can be restricted. This may be achieved by reducing the supply of material to a particular crystal face or the specific surface energy, i.e. in the presence of some additives,<sup>128</sup>.

Good examples of such additives are polymers which can be adsorbed preferentially on specific crystallographic planes, thereby orienting the growth in a

particular direction (the growth direction is determined by the slowest growing crystal face with the lowest surface energy)<sup>128</sup>. For instance, polyacrylic acid and polyethylene-oxide-block-polymethacrylic acid can adsorb specifically on {100}, and {110} crystallographic planes of barium titanate reducing their surface energy<sup>275</sup>. It is thus, expected that the growth direction of BT may be oriented in these directions. Although some morphological changes have been observed by Bagwell *et al.*<sup>275</sup>, no anisotropic growth was reported in this study and the barium titanate particles formed in the presence of the polymeric species were rounder than those formed without any polymeric additives. In contrast, oriented growth of PZT single crystals has been promoted by the specific adsorption of poly(vinyl alcohol) (PVA) and poly(acrylic acid) (PAA) on (001) crystallographic planes<sup>101</sup>, resulting in the formation of PZT NWs. The large surface energy of the exposed (001) plane was reduced by the adsorption of PVA by hydrogen bonding. The energy reduction was further enhanced by the adsorption of PAA through carboxy group chemical bonding<sup>101</sup>.

Using laurylamine as an additive, NRs of BT were prepared by a combined route based on sol-gel and surfactant templated methods at low temperature<sup>102</sup>. Isolated single-crystal, cubic perovskite BT nanorods with diameters ranging from 20 to 80 nm were formed by an oriented attachment mechanism<sup>139</sup>. The surfactant adsorbed on specific crystalline surfaces of the nanoparticles and modified their growth direction. Therefore, the shape and size of particles in the system can be altered by oriented attachment of the primary nanoparticles. Depending on the orientation, further oriented attachment will result in the formation of rod-shaped structures<sup>102</sup>.

However, the effect of additives on the crystal growth of BT particles has not been addressed systematically. In this chapter the results and discussion of the effect of different types of additives assisted the synthesis of BT nanopowders are presented. Poly(acrylic acid) (PAA) and poly(vinyl pyrrolidone) (PVP) are used as polymers, sodium dodecylsulfate (SDS), as anionic surfactant, and (D-) fructose and hydroxypropylmethylcellulose (HPMC), as carbohydrates (saccharides). This study was done within the action COST 539 – ELENA at

EPFL, Switzerland in the collaboration with Dr. Anne Aimable and Prof. Dr. Paul Bowen.

## **5.2 Materials preparation**

Barium hydroxide,  $\text{Ba}(\text{OH})_2 \cdot 8\text{H}_2\text{O}$  (Merck, 98% purity) and titanium n-butoxide,  $\text{Ti}(\text{n-OBu})_4$  (Aldrich, 97% purity) were used as barium and titanium precursors, respectively. Poly(acrylic acid) (PAA, Aldrich,  $M_w = 2000$ ), poly(vinylpyrrolidone), (PVP, Acros Organics,  $M_w = 8000$ ), (D-) fructose (Fru, Acros Organics, 99% purity), hydroxy-propylmethylcellulose (HPMC 100, Sigma) and sodium dodecylsulfate (SDS, Aldrich, p.a.) were used as additives. The barium titanate synthesis was initiated by dissolving 7.45 g (~0.02 moles) of  $\text{Ba}(\text{OH})_2 \cdot 8\text{H}_2\text{O}$  in 50.7 g of ultra-pure distilled water. A supersaturated solution of barium hydroxide was obtained at 90 °C. At this temperature 50 g of the solution was filtered and the desired amount of additives introduced. The concentration of additives was  $0.4 \text{ gdm}^{-3}$  and  $5 \text{ gdm}^{-3}$  for [low] and [high] concentration, respectively. The mixture of barium hydroxide and additives was cooled down to room temperature and 5.7 ml (~0.02 moles) of  $\text{Ti}(\text{n-OBu})_4$  was added under vigorous stirring. A rapid formation of a white precipitate of hydrous titanium oxide in alkaline solution was noticed. The reaction mixture was immersed in a water bath at 96 °C and kept at this temperature for 30 minutes. In the case of high concentration of PAA and HPMC, syntheses at temperatures as low as 60 and 80 °C, respectively were performed in order to better define these additives effect.

The obtained powders are indexed with the abbreviations BTPAA, BTPVP, BTFru, BTHPMC or BTSDS, corresponding to the additive used in each synthesis. The additive concentration was indexed as [low] and [high], respectively. BTblank corresponds to the same synthesis but without any additive (Table 5.1).

The samples were characterized by XRD, Raman, FTIR, SEM and TEM, DLS and TGA.

**Table 5.1 Samples index for non-template additives assisted synthesis of BT**

Additive	Concentration	
	Low = 0.4 gdm <sup>-3</sup>	High = 5 gdm <sup>-3</sup>
0	BTblank	
PAA	BTPAA[low]	BTPAA[high]
PVP	BTPVP[low]	BTPVP[high]
SDS	BTSDS[low]	BTSDS[high]
HPMC	BTHPMC[low]	BTHPMC[high]
D-Fructose	BTFru[low]	BTFru[high]

XRD peak broadening (111) was used to determine the size of the primary crystallites using the Scherrer equation (Eq. 5.1):

$$d_{XRD} = \frac{K \cdot \lambda_x}{\beta_{xp} \cdot \cos(\theta)} \quad 5.1$$

where K is equal to 0.9,  $\lambda_x$  stands for the X-ray wavelength,  $\beta_{xp}$  for the line broadening at half the maximum intensity of the diffraction peak, and  $\theta$  is the Bragg angle. The instrumental broadening was determined using alumina with a large crystal size (> 1  $\mu\text{m}$ ).

The size of the primary particles,  $d_{BET}$  (nm), were calculated by assuming spherical monodisperse particles (Eq. 5.2), with  $\rho$  the density of the material ( $\rho = 6.017 \text{ g.cm}^{-3}$ ).

$$d_{BET} = \frac{6000}{S_{BET} \cdot \rho} \quad 5.2$$

where  $S_{BET}$  ( $\text{m}^2.\text{g}^{-1}$ ) states for specific surface areas estimated from  $\text{N}_2$  adsorption isotherms by BET method (see chapter 2).

The median size  $d_{v50}$  of the distribution is compared to  $d_{BET}$ , to get an estimation of the agglomeration of the particles ( $F_{agg}$  is the factor of agglomeration):

$$F_{agg} = \frac{d_{v50}}{d_{BET}} \quad 5.3$$

## 5.3 Results

### 5.3.1 Using Polymers

Figure 5.1 presents the X-ray diffraction patterns (Figure 5.1a) and Raman spectra (Figure 5.1b) of the samples prepared in the presence of polyelectrolytes (PAA and PVP). For comparison the pattern (spectra) of blank sample (without additive-BT) is presented as well. As can be observed the patterns can be indexed to cubic BT (JCPDF no. 31-0174). The formation of barium titanate is noticed independent on the PAA or PVP concentration and this idea is also sustained by the Raman spectra presented in Figure 5.1b.

Eight Raman active modes are expected for tetragonal BT with a space group  $P4mm$ ,  $3A_{1g} + B_{1g} + 4E_g$ .<sup>256</sup> The peaks at around 517, 253, and 185  $\text{cm}^{-1}$  are assigned to the fundamental TO modes (transverse component of the optical mode) of A1 symmetry and the peak at 307  $\text{cm}^{-1}$  is assigned to the B1 mode, indicating an asymmetry within the  $\text{TiO}_6$  octahedra of BT on a local scale. The broadband at around 715  $\text{cm}^{-1}$  is related to the highest frequency longitudinal optical mode (LO) of A1 symmetry. If the sharpness of the peak at 307  $\text{cm}^{-1}$  is reduced and becomes indistinct then the tetragonal phase is not dominant<sup>141</sup>, as can be noticed in the case of the samples synthesized in the presence of polyelectrolytes (Figure 5.1b) when bands at around 185, 300 (small shoulder at ~ 272) and two sharp peaks at 516 and 715  $\text{cm}^{-1}$  are present.

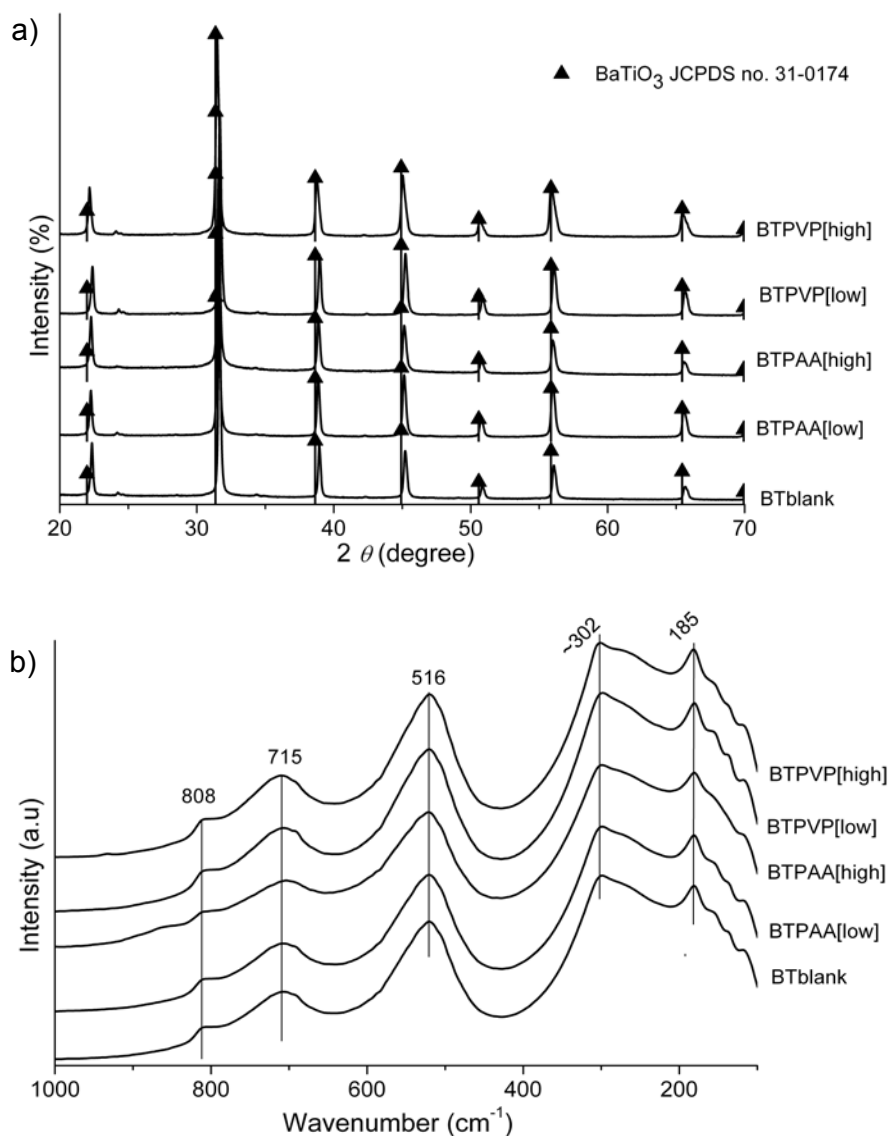


**Figure 5.1 a) X-ray diffraction patterns and b) Raman spectra of the samples prepared in the presence of polymers –PAA[low][high] and PVP[low][high] compared to the blank sample. The formation of cubic BT is observed independently on additive concentration.**

From the broadening of (111) peak of BT and using the Scherrer equation (after correction for instrumental broadening), the crystallite sizes ( $d_{XRD}$ , nm) were calculated and are presented in Table 5.2.

**Table 5.2** The specific surface areas ( $S_{\text{BET}}$ ), the equivalent spherical particle diameters ( $d_{\text{BET}}$ ), the crystallite size ( $d_{\text{XRD}}$ ) and the factor of aggregation ( $F_{\text{agg}}$  factor) of the samples obtained at 96 °C.

Sample index	$S_{\text{BET}}$ (m <sup>2</sup> /g)	$d_{\text{BET}}$ (nm)	$d_{\text{XRD}}$ (nm)	$F_{\text{agg}}$
BT <sub>blank</sub>	13.5	74	70	3
BT <sub>PAA[low]</sub>	18.6	54	61	22
BT <sub>PAA[high]</sub>	18.5	54	58	21
BT <sub>PVP[low]</sub>	16.4	61	63	31
BT <sub>PVP[high]</sub>	16.4	61	34	4
BT <sub>SDS[low]</sub>	14.9	67	33	13
BT <sub>SDS[high]</sub>	54.7	18	22	207
BT <sub>HPMC[low]</sub>	19.2	52	65	46
BT <sub>HPMC[high]</sub>	30.5	33	26	69
BT <sub>Fru[low]</sub>	21.0	47	59	39
BT <sub>Fru[high]</sub>	160.0	6	N/A	N/A

Included in Table 5.2 are also the specific surface areas ( $S_{\text{BET}}$ ) and the equivalent spherical particle diameters ( $d_{\text{BET}}$ ) of these samples calculated from the equation,  $d_{\text{BET}}$  (μm) =  $6/(\rho S_{\text{BET}})$ , where  $\rho$  stands for density ( $\rho_{\text{BT}} = 6.017 \text{ g/cm}^3$ )<sup>274</sup> and  $S_{\text{BET}}$  for the specific surface area (in m<sup>2</sup>/g). At low polyelectrolyte concentration  $S_{\text{BET}}$  is always slightly higher than the one of the blank sample. And in agreement, the crystallite size is lower than the corresponding value of the blank sample when low concentration of additives is used. For PVP although no change in  $S_{\text{BET}}$  with increase of the additive concentration occurred, the crystallite size decrease from 70 to 34 nm when the concentration of the additive was increased.

Figure 5.2 presents the SEM micrographs of the samples prepared in the presence of polyelectrolytes. For comparison the SEM image of blank sample (without additive-BT) is presented as well (Figure 5.2a). One can noticed that the sample synthesized without additives is characterized by small round shaped particles, with an average diameter of 200 nm.

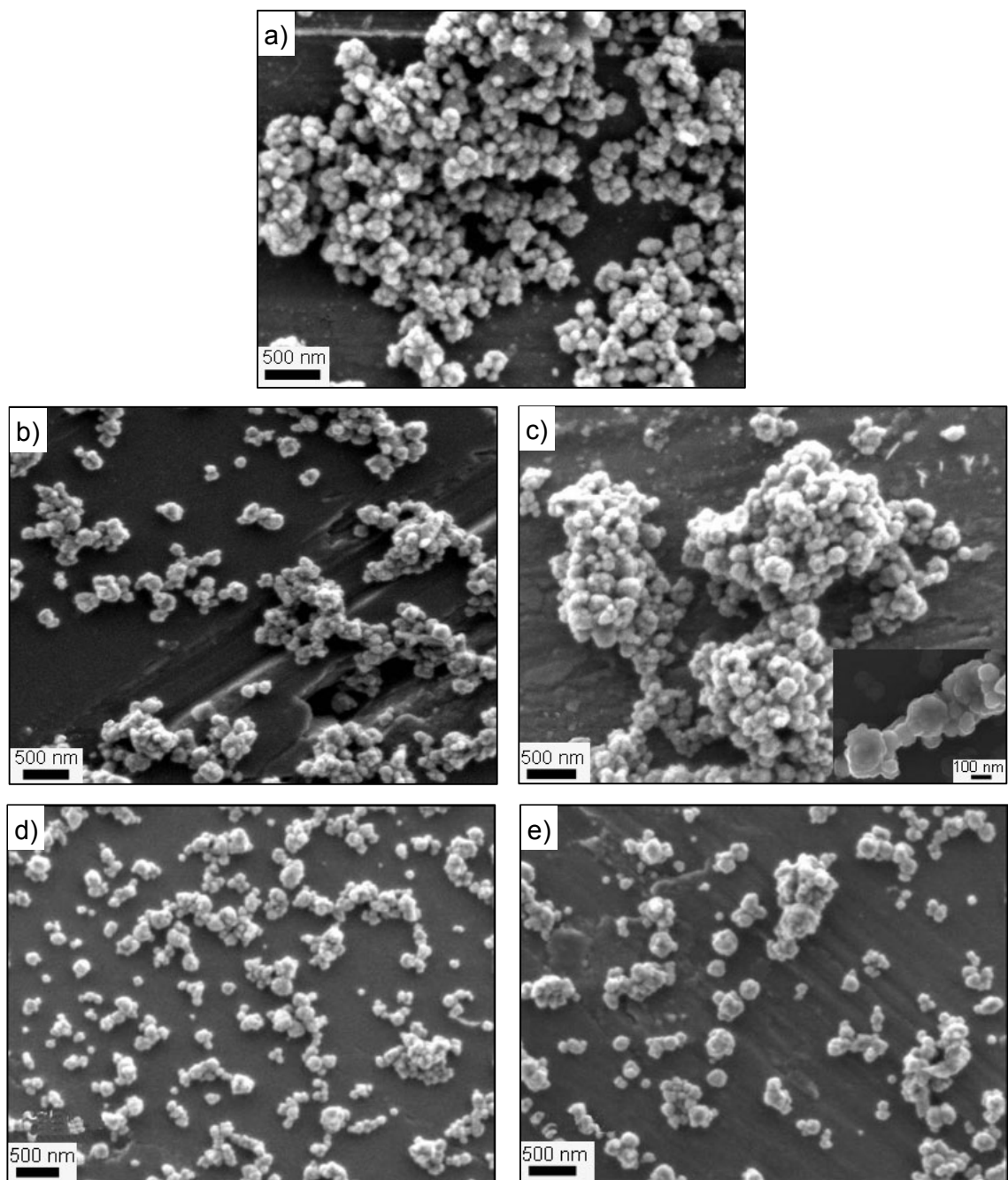


**Figure 5.2 SEM micrographs of : a) blank sample, BT; b) BTPAA[low]; c) BTPAA[high]; d) BTPVP[low] and e) BTPVP[high]. The images illustrate the oriented aggregation in the case of PAA and the dispersive for PVP.**

The morphology of barium titanate particles obtained in the presence of PAA at low and high concentration (Figures 5.2b and 5.2c) is similar to the blank sample,

the average is  $\sim 180$  nm and the degree of agglomeration increases with PAA concentration. In the presence of high PAA content the particle agglomeration follows a certain alignment as indicated in the inset of Figure 5.2c. The directed aggregation was also observed by TEM analysis and is presented in Figure 5.3. The selected area electron diffraction (SAED) pattern (see inset in Figure 5.3) demonstrates that the aggregation directions are along the  $\langle 001 \rangle$  direction of the cubic lattice. This is typical for the growth of perovskite crystals where the A and B cations have  $2^+$  and  $4^+$  valence states, respectively, because the  $\{001\}$  facets are neutral and have the lowest interfacial energy with the surrounding media.

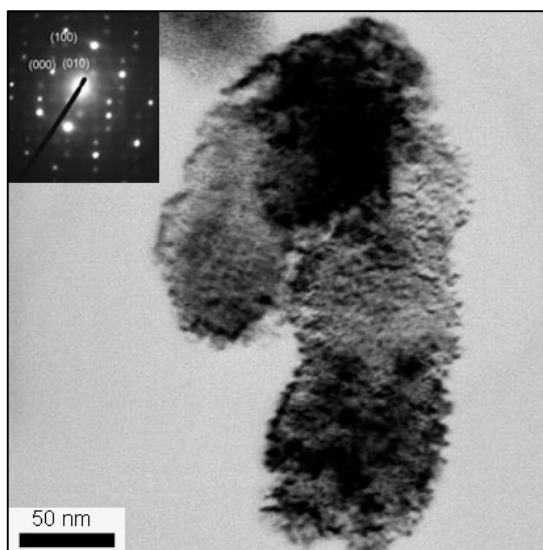


**Figure 5.3 TEM image of the sample prepared in the presence of PAA at high concentration; the inset presents the SAED of this sample. The crystal oriented attachment is confirmed.**

The morphology of the samples obtained in the presence of PVP for low and high concentrations are illustrated in Figure 5.2d and 5.2e, respectively. In both cases more homogeneous and dispersed particles compared to the blank sample can be noticed. The SEM observation is in agreement with the small agglomeration factor,  $F_{agg}$  (Table 5.2) when the PVP concentration increases. The average particle size determined by SEM is comparable to the sample prepared without additive ( $\sim 200$  nm).

Figure 5.4 presents the TGA analysis of the powders obtained in the presence of PAA compared to the blank sample.

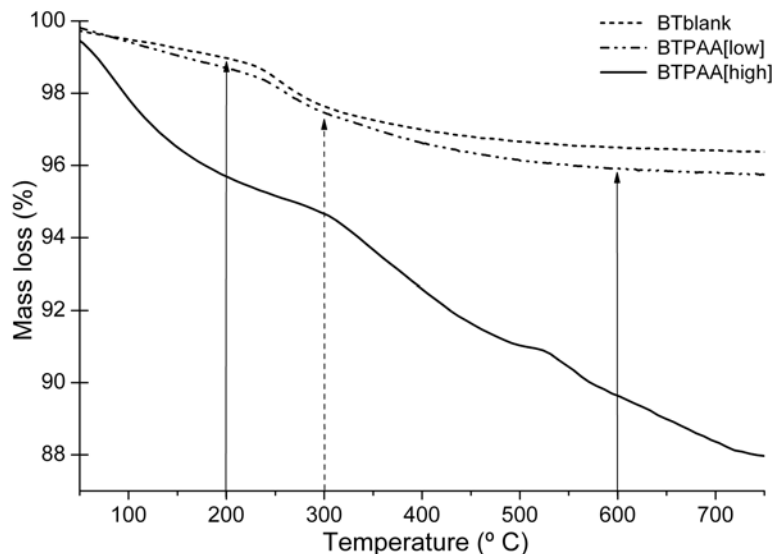


**Figure 5.4 TGA curves of the samples prepared in the presence of PAA at [low] and [high] concentration comparing to the blank sample showing higher PAA adsorption when increasing the concentration.**

The total weight loss of barium titanate nanopowders consists of two important contributions: below  $\sim 200$  °C from residual physically adsorbed water, and in the range of  $\sim 200$  °C to  $600$  °C from chemically bound hydroxyl groups and decomposition of organic groups<sup>276</sup>. The weight losses calculated from the TGA curves for the additive assisted synthesized samples are presented in Table 5.3. At low concentration of all additives the weight loss is similar to the blank sample. In  $200 - 600$  °C temperature range the increase in additive concentration results in around the double weight loss. The only exception is for PVP that seems to not to be adsorbed at the particles surface.

### 5.3.2 Using surfactants

Figure 5.5 presents the X-ray diffraction patterns (Figure 5.5a) and Raman spectra (Figure 5.5b) of the samples prepared from SDS at low and high

concentration. For comparison the pattern of blank sample (without additive-BT) is also displayed.

**Table 5.3 Weight loss percentages calculated from TGA curves of the samples.**

Sample	Mass Loss (%)		
	< 200°C	200-600°C	600-800°C
BT <sub>blank</sub>	0.9	2.5	0.2
BT <sub>PAA[low]</sub>	1.3	2.8	0.3
BT <sub>PAA[high]</sub>	4.1	6.0	1.9
BT <sub>PVP[low]</sub>	1.0	2.5	0.3
BT <sub>PVP[high]</sub>	1.0	2.6	0.2
BT <sub>SDS[low]</sub>	1.1	2.5	0.2
BT <sub>SDS[high]</sub>	3.0	4.9	0.4
BT <sub>HPMC[low]</sub>	1.3	2.9	0.2
BT <sub>HPMC[high]</sub>	1.7	6.3	0.2
BT <sub>Fru[low]</sub>	1.7	2.3	0.3
BT <sub>Fru[high]</sub>	10.1	6.4	1.1

The patterns of these samples are also indexed to a cubic BT as in the case of polyelectrolytes. A shift of the X-ray peaks to low angles was observed when SDS was used in low concentration. High concentrations of SDS result in contamination with BaCO<sub>3</sub> (Figure 5.5a). These results are in agreement with the Raman spectra (Figure 5.5b) where no sharp band at 307 cm<sup>-1</sup> is noticed, meaning that the barium titanate phase is predominately cubic.

The crystallite size of low SDS concentration sample (33 nm) is 50% lower than the crystallite size in the blank sample (Table 5.2). At high SDS concentration a substantial increase of the specific surface area and an accentuated decrease of the crystallite size are observed.

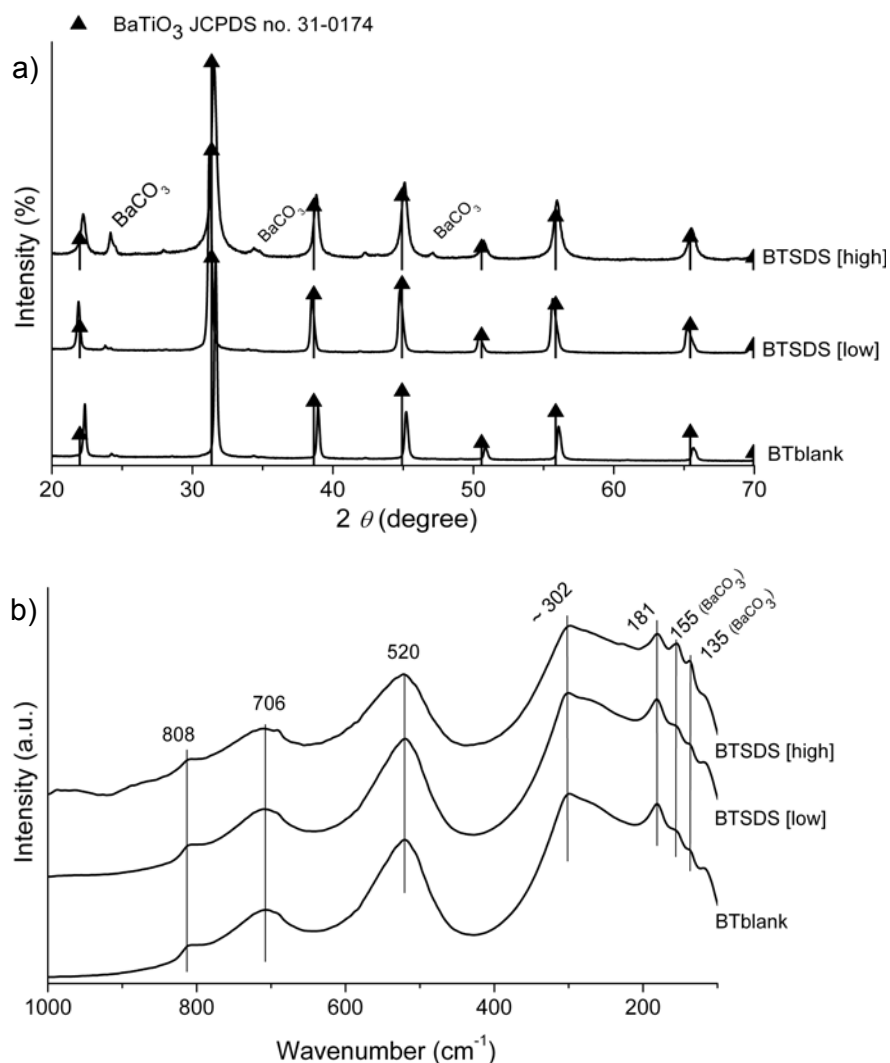


**Figure 5.5 a) X-ray diffraction patterns and b) Raman spectra of the samples prepared in the presence of anionic surfactant –SDS[low][high] compared to the blank sample. It is illustrating the formation of BT independently on SDS concentration**

Round shaped barium titanate particles with  $\sim 150$  nm average particle size are obtained in the presence of SDS at low and high concentration as can be seen in the SEM images illustrated in Figures 5.6a and 5.6b, respectively. It can be also noticed that the degree of agglomeration is higher when SDS is used in

comparison with the blank sample (Figure 5.2a). This is also indicated by the high value of the agglomeration factor,  $F_{agg}$  (Table 5.2).

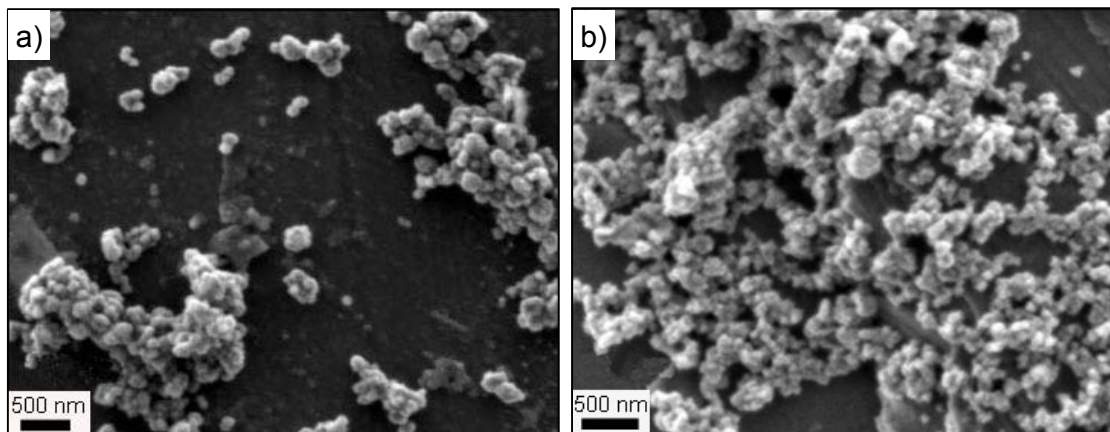


**Figure 5.6 SEM micrographs of a) SDS[low]; b) SDS[high]. High degree of agglomeration at high concentration of SDS.**

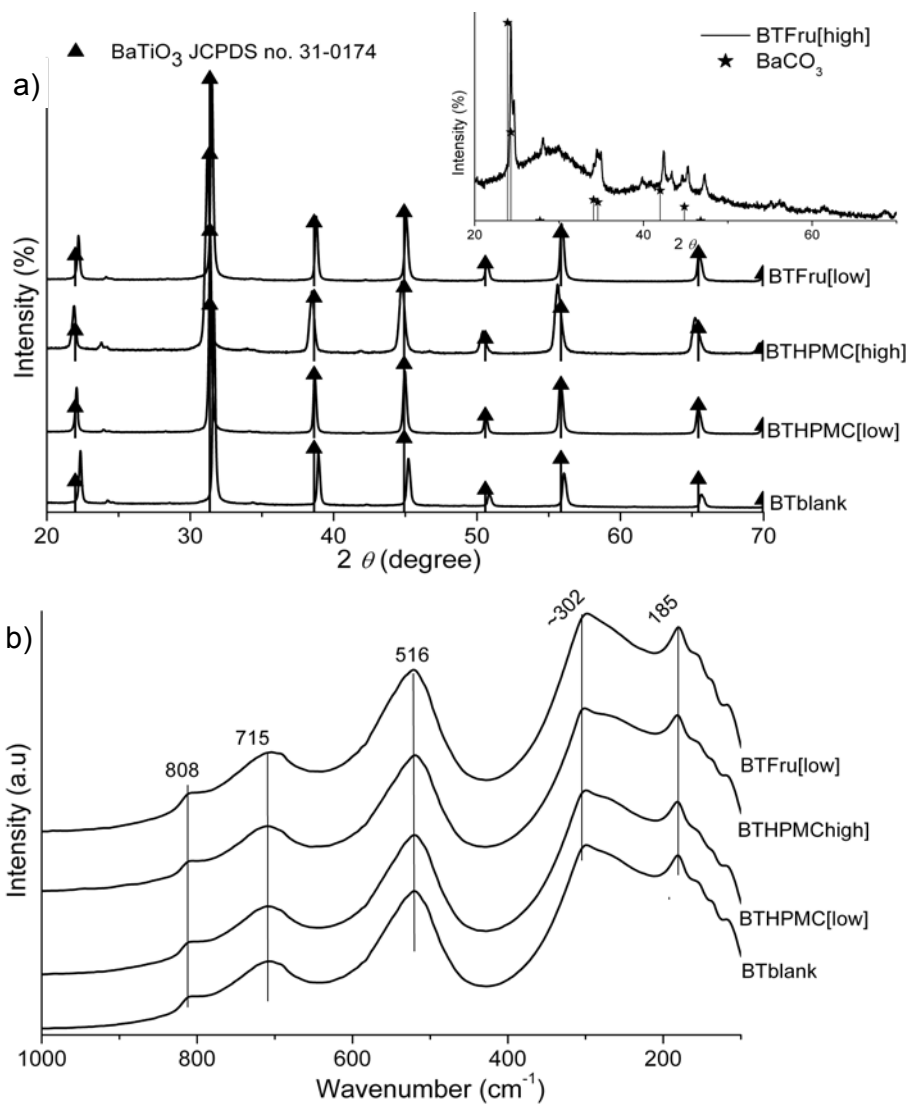
### 5.3.3 Using carbohydrates

Figure 5.7 presents the X-ray diffraction patterns (Figure 5.7a) and Raman spectra (Figure 5.7b) of the samples prepared from HPMC and Fructose at low and high concentration in comparison with the blank sample.

When HPMC is added cubic barium titanate is formed independent on the additive concentration (Figure 5.7a). The formation of predominately cubic phase is also sustained by the Raman study (Figure 5.7b). At high concentration of HPMC a significant shift of the diffraction peaks to low  $2\theta$  values (Figure 5.7a) occurs and at the same time barium carbonate is detected.

An interesting result is observed at high HPMC concentration when a substantial increase of the specific surface area and an accentuated decrease of the crystallite size are observed (Table 5.2).

In the case of Fructose cubic barium titanate is only formed at low additive concentration (Figure 5.7a and 5.7b). For high concentrations an amorphous phase together with barium carbonate is identified (see inset of Figure 5.7a).



**Figure 5.7 a) X-ray diffraction patterns and b) Raman spectra of the samples prepared in the presence of carbohydrates- HPMC[low][high] and D-Fructose[low] (D-Fructose[high] in the inset) compared to the blank sample. It is showing the formation of BT in all cases except for BTFru[high].**

Figure 5.8 presents the SEM images of the samples obtained in the presence of HPMC at low (Figure 5.8a) and high concentration (Figure 5.8b). For

the case of low HPMC concentration equiaxed particles are observed as in the blank sample (Figure 5.2a).

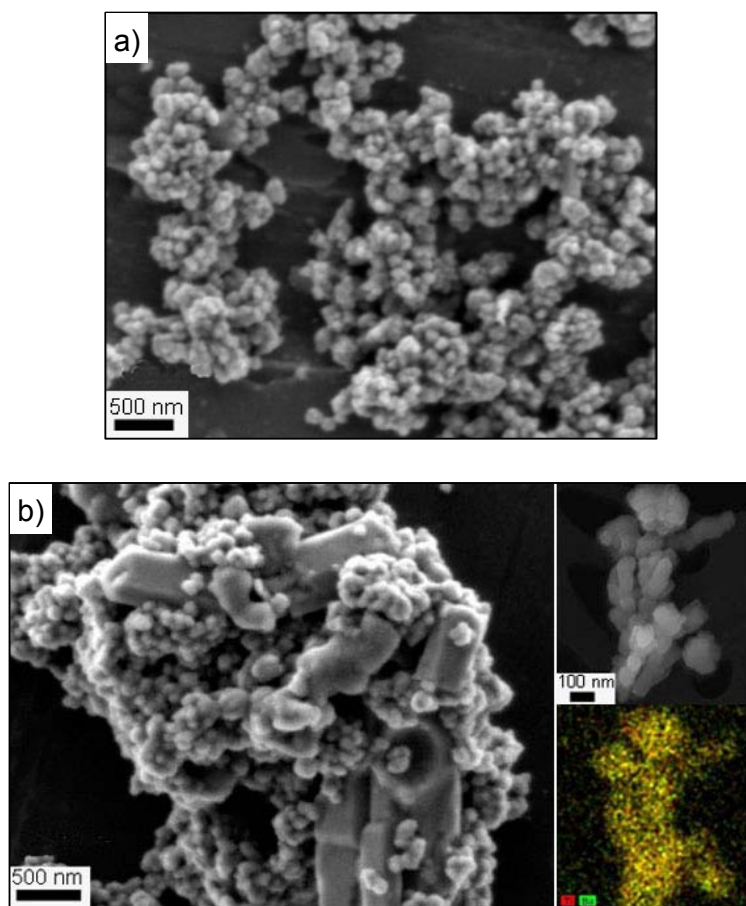


**Figure 5.8 SEM micrographs of a) HPMC[low]; b) HPMC[high]; the inset presents the SEM X-Ray mapping of the sample HPMC[high]. Various morphologies are observed for high concentration of HPMC.**

At high concentration of HPMC morphologies are rather different; they include small agglomerated particles with rough surface, dendritic particles with a smooth surface and particles with parallelepiped shape (Figure 5.8b). SEM X-Ray mapping confirmed that Ti and Ba are homogeneously distributed in all observed morphologies (see inset of Figure 5.8b).

For the samples synthesized in the presence of low concentration of D-Fructose equiaxed barium titanate particles are formed similar to all the previous ones (Figure 5.9a). However, at high concentrations of D-Fructose large

agglomerates of equiaxed particles, which seem to be organized into an ordered porous structure, were formed (Figure 5.9b). The porous nature of these particles is in agreement with the very high specific surface area (Table 5.2) and the highest weight loss below 200 °C (Table 5.3) obtained for high concentrations of Fructose.

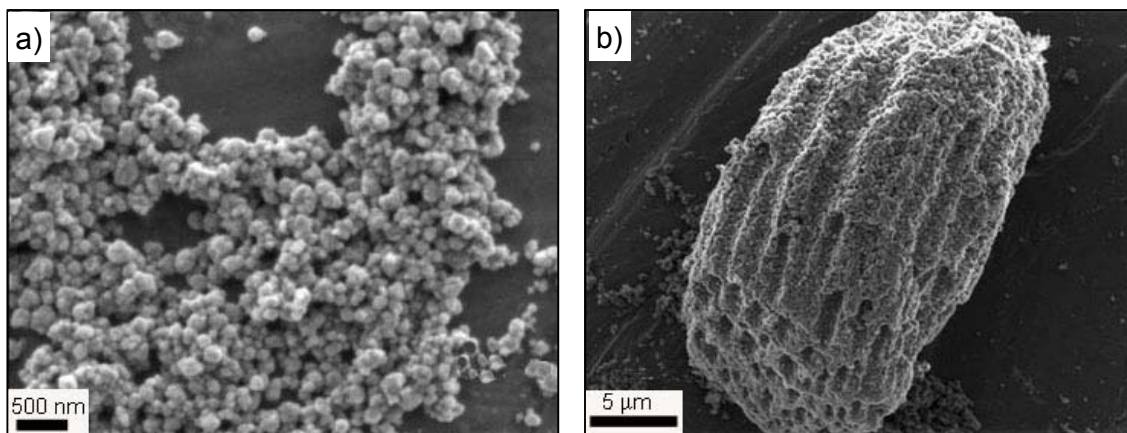


**Figure 5.9 SEM micrographs of a) Fru[low]; b) Fru[high]. Cocoon shaped aggregates are formed for high concentration of Fructose.**

Considering that the crystallization process at 96 °C is quite fast (only 30 minutes are sufficient for the formation of BT) experiments at lower temperatures were carried out. Little effect was seen except for PAA assisted BT synthesis. Figure 5.10 presents the TEM images of the obtained sample, mainly represented by amorphous round shaped particles with small sizes illustrated in the left insets. However, few particles with crystalline features, shown on the right side of Figure 5.10b, are also present in which directed aggregation along [100] direction of cubic BT is visible (see SAED inset), similarly to the sample prepared at 96 °C (Figure 5.2c and 5.3). These results suggest that PAA definitively promote oriented attachment of the BT particles.

## 5.4 Discussion

The results presented above and summarized in Table 5.4, indicate that crystalline barium titanate can be synthesized in the presence of PAA, PVP, SDS

and HPMC at both low and high concentrations. The only exception is the sample prepared with high concentration of D-fructose in which BT was not formed.

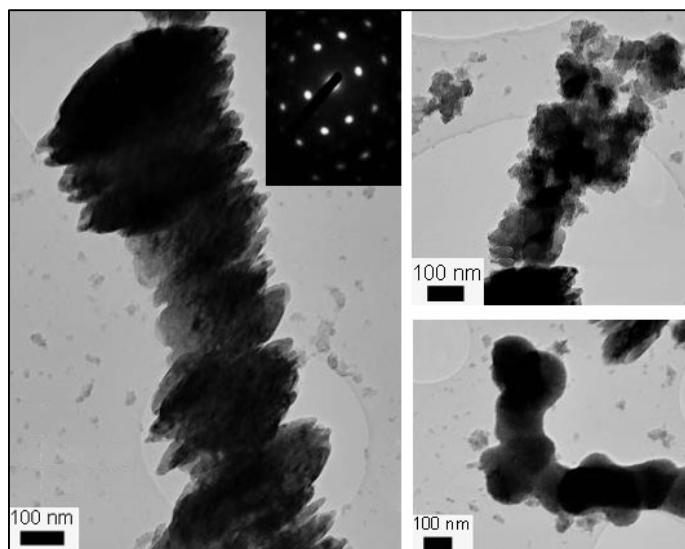


**Figure 5.10** TEM micrographs of the samples prepared at 80 °C in the presence of PAA at high concentration showing the oriented aggregation of the particles.

However, there are noticeable differences in the morphology of BT particles:

- PAA promotes oriented aggregation of BT particles;
- The increase of PVP and HPMC concentration led to the decrease of the crystallite size;
- SDA originates the smallest crystallite size of all prepared samples.

Kinetic growth factors can be drastically changed in the presence of additives, which can preferentially adsorb on a specific crystal face.<sup>128</sup> The strength of the adsorption processes influences the change of the crystal habit. From the values of the total weight loss (Table 5.3) one can observe that all the additives are adsorbed to the barium titanate particles surface at high concentration. In the following sections one will discuss if the adsorption of the additives effectively changes the growth kinetics leading to changes in the crystal habit.

**Table 5.4 Summary of the main results of BT synthesis by additive-assisted method.**

	[Additive]	Crystallographic Phase	Microstructure	Weight loss Compared with blank	Particle size Compared with blank	$d_{XRD}$ Compared with blank
PAA	Low	BT	Isotropic aggregates of round shape	Similar	Slightly higher	Slightly lower
	High	BT	Directed aggregation of round shape	Double	Slightly higher	Slightly lower
PVP	Low	BT	Dispersed round shape	Similar	Slightly higher	Slightly lower
	High	BT	Dispersed round shape	Similar	Slightly higher	Half
SDS	Low	BT	Round shape	Similar	Slightly higher	Half
	High	BT+ BaCO <sub>3</sub>	Round shape	Double	higher	one third
HPMC	Low	BT	Round shape	Similar	Slightly higher	Slightly lower
	High	BT+ BaCO <sub>3</sub>	Round shape	Double	higher	one third
Fru	Low	BT	Round shape	Similar	Slightly higher	Slightly ↓
	High	BaCO <sub>3</sub> Amorphous material	Porous cocoon shape	Double	nine times higher	n.a.

#### 5.4.1 Effect of PAA

Increasing PAA concentration promotes the direct aggregation of BT particles (Figure 5.2c, Figure 5.3 and 5.10). There are two main ways for PAA

adsorption at high pH; one is through hydrogen bonding and the second one by specific bonding of the polymer to charged sites at the surface<sup>275</sup>. The PAA is fully ionized at the working pH (>12) and so free COO<sup>-</sup> groups are present along the polymer chain. Taking into account that at pH>10 barium titanate particles have negative surface charges<sup>277</sup> the most probable adsorption mechanism of PAA on the particle surface is by specific bonding created by Ba bridges<sup>278</sup>. However, this situation is favored by the formation of monodentate Ba-PAA complex (Ba<sup>+</sup>-COO). If Ba<sup>2+</sup> ions form strongly bounded bidentate species, no positive charge remains to bind the polymer with the barium titanate surface sites and the polymer is trapped during precipitation rather than adsorbed onto the particle surface. The porous features of BT particles prepared with PAA (Figures 5.3 and 5.10) and the similar values of S<sub>BET</sub> independent on the additive concentration are an indication of the trapping of at least some of the PAA during BT precipitation. Therefore, in the present conditions, PAA influences BT nucleation by modifying the quantity of Ba<sup>2+</sup> in solution.

The direct aggregation observed when the PAA concentration increases (Figures 5.2c, 5.3 and 5.10) indicates that this additive influences also the growth of BT. These results suggest that the growth process is controlled by an aggregation mechanism, oriented attachment<sup>246</sup>. A similar mechanism has been reported for the growth of anisotropic KNbO<sub>3</sub> nanorods<sup>148</sup> and TiO<sub>2</sub> (anatase) nanoparticles<sup>246</sup>. The oriented attachment takes place when two adjacent particles come into the same crystallographic orientation, with high-energy faces, fuse and eliminate these faces and the result is an aggregate with directed orientation<sup>249</sup>. It is then suggested that in the present study PAA could preferentially adsorb on high energy BT crystallographic faces, decreasing the growth rate of these faces and inducing the oriented attachment of BT particles. It can be therefore stated that PAA limits the growth kinetics of BT by decreasing the surface energy and so decreasing the growth rates of specific crystallographic faces. So PAA both adsorbs onto high energy surfaces and is trapped during the precipitation.

### **5.4.2 Effect of PVP**

PVP is a water soluble polymer made from the monomer N-vinyl pyrrolidone with a basic character <sup>279</sup>. PVP is a strong Lewis base and may strongly interact with other molecules by the formation of hydrogen bonds and act as proton acceptor. Due to these properties PVP can be co-ordinately bonded to the surface of the ions and to form a protection layer, which impedes further aggregation, acting as both growth inhibitor and dispersant <sup>280</sup>. This situation was observed in the case of Ag particles growth when smaller particles are formed due to the protection layer formed by coordinative bond between Ag<sup>+</sup> and N in PVP <sup>280</sup>.

In this study as shown in Figure 5.1a monophasic BT is formed for both PVP concentrations and the particles morphology is not changed in the presence of PVP, as round shape particles with diameters between 80-100 nm similar to the blank samples have been obtained. Thermogravimetric analysis (Table 5.3) suggests that no effective adsorption of this polymer on the surface of barium titanate particles takes place even at high concentration. On the other hand, comparing to the blank sample more disperse and homogeneous particles are formed (Figure 5.2d and 5.2e); one cannot have steric repulsion unless the PVP adsorbs. In addition, the increased stability of BT could be related with the high viscosity of PVP aqueous solutions <sup>281</sup>, which reduces the mobility of the stable nuclei and consequently the agglomeration. The reduction of the crystallite size (Table 5.2) from 70 nm (for the blank) to 63 nm (for low PVP concentration) and to 34 nm (for high PVP concentration) further indicates that PVP is influencing the growth of BT but is not acting as a crystal habit modifier.

### **5.4.3 Effect of SDS**

SDS is an anionic surfactant with critical micelle concentration of 0.252 g/100 cm<sup>3</sup> at 30 °C <sup>282</sup>. It is known that the critical micelle concentration increases with temperature and decreases with increase of the ionic strength. In alkaline medium the ionic strength is higher as the pH increases. Under the present experimental conditions (pH > 12 and SDS concentration more than 0.4 g/l) SDS is forming micelles. The X-ray patterns (Figure 5.5a) show that barium titanate phase

was obtained for both SDS concentrations; however a significant amount of barium carbonate is formed at high SDS content. This result, supported by the high  $S_{\text{BET}}$  (porous structure due to unreacted titanium hydroxide gel <sup>283</sup>) observed when high concentrations of surfactant (Table 5.2) were used, indicates that SDS is avoiding or delaying the reaction between the barium and the titanium species, and so BT nucleation.

As stated in the introduction, surfactants can influence the growth in two ways; as a growth inhibitor when creating micelles <sup>284</sup> and/or as crystal shape modifier when acting as a capping molecule <sup>102</sup>. In the present study SDS rather acted as growth inhibitor than as crystal modifier as the crystallite size is drastically reduced when using SDS (Table 5.2) and no changes in the particle shape have been noticed. However, the colloidal stability was reduced when using SDS and more agglomerated powders were obtained (Figure 5.6 and Table 5.2).

#### **5.4.4 Effect of HPMC**

The HPMC is a polysaccharide chemically derived from cellulose by insertion of hydrophobic moieties such as hydroxypropyl and methyl. Despite the introduction of these hydrophobic groups, HPMC presents a linear polymeric chain with a high hydrophilic character due to the presence of polyhydroxy groups on the molecular chains, which make the polymer water soluble <sup>285</sup>. The hydrophobic parts of HPMC are important being responsible for its surface activity (as in a polysoap) and unique hydration-dehydration characteristics.

At low HPMC concentration, the barium titanate sample obtained is quite similar to the blank sample. On the contrary, with high HPMC concentrations the synthesis of BT was strongly modified: high  $S_{\text{BET}}$ , high weight loss, and considerable amount of  $\text{BaCO}_3$ . These results can indicate that HPMC is delaying the reaction between barium and titanium species as observed in the case of SDS, perhaps because HPMC is strongly attached to the titanium hydroxide gel surface and thus impedes its dissolution.

Moreover the crystallite size drastically decreases from 70 nm (in the blank) to 26 nm (at high HPMC concentration) (Table 5.2) and different

morphologies were formed (Figure 5.8*b*). These results indicate that HPMC is acting more as growth inhibitor than as crystal growth modifier. HPMC can act as a growth inhibitor because the crystal growth can be regulated and restricted by the three-dimension network structure of HPMC gel formed when increasing the synthesis temperature and additive concentration.

#### **5.4.5 Effect of D-Fructose**

In this study the most evident effect of additive itself and its concentration on the BT crystallization was observed in the case of D-Fructose. This is a water soluble monosaccharide with a cycle structure<sup>285</sup>. Low D-fructose concentration did not affect the formation of BT (Figure 5.7). However, when a high concentration of D-Fructose was added, no BT was formed (see inset of Figure 5.7*a*). Moreover, it is possible that the hydroxyl groups of D-fructose interacted with the barium cations and the titanium hydroxide species forming intermediary porous amorphous phase (Figure 5.9*b*) that should be responsible for the high  $S_{BET}$  of the Fru[high] sample (Table 5.2). This porous structure is very hygroscopic losing a high percentage (10.1%) of water below 200 °C (Table 5.3).

It is evident then, that the energy barrier for barium titanate nucleation is increased as the additive concentration increases. Similar behavior has been observed in the case of  $CaCO_3$  crystallization in the presence of saccharides as organic crystal modifiers when the nucleation of calcite was strongly dependent on the saccharide concentration<sup>286</sup>. This behavior is probably an expression of Ostwald's step rule which stipulates that a metastable phase's nucleation rate can be higher than those of the stable phase due to the local decrease of the supersaturation<sup>287</sup>. However, how saccharides, in general, and fructose, in particular, affect the crystallization acting as crystal modifiers, it is not yet elucidated. It is proposed that in the particular case of BT the local decrease of supersaturation can be due to formation of stable Ba-fructose complexes which restrict the reaction with titanium precursor and so the crystallization of BT.

## 5.5 Summing up

Poly(acrylic acid) (PAA), poly(vinyl pyrrolidone) (PVP), sodium dodecylsulfate (SDS), (D-)fructose and hydroxypropylmethylcellulose (HPMC) were used as additives to control the growth of BT particles in aqueous synthesis. The different structural and chemical nature of each additive governed the BT growth under the aqueous conditions. At low concentrations the additives did not affect the crystallization of BT. The main achievements regarding the effect of additives at high concentration on the BT crystallization are summarized in Figure 5.11. For high concentration of PAA the additive is specifically adsorbed on the BT crystallographic planes, decreasing the energy of these faces and promoting the oriented attachment of the particles. PVP seems not to adsorb on the BT particles surfaces but it acts as a dispersive agent and as growth inhibitor when increasing the additive concentration by modifying the solution viscosity. SDS in high concentration forms micelles, acting as growth inhibitor due to the limitation of mass transport of barium and titanium species.

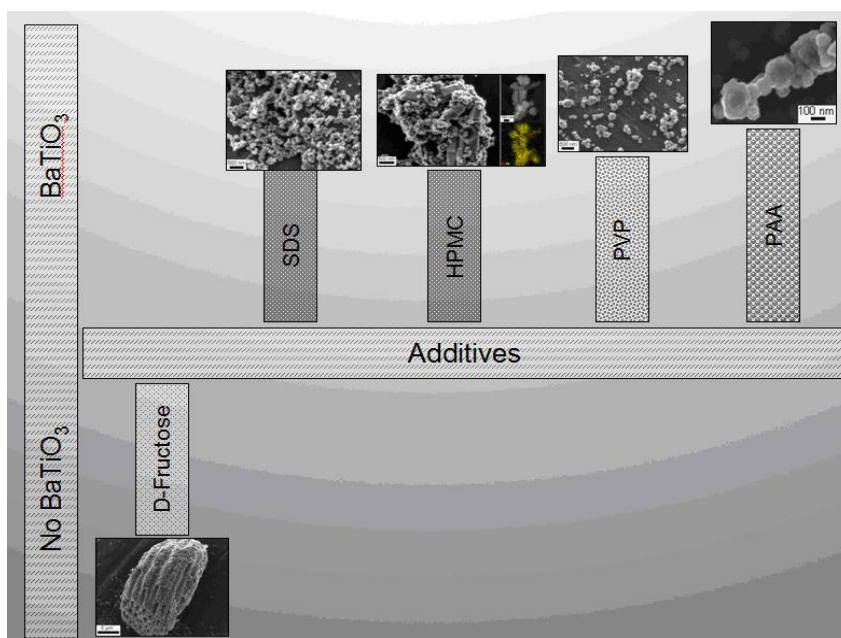


Figure 5.11 Summary of non template additive-assisted aqueous synthesis of BT.

The inverse solubility of HPMC with the increase of the additive concentration and of the synthesis temperature may be the reason for BT growth inhibition. Finally, D-fructose in high content seems to change the energy barrier of BT nucleation presenting a threshold concentration for the nucleation.

Although the present study gives useful insights on how additives control barium titanate growth from aqueous solutions, it demonstrates that the morphological control of complex oxides by chemical methods is not a trivial task and suggests that in order to control the morphology of BT particles by aqueous synthesis a fast, and homogenous nucleation is required. In addition among the analyzed additives the most promising crystal habit modifier seems to be PAA.

## 6 General Conclusions and Future Work

To find easy and low cost methods for the preparation of anisometric ferroelectric materials is an important prerequisite for the understanding of the size – shape - properties relationship in nano ferroelectrics envisaging future applications. As referred above, this has motivated the work of this thesis which was dedicated to exploit strategies for the morphology control of BT particulates. For this propose our work has addressed two low cost bottom-up synthesis approaches: a chemical template methodology, starting from TiNTs as templating agents and a non template additive assisted syntheses. Based on this study, we have come to the following general out puts and conclusions:

1. The initial part of the present work dedicated to systematic studies of titanium based NTs to be used as template for the further growth of BT demonstrated that layered titanate nanotubes (TiNTs) with general formula  $A_2Ti_2O_5$ , and not anatase as others claimed, can be prepared by hydrothermal method in high alkaline medium starting from commercial  $TiO_2$  (anatase and rutile). It was also established that the tubular shape was formed during the hydrothermal synthesis and it is not related with the after synthesis washing process, clarifying the under going discussion on the topic.(Maxim *et al. Journal of Porous Materials*, 2010)

2. The systematic studies of the template role of TiNTs for the anisotropic growth of BT in solution based hydrothermal synthesis established the formation of dendritic particles in the temperature range from 90 to 200 °C. For the formation of anisometric BT two mechanisms take place depending on the temperature and time. At low temperature and short time ‘wild’ type dendritic particles with pseudo-cubic structure have been formed by a phase boundary topotactic reaction on the TiNTs surface. At intermediate temperature and time round shaped particles of BT were formed. Finally, at high temperature and longer time ‘seaweed’ type dendrites with predominately tetragonal structure were obtained. In the last case

the BT crystallization process was controlled by a dissolution-precipitation mechanism. By piezoelectric force microscopy measurements it is demonstrated that the “seaweed” type BT dendrites have higher piezoactivity than the “wild” type and it is clearly revealed the role of the structure and the lattice defect concentration on the polarization coherency and ferroelectric order of the dendritic particles. (Maxim *et al.* *Processing and Application of Ceramics* 2010; *Crystal Growth & Design* 2008 and 2010) These results proved that the use of Ti based nanotubes as template agent for the growth of 1D structures of perovskite based materials is not trivial and questioned the reported observations of Mao *et al.*<sup>114</sup>.

3. The role of the TiNTs on the anisotropic growth of barium titanate in vapor phase reaction is described for the first time in this work. For that an original approach based on chemical vapor deposition of a metalorganic barium precursor (MoCVD) on TiNTs was proposed. When the annealing temperature and titanium concentration increase the barium titanate nanoparticles seem to segregate and NRs of barium deficient phases are formed. Round shaped BT nanocrystals nucleated at the TiNTs surface independently on the barium concentration. (Maxim *et al.* *Chem. Mater.* to be submitted)

4. Using non template additive assisted syntheses the effect of additives on the morphological control of BT particles was systematically addressed. Different types of additives were tested on the synthesis of BT and the structural changes of the nanoparticles assessed and related with the nature of the additive. It was proved that additives can be used as crystal growth modifiers by changing the growth habit or kinetically controlling the growth rate of the various crystallographic facets of the crystals. All the tested additives influence the growth of BT, but their role is distinctly different; poly(acrylic acid) (PAA) adsorbs on specific crystallographic faces changing the growth kinetics and inducing the oriented attachment of the particles; poly(vinyl pyrrolidone) (PVP), sodium dodecylsulfate (SDS) and hydroxypropylmethylcellulose (HPMC) act as growth inhibitors rather than crystal habit modifiers resulting in small crystals (26 nm); and D-Fructose appears to increase the activation energy for nucleation and no

crystalline BT is formed under the same conditions used for the other additives.(Maxim *et al. Microscopy and Microanalysis* 2009 and *Crystal Growth &Design* 2010)

### **Future work**

This thesis is a systematic but not complete study of the chemical template and non template additives assisted methods for the morphology control of BT particles.

➤ Although the TiNTs template function has been clarified in solution based hydrothermal synthesis, in vapor phase reaction the process needs to be optimized, namely Ba/Ti stoichiometry control to obtain pure perovskite phase. Kinetic analysis similar to the one performed for the hydrothermal synthesis should be made. The use of films of TiNTs arrays can also help for the Ba/Ti stoichiometry control in the MoCVD approach.

➤ Beside the chemical template methods the physical template approaches (need to remove the template by post-synthesis techniques) have been proposed in the last years. Within this context, templating against existing nanostructures like CNTs or self assembled molecular structures such as hexadecyltrimethylammonium (Cetrimonium) bromide CTAB which forms rod like micelles above the critical micellar concentration and amphiphilic diblock copolymer poly(ethylene-co-butylene)-b-poly(ethylene oxide), (referred to as KLE) which produce porous nanoscale frameworks with small and medium pore sizes are interesting to be considered.

➤ In this work the non template additives studied gave useful insights on the effect of additives on the BT crystallization and the most promising seemed to be PAA. However homogenous and fast nucleation in the presence of only PAA or together with other polymers as PVA should be systematically studied.

➤ Another interesting idea is the electrospinning method which has been recently explored as a highly versatile and simple method to process polymer-containing solutions or melts into continuous fibers with diameters ranging from micro- to nanometers. This technique involves the use of a high voltage to charge the surface of a polymer solution droplet and thereby induce the ejection of a liquid jet through a spinneret. Owing to the bending instability, the jet is subsequently stretched many times to form continuous, ultrathin fibers. Therefore the electrospinning using a solution that contained poly(vinylpyrrolidone) and a sol-gel solution of a ferroelectric material may be well thought-out.

## References

1. Valasek, J. Piezo-electric and allied phenomena in Rochelle salt. *Physical Review* **1921**, 17 (4), 475-481.
2. Jona, F.; Shirane, G. *Ferroelectric Crystals*; Pergamon Press: Oxford, **1962**.
3. Fatuzzo, E.; Merz, W. J. *Ferroelectricity*; North-Holland Publisher: Amsterdam, **1967**.
4. Lines, M. E.; Glass, A. M. *Principles and Applications of Ferroelectrics and Related Materials*; Clarendon Press: Oxford, **1977**.
5. Xu, Y. *Ferroelectric Materials and their Applications*; North-Holland Elsevier Sci.Publ.: Amsterdam, **1991**.
6. Uchino, K. *Ferroelectric Devices*; Marcel Dekker Inc.: New York, **2000**.
7. Jaffe, B.; Cook, W. R.; Jaffe, H. *Piezoelectric Ceramics*; Academic Press: London and New York, **1971**.
8. Ikeda, T. *Fundamentals of piezoelectricity*; Oxford University Press: New York, **1990**.
9. Waanders, J. W. *Piezoelectric Ceramics: Properties and Applications*; Philips Components: Eindhoven-The Netherlands, **1991**.
10. Haertling, G. H. Ferroelectric ceramics: History and technology. *Journal of the American Ceramic Society* **1999**, 82 (4), 797-818.
11. Nettleto, R. E. Ferroelectric Phase Transitions - Review of Theory and Experiment .9. Specific Heat. *Ferroelectrics* **1971**, 2 (1), 5.
12. Nettleto, R. E. Ferroelectric Phase Transitions Review of Theory and Experiment .10. Phonon Renormalization and Theory of Spontaneous Polarization. *Ferroelectrics* **1971**, 2 (2), 77.
13. Nettleto, R. E. Ferroelectric Phase Transitions - A Review of Theory and Experiment .1. Conclusions. *Ferroelectrics* **1971**, 2 (2), 93.
14. Evans, H. T. *An X-Ray Diffraction Study of Barium Titanate*; Massachusetts Institute of Technology, **1953**.

15. Petkov, V.; Gateshki, M.; Niederberger, M.; Ren, Y. Atomic-scale structure of nanocrystalline  $\text{Ba}_x\text{Sr}_{1-x}\text{TiO}_3$  ( $x = 1, 0.5, 0$ ) by X-ray diffraction and the atomic pair distribution function technique. *Chemistry of Materials* **2006**, *18* (3), 814-821.
16. Cochran, W. Crystal Stability and the Theory of Ferroelectricity. *Physical Review Letters* **1959**, *3* (9), 412-414.
17. Cochran, W. Crystal Stability and the Theory of Ferroelectricity. *Advances in Physics* **1960**, *9* (36), 387-423.
18. Cochran, W. Crystal Stability and the Theory of Ferroelectricity .2. Piezoelectric Crystals. *Advances in Physics* **1961**, *10* (40), 401-420.
19. Blinc, R.; Zeks, B. *Soft Modes in Ferroelectric and Antiferroelectrics*; Elsevier: New York, **1974**.
20. Moulson, J.; Herbert, J. M. *Electroceramics*; Chapman and Hall: London, **1990**.
21. Matthias, B.; Vonhippel, A. Domain Structure and Dielectric Response of Barium Titanate Single Crystals. *Physical Review* **1948**, *73* (11), 1378-1384.
22. Arlt, G. Twinning in Ferroelectric and Ferroelastic Ceramics - Stress Relief. *Journal of Materials Science* **1990**, *25* (6), 2655-2666.
23. Vilarinho, P. Functional Materials: Properties, Processing and Applications. In *Scanning Probe Microscopy: Characterization, Nanofabrication and Device Application of Functional Materials*, Kluwer Academic: Netherlands, **2005**.
24. Mitchell, R. H. *Perovskite- Modern and Ancient*; Almaz Press Inc.: Ontario, Canada, **2002**.
25. Goldschmidt V.M. *Geochemisce Verterlungsgesetze der Elemente*; Norske Videnskap: Oslo, **1927**.
26. Bhalla, A. S.; Guo, R.; Roy, R. The perovskite structure –a review of its role in ceramic science and technology. *Materials Research Innovations* **2000**, *4*, 3-26.

27. Kauffman, G. B. Victor Moritz Goldschmidt (1888–1947): A Tribute to the Founder of Modern Geochemistry on the Fiftieth Anniversary of His Death. *The Chemical Educator* **1997**, 2 (5), 1-26.
28. Evans, H. An X-ray diffraction study of tetragonal barium titanate. *Acta Crystallographica* **1961**, 14 (10), 1019-1026.
29. Megaw, H. Refinement of the structure of BaTiO<sub>3</sub> and other ferroelectrics. *Acta Crystallographica* **1962**, 15 (10), 972-973.
30. Hennings, D.; Klee, M.; Waser, R. Advanced Dielectrics - Bulk Ceramics and Thin-Films. *Advanced Materials* **1991**, 3 (7-8), 334-340.
31. Yoon, J.; Lee, K.; Lee, S. Analysis the Reliability of Multilayer Ceramic Capacitor with inner Ni Electrode under highly Accelerated Life Test Conditions. *Transactions on Electrical and Electronic Materials* **2009**, 10 (1), 5-8.
32. Buchanan, R. C. *Ceramic Materials for Electronics - Processing, Properties and Applications*; Marcel Dekker: New York, **1986**.
33. Breder, K.; Wereszczak, A.; Riester, L.; Kirkland, T. P.; Bridge, R. J. *Determination of Strength for Reliability Analysis of Multilayer Ceramic Capacitors*; John Wiley & Sons, Inc.: **1999**.
34. Merz, W. J. Domain Formation and Domain Wall Motions in Ferroelectric BaTiO<sub>3</sub> Single Crystals. *Physical Review* **1954**, 95 (3), 690-698.
35. Scott, J. F.; Paz de Araujo, C. A. Ferroelectric Memories. *Science* **1989**, 246 (4936), 1400-1405.
36. Scott, J. F. *Ferroelectric Memories*; Springer Series in Advanced Microelectronics: **2000**; Vol. 3.
37. Auciello, O.; Scott, J. F.; Ramesh, R. The Physics of Ferroelectric Memories. *Physics Today* **1998**, 51 (7), 22-27.
38. Eaton, S. S.; Bulter, D.; Parris, M.; Butler, D.; [Anon] Ferroelectric capacitor operating method with polarisation retention using write pulse coupled to capacitor electrode which is open circuited before pulse terminates. EP338158-A2; JP1277395-A; AU8822954-A; US4893272-A; EP338158-B1; DE3887130-G.

39. Internet Communication **2006**.  
<http://www.itrs.net/Links/2006Update/2006UpdateFinal.htm>
40. Schilling, A.; Bowman, R. M.; Catalan, G.; Scott, J. F.; Gregg, J. M. Morphological control of polar orientation in single-crystal ferroelectric nanowires. *Nano Letters* **2007**, 7 (12), 3787-3791.
41. Zambrano, R. Challenges for Integration of Embedded FeRAMs in the sub-180 nm Regime. *Integrated Ferroelectrics: An International Journal* **2003**, 53 (1), 247-255.
42. Yun, W. S.; Urban, J. J.; Gu, Q.; Park, H. Ferroelectric Properties of Individual Barium Titanate Nanowires Investigated by Scanned Probe Microscopy. *Nano Letters* **2002**, 2 (No.5), 447-450.
43. Burda, C.; Chen, X.; Narayanan, R.; El-Sayed, M. A. Chemistry and Properties of Nanocrystals of Different Shapes. *Chemical Review* **2005**, 105, 1025-1102.
44. Peng, X. G.; Manna, L.; Yang, W. D.; Wickham, J.; Scher, E.; Kadavanich, A.; Alivisatos, A. P. Shape control of CdSe nanocrystals. *Nature* **2000**, 404 (6773), 59-61.
45. Wang, Y.; Herron, N. Nanometer-Sized Semiconductor Clusters - Materials Synthesis, Quantum Size Effects, and Photophysical Properties. *Journal of Physical Chemistry* **1991**, 95 (2), 525-532.
46. Kanzig, W.; Peter, M. Critical Domain Size in Ferroelectrics. *Physical Review* **1952**, 85 (5), 940-941.
47. ANliker, M.; Brugger, H. R.; Kanzig, W. *Helvetica Physica Acta* **1954**, 27, 99.
48. Arlt, G.; Hennings, D.; Dewith, G. Dielectric-Properties of Fine-Grained Barium-Titanate Ceramics. *Journal of Applied Physics* **1985**, 58 (4), 1619-1625.
49. Zhao, Z.; Buscaglia, V.; Viviani, M.; Buscaglia, M. T.; Mitoseriu, L.; Testino, A.; Nygren, M.; Johnsson, M.; Nanni, P. Grain-size effects on the ferroelectric behavior of dense nanocrystalline BaTiO<sub>3</sub> ceramics. *Physical Review B* **2004**, 70 (2).
50. Buscaglia, V.; Buscaglia, M. T.; Viviani, M.; Mitoseriu, L.; Nanni, P.; Trefiletti, V.; Piaggio, P.; Gregora, I.; Ostapchuk, T.; Pokorny, J.; Petzelt, J. Grain size and grain boundary-related effects on the properties of

- nanocrystalline barium titanate ceramics. *Journal of the European Ceramic Society* **2006**, 26 (14), 2889-2898.
51. Young, R. A. *The Rietveld Method*; Oxford University Press: **1995**.
  52. Frey, M. H.; Payne, D. A. Grain-size effect on structure and phase transformations for barium titanate. *Physical Review B* **1996**, 54 (5), 3158-3168.
  53. Shiratori, Y.; Pithan, C.; Dornseiffer, J.; Waser, R. Raman scattering studies on nanocrystalline BaTiO<sub>3</sub> - Part I - isolated particles and aggregates. *Journal of Raman Spectroscopy* **2007**, 38 (10), 1288-1299.
  54. Shiratori, Y.; Pithan, C.; Dornseiffer, J.; Waser, R. Raman scattering studies on nanocrystalline BaTiO<sub>3</sub> - Part II - consolidated polycrystalline ceramics. *Journal of Raman Spectroscopy* **2007**, 38 (10), 1300-1306.
  55. Ostapchuk, T.; Petzelt, J.; Savinov, M.; Buscaglia, V.; Mitoseriu, L. Grain-size effect in BaTiO<sub>3</sub> ceramics: study by far infrared spectroscopy. *Phase Transitions* **2006**, 79 (6-7), 361-373.
  56. Petzelt, J. Soft Mode Behavior in Cubic and Tetragonal BaTiO<sub>3</sub> Crystals and Ceramics: Review on the Results of Dielectric Spectroscopy. *Ferroelectrics* **2008**, 375, 156-164.
  57. Buscaglia, M. T.; Buscaglia, V.; Viviani, M.; Petzelt, J.; Savinov, M.; Mitoseriu, L.; Testino, A.; Nanni, P.; Harnagea, C.; Zhao, Z.; Nygren, M. Ferroelectric properties of dense nanocrystalline BaTiO<sub>3</sub> ceramics. *Nanotechnology* **2004**, 15 (9), 1113-1117.
  58. Mitoseriu, L.; Harnagea, C.; Nanni, P.; Testino, A.; Buscaglia, M. T.; Buscaglia, V.; Viviani, M.; Zhao, Z.; Nygren, M. Local switching properties of dense nanocrystalline BaTiO<sub>3</sub> ceramics. *Applied Physics Letters* **2004**, 84 (13), 2418-2420.
  59. Kataoka, M.; Suda, K.; Ishizawa, N.; Marumo, F.; Shimizugawa, Y.; Ohsumi, K. Determination of the *c/a* Ratio of a Submicrometer-Sized Crystal of Tetragonal Barium-Titanate by the Synchrotron-Radiation. *Nippon Seramikkusu Kyokai Gakujutsu Ronbunshi-Journal of the Ceramic Society of Japan* **1994**, 102 (2), 213-216.
  60. Schlag, S.; Eicke, H. F. Size Driven Phase-Transition in Nanocrystalline BaTiO<sub>3</sub>. *Solid State Commun* **1994**, 91 (11), 883-887.

61. Wang, X. H.; Deng, X. Y.; Wen, H.; Li, L. T. Phase transition and high dielectric constant of bulk dense nanograin barium titanate ceramics. *Applied Physics Letters* **2006**, *89* (16).
62. Junquera, J.; Ghosez, P. Critical thickness for ferroelectricity in perovskite ultrathin films. *Nature* **2003**, *422* (6931), 506-509.
63. Kim, Y. S.; Kim, D. H.; Kim, J. D.; Chang, Y. J.; Noh, T. W.; Kong, J. H.; Char, K.; Park, Y. D.; Bu, S. D.; Yoon, J. G.; Chung, J. S. Critical thickness of ultrathin ferroelectric BaTiO<sub>3</sub> films. *Applied Physics Letters* **2005**, *86* (10), 102907-3.
64. Fong, D. D.; Stephenson, G. B.; Streiffer, S. K.; Eastman, J. A.; Auciello, O.; Fuoss, P. H.; Thompson, C. Ferroelectricity in ultrathin perovskite films. *Science* **2004**, *304* (5677), 1650-1653.
65. Luo, Y.; Szafraniak, I.; Nagarajan, V.; Wehrspohn, R. B.; Steinhart, M.; Wendorff, J. H.; Zakharov, N. D.; Ramesh, R.; Alexe, M. Ferroelectric lead zirconate titanate and barium titanate nanotubes. *Integrated Ferroelectrics* **2003**, *59*, 1513-1520.
66. Luo, Y.; Szafraniak, I.; Zakharov, N. D.; Nagarajan, V.; Steinhart, M.; Wehrspohn, R. B.; Wendorff, J. H.; Ramesh, R.; Alexe, M. Nanoshell tubes of ferroelectric lead zirconate titanate and barium titanate. *Applied Physics Letters* **2003**, *83* (3), 440-442.
67. Spanier, J. E.; Kolpak, A. M.; Urban, J. J.; Grinberg, I.; Ouyang, L.; Yun, W. S.; Rappe, A. M.; Park, H. Ferroelectric Phase Transition in Individual Single-Crystalline BaTiO<sub>3</sub> Nanowires. *Nano Letters* **2006**, *6* (4), 735-739.
68. Wang, Z. Y.; Hu, J.; Yu, M. F. One-dimensional ferroelectric monodomain formation in single crystalline BaTiO<sub>3</sub> nanowire. *Applied Physics Letters* **2006**, *89* (26).
69. Lin, S.; Lu, T.; Jin, C. Q.; Wang, X. H. Size effect on the dielectric properties of BaTiO<sub>3</sub> nanoceramics in a modified Ginsburg-Landau-Devonshire thermodynamic theory. *Physical Review B* **2006**, *74* (13).
70. Glinchuk, M. D.; Zaulychny, B. Y.; Stephanovich, V. A. Properties of thin ferroelectric film with different electrodes. *Ferroelectrics* **2008**, *363*, 251-261.
71. Kretschmer, R.; Binder, K. Surface effects on phase transitions in ferroelectrics and dipolar magnets. *Physical Review B* **1979**, *20* (3), 1065.

- 
72. Morozovska, A. N.; Eliseev, E. A.; Glinchuk, M. D. Size effects and depolarization field influence on the phase diagrams of cylindrical ferroelectric nanoparticles. *Physica B-Condensed Matter* **2007**, *387* (1-2), 358-366.
  73. Petkov, V.; Buscaglia, V.; Buscaglia, M. T.; Zhao, Z.; Ren, Y. Structural coherence and ferroelectricity decay in submicron- and nano-sized perovskites. *Physical Review B* **2008**, *78* (5).
  74. Smith, M. B.; Page, K.; Siegrist, T.; Redmond, P. L.; Walter, E. C.; Seshadri, R.; Brus, L. E.; Steigerwald, M. L. Crystal Structure and the Paraelectric-to-Ferroelectric Phase Transition of Nanoscale BaTiO<sub>3</sub>. *Journal of the American Chemical Society* **2008**, *130* (22), 6955-6963.
  75. Pertsev, N. A.; Zembilgotov, A. G.; Tagantsev, A. K. Effect of Mechanical Boundary Conditions on Phase Diagrams of Epitaxial Ferroelectric Thin Films. *Physical Review Letters* **1998**, *80* (9), 1988.
  76. Nix, W. Mechanical properties of thin films. *Metallurgical and Materials Transactions A* **1989**, *20* (11), 2217-2245.
  77. Haeni, J. H.; Irvin, P.; Chang, W.; Uecker, R.; Reiche, P.; Li, Y. L.; Choudhury, S.; Tian, W.; Hawley, M. E.; Craigo, B.; Tagantsev, A. K.; Pan, X. Q.; Streiffer, S. K.; Chen, L. Q.; Kirchoefer, S. W.; Levy, J.; Schlom, D. G. Room-temperature ferroelectricity in strained SrTiO<sub>3</sub>. *Nature* **2004**, *430* (7001), 758-761.
  78. Choi, K. J.; Biegalski, M.; Li, Y. L.; Sharan, A.; Schubert, J.; Uecker, R.; Reiche, P.; Chen, Y. B.; Pan, X. Q.; Gopalan, V.; Chen, L. Q.; Schlom, D. G.; Eom, C. B. Enhancement of ferroelectricity in strained BaTiO<sub>3</sub> thin films. *Science* **2004**, *306* (5698), 1005-1009.
  79. Lee, H. N.; Christen, H. M.; Chisholm, M. F.; Rouleau, C. M.; Lowndes, D. H. Strong polarization enhancement in asymmetric three-component ferroelectric superlattices. *Nature* **2005**, *433* (7024), 395-399.
  80. Fu, H.; Bellaiche, L. Ferroelectricity in barium titanate quantum dots and wires. *Physical Review Letters* **2003**, *91* (25).
  81. Ginzburg, V. L.; Gorbatshevich, A. A.; Kopayev, Y.; Volkov, B. A. On the problem of superdiamagnetism. *Solid State Commun* **1984**, *50* (4), 339-343.
  82. Naumov, I. I.; Bellaiche, L.; Fu, H. Unusual phase transitions in ferroelectric nanodisks and nanorods. *Nature* **2004**, *432*, 737-740.

83. Scott, J. F. Nanoferroelectrics: statics and dynamics. *Journal of Physics-Condensed Matter* **2006**, *18* (17), R361-R386.
84. Gorbatsevich, A. A.; Kopaev, Y. Toroidal order in crystals. *Ferroelectrics* **1994**, *161* (1), 321-334.
85. Vivekanandan, R.; Kutty, T. R. N. Characterization of barium titanate fine powders formed from hydrothermal crystallization. *Powder Technology* **1989**, *57* (3), 181-192.
86. Waser, R. Solubility of Hydrogen Defects in Doped and Undoped BaTiO<sub>3</sub>. *Journal of the American Ceramic Society* **1988**, *71* (1), 58-63.
87. Baikov, Y. M.; Shalkova, E. K. Hydrogen in Perovskites. *Journal of Solid State Chemistry* **1992**, *97* (1), 224-227.
88. Hennings, D.; Schreinemacher, S. Characterization of hydrothermal barium titanate. *Journal of the European Ceramic Society* **1992**, *9* (1), 41-46.
89. Begg, B. D.; Vance, E. R.; Nowotny, J. Effect of Particle-Size on the Room-Temperature Crystal-Structure of Barium-Titanate. *Journal of the American Ceramic Society* **1994**, *77* (12), 3186-3192.
90. Chu, M. W.; Szafraniak, I.; Scholz, R.; Harnagea, C.; Hesse, D.; Alexe, M.; Gosele, U. Impact of misfit dislocations on the polarization instability of epitaxial nanostructured ferroelectric perovskites. *Nature Materials* **2004**, *3* (2), 87-90.
91. Mead, C. A. Anomalous Capacitance of Thin Dielectric Structures. *Physical Review Letters* **1961**, *6* (10), 545-&.
92. Zhou, C.; News, D. M. Intrinsic dead layer effect and the performance of ferroelectric thin film capacitors. *Journal of Applied Physics* **1997**, *82* (6), 3081-3088.
93. Sirenko, A. A.; Bernhard, C.; Golnik, A.; Clark, A. M.; Hao, J. H.; Si, W. D.; Xi, X. X. Soft-mode hardening in SrTiO<sub>3</sub> thin films. *Nature* **2000**, *404* (6776), 373-376.
94. Stengel, M.; Spaldin, N. A. Origin of the dielectric dead layer in nanoscale capacitors. *Nature* **2006**, *443* (7112), 679-682.

95. McMillen, M.; Mcquaid, R. G. P.; Haire, S. C.; McLaughlin, C. D.; Chang, L. W.; Schilling, A.; Gregg, J. M. The influence of notches on domain dynamics in ferroelectric nanowires. *Applied Physicss Letters* **2010**, *96* (4).
96. Louis, L.; Gemeiner, P.; Ponomareva, I.; Bellaiche, L.; Geneste, G.; Ma, W.; Setter, N.; Dkhil, B. Low-Symmetry Phases in Ferroelectric Nanowires. *Nano Letters* **2010**, *10*, 1177-1183.
97. Gruverman, A.; Kholkin, A. Nanoscale ferroelectrics: processing, characterization and future trends. *Reports on Progress in Physics* **2006**, *69*, 2443-2474.
98. Xia, Y.; Yang, P.; Sun, Y.; Wu, Y.; Mayers, B.; Gates, B.; Yin, Y.; Kim, F.; Yan, H. One -Dimensional Nanostructures: Synthesis, Characterization, and Applications. *Advanced Materials* **2003**, *15* (No. 5), 353-389.
99. Stanishevsky, A.; Aggarwal, S.; Prakash, A. S.; Melngailis, J.; Ramesh, R. Focused ion-beam patterning of nanoscale ferroelectric capacitors. *Journal of Vacuum Science & Technology B* **1998**, *16* (6), 3899-3902.
100. Alexe, M.; Harnagea, C.; Hesse, D.; Gosele, U. Patterning and switching of nanosize ferroelectric memory cells. *Applied Physics Letters* **1999**, *75* (12), 1793-1795.
101. Xu, G.; Ren, Z. H.; Du, P. Y.; Weng, W. J.; Shen, G.; Han, G. R. Polymer-assisted hydrothermal synthesis of single-crystalline tetragonal perovskite  $\text{PbZr}_{0.52}\text{Ti}_{0.48}\text{O}_3$  nanowires. *Advanced Materials* **2005**, *17* (7), 907-910.
102. Zhang, S. Y.; Jiang, F. S.; Qu, G.; Lin, C. Y. Synthesis of single-crystalline perovskite barium titanate nanorods by a combined route based on sol-gel and surfactant-templated methods. *Materials Letters* **2008**, *62* (16), 2225-2228.
103. Limmer, S. J.; Seraji, S.; Forbess, M. J.; Wu, Y.; Chou, T. P.; Nguyen, C.; Cao, G. Z. Electrophoretic growth of lead zirconate titanate nanorods. *Advanced Materials* **2001**, *13* (16), 1269-1272.
104. Limmer, S. J.; Seraji, S.; Wu, Y.; Chou, T. P.; Nguyen, C.; Cao, G. Z. Template-based growth of various oxide nanorods by sol-gel electrophoresis. *Advanced Functional Materials* **2002**, *12* (1), 59-64.
105. Limmer, S. J.; Cao, G. Sol-gel Electrophoretic Deposition for the Growth of Oxide Nanorods. *Advanced Materials* **2003**, *15* (5), 427-431.

106. Hernandez, B. A.; Chang, K.-S.; Fisher, R. E.; Dorhout, P. K. Sol-Gel Template Synthesis and Characterization of BaTiO<sub>3</sub> and PbTiO<sub>3</sub> Nanotubes. *Chemistry of Materials* **2002**, *14*, 480-482.
107. Morrison, F. D.; Luo, Y.; Szafraniak, I.; Nagarajan, V.; Wehrspohn, R. B.; Steinhart, M.; Wendorff, J. H.; Zakharov, N. D.; Mishina E.D.; Vorotilov, K. A.; Sigov, A. S.; Nabayashi, S.; Alexe, M.; Ramesh, R.; Scott, J. F. Ferroelectric Nanotubes. *Reviews on Advanced Materials Science* **2003**, *4*, 114-122.
108. Park, T.-J.; Mao, Y.; Wong, S. S. Synthesis and characterization of multiferroic BiFeO<sub>3</sub> nanotubes. *Chemical Communications* **2004**, (2708), 2709.
109. Zhao, L.; Steinhart, M.; Yosef, M.; Lee, S. K.; Schlecht, S. Large-scale template-assisted growth of LiNbO<sub>3</sub> one-dimensional nanostructures for nano-sensors. *Sensors and Actuators B* **2005**.
110. Mishina, E. D.; Vorotilov, K. A.; Vasil'ev, V. A.; Sigov, A. S.; Ohta, N.; Nakabayashi, S. Porous silicon-based ferroelectric nanostructures. *Journal of Experimental and Theoretical Physics* **2002**, *95* (3), 502-504.
111. Steinhart, M.; Wehrspohn, R. B.; sele, U.; Wendorff, J. H. Nanotubes by template wetting: A modular assembly system. *Angewandte Chemie - International Edition* **2004**, *43* (11), 1334-1344.
112. Huffman, M. Liquid source misted chemical deposition (LSMCD) critical review. *Integrated Ferroelectrics: An International Journal* **1995**, *10* (1), 39-53.
113. Limmer, S. J.; Cao, G. Z. Sol-gel electrophoretic deposition for the growth of oxide nanorods. *Advanced Materials* **2003**, *15* (5), 427-431.
114. Mao, Y.; Banerjee, S.; Wong, S. S. Hydrothermal synthesis of perovskite nanotubes. *Chemical Communications* **2003**, 408-409.
115. Mao, Y.; Park, T.-J.; Zhang, F.; Zhou, H.; Wong, S. S. Environmentally Friendly Methodologies of Nanostructure Synthesis. *Small* **2007**, *3* (7), 1122-1139.
116. Bao, N. Z.; Shen, L. M.; Srinivasan, G.; Yanagisawa, K.; Gupta, A. Shape-controlled monocrystalline ferroelectric barium titanate nanostructures: From nanotubes and nanowires to ordered nanostructures. *Journal of Physical Chemistry C* **2008**, *112* (23), 8634-8642.

117. Buscaglia, M. T.; Harnagea, C.; Dappiagi, M.; Buscaglia, V.; Pignolet, A.; Nanni, P. Ferroelectric BaTiO<sub>3</sub> Nanowires by a Topochemical Solid-State Reaction. *Chemistry of Materials* **2009**, *21* (21), 5058-5065.
118. Kang, S. O.; Park, B. H.; Kim, Y. I. Growth mechanism of shape-controlled barium titanate nanostructures through soft chemical reaction. *Crystal Growth & Design* **2008**, *8* (9), 3180-3186.
119. Padture, N. P.; Wei, X. Z. Hydrothermal synthesis of thin films of barium titanate ceramic nano-tubes at 200 degrees C. *Journal of the American Ceramic Society* **2003**, *86* (12), 2215-2217.
120. Poyato, R.; Huey, B. D.; Padture, N. P. Local piezoelectric and ferroelectric responses in nanotube-patterned thin films of BaTiO<sub>3</sub> synthesized hydrothermally at 200 degrees C. *Journal of Materials Research* **2006**, *21* (3), 547-551.
121. Zhao, J. L.; Wang, X. H.; Chen, R. Z.; Li, L. T. Synthesis of thin films of barium titanate and barium strontium titanate nanotubes on titanium substrates. *Materials Letters* **2005**, *59* (18), 2329-2332.
122. Urban, J. J.; Yun, W. S. G. Q. P. H. Synthesis of Single-Crystalline Perovskite Nanorods Composed of Barium Titanate and Strontium Titanate. *Journal of the American Chemical Society* **2002**, *124* (No.7), 1186-1187.
123. Urban, J. J.; Spanier, J. E.; Ouyang, L. Y. W. S.; Park, H. Single-Crystalline Barium Titanate Nanowires. *Advanced Materials* **2003**, *15* (No.5), 423-426.
124. O'Brien, S.; Brus, L.; Murray, C. B. Synthesis of Monodisperse Nanoparticles of Barium Titanate: Toward a Generalized Strategy of Oxide Nanoparticle Synthesis. *Journal of the American Chemical Society* **2001**, *123*, 12085-12086.
125. Manna, L.; Scher, E. C.; Alivisatos, A. P. Synthesis of soluble and processable rod-, arrow-, teardrop-, and tetrapod-shaped CdSe nanocrystals. *Journal of the American Chemical Society* **2000**, *122* (51), 12700-12706.
126. Mao, Y.; Banerjee, S.; Wong, S. S. Large-Scale Synthesis of Single-Crystalline Perovskite Nanostructures. *Journal of the American Chemical Society* **2003**, *125*, 15718-15719.
127. Mao, Y. Nanostructured Transition Metal Oxide Materials: Synthesis, Characterization, and Properties. Stony Brook University, **2006**.

128. Dirksen, J. A.; Ring, T. A. Fundamentals of Crystallization: Kinetic Effects on Particle Size Distributions and Morphology. *Chemical Engineering Science* **1991**, *46* (10), 2389-2427.
129. Puntès, V. F.; Krishnan, K. M.; Alivisatos, A. P. Colloidal Nanocrystal Shape and Size Control: The Case of Cobalt. *Science* **2001**, *291* (5511), 2115-2117.
130. Murphy, C. J.; Jana, N. R. Controlling the aspect ratio of inorganic nanorods and nanowires. *Advanced Materials* **2002**, *14* (1), 80-82.
131. Filankembo, A.; Giorgio, S.; Lisiecki, I.; Pileni, M. P. Is the anion the major parameter in the shape control of nanocrystals? *Journal of Physical Chemistry B* **2003**, *107* (30), 7492-7500.
132. Filankembo, A.; Pileni, M. P. Is the template of self-colloidal assemblies the only factor that controls nanocrystal shapes? *Journal of Physical Chemistry B* **2000**, *104* (25), 5865-5868.
133. Ren, Z. H.; Xu, G.; Wei, X.; Liu, Y.; Shen, G.; Han, G. R. Shape evolution of Pb (Zr,Ti)O<sub>3</sub> nanocrystals under hydrothermal conditions. *Journal of the American Ceramic Society* **2007**, *90* (8), 2645-2648.
134. Paik, U.; Hackley, V. A.; Lee, J.; Lee, S. Effect of poly(acrylic acid) and poly(vinyl alcohol) on the solubility of colloidal BaTiO<sub>3</sub> in an aqueous medium. *Journal of Materials Research* **2003**, *18* (5), 1266-1274.
135. de Laat, A. W. M.; van den Heuvel, G. L. T. Molecular weight fractionation in the adsorption of polyacrylic acid salts onto BaTiO<sub>3</sub>. *Colloids and Surfaces A: Physicochemical and Engineering Aspects* **1995**, *98* (1-2), 53-59.
136. Saravanan, L.; Subramanian, S. Surface chemical studies on the competitive adsorption poly(ethylene glycol) and ammonium poly(methacrylate) onto of alumina. *Journal of Colloid and Interface Science* **2005**, *284* (2), 363-377.
137. Banfield, J. F.; Welch, S. A.; Zhang, H.; Ebert, T. T.; Penn, R. L. Aggregation-Based Crystal Growth and Microstructure Development in Natural Iron Oxyhydroxide Biomineralization Products. *Science* **2000**, *289* (5480), 751-754.
138. Alivisatos, A. P. BIOMINERALIZATION: Enhanced: Naturally Aligned Nanocrystals. *Science* **2000**, *289* (5480), 736-737.

139. Penn, R. L.; Banfield, J. F. Imperfect Oriented Attachment: Dislocation Generation in Defect-Free Nanocrystals. *Science* **1998**, *281* (5379), 969-971.
140. Joshi, U. A.; Lee, J. S. Template-free hydrothermal synthesis of single-crystalline barium titanate and strontium titanate nanowires. *Small* **2005**, *1* (12), 1172-1176.
141. Joshi, U. A.; Yoon, S.; Balk, S.; Lee, J. S. Surfactant-free hydrothermal synthesis of highly tetragonal barium titanate nanowires: A structural investigation. *Journal of Physical Chemistry B* **2006**, *110* (25), 12249-12256.
142. Yu, S. H.; Kiu, B.; Mo, M. S.; Huang, J. H.; Liu, X. M.; Qian, Y. T. General Synthesis of Single-Crystal Tungstate Nanorods/Nanowires: A Facile, Low-temperature Solution Approach. *Advanced Functional Materials* **2003**, *13* (6), 639-647.
143. Wang, W.; Xu, C.; Wang, G.; Liu, Y.; Zheng, C. Preparation of Smooth Single-Crystal  $Mn_3O_4$  Nanowires. *Advanced Materials*. **2002**, *14* (11), 837-840.
144. Quere, D.; di Meglio, J. M.; Brochard-Wyart, F. Spreading of Liquids on Highly Curved Surfaces. *Science* **1990**, *249* (4974), 1256-1260.
145. Mullin, J. W. *Crystallization*; Butterworth-Heinemann: Oxford, **1997**.
146. Nielsen, A. E. *Kinetics of Precipitation*; Pergamon Press: Oxford, **1964**.
147. Vasco, E.; Magrez, A.; Forro, L.; Setter, N. Growth Kinetics of One-Dimensional  $KNbO_3$  Nanostructures by Hydrothermal Processing Routes. *Journal of Physical Chemistry B* **2005**, *109*, 14331-14334.
148. Magrez, A.; Vasco, E.; Seo, J. W.; Dieker, C.; Setter, N.; Forro, L. Growth of single-crystalline  $KNbO_3$  nanostructures. *Journal of Physical Chemistry B* **2006**, *110* (1), 58-61.
149. Yuh, J.; Perez, L.; Sigmund, W. M.; Nino, J. C. Sol-gel based synthesis of complex oxide nanofibers. *Journal of Sol-Gel Science and Technology* **2007**, *42* (3), 323-329.
150. Hu, J.; Odom, T. W.; Lieber, C. M. Chemistry and Physics in One Dimension: Synthesis and Properties of Nanowires and Nanotubes. *Accounts of Chemical Research* **1999**, *32*, 435-445.

151. Patzke, R. G.; Krumeich, F.; Neasper, R. Oxidic Nanotubes and Nanorods-Anisotropic Modules for a Future Nanotechnology. *Angewandte Chemie International Edition* **2002**, *41*, 2446-2461.
152. Rao, C. N. R.; Nath, M. Inorganic nanotubes. *Dalton Transactions* **2003**, 1-24.
153. Ishikawa, K.; Nomura, T.; Okada, N.; Takada, K. Size effect on the phase transition in PbTiO<sub>3</sub> fine particles. *Jpn J Appl Phys Part 1 Regul Pap Short Note Rev Pap* **1996**, *35* (9 SUPPL. B), 5196-5198.
154. Berger, S. Size effect on ferroelectric behavior. *Transactions of the Indian Institute of Metals* **2005**, *58* (6), 1141-1156.
155. Uchino, K.; Sadanaga, E.; Hirose, T. Dependence of the Crystal structure on Particle Size in Barium Titanate. *Journal of the American Ceramic Society* **1989**, *72* (8), 1555-1558.
156. Shao, S.; Zhang, J.; Zhang, Z.; Zheng, P.; Zhao, M.; Li, J.; Wang, C. High piezoelectric properties and domain configuration in BaTiO<sub>3</sub> ceramics obtained through the solid-state reaction route. *Journal of Physics D: Applied Physics* **2008**, *41*, 125408.
157. Byrappa, K.; Yoshimura M. *Handbook of Hydrothermal Technology*; Noyes Publications: Park Ridge (N.J.), **2001**.
158. Laudise, R. A.; Nielsen, J. W. Hydrothermal Crystal Growth. *Solid State Physics-Advances in Research and Applications* **1961**, *12*, 149-222.
159. Rabenau, A.; Rau, H. Crystal Growth and Chemical Synthesis Under Hydrothermal Conditions. *Philips Technical Review* **1969**, *30* (4), 89-&.
160. Ganeev, I. G.; Rumjantsev, V. N. Physicochemical Aspect of Hydrothermal Crystal-Growth. *Acta Crystallographica Section A* **1975**, *31*, S209-S210.
161. Lencka, M. M.; Riman, R. E. Thermodynamic Modeling of Hydrothermal Synthesis of Ceramic Powders. *Chemistry of Materials* **1993**, *5* (1), 61-70.
162. Riman, R. E.; Lencka, M.; McCandlish, L.; Gersten, B. L.; Anderko, A.; Cho, S.-B. Intelligent Engineereing on Hydrothermal Reaction. **1996**; pp 148-151.

- 
163. Lee, B. I.; Wang, M.; Yoon, D.; Hu, M. Aqueous processing of barium titanate powders. *Journal of Ceramic Processing Research* **2003**, *4* (1), 17-24.
164. Eckert Jr., J. O.; Hung-Houston, C. C.; Gersten, B. L.; Lencka, M. M.; Riman, R. E. Kinetics and Mechanisms of Hydrothermal Synthesis of Barium Titanate. *Journal of the American Ceramic Society* **1996**, *79* (11), 2929-2939.
165. Hertl, W. Kinetics of Barium Titanate Synthesis. *Journal of the American Ceramic Society* **1988**, *71* (10), 879-883.
166. Testino, A.; Buscaglia, V.; Buscaglia, M. T.; Viviani, M.; Nanni, P. Kinetic Modeling of Aqueous and Hydrothermal Synthesis of Barium Titanate (BaTiO<sub>3</sub>). *Chemistry of Materials* **2005**, *17*, 5346-5356.
167. Feng, Q.; Hirasawa, M.; Yanagisawa, K. Synthesis of crystal-axis-oriented BaTiO<sub>3</sub> and anatase platelike particles by a hydrothermal soft chemical process. *Chemistry of Materials* **2001**, *13* (2), 290-296.
168. Hennings, D.; Rosenstein, G.; Schreinemacher, H. Hydrothermal Preparation of Barium Titanate from Barium-Titanium Acetate Gel Precursors. *Journal of the European Ceramic Society* **1991**, *8*, 107-115.
169. Moon, J.; Kerchner, J. A.; Krarup, H.; Adair, J. H. Hydrothermal synthesis of ferroelectric perovskites from chemically modified titanium isopropoxide and acetate salts. *Journal of Materials Research* **1999**, *14* (2), 425-435.
170. Viviani, M.; Buscaglia, M. T.; Testino, A.; Buscaglia, V.; Bowen, P.; Nanni, P. The influence of concentration on the formation of BaTiO<sub>3</sub> by direct reaction of TiCl<sub>4</sub> with Ba(OH)<sub>2</sub> in aqueous solution. *Journal of the European Ceramic Society* **2003**, *23*, 1383-1390.
171. Li, Y.; Gao, X. P.; Li, G. R.; Pan, G. L.; Yan, T. Y.; Zhu, H. Y. Titanate Nanofiber Reactivity: Fabrication of MTiO<sub>3</sub> (M = Ca, Sr, and Ba) Perovskite Oxides. *Journal of Physical Chemistry C* **2009**, *113* (11), 4386-4394.
172. Internet Communication **2009**. <http://www.icdd.com/>
173. Als-Nielsen, J.; McMorrow, D. *Elements of Modern X-ray Physics*; John Wiley & Sons Ltd.: London, **2001**.
174. Cullity, B. D. *Elements of X-ray Diffraction*; 2nd Ed ed.; Addison-Wesley: London, **1978**.

175. Dinnebier, R. E.; Billinge, S. J. L. *Powder Diffraction: Theory and Practice*; The Royal Society of Chemistry: Cambridge, **2008**.
176. CCP14 Internet Communication **2010**.  
[http://www.ccp14.ac.uk/solution/rietveld\\_software/](http://www.ccp14.ac.uk/solution/rietveld_software/)
177. *JADE*, version 5.0; 2004
178. Moon, J.; Suvaci, E.; Morrone, A.; Costantino, S. A.; Adair, J. H. Formation mechanisms and morphological changes during the hydrothermal synthesis of BaTiO<sub>3</sub> particles from a chemically modified, amorphous titanium (hydrous) oxide precursor. *Journal of the European Ceramic Society* **2003**, 23 (12), 2153-2161.
179. Gans, P. *Vibrating molecules: an introduction to the interpretation of infrared and raman spectra*; Chapman and Hall: London, 1971.
180. Internet Communication 2009. [www.wikipedia.com](http://www.wikipedia.com)
181. Coates, J. Interpretation of Infrared Spectra, A Practical Approach. *Encyclopedia of Analytical Chemistry* ed.; Meyers, R. A., Ed.; John Wiley & Sons Ltd: Chichester, **2000**; pp 10815-10837.
182. West, A. *Solid State Chemistry*; John Wiley & Sons Ltd.: London, **1984**.
183. Last, J. T. Infrared-Absorption Studies on Barium Titanate and Related Materials. *Phys. Rev.* **1957**, 105 (6), 1740-1750.
184. Rimai, L.; Parsons, J. L.; Hickmott, J. T. Raman Spectrum of Long-Wavelength Phonons in Tetragonal Barium Titanate. *Physical Reviews.* **1968**, 168 (2), 623-630.
185. *Encyclopedia of Materials: Science and Technology*; Elsevier Ltd.: **2007**.
186. Williams, D. B.; Carter, C. B. *Transmission Electron Microscopy*; Plenum Press: New York and London, **1996**.
187. Paul Preuss Internet Communication **2001**.  
[http://www.lbl.gov/Publications/Currents/Archive/May-18-2001.html#\\_Hlk514817949](http://www.lbl.gov/Publications/Currents/Archive/May-18-2001.html#_Hlk514817949)
188. Nellist, P. D.; Chisholm, M. F.; Dellby, N.; Krivanek, O. L.; Murfitt, M. F.; Szilagy, Z. S.; Lupini, A. R.; Borisevich, A.; Sides, W. H., Jr.; Pennycook, S.

- J. Direct Sub-Angstrom Imaging of a Crystal Lattice. *Science* **2004**, 305 (5691), 1741.
189. Office of Basic Energy Sciences Internet Communication **2009**.  
[http://www.sc.doe.gov/bes/scale\\_of\\_things.html](http://www.sc.doe.gov/bes/scale_of_things.html)
190. Goldstein, J.; Newbury, D.; Joy, D.; Lyman, C.; Echlin, P.; Sawyer, L.; Michael, J. *Scanning Electron Microscopy and X-Ray Microanalysis*; Kluwer Academic, Plenum Publishers: New York, **2003**.
191. McMullan, D. Internet Communication **1993**.  
<http://www-g.eng.cam.ac.uk/125/achievements/mcmullan/mcm.htm>
192. Egerton, R. F. *Electron Energy Loss Spectroscopy in the Electron Microscope*; Plenum: New York, **1996**.
193. Taub, M.; Menzel, B.; Khanna, G.; Lilleodden, E. *SPM Training Manual*; Laboratory for Advanced Materials, Stanford University: **2003**.
194. Kalinin, S. V.; Rar, A.; Jesse, S. A decade of piezoresponse force microscopy: Progress, challenges, and opportunities. *Ieee Transactions on Ultrasonics Ferroelectrics and Frequency Control* **2006**, 53 (12), 2226-2252.
195. Gruverman, A.; Kalinin, S. V. Piezoresponse force microscopy and recent advances in nanoscale studies of ferroelectrics. *Journal of Materials Science* **2006**, 41 (1), 107-116.
196. Gruverman, A. Personal Communication at CNMS Workshop on PFM, Oak Ridge National Laboratory, October 8-9 **2007**.
197. Eliseev, E. A.; Kalinin, S. V.; Jesse, S.; Bravina, S. L.; Morozovska, A. N. Electromechanical detection in scanning probe microscopy: Tip models and materials contrast. *Journal of Applied Physics* **2007**, 102 (1).
198. Jesse, S.; Baddorf, A. P.; Kalinin, S. V. Dynamic behaviour in piezoresponse force microscopy. *Nanotechnology* **2006**, 17 (6), 1615-1628.
199. Harnagea, C. Local piezoelectric response and domain structures in ferroelectric thin films investigated by voltage-modulated force microscopy. **2001**, <http://sundoc.bibliothek.uni-halle.de/diss-online/01/01H318/prom.pdf>.
200. Jesse, S.; Lee, H. N.; Kalinin, S. V. Quantitative mapping of switching behavior in piezoresponse force microscopy. *Review of Scientific Instruments* **2006**, 77 (7).

201. Eng, L. M.; Guntherodt, H. J.; Rosenman, G.; Skliar, A.; Oron, M.; Katz, M.; Eger, D. Nondestructive imaging and characterization of ferroelectric domains in periodically poled crystals. *Journal Applied Physics* **1998**, *83* (11), 5973-5977.
202. Eng, L. M.; Abplanalp, M.; Guner, P. Ferroelectric domain switching in triglycine sulphate and barium-titanate bulk single crystals by scanning force microscopy. *Applied Physics A-Materials Science & Processing* **1998**, *66*, S679-S683.
203. Suyal, G.; Colla, E.; Gysel, R.; Cantoni, M.; Setter, N. Piezoelectric response and polarization switching in small anisotropic perovskite particles. *Nano Letters* **2004**, *4* (7), 1339-1342.
204. Speyer, R. F. *Thermo gravimetric analysis*; Dekker, Marcel: New York, **1994**.
205. Navrotsky, A. Energetics and crystal chemical systematics among ilmenite, lithium niobate, and perovskite structures. *Chemistry of Materials* **1998**, *10* (10), 2787-2793.
206. Pecora, R. Dynamic Light Scattering Measurement of Nanometer Particles in Liquids. *Journal of Nanoparticle Research* **2000**, *2* (2), 123-131.
207. Seymour, L.; Shields, J. E. *Powder Surface Area and Porosity*; Kluwer Academic Publishers Group: **1991**.
208. Grigorieva, A. V.; Goodilin, E. A.; Derlyukova, L. E.; Anufrieva, T. A.; Tarasov, A. B.; Dobrovolskii, Y. A.; Tretyakov, Y. D. Titania nanotubes supported platinum catalyst in CO oxidation process. *Applied Catalysis A-General* **2009**, *362* (1-2), 20-25.
209. Chary, V. R. K.; Kishan, G.; Bhaskar, T.; Sivaraj, C. Structure and Reactivity of Vanadium Oxide Catalysts Supported on Anatase TiO<sub>2</sub>. *Journal of Physical Chemistry B* **1998**, *102* (No.35), 6792-6798.
210. Wei, F. Y.; Sang, L. Highly Photocatalytic Active and Easily Recycled Sulfur-Doped TiO<sub>2</sub> Nanotubes. *Chinese Journal of Catalysis* **2009**, *30* (4), 335-339.
211. Woan, K.; Pyrgiotakis, G.; Sigmund, W. Photocatalytic Carbon-Nanotube-TiO<sub>2</sub> Composites. *Advanced Materials* **2009**, *21* (21), 2233-2239.
212. Kavan, L.; Rathousky, J.; Gratzel, M.; Shklover, V.; Zukal, A. *Journal of Physical Chemistry B* **2000**, *104*, 12012-12020.

213. Rather, S. U.; Mehraj-Ud-Din, N.; Zacharia, R.; Hwang, S. W.; Kim, A. R.; Nahm, K. S. Hydrogen storage of nanostructured TiO<sub>2</sub>-impregnated carbon nanotubes. *International Journal of Hydrogen Energy* **2009**, *34* (2), 961-966.
214. Li, X. D.; Zhang, D. W.; Sun, Z.; Chen, Y. W.; Huang, S. M. Metal-free indoline-dye-sensitized TiO<sub>2</sub> nanotube solar cells. *Microelectronics Journal* **2009**, *40* (1), 108-114.
215. O'Regan, B.; Gratzel, M. A low-cost, high-efficiency solar cell based on dye-sensitized colloidal TiO<sub>2</sub> films. *Nature* **1991**, *353*, 737-740.
216. Hoyer, P. Formation of a Titanium Dioxide Nanotube Array. *Langmuir* **1996**, *12*, 1411-1413.
217. Kasuga, T.; Hiramatsu, M.; Hoson, A.; Sekino, T.; Niihara, K. Formation of Titanium Oxide Nanotube . *Langmuir* **1998**, *14*, 3160-3163.
218. Kasuga, T.; Hiramatsu, M.; Hoson, A.; Sekino, T.; Niihara, K. Titania Nanotubes Prepared by Chemical Processing. *Advanced Materials* **1999**, *11* (15), 1307-1311.
219. Chen, Q.; Du, G.; Zhang, S.; Peng, L.-M. The structure of trititanate nanotubes. *Acta Crystallographica B* **2002**, *58*, 587-593.
220. Ma, R.; Bando, Y.; Sasaki, T. Nanotubes of lepidocrocite titanates. *Chemical Physics Letters* **2003**, *380*, 577-582.
221. Yoshida, R.; Suzuki, Y.; Yoshikawa, S. Effects of synthetic conditions and heat-treatment on the structure of partially ion-exchanged titanate nanotubes. *Materials Chemistry and Physics* **2005**, *91* (2-3), 409-416.
222. Tsai, C.-C.; Teng, H. Structural Features of Nanotubes Synthesized from NaOH Treatment on TiO<sub>2</sub> with Different Post-Treatments. *Chem. Mater.* **2006**, *18*, 367-373.
223. Ou, H. H.; Lo, S. L. Review of titania nanotubes synthesized via the hydrothermal treatment: Fabrication, modification, and application. *Separation and Purification Technology* **2007**, *58*, 179-191.
224. Bavykin, D. V.; Friedrich, J. M.; Walsh, F. C. Protonated Titanates and TiO<sub>2</sub> Nanostructured materials: Synthesis, Properties and Applications. *Advanced Materials* **2006**, *18*, 2807-2824.

225. Yang, J.; Jin, Z.; Wang, X.; Li, W.; Zhang, J.; Zhang, S.; Guo, X.; Zhang, Z. Study on composition, structure and formation process of nanotube  $\text{Na}_2\text{Ti}_2\text{O}_4(\text{OH})_2$ . *Dalton Transactions* **2003**, 3898-3901.
226. Du, G. H.; Chen, Q.; Che, R. C.; Yuan, Z.-Y.; Peng, L.-M. Preparation and structure analysis of titanium oxide nanotubes. *Applied Physics Letters* **2001**, 79 (22), 3702-3704.
227. Bao, N. Z.; Shen, L. M.; Gupta, A.; Tatarenko, A.; Srinivasan, G.; Yanagisawa, K. Size-controlled one-dimensional monocrystalline  $\text{BaTiO}_3$  nanostructures. *Applied Physics Letters* **2009**, 94 (25).
228. Qian, L.; Du, Z.-L.; Yang, S.-I.; Jin, Z. Raman study of titania nanotube by soft chemical process. *Journal of Molecular Structure* **2005**, 749, 103-107.
229. Izawa, H.; Kikkawa, S.; Koizumul, M. Ion Exchange and Dehydration of Layered Titanates,  $\text{Na}_2\text{Ti}_3\text{O}_7$  and  $\text{K}_2\text{Ti}_4\text{O}_9$ . *Journal of Physical Chemistry* **1982**, 86, 5023-5026.
230. Byeon, S. H.; Lee, S. O.; Kim, H. J. Structure and Raman Spectra of Layered Titanium Oxides. *Journal of Solid State Chemistry* **1997**, 130, 110-116.
231. Zhang, M.; Jin, Z.; Zhang, J.; Guo, X.; Yang, J.; Li, W.; Wang, X.; Zhang, Z. Effect of annealing temperature on morphology, structure and photocatalytic behavior of nanotubed  $\text{H}_2\text{Ti}_2\text{O}_4(\text{OH})_2$ . *Journal of Molecular Catalysis A: Chemical* **2004**, 217, 203-210.
232. Nian, J.-N.; Teng, H. Hydrothermal Synthesis of Single-Crystalline Anatase  $\text{TiO}_2$  Nanorods with Nanotubes as the Precursor. *Journal of Physical Chemistry B* **2006**, 110, 4193-4198.
233. Zhang, S.; Peng, L.-M.; Chen, Q.; Du, G.; Dawson, G.; Zhou, W. Z. Formation Mechanism of  $\text{H}_2\text{Ti}_3\text{O}_7$  Nanotubes. *Physical Review Letters* **2003**, 91 (25), 256103-1-256103-4.
234. Chen, Q.; Zhou, W.; Du, G.; Peng, L.-M. Trititanate Nanotubes made via a Single Alkali Treatment. *Advanced Materials* **2002**, 14 (17), 1208-1211.
235. Thorne, A.; Kruth, A.; Tunstall, D.; Irvine, J. T. S.; Zhou, W. Formation, Structure, and Stability of Titanate Nanotubes and their Proton Conductivity. *Journal of Physical Chemistry B* **2005**, 109, 5439-5444.

- 
236. Bavykin, D. V.; Friedrich, J. M.; Lapkin, A. A.; Walsh, F. C. Stability of Aqueous Suspensions of Titanate Nanotubes. *Chemistry of Materials* **2006**, *18*, 1124-1129.
237. Yuan, Z.-Y.; Su, B.-L. Titanium oxide nanotubes, nanofibers and nanowires. *Colloids and Surfaces A: Physicochem. Eng. Aspects* **2004**, *241*, 173-183.
238. Ma, R.; Fukuda, K.; Sasaki, T.; Osada, M.; Bando, Y. Structural Features of Titanate Nanotubes/Nanobelts Revealed by Raman, X-ray Absorption Fine Structure and Electron Diffraction Characterizations. *Journal of Physical Chemistry B* **2005**, *109*, 6210-6214.
239. Tsai, C. C.; Teng, H. Nanotube formation from a sodium titanate powder via low-temperature acid treatment. *Langmuir* **2008**, *24* (7), 3434-3438.
240. Sasaki, T.; Watanabe, M. Osmotic swelling to exfoliation. Exceptionally high degrees of hydration of a layered titanate. *Journal of the American Chemical Society* **1998**, *120* (19), 4682-4689.
241. Kim, G. S.; Seo, H. K.; Godble, V. P.; Kim, Y. S.; Yang, O. B.; Shin, H. S. Electrophoretic deposition of titanate nanotubes from commercial titania nanoparticles: Application to dye-sensitized solar cells. *Electrochemistry Communications* **2006**, *8* (6), 961-966.
242. Kim, G. S.; Godbole, V. P.; Seo, H. K.; Kim, Y. S.; Shin, H. S. Sodium removal from titanate nanotubes in electrodeposition process. *Electrochemistry Communications* **2006**, *8* (3), 471-474.
243. Kim, G. S.; Ansari, S. G.; Seo, H. K.; Kim, Y. S.; Shin, H. S. Effect of annealing temperature on structural and bonded states of titanate nanotube films. *J Appl Phys* **2007**, *101* (2), 024314-1-024314-6.
244. Qamar, M.; Yoon, C. R.; Oh, H. J.; Kim, D. H.; Jho, J. H.; Lee, K. S.; Lee, W. J.; Lee, H. G.; Kim, S. J. Effect of post treatments on the structure and thermal stability of titanate nanotubes. *Nanotechnology* **2006**, *17* (24), 5922-5929.
245. Boercker, J. E.; Enache-Pommer, E.; Aydil, E. S. Growth mechanism of titanium dioxide nanowires for dye-sensitized solar cells. *Nanotechnology* **2008**, *19* (9).
246. Penn, R. L.; Banfield, J. F. Morphology development and crystal growth in nanocrystalline aggregates under hydrothermal conditions: Insights from titania. *Geochimica et Cosmochimica Acta* **1999**, *63* (10), 1549-1557.

- 
247. Kolen'ko, Y. V.; Kovnir, K. A.; Gavrilov, A. I.; Garshev, A. V.; Frantti, J.; Lebedev, O. I.; Churagulov, B. R.; van Tendeloo, G.; Yoshimura, M. Hydrothermal Synthesis and Characterization of Nanorods of Various Titanates and Titanium Dioxide. *J. Phys. Chem. B* **2006**, *110*, 4030-4038.
248. Mao, Y.; Wong, S. S. Size- and Shape-Dependent Transformation of Nanosized Titanate into Analogous Anatase Titania Nanostructures. *J. Am. Chem. Soc.* **2006**, *128*, 8217-8226.
249. Meldrum, F. C.; Colfen, H. Controlling Mineral Morphologies and Structures in Biological and Synthetic Systems. *Chemical Reviews* **2008**, *108* (11), 4332-4432.
250. Smith, J. R.; Walsh, F. C.; Clarke, R. L. Reviews in applied electrochemistry. Number 50 - Electrodes based on Magneli phase titanium oxides: the properties and applications of Ebonex (R) materials. *Journal of Applied Electrochemistry* **1998**, *28* (10), 1021-1033.
251. Langlade, C.; Vannes, B.; Sarnet, T.; Autric, M. Characterization of titanium oxide films with Magneli structure elaborated by a sol-gel route. *Applied Surface Science* **2002**, *186* (1-4), 145-149.
252. Han, W. Q.; Zhang, Y. Magneli phases  $Ti_nO_{2n-1}$  nanowires: Formation, optical, and transport properties. *Applied Physics Letters* **2008**, *92* (20).
253. Watanabe, M.; Ugarte, W. Raman study of order-disorder transition of bipolarons in  $Ti_4O_7$ . *Physica Status Solidi (C)* **2006**, *3* (10), 3456-3459.
254. Scott, J. F.; Morrison, F. D.; Miyake, M.; Zubko, P.; Lou, X. J.; Kugler, V. M.; Rios, S.; Zhang, M.; Tatsuta, T.; Tsuji, O.; Leedham, T. J. Recent materials characterizations of [2D] and [3D] thin film ferroelectric structures. *Journal of the American Ceramic Society* **2005**, *88* (7), 1691-1701.
255. Hennings, D. Review of Chemical Preparation Routes for Barium Titanate. *British Ceramic Proceedings* **1989**, *41*, 1-10.
256. Asiaie, R.; Zhu, W.; Akbar, S. A.; Dutta, P. K. Characterization of Submicron Particles of Tetragonal  $BaTiO_3$ . *Chemistry of Materials* **1996**, *8* (1), 226-234.
257. Begg, B. D.; Finnie, K. S.; Vance, E. R. Raman study of the relationship between room-temperature tetragonality and the Curie point of barium titanate. *Journal of the American Ceramic Society* **1996**, *79* (10), 2666-2672.

- 
258. Karma, A. Lectures on Dendritic Growth. In *Branching in Nature*, Fleury, V., Gouyet, J. F., Leonetti, M., Eds.; Springer-Verlag: **2001**; pp 365-401.
259. Walton, R. I.; Millange, F.; Smith, R. I.; Hansen, T. C.; O'Hare, D. Real Time Observation of the Hydrothermal Crystallization of Barium Titanate Using in Situ Neutron Powder Diffraction. *J. Am. Chem. Soc.* **2001**, *123*, 12547-12555.
260. Testino, A.; Buscaglia, M. T.; Buscaglia, V.; Viviani, M.; Bottino, C.; Nanni, P. Kinetics and mechanism of aqueous chemical synthesis of BaTiO<sub>3</sub> particles. *Chemistry of Materials* **2004**, *16* (8), 1536-1543.
261. Hancock, J. D.; Sharp, J. H. Method of Comparing Solid-State Kinetic Data and Its Application to Decomposition of Kaolinite, Brucite, and BaCO<sub>3</sub>. *Journal of the American Ceramic Society* **1972**, *55* (2), 74-77.
262. Avrami, M. Kinetics of phase change I - General theory. *Journal of Chemical Physics* **1939**, *7* (12), 1103-1112.
263. Avrami, M. Granulation, Phase Change, and Microstructure - Kinetics of Phase Change. III. *Journal of Chemical Physics* **1941**, *9* (2), 177-184.
264. Busca, G.; Buscaglia, V.; Leoni, M.; Nanni, P. Solid-State and Surface Spectroscopic Characterization of BaTiO<sub>3</sub> Fine Powders. *Chemistry of Materials* **1994**, *6* (7), 955-961.
265. Clark, I. J.; Takeuchi, T.; Ohtori, N.; Sinclair, D. C. Hydrothermal synthesis and characterisation of BaTiO<sub>3</sub> fine powders: precursors, polymorphism and properties. *Journal of Materials Chemistry*. **1999**, *9*, 83-91.
266. Vivekanandan, R.; Philip, S.; Kutty, T. R. N. Hydrothermal Preparation of Ba(Ti,Zr)O<sub>3</sub> Fine Powders. *Materials Research Bulletin* **1987**, *22* (1), 99-108.
267. Kawasaki, S.; Catalan, G.; Fan, H. J.; Saad, M. M.; Gregg, J. M.; Correa-Duarte, M. A.; Rybczynski, J.; Morrison, F. D.; Tatsuta, T.; Tsuji, O.; Scott, J. F. Conformal oxide coating of carbon nanotubes. *Applied Physics Letters* **2008**, *92* (5).
268. Hennings, D. F. K.; Metzmaier, C.; Schreinemacher, B. S. Defect chemistry and microstructure of hydrothermal barium titanate. *Journal of the American Ceramic Society* **2001**, *84* (1), 179-182.
269. Wu, A.; Vilarinho, P. M.; Shvartsman, V. V.; Suchaneck, G.; Kholkin, A. L. Domain populations in lead zirconate titanate thin films of different

- compositions via piezoresponse force microscopy. *Nanotechnology* **2005**, *16* (11), 2587-2595.
270. Doellein, G.; [Anon] Chemical vapour deposition of oxide films used in MOCVD for uniform vaporisation rate, obtd. by treating aq. soln. or suspension of metal (hydr)oxide with tri- or tetra:methyl-heptan-3,5-di:one etc. EP504706-A; EP504706-A1; DE4108731-A; JP5239066-A; EP504706-B1; DE59202582-G; US5451434-A; US5518536-A, Jan 5, **1996**.
271. Felgner, K.-H.; Mnller, T.; Langhammer, H. T.; Abicht, H.-P. On the formation of BaTiO<sub>3</sub> from BaCO<sub>3</sub> and TiO<sub>2</sub> by microwave and conventional heating. *Materials Letters* **2004**, *58* (12-13), 1943-1947.
272. Simon-Seveyrat, L.; Hajjaji, A.; Emziane, Y.; Guiffard, B.; Guyomar, D. Re-investigation of synthesis of BaTiO<sub>3</sub> by conventional solid-state reaction and oxalate coprecipitation route for piezoelectric applications. *Ceramics International* **2007**, *33* (1), 35-40.
273. Gallegos-Orozco, V.; Martinez-Sanchez, R.; Espinosa-Magala, F. In situ characterization of the ferroelectric transition in BaTiO<sub>3</sub> by EELS and comparison with ab initio methods. *Physical Review B* **2008**, *77* (4), 045128.
274. *Handbook of Chemistry and Physics*; 67th ed.; CRC Press: **1986**.
275. Bagwell, R. B.; Sindel, J.; Sigmund, W. Morphological evolution of barium titanate synthesized in water in the presence of polymeric species. *Journal of Materials Research* **1999**, *14* (5), 1844-1851.
276. Ciftci, E.; Rahaman, M. N. Hydrothermal precipitation and characterization of nanocrystalline BaTiO<sub>3</sub> particles. *Journal of Materials Science* **2001**, *36* (20), 4875-4882.
277. Chen, Z. C.; Ring, T. A.; Lemaitre, J. Stabilization and Processing of Aqueous BaTiO<sub>3</sub> Suspension with Polyacrylic-Acid. *Jouranl of the American Ceramic Society* **1992**, *75* (12), 3201-3208.
278. Pochard, I.; Couchot, P.; Foissy, A. Potentiometric and conductometric analysis of the binding of Barium ions with alkali polyacrylate. *Colloid & Polymer Science* **1998**, *276* (12), 1088-1097.
279. Bury, R.; Desmazieres, B.; Treiner, C. Interactions between poly(vinylpyrrolidone) and ionic surfactants at various solid/water interfaces: a calorimetric investigation. *Colloids and Surfaces A: Physicochemical and Engineering Aspects* **1997**, *127* (1-3), 113-124.

280. Wang, H.; Qiao, X.; Chen, J.; Wang, X.; Ding, S. Mechanisms of PVP in the preparation of silver nanoparticles. *Materials Chemistry and Physics* **2005**, *94*, 449-453.
281. Kobayashi, Y.; Kosuge, A.; Konno, M. Fabrication of high concentration barium titanate/polyvinylpyrrolidone nano-composite thin films and their dielectric properties. *Applied Surface Science* **2008**, *255* (5), 2723-2729.
282. Sovilj, V. J.; Petrovic, L. B. Influence of hydroxypropylmethyl cellulose-sodium dodecylsulfate interaction on the solution conductivity and viscosity and emulsion stability. *Carbohydrate Polymers* **2006**, *64* (1), 41-49.
283. Brinker, C. J.; Scherer, G. W. *Sol-Gel Science*; Academic Press: San Diego (CA), **1990**.
284. Hung, K. M.; Yang, W. D.; Huang, C. C. Preparation of nanometer-sized barium titanate powders by a sol-precipitation process with surfactants. *Journal of the European Ceramic Society* **2003**, *23* (11), 1901-1910.
285. Isbell, H. S. *Carbohydrates in Solution*; American Chemical Society: Washington, **1973**.
286. Dickinson, S. R.; McGrath, K. M. Aqueous Precipitation of Calcium Carbonate Modified by Hydroxyl-Containing Compounds. *Cryst. Growth Des.* **2004**, *4* (6), 1411-1418.
287. Markov, I. V. *Crystal Growth for Beginners*; World Scientific Publishing Co. Pte. Ltd.: **1995**.

## List of publications

1. Maxim, F.; Ferreira, P.; Vilarinho, P. M. Influence of the neutralization process on the preparation of titanate nanotubes by hydrothermal synthesis. *Journal of Porous Materials* **2010**. DOI:10.1007/s10934-010-9354-8.
2. Maxim, F.; Ferreira, P.; Vilarinho, P.; Reaney, I.; Aimable, A.; Bowen, P. Solution based approaches for the morphology control of BaTiO<sub>3</sub> particulates. *Processing and Application of Ceramics* **2010**, 4 (3), 115-125.
3. Maxim, F.; Ferreira, P.; Vilarinho, P. M.; Reaney, I. Hydrothermal synthesis and crystal growth studies of BaTiO<sub>3</sub> using Ti nanotube precursors. *Crystal Growth & Design* **2008**, 8 (9), 3309-3315.
4. Maxim, F.; Vilarinho, P. M.; Ferreira, P.; Reaney, I.; Levin, I. Kinetic Study of the Static Hydrothermal Synthesis of BaTiO<sub>3</sub> using Titanate Nanotubes Precursors. *Crystal Growth & Design* **2010**, *in press*.
5. Maxim, F.; Ferreira, P.; Willinger, M.; Borges, R.; Godinho, M.; Vilarinho, P. The resistance of BaTiO<sub>3</sub> to cast 1D shape by chemical template approach. *Chem. Mater.* **2010**, *to be submitted*.
6. Maxim, F.; Ferreira, P.; Vilarinho, P. M.; Aimable, A.; Bowen, P. Electron-microscopic observation of BaTiO<sub>3</sub> prepared by additive assisted aqueous synthesis. *Microscopy and Microanalysis* **2009**, 15 (Supplement S3), 51-52.
7. Maxim, F.; Ferreira, P.; Vilarinho, P. M.; Aimable, A.; Bowen, P. Additive-assisted aqueous synthesis of BaTiO<sub>3</sub> nanopowders. *Crystal Growth & Design* **2010**, 10, 3996-4004.